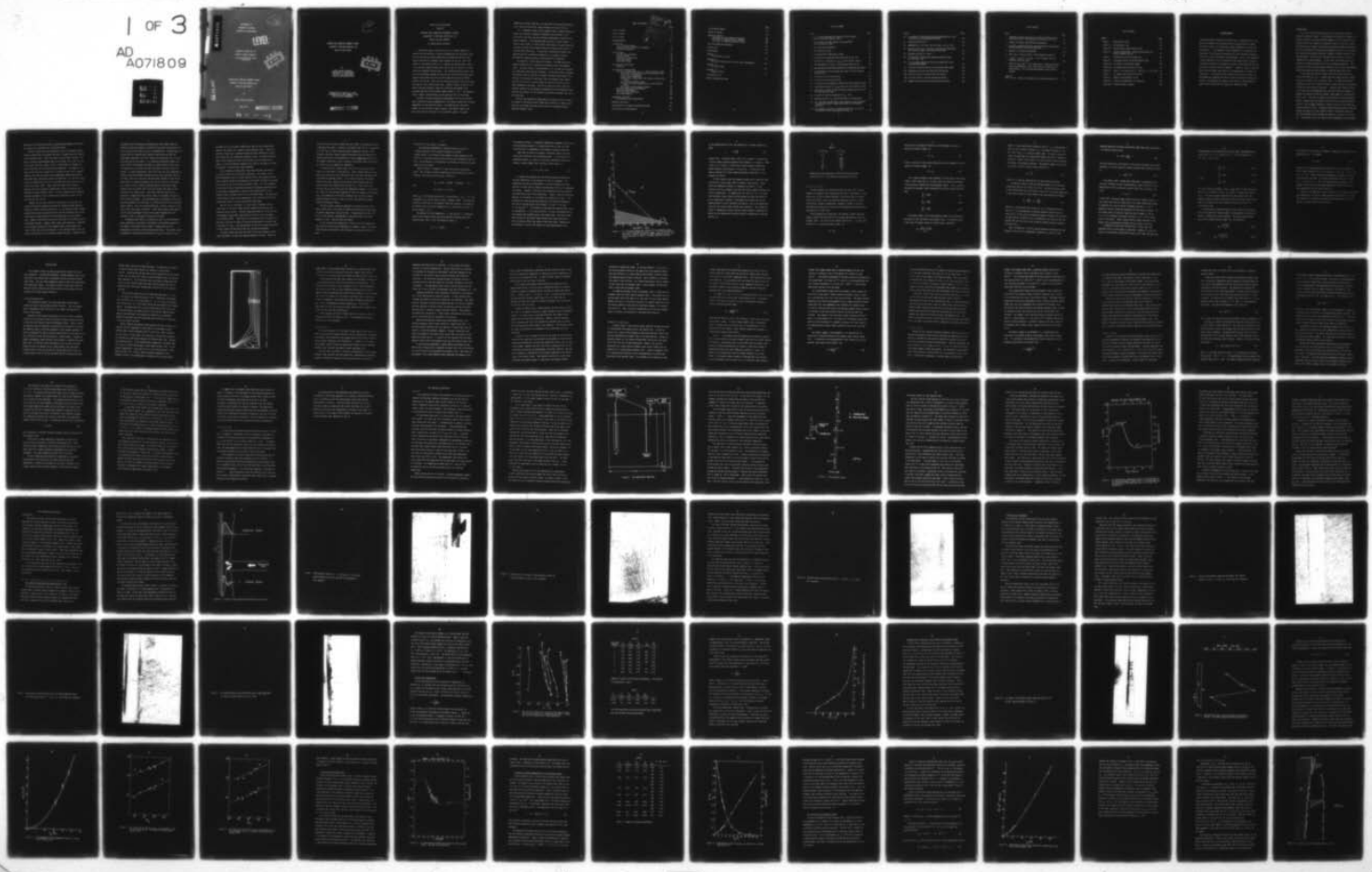
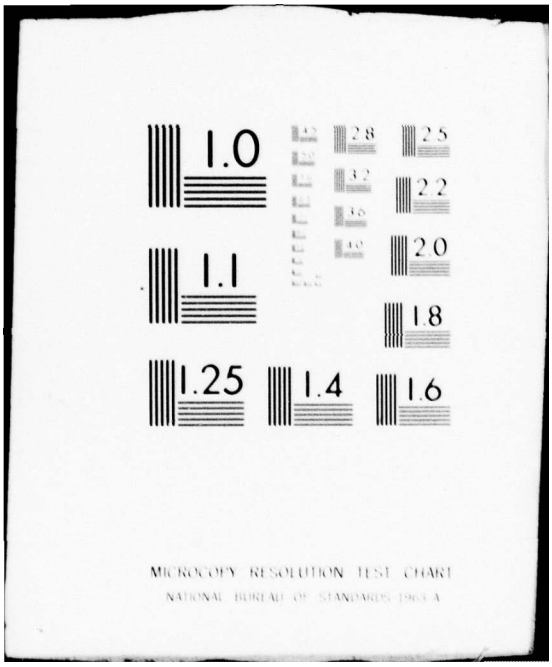
AD-A071 809 WASHINGTON UNIV SEATTLE DEPT OF ATMOSPHERIC SCIENCES F/G 8/12
LAMINAR AND TURBULENT BOUNDARY LAYERS ADJACENT TO MELTING VERTI--ETC(U)
MAY 79 E G JOSBERGER N00014-76-C-0234
UNCLASSIFIED SCIENTIFIC-16 NL

1 OF 3
AD A071809




1.0
1.1
1.25
1.4
1.6
2.8
2.5
2.2
2.0
1.8
MICROCOPY RESOLUTION TEST CHART
NATIONAL BUREAU OF STANDARDS 1963 A

AD A071809

DEPARTMENT OF
ATMOSPHERIC SCIENCES
UNIVERSITY OF WASHINGTON

LEVEL

SCIENTIFIC REPORT NO. 16
OFFICE OF NAVAL RESEARCH
Contract N00014-76-C-0234
NR 307-252

DDC
RECEIVED
JUL 27 1979
C

LAMINAR AND TURBULENT BOUNDARY LAYERS ADJACENT TO MELTING VERTICAL ICE WALLS IN SALT WATER

by

Edward George Josberger

May 1979

DISTRIBUTION UNLIMITED

DDC FILE COPY

79 07 26 004

12

LAMINAR AND TURBULENT BOUNDARY LAYERS ADJACENT TO MELTING VERTICAL ICE WALLS IN SALT WATER

DDC
RECEIVED
JUL 27 1979
C

by

Edward George Josberger
Department of Oceanography
University of Washington
Seattle, Washington 98195

REPRODUCTION IN WHOLE OR IN PART
IS PERMITTED FOR ANY PURPOSE OF THE
UNITED STATES GOVERNMENT

DISTRIBUTION UNLIMITED

University of Washington

Abstract

LAMINAR AND TURBULENT BOUNDARY LAYERS ADJACENT TO MELTING VERTICAL ICE WALLS IN SALT WATER

by Edward George Josberger

A laboratory study of melting vertical ice sheets immersed in sodium chloride solutions of oceanic temperatures and salinities found that the convective motions generated by the melting consist of two regions confined to a boundary layer adjacent to the ice. The first region, at the bottom of the ice, is laminar and bidirectional, with a 2 to 3 mm thick upward flowing layer next to the ice inside of a 10 mm thick outer downward flowing layer. This bidirectionality results from the large difference between the thermal and saline diffusivities which contain dilute water near the ice and allows the cooling to diffuse further from the ice. Near the ice, dilute cold water rises; while away from the ice, cold saline water sinks. Second, further up the ice, the inner layer goes through a region of transition and becomes fully turbulent when the saline Grashof number reaches 2×10^8. The turbulent flow is upward, unidirectional and the dominant flow in the oceans.

Ice-water interface temperature measurements over the ice surface show a vertically varying temperature in the laminar region and a uniform temperature in the turbulent region. The measured melt rates were highest in the transition region, lowest in the laminar region, and had a slow vertical variation in the turbulent region. For water

temperatures greater than 25°C, the turbulent flow reversed direction and a laminar bidirectional region formed at the top of the ice.

In a theoretical study of the turbulent flow, an eddy diffusivity models the turbulent transport of momentum, salt and heat in the conservation equations and the laboratory measurements determine the model parameters. The turbulent model consists of three regions: a laminar inner region, an intermediate region where the eddy diffusivity increases linearly with distance from the ice and an outer region of constant eddy diffusivity. A similarity transformation reduces the governing partial differential equations to a system of ordinary differential equations which are then numerically integrated.

The numerical results show the following: The eddy diffusivity depends parabolically on the density difference across the boundary layer. The major effect of the turbulence is to increase the transport of dilute water away from the interface. The dilution effect overwhelms the thermal effect on density to produce a unidirectional upward flow. Finally, the injection of melt water into the boundary layer reduces the salt flux to the ice which lowers the interface salinity as the water temperature increases. Use of the results to form a zero net buoyancy condition on the buoyancy integrated across the boundary layer predicts the reversal of the turbulent flow which accurately fits all of the known data.

Salinity and temperature measurements with depth in the vicinity of an iceberg in the North Atlantic Ocean show variations in these quantities near the iceberg that may be the result of the upward flowing turbulent boundary layer.

Accession For
NTIS GRA&I
DDC TAB
Unannounced
Justification
By
Distribution/
Availability Codes
Dist | Avail and/or special
A

TABLE OF CONTENTS

	Page
List of Figures	iv
List of Tables	vi
List of Plates	vii
Acknowledgments	viii
Introduction	1
Ice in the World Ocean	1
Freezing Point and Density of Seawater	6
Dimensional Analysis	10
Previous Work	16
Ice Melting Experiments	16
Laminar Studies	19
Transition to Turbulence	22
Turbulent Studies	25
The Present Study	30
The Laboratory Experiment	32
Apparatus	32
The Laboratory Observations	42
The Case of Bubble-Free Ice, T_d < 20°C and Vertical Wall	42
The laminar bidirectional and unidirectional flows	42
Transition to turbulence	49
Laminar wall temperatures	54
Observations of melting in the laminar bidirectional region	59
The turbulent boundary layer	66
Ice-water interface temperatures in the turbulent region	68
Melt rates in the turbulent region	71
The High Temperature Flow Reversal	75
Bubble Ice Experiments	81
The Tilted Wall Experiment	84
Concluding Remarks	89
Fundamental Equations	90
The Boundary Layer Approximation	93
Boundary Conditions	98
Transformation to a Moving Coordinate System	107
The Similarity Transformation	110

	Page
The Turbulent Model	117
Numerical Scheme	123
Numerical Results	127
Evaluation of the Turbulent Parameters	127
The Effect of Blowing at the Interface	141
The Effect of Opposing Buoyancy Forces	142
The High Temperature Reversal	145
Conclusions	150
Bibliography	153
Appendix I	
The Equation of State	156
Appendix II	
Molecular Diffusivities of Salt, Heat and Momentum	158
Appendix III	
The Field Study	160
Appendix IV	
Computer Tables	170
Distribution List	
Report Documentation Page	

LIST OF FIGURES

Figure		Page
1.	A T-S diagram showing the location of the freezing curve and maximum density curve.	8
2.	Ice profiles over the course of an experiment [from Sandstrom (1919)].	18
3.	The experimental apparatus.	34
4.	The thermistor array.	36
5.	A representative thermistor record.	39
6.	A sketch of the observed flow field next to the ice.	44
7.	The vertical variation of T_w/T_{fp} in the laminar region.	55
8.	The dependence of $\overline{T}_w/T_{fp}$ in the laminar region on T_d.	58
9.	Representative melt rate distribution as measured by transit.	61
10.	The dependence of the average melt rate, M, in the laminar region on T_d.	63
11.	Correlation of Nu and Sh on Gr_S.	64
12.	Correlation of Nu and Sh on Gr_T.	65
13.	A representative thermistor record from the turbulent region.	67
14.	Experimental values of T_w/T_{fp} and M_x for the turbulent flow.	70
15.	Experimental values of the vertically averaged melt rate, $\overline{M}$, for the turbulent flow.	73
16.	A sketch of the flow observed for $T_d > 25°C$.	76
17.	Measured values of T_w from the variable tilt experiment.	88
18.	The coordinate system used in the analysis of the turbulent flow and the control volume used to derive the boundary conditions.	91
19.	The assumed variation of the eddy diffusivity, A, and its relationship to the mean upward velocity, $\overline{u}$.	118

Figure		Page
20.	A sequence of linear approximations converging to a root illustrating the Newton-Raphson method.	125
21.	Computed profiles of f'.	130
22.	Dependence of $\phi'(0)$ and $\theta'(0)$ on A and $\Delta\eta$ at T_d = 4°C.	132
23.	Locus of points for $\phi'(0)$ and $\theta'(0)$ from the experiments and from four models of the eddy diffusivity.	134
24.	Computed profiles of ϕ and θ.	136
25.	The effects of blowing and opposing buoyancy forces on $\phi'(0)$ and $\theta'(0)$.	143
26.	A T-S diagram showing the far-field conditions of the turbulent experiments.	147
27.	Location of the STD casts and the observed melt plume.	164
28.	Temperature profiles from the first STD section.	165
29a.	Salinity profiles from the first STD section.	167
29b.	Salinity profiles from the second STD section.	167
30.	Temperature profiles from the second STD section.	168

LIST OF TABLES

Table		Page
1.	Temperature change necessary to offset the density change resulting from a 1 $^{o}/_{oo}$ decrease in salinity at 30 $^{o}/_{oo}$.	10
2.	Summary of laminar bidirectional experiments.	56
3.	Far-field conditions for the two unidirectional experiments and the resulting interface conditions.	56
4.	Summary of turbulent experiments.	69
5.	Step size in each division of the integration interval.	126
6.	$\phi'_{lab}(0)$, $\theta'_{lab}(0)$, $f'_{lab}(0)$, a and b computed from the smoothed laboratory data.	128
7.	Values of f'_{max} and $f(\infty)$ for three cases: Opposing buoyancy forces with blowing, $\rho(S,T)$; density only a function of S with blowing, $\rho(S)$; and opposing buoyancy forces without blowing.	140
Appendix IV-1 - IV-15.	Numerical solutions of the governing equations	171

LIST OF PLATES

Number		Page
Plate I.	Bidirectional flow	45
Plate II.	Bidirectional flow	46
Plate III.	Unidirectional upward laminar flow	48
Plate IV.	Laminar bidirectional region and horizontal jet flowing towards the ice	51
Plate V.	Bifurcation of the horizontal jet	52
Plate VI.	Increased melting at the bifurcation point	53
Plate VII.	Ice shape in the laminar region	60
Plate VIII.	Ice shape after melting for 23 min	77
Plate IX.	Cusps in ice surface for T_∞ = 26.0°C, S_∞ = 31.0 $^{o}/_{oo}$	78
Plate X.	Ice shape after melting for 20 min	79
Plate XI.	Bubble ice experiment, 5% CO_2	83
Plate XII.	Tilted ice experiment, tilt angle 60°	86
Plate XIII.	A North Atlantic iceberg	161

ACKNOWLEDGMENTS

I extend my deepest gratitude and thanks to Dr. Seelye Martin for the advice and guidance that he gave me and for the patience he showed during this study; his strong moral support enabled me to finish this dissertation. I am indebted to Peter Kauffman for his ingenuity and cleverness in the design and construction of the laboratory apparatus and for his help in performing the experiments. Also in the laboratory, I credit David Bell for the invention of the bubble-free ice machine. I thank Jerre Bradt for stimulating scientific discussions and his help and advice in dealing with the computer. I thank Dr. David G. Mountain and the United States Coast Guard for the opportunity to conduct the field work. I also thank Miriam Lorette for her able assistance in procurement and budgeting and Phyllis Brien for typing the manuscript. Finally, I acknowledge the support of the Office of Naval Research under Task No. NR307-252 and Contract No. N0014-76-C-0234.

INTRODUCTION

Ice, in the form of glacier and sea ice, is the most striking feature of the polar oceans. The discovery of off-shore oil deposits in the Arctic Ocean, the possible establishment of a krill fishery in the Southern Ocean, and icebergs as a possible source of fresh water makes understanding the complex ice-sea-water interaction phenomena imperative. While the formation, distribution and movement of pack ice in the ocean has received considerable attention in AIDJEX, the melt processes have been neglected. In particular, the melting of a vertical ice wall in seawater has not been examined. In this case, the melting cools and dilutes the seawater adjacent to the ice to produce convection. This convection results from the complex diffusion of salt, heat and momentum where the thermal and saline effects on density oppose each other.

In the ocean the vertical length scale for sea and glacier ice varies from 250 m to 0.5 m. Icebergs have the largest vertical length scale of all oceanic ice, as large as 250 m. An iceberg forms when a tidewater glacier or an iceshelf calves or breaks and sets a large piece of glacier ice drifting on the ocean. Paterson (1975) defines glacier ice as snow that has metamorphosed to the point where the trapped air pockets are sealed off from one another; the trapped air volume varies from 0 to 7%. The vast ice shelves of the Antarctic Continent produce tabular icebergs that have depths up to 250 m and a typical horizontal scale of 1 km, although icebergs as large as 50 km on a side have been reported (McClain, 1978). The Amery, Ronne-Filchner and Ross iceshelves produce the majority of the icebergs found in the Southern Ocean and Hult and Ostrander (1973) estimate the input of ice to be 6×10^{15} kg yr^{-1}. The effect of this ice input on the oceanography of the Southern

Ocean may be significant and only a thorough understanding of the melting process will determine the ice melting effects.

Glaciers flowing from the Greenland ice cap in the North Atlantic produce icebergs that are smaller and fewer in number than the icebergs in the Southern Ocean. Plate XIII shows a typical North Atlantic iceberg; it measures approximately 120 m on the water line, rises 30 m out of the water, and has a depth of 100 m. North Atlantic icebergs are usually unstable with rolling occurring frequently. The number of icebergs varies from year to year but in a heavy ice year over a thousand icebergs find their way south of the Grand Banks (Neuman and Pierson, 1966) where they constitute a hazard to navigation. In 1912 the Titanic struck an iceberg near the "Tail of the Bank" and sank with the loss of 1,502 lives (Lord, 1976). Today, even with radar, small bergs or growlers may not be detected in heavy seas or pack ice and they still represent a hazard (Ruffman, 1976). In 1977 a Canadian ferry bound for Labrador presumably struck a growler while operating in pack ice and sank without loss of life.

Icebergs are not only a hazard to navigation, but they may also increase biological productivity around the iceberg through upwelling driven by dilution from the melting ice. In the Southern Ocean icebergs extend below the main pycnocline at 50 m and the convection next to the iceberg may transport nutrients from the deep water into the photic zone. However, controversy exists over the effect of the melting on the surrounding seawater. Neshyba (1977) states that upwelling is important in the primary production of the Southern Ocean, while Huppert and Turner (1978) feel that stratification in the Southern Ocean limits the vertical convection and no significant upwelling occurs. Neshyba (1977)

estimates that the convection associated with the sidewall melting supplies significant amounts of nutrients from below the pycnocline at 50 m to the surface layers for use in photosynthesis. Neshyba based his calculations on turbulent heat transfer coefficients derived from experiments where heat, not salt, created the buoyant driving, a procedure that may not be correct. In a laboratory experiment Huppert and Turner (1978) investigated the effect of stratification on the convection adjacent to a vertical ice wall and found a cellular convection pattern. In their experiments, with 0.25 m long ice slabs submerged in linearly stratified sodium chloride solutions, the cold water near the ice sank a few 10's of mm until the melt water reached its own density level where it flowed horizontally out into the interior of the tank. As a result of this cellular convective pattern, horizontal ridges formed on the ice surface with a vertical length scale equal to the convective cell length scale. They assert that the vertical step structure in temperature and salinity found in the Weddell Sea may be due to melting icebergs. They performed their experiments at 20°C with salinity gradients up to 100 $^{o}/_{oo}$ m^{-1}, conditions which do not represent oceanic values. Also, for uniform conditions I found a reversal in the flow at 20°C and oceanic salinities. These factors make direct application of Turner and Huppert's work to the ocean inappropriate; the reversal at 20°C is discussed in the results section.

To determine the effect of a melting ice wall on the surrounding water properties in the ocean, I performed a field program adjacent to an iceberg in the North Atlantic Ocean in cooperation with the International Ice Patrol, United States Coast Guard. The results, given in Appendix III, show cooling and dilution of up to 3°C and 0.5 $^{o}/_{oo}$ in

the upper 30 m of the water column within 200 m of the iceberg which supports the concept of an upward flowing boundary layer. Plate XIII shows the iceberg and a prominant waterline notch, denoted by arrow A, which shows that the iceberg has recently rolled. The upper horizontal edge of the iceberg was once a vertical wall and this polished wall shows no sign of horizontal ridging on the scale of ten meters as would be expected if stratification were important.

Since icebergs are pure water, they have long been considered as a source of water for drinking and irrigation. For example, H.R.H. Prince Mohamad Al-Faisal, a Saudi Arabian Prince, has proposed the towing of tabular icebergs from Antarctica to the Gulf of Arabia to provide fresh water for his arid country (Husseiny, 1978). For this scheme to be successful, the melting processes must be thoroughly understood over a wide range of temperatures, from near the freezing point in the Southern Ocean to greater than 20°C in the Indian Ocean. The convective mixing processes must also be understood if the collection of the subsurface melt water is used to provide the fresh water.

Not all ice in the oceans is in the form of icebergs; sea ice covers most of the Arctic Ocean and the Southern Ocean during their respective polar winters. Pressure ridge keels made of sea ice and sea ice adjacent to open water have vertical scales of 0.5 to 10 meters. Cox and Weeks (1974) show that sea ice contains salt; first-year ice may have a salinity as high as 20 $^{o}/_{oo}$ while multiyear ice usually has a salinity of 2 $^{o}/_{oo}$. The low multiyear ice salinity allows the results of this study to be applied to most sea ice melting phenomena.

Pressure ridges form when two sheets of sea ice converge, usually under atmospheric forcing, and undergo mechanical failure. Blocks of

sea ice pile up and form a ridge; the sail, which is the portion of the ridge above the water, is usually a few meters high, but it is supported by a keel tens of meters below the water (Parmerter and Coon, 1972). Pressure ridge keels menace submarine navigation and are important in modeling the motions of the Beaufort ice pack (AIDJEX Bulletin No. 23). The random orientation of the ice blocks in the keels gives the melting of tilted ice walls geophysical importance.

Ice with vertical length scales of 0.5 m to 1.0 m occurs when a lead or a polyna opens in the pack ice. Solar radiation warms the seawater and a fraction of this heat melts the ice at the lead edges forming convective boundary layers. In a similar situation, the spring runoff from rivers flowing into the Arctic Ocean produces warm low salinity water that rapidly melts the sea ice. In this case, the salinity can be below 25 $^{o}/_{oo}$ and the temperature between -1.2°C and 4°C. As a result of the nonlinear equation of state for seawater, in the lead case, the temperature and salinity anomalies due to melting produce opposing buoyancy forces; in the river case, the anomalies produce reinforcing buoyancy forces.

Vertical natural convection adjacent to ice walls occurs in the polar oceans over a wide range of length scales driven by a wide range of ambient temperatures and salinities. To understand fully the role of ice in the physical oceanography of the polar oceans, the fluid dynamics of this convection must be studied.

In the following two subsections I discuss first the equation of state and the freezing point dependence of seawater; second, the dimensional analysis applicable to the flow next to a melting vertical ice wall.

Freezing Point and Density of Seawater

The convection generated by a melting vertical ice wall is a complex problem in fluid dynamics because it involves a phase change, a fluid density that depends on both temperature and salinity in a nonlinear fashion and the diffusion of momentum, heat and salt. The difference in the molecular coefficients of diffusion further complicates the problem.

When ice melts in seawater, it cools and dilutes the adjacent water. The ice-water interface temperature and salinity must be on the freezing curve given by Fujino et al. (1974) as

$$T_{fp} = -0.036 - 0.0499S - 0.000112S^2 \qquad (1)$$

for

$$17.7\ ^{o}/_{oo} \leq S \leq 35\ ^{o}/_{oo}$$

where T_{fp} is the freezing point and S is the salinity. For $S < 17.7\ ^{o}/_{oo}$ I computed T_{fp} using the results given in Kaufman (1960). The interface conditions as derived in the boundary conditions chapter, also depend on the melting rate so the wall temperature T_w and the wall salinity S_w are not known *a priori*.

The ambient far-field temperature T_∞ and salinity S_∞ determine the far-field freezing point and the temperature elevation above the freezing point, which I call the thermal driving, T_d,

$$T_d = T_\infty - T_{fp}(S_\infty) \quad . \qquad (2)$$

The thermal driving is a convenient temperature parameter to use in ice melting problems because it is determined solely by the far-field conditions and is independent of the unknown interface conditions.

When fresh ice melts in seawater, convection results from the cooling and diluting of the surrounding water. If the interior ice temperature equals T_w, then all of the heat transferred to the ice produces a phase change, which requires a latent heat L of

$$L = 3.3 \times 10^5 \text{ J kg}^{-1} \quad . \tag{3}$$

To compute the buoyancy that the melting generates requires an accurate formulation of the equation of state for seawater. For compactness and ease of manipulation, I use the formulation of the equation of state given by Gebhart and Mollendorf (1977) at 1 atmosphere of pressure. Appendix I gives both the formulation and the values of the coefficients used in the formulation. Figure 1 shows the nonlinear behavior of the density of salt water as a function of S and T. The existence of a density maximum exemplifies the nonlinear dependence. The line of maximum density lies between S = 0 and T = 4°C, and S = 25 $^{o}/_{oo}$ and T = -1.4°C where it intersects the freezing point line; for temperatures > -1.4°C and salinities > 25 $^{o}/_{oo}$ the maximum density lies beneath the freezing curve in the frozen zone. The figure shows that dilution of salt water always produces less dense water while cooling produces either less dense or more dense water, depending on the location of T and S with respect to the maximum density line.

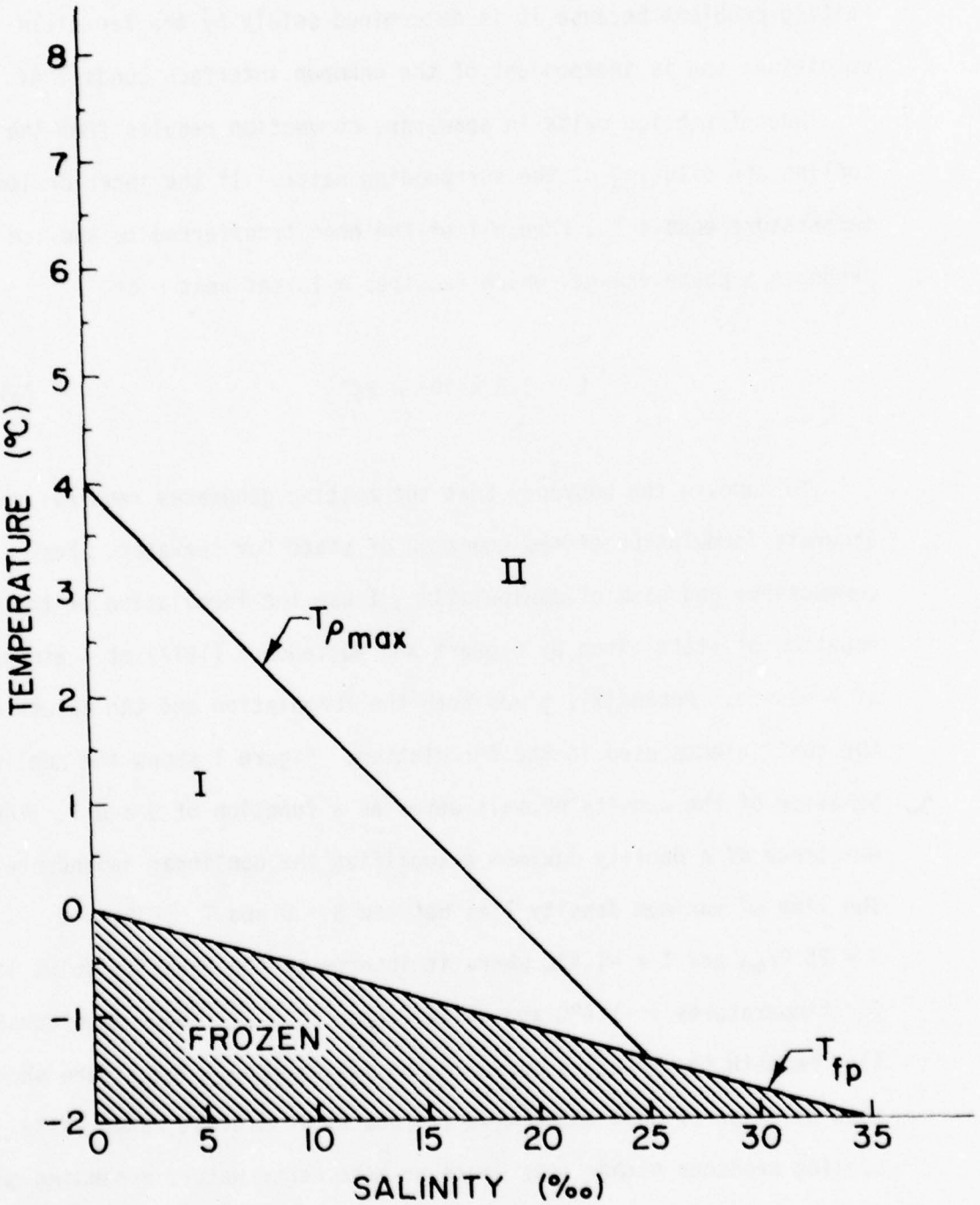


Figure 1. A T-S diagram showing the location of the freezing curve, T_{fp}, and maximum density curve, $T_{\rho max}$. Far-field conditions in region I produce reinforcing upward buoyancy forces; far-field conditions in region II produce opposing buoyancy forces.

At the maximum density line, the coefficient of thermal expansion α, where

$$\alpha = \frac{1}{\rho} \frac{\partial \rho}{\partial T} \tag{4}$$

changes sign. Therefore, when T and S lie in region II, cooling and dilution produce opposing buoyancy forces because α is negative. When T and S lie in region I, cooling and dilution produce reinforcing upward buoyancy forces because α is positive. In fresh water the density maximum at 4°C gives opposing buoyancy forces when T_∞ lies between 4°C and 8°C.

For most oceanic cases the buoyancy forces are in opposition and dilution has a much larger effect on density than cooling. Table 1 gives the temperature change, ΔT, necessary to offset a 1 $^{o}/_{oo}$ dilution of 30 $^{o}/_{oo}$ seawater such that the density remains constant for various temperatures. At temperatures less than 6°C, ΔT is so large that the water freezes before cooling enough to offset the dilution. As the temperature increases ΔT decreases, which means that at low temperatures the salinity dominates the density, but as the temperature increases the thermal effect becomes more important. The increasing effect of temperature results from the almost parabolic dependence of density on the temperature elevation above the temperature of maximum density, T_m.

Table 1

$S = 30\ ^{o}/_{oo}$	$S = 1\ ^{o}/_{oo}$
T(°C)	T(°C)
0	-23.4
2	-13.6
4	-9.7
6	-7.6
8	-6.3
10	-5.4
20	-3.2

Temperature change necessary to offset the density change resulting from a $1\ ^{o}/_{oo}$ decrease in salinity at $30\ ^{o}/_{oo}$.

Dimensional Analysis

The flow adjacent to a melting vertical ice wall falls into the category of boundary layer flow because the flow is contained in a thin region next to the ice whose thickness is much less than its length. Schlichting (1960) scales the equations governing the flow to obtain relationships between nondimensional parameters formed by combining the molecular properties of the fluid with themselves and the physical characteristics of the flow.

Three nondimensional quantities, the Schmidt, Prandtl and Lewis numbers, govern the distribution of salt, heat, and momentum within the boundary layer. The ratio of the thermal diffusivity κ to the saline diffusivity D defines the Lewis number Le;

$$Le = \frac{\kappa}{D} \quad . \tag{5}$$

The ratio of the thermal diffusivity to the kinematic viscosity ν defines the Prandtl number Pr;

$$Pr = \frac{\nu}{\kappa} \quad . \tag{6}$$

Finally, the ratio of the saline diffusivity to the kinematic viscosity defines the Schmidt number Sc;

$$Sc = \frac{\nu}{D} \quad . \tag{7}$$

For a laminar boundary layer adjacent to a flat plate, Schlichting (1960, p. 300) shows that Pr, Sc and Le give the relative thicknesses of the velocity, thermal and saline boundary layers. If δ_u, δ_H and δ_S represent the boundary layer thicknesses for velocity, heat, and salt, then

$$\frac{\delta_H}{\delta_u} \simeq \sqrt{1/Pr} \quad , \tag{8-a}$$

$$\frac{\delta_S}{\delta_u} \simeq \sqrt{1/Sc} \quad , \tag{8-b}$$

$$\frac{\delta_S}{\delta_H} \simeq \sqrt{1/Le} \quad . \tag{8-c}$$

The Grashof number, Gr, and the Reynolds number, Re, characterize the nature of the flow within the boundary layer. The Grashof number is the ratio of buoyant forces to viscous forces, defined as

$$Gr = \frac{g(\rho_w - \rho_\infty)\ell_x^3}{\rho_\infty \nu^2} \tag{9}$$

where g is the acceleration of gravity 9.8 m s^{-2}, ρ_w is the density of water at the ice-water interface, ρ_∞ is the density of water in the far field, and ℓ_x is a vertical length scale. For purely convective flows, the magnitude of Gr determines whether the flow is laminar or turbulent. Turner (1973) gives 10^9 as the critical value of Gr where the laminar flow becomes turbulent. The Reynolds number is the ratio of inertial forces to viscous forces, defined as

$$Re = \frac{u\ell_x}{\nu} \tag{10}$$

where u is a velocity characteristic of the convective motions.

The Nusselt number, Nu and the Sherwood number, Sh, are the non-dimensional heat or salt fluxes to the ice. Nu and Sh are the ratios of the observed heat and salt fluxes to the ice at a distance downstream to the purely diffusive fluxes based on the same downstream distance:

$$Nu = \frac{F_H \ell_x}{\kappa \Delta T}, \quad Sh = \frac{F_S \ell_x}{D \Delta S} \tag{11}$$

where F_H is the observed heat to the ice, F_S is the observed salt to the ice, ΔT is the temperature difference between interface and far-field, and ΔS is the salinity difference between interface and far-field. The heat and salt transfer to the ice depends on the flow past the ice; buoyant flow and flow due to the ice moving through the water comprise the total flow.

Next, to determine if free or forced convection dominates the flow adjacent to the ice for oceanographic conditions, a scaling of the

momentum equations following Schlichting (1960) shows that free convection becomes important when

$$Gr \simeq Re^2 \text{ or } \frac{Gr}{Re^2} \simeq 1 \quad . \tag{12}$$

Using the definitions of Re and Gr, (12) gives an estimate of the speed necessary for forced convection effects to equal free convection effects as

$$u \simeq (g\frac{\Delta\rho}{\rho}\, \ell_x)^{1/2} \quad . \tag{13}$$

For oceanic cases I assume that fresh water is generated at the ice-water interface so that a characteristic value of $g\,\frac{\Delta\rho}{\rho}$ is 0.1 m s^{-2}. Substitution of this value and a value of 100 m for ℓ_x into Eq. (13) gives

$$u \approx 3 \text{ m s}^{-1} \quad . \tag{14}$$

In June 1977 I observed drogue studies next to an iceberg by the U. S. Coast Guard that show the iceberg and a 75 m deep window shade drogue to separate at a rate of several kilometers per day or ~.3 m s^{-1}. Therefore, natural convection dominates the flow near an iceberg. For the length scales of pressure ridges and sea ice edges, a flow of 1 m s^{-1} will overwhelm the buoyant flow but a 1 m s^{-1} flow is quite high for the oceans. Hence, buoyant motions remain important at all length scales and determine the heat and salt fluxes to the ice.

In seawater the molecular diffusivities of salt, heat, and momentum differ by three orders of magnitude. Appendix II gives the values of the molecular diffusivities used in this study and shows that

the magnitudes of the diffusivities of salt, heat, and momentum are, respectively, 10^{-9}, 10^{-7}, and 10^{-6} m^2 s^{-1}. For the laminar case, Eqs. (8a, b, and c) give

$$\frac{\delta_H}{\delta_u} \simeq 0.3 \ , \tag{15-a}$$

$$\frac{\delta_S}{\delta_u} \simeq 0.02, \tag{15-b}$$

so that

$$\frac{\delta_S}{\delta_H} \simeq 0.07 \ . \tag{15-c}$$

The large difference between δ_S and δ_H shows that the opposing buoyancy forces act in different regions of δ_u which is larger than either δ_H or δ_S. The upward buoyancy dominates the inner region while the downward buoyancy dominates the outer region; the present study found that in the laminar case, this buoyancy distribution produces a bidirectional flow.

The existence of opposing buoyancy forces allows for the definition of two additional Grashof numbers to characterize the individual effects of thermal and saline buoyancy. The saline Grashof number, Gr_S, and the thermal Grashof number, Gr_T, are defined as

$$Gr_S = \frac{g\beta(\Delta S)\ell_x^3}{\nu^2} \tag{16-a}$$

and

$$Gr_T = \frac{g|\alpha|(\Delta T)\ell_x^3}{\nu^2} \ . \tag{16-b}$$

This definition of Gr_T uses $|\alpha|$ because α changes sign near the line of maximum density. For seawater

$$Gr \simeq Gr_S \tag{17}$$

because salinity dominates density and $Gr_S >> Gr_T$. As an example, for a 200 m deep iceberg with $\Delta S = 35\ ^{o}/_{oo}$ and $\Delta T = 4°C$, $Gr_S = 7 \times 10^{17}$ and $Gr_T = 9 \times 10^{15}$. Hence, the buoyancy generated by changes in salinity should dominate the flow. The present study shows that this is true at $T_\infty < 20°C$ but for $T_\infty > 20°C$, the thermal effects dominate. This reversal results from the increased temperature effect on density at high temperatures and the large value of Le.

Finally, Gr exceeds the critical value of 10^9 for oceanic salinities and temperatures for vertical length scales greater than 0.5 m. Thus, the convection is turbulent for length scales greater than 0.5 m and laminar for length scales less than 0.5 m.

Previous Work

This chapter reviews the previous work which divides into four main categories: ice melting experiments, laminar boundary layer flows, transition from laminar flow to turbulent flow and turbulent boundary layer flows. The last three categories further divide into experimental and theoretical studies. The laminar studies include both single and multiple species diffusion while the transition and turbulent studies consider only single species diffusion.

Ice Melting Experiments

The literature contains only three experiments where natural convection results from melting vertical ice walls. The first experiment by Sandstrom (1919) took place in salt water, the second took place in fresh water.

Sandstrom (1919) placed large blocks of ice in a tank of seawater to model the circulation driven by melting ice sheets during the spring in both the North Atlantic Ocean and Norwegian fjords. Figure 2 shows the apparatus and the observed ice ablation and circulation in the tank. The apparatus bears a striking resemblance to the present apparatus in that he recognized the need to control stratification in the tank and he also used dye to trace the fluid motions. Walfrid Ekman, a founder of modern oceanography, made miniature current meters to measure the fluid velocities. At 100 mm up from the bottom of the ice block the water flowed horizontally towards the ice, then divided, with some water flowing up next to the ice and the rest flowing down next to the ice. A notch formed in the ice at the jet level and the ice above the notch

melted faster than the ice below the notch. A comparison of Figure 2 to Plate VI shows these results are identical to the present results. Sandstrom did not describe an inner upward flow at the bottom of the ice, but since this layer is only millimeters thick, he may not have observed it. He did describe cold fresh water flowing away from the ice at the surface, warm salty water flowing towards the ice at depth and cold salty water flowing away from the ice at the bottom of the tank.

The far-field conditions for the 1904 experiment were T_∞ = +8°C, S_∞ = 30 $^{o}/_{oo}$ for a thermal driving of 9.6°C. Determining the average wall salinity at T_d = 9.6 from Figure 8, S_w = 4.2 $^{o}/_{oo}$, and taking the critical Gr_S = 1.6 x 10^8 yields 140 mm for the length of the laminar region. The additional flow of low salinity water up the side of the ice from melting on the bottom results in the shorter laminar region because the additional flow hastens the transition to turbulence. Sandstrom concluded from this experiment that ice melting is important in driving oceanic currents.

Second, Bendell and Gebhart (1976) measured the heat transfer to a vertical ice wall submerged in fresh water to investigate the heat transfer when a density maximum exists in the fluid. When a vertical ice wall melts in fresh water, the existence of the density maximum at 4°C provides the conditions necessary for bidirectional flow. Consider the following cases: If the ambient water temperature is greater than 8°C, then all of the cooled water is more dense and must sink. If the ambient temperature is less than 4°C, all of the cooled water is less dense and must rise. Finally, when the ambient temperature lies between 4 and 8°C, less dense water is found near the ice while more

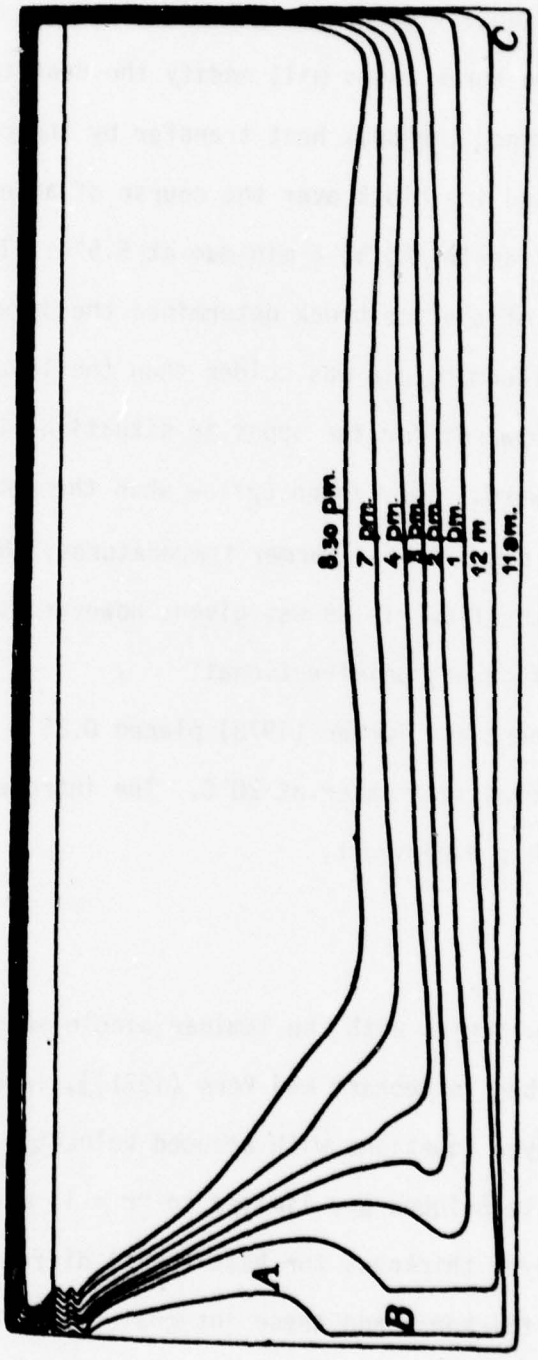


Figure 2. Ice profiles over the course of an experiment [from Sandstrom (1919)].

dense water is found further away from the ice, a situation which may yield a bidirectional flow next to the ice. Hence, the different convection in the three cases will modify the heat transfer to the ice.

They determined the bulk heat transfer by the change in weight of a counter-weighted ice block over the course of an experiment. They found the heat transfer to be a minimum at 5.5°C. Two thermocouples, one at each end of the ice block determined the direction of flow. When the upper thermocouple was colder than the lower one, they assumed the flow to be upward; for the opposite situation, they assumed the flow to be downward. They found upflow when the ambient temperature was < 5.6°C and downflow for warmer temperatures. No detailed description of the flow fields was given; however, they assumed in all cases that the flow was unidirectional.

Third, Huppert and Turner (1978) placed 0.25 m long ice slabs in linearly stratified salt water at 20°C. The introduction contains a discussion of this experiment.

Laminar Studies

This review begins with the laminar single species flow; prior to 1954 [as described in Gebhart and Pera (1971)], investigators integrated the boundary layer equations with assumed velocity and species profiles. These integral techniques are limited to $Pr \simeq 1$; when Pr is not near 1, the boundary layer thickness for heat (salt) differs from the momentum boundary layer thickness and these integral techniques fail.

Ostrach (1953) performed a similarity transformation of the laminar boundary layer equations and then numerically integrated the resulting ordinary differential equations with Pr varying from .01 to 1000 to

determine the effect of Pr on the flow. In this study the blowing velocity at the wall equaled zero. Ostrach found that on increasing Pr decreases the thickness of the thermal layer when compared to the thickness of the velocity layer and also decreases the convective velocities. The velocities decrease because the buoyant driving is contained close to the wall where the frictional influence of the wall is greatest. The experimental work cited in Ostrach agrees with the theory for Pr up to 100 but no experiments have been performed at $Pr < 100$.

LaPadula and Mueller (1970) performed a theoretical investigation of a solid freezing onto a vertical surface. In their analysis they included the effect of suction or blowing at the interface. They found that for freezing, the mass flux towards the wall, or suction, enhances the heat transfer to the wall while, for melting, the mass flux away from the wall, or blowing, reduces the heat transfer. These effects increased with increasing Pr. These results indicate that the blowing due to ice melting must be included in our analysis.

When multiple species diffuse across the boundary layer, the resulting buoyancy forces either reinforce or oppose each other. In multiple species diffusion the first species is usually heat, and the second is a dissolved chemical compound. The most interesting case, which corresponds to the oceanic case, occurs when the buoyancy forces oppose each other and $Le >> 1$, which will both separate the individual buoyancy forces within the boundary layer and yield bidirectional flow.

In two previous experimental studies Adams and McFadden and Den Bouter used a heated plate to generate an upward force while sublimation of a solid from the plate generated the downward force. When water was the ambient fluid, electrochemical means generated the downward force.

These studies concentrated on measuring the heat and mass fluxes at the wall for a known wall temperature or measuring the wall temperature and mass flux for a known heat flux. In both of these studies an adequate description of the flow field is missing.

First, Adams and McFadden (1966) performed an experiment with opposing body forces in air by using a sublimating plate of p-dichorobenzene to produce the downward force, and heat to produce the upward force. In their case Pr = .73 and Sc = 2.23. For opposing body forces, the heat and mass transfer results were 10 to 15% lower than the theoretical predictions given by integral techniques and no discussion of the flow field was given.

Second, Den Bouter et al. (1968) measured the heat and mass transfer rates in an aqueous solution of copper sulphate to verify McFadden's results. For body forces in the same direction, the transfer rates agreed with the analytical predictions. However, when the buoyancy effects opposed each other, the observations deviated from the theory. The flow observations were stated in one sentence: "The flow was either up, down or oscillatory"; the method of flow visualization was not discussed.

Previous to 1971, theoretical work on the effect of multiple body forces on the convection received black box treatment in that the best correlation between Nu or Sh and some combination of Gr_T, Gr_S, Pr, and Sc was sought. Gebhart and Pera (1971) give a thorough review of the literature and discuss the shortcomings of previous theories, then perform a numerical investigation of the laminar equations on the assumption of self-similar flows. They present solutions for a wide range of Prandtl and Schmidt number in cases where the buoyancy effects

reinforce or oppose each other. In the case where Pr = Sc or Le = 1, the various species diffuse at the same rate so the buoyancy results from the diffusion of a single species whose effect on density equals the combined species effect on density. More interesting situations arise when Pr and Sc differ. For reinforcing buoyancy forces, Gebhart and Pera show that the boundary layer is more energetic and narrower than a single species boundary layer.

For opposing buoyancy forces, the boundary layer is wider and less energetic than the single species boundary layer. The possibility of a bidirectional flow exists when Le is very small or very large; however, Gebhart and Pera do not present solutions for oceanic values of Sc nor for density anomalies that would be found when seawater is in contact with fresh ice. Their similarity formulation only allows the boundary layers to thicken and accelerate in the downstream direction.

Transition to Turbulence

In nature laminar flows quickly become turbulent through the growth of infinitesimal disturbances within the laminar flow. A stability analysis of a laminar flow proceeds by perturbing the mean laminar flow and then determining the growth rates of the perturbations. Because no adequate analysis of the laminar bidirectional flow exists, the stability of this flow has not been determined. However, the stability properties of a single species boundary layer yields insight into the transition of a bidirectional boundary layer. Hieber and Gebhart (1971, a, b) analyzed the stability of the flow generated by a uniform heat flux from a flat vertical plate. This problem is not identical to the

present experiments but the physical processes are similar and the authors describe a method that can be used to convert from a uniform flux case to a uniform wall temperature case. They identified two modes of instability: one associated with the instability that arises from the shape of the velocity profile, an Orr-Sommerfeld instability, and the other related to the coupling of momentum and heat through the buoyancy term in the momentum equation.

For small Pr, $-0.01 < Pr < 0.1$, the coupling effect has little effect on the stability or the position of the neutral curve. The neutral curve is the locus of points on a plot of perturbation frequency versus a modified Grashof number

$$G^* = 5\left(\frac{g\beta q x^4}{5k\nu^2}\right)^{1/5} , \qquad (18)$$

such that the imaginary part of the frequency is zero hence, the waves do not grow or decay. In small Prandtl number flows, the momentum layer is narrower than the thermal layer so a perturbation in the velocity field only advects a small thermal change that produces an insignificant buoyancy perturbation.

For $Pr >> 1$ the buoyant coupling dominates the instability mechanism, and the neutral curve moves towards lower modified Grashof numbers. For large Pr, the momentum layer is much wider than the thermal layer, so that a velocity perturbation will advect a significant change in temperature because the local temperature gradient is large. The changes in the temperature field can produce momentum in two ways: First, if the buoyant thermal anomaly is advected away from the wall, it will accelerate the flow since it is in a region of lower buoyancy.

Second, less buoyant water that is advected towards the wall will increase its buoyancy since it has moved into a region of lower density. The expected wavelength of the most unstable disturbance for the coupled mode is of order $xPr^{-1/2}$, while for the uncoupled mode the most unstable wavelength is of order xPr^{-1}, where x is the distance downstream from the tip of the plate.

In an experimental study Jaluria and Gebhart (1974) studied the transition of the natural laminar convective boundary layer in water for a uniform heat flux from a flat vertical plate. They made combined temperature and velocity measurements using a copper-constantan thermocouple and a hot wire anemometer that traversed the boundary layer. The results show that the velocity and thermal boundary layers increase in thickness as both the distance from the tip and the heat flux increase. The changes in the transition region correlate with G^*/x^n where n is approximately 0.5. The factor of $1/x^n$ appears because the growth of the disturbances is probably related to the local values of the momentum and/or energy fluxes, quantities that do not correlate on G^*.

The authors suggest a new parameter, E, to characterize the transition to turbulence based on the boundary layer kinetic energy flux. E is defined as the nondimensional kinetic energy flux of the boundary layer based on the laminar flow:

$$E = G^*\left(\frac{\nu^2}{gx^3}\right)^{2/15} \quad . \tag{19}$$

Using the conversion given by the authors to convert from uniform flux to isothermal conditions, the value of E for my experiments is 18, with x equal to the length of the laminar regime. This value agrees remarkably well with values of E from 13 to 24 from experiments cited in Jaluria and Gebhart performed at Prandtl numbers 0.7 to 12. This suggests that the transition to turbulence does depend on the available kinetic energy from which the small disturbances can draw their energy.

These past studies show that the stability properties of a single species flow are quite well known and that similar stability characteristics exist for the bidirectional case. In the bidirectional case the inner saline layer, with its large buoyant forcing and high Schmidt number, dominates the stability of the flow while the outer thermal layer modifies the stability characteristics of the flow by changing the velocity distribution across the boundary layer. The effect of blowing at the wall on the stability has not been investigated and it may have a significant effect, especially at high Schmidt number.

Turbulent Studies

Studies of the turbulent convective boundary layer are scarce; the previous experimental studies do not represent the complexities of ice melting in seawater and the previous theoretical analyses use results from forced convection theory and experiments. Previous experiments had heat diffusing in air or water, for Pr = 0.73 or 10.0, where the resulting thermal anomaly creates the buoyancy. An electrically heated metal plate either produces a uniform heat flux to the ambient fluid or maintains a uniform wall temperature. Neither theory nor experiment

Second, less buoyant water that is advected towards the wall will increase its buoyancy since it has moved into a region of lower density. The expected wavelength of the most unstable disturbance for the coupled mode is of order $xPr^{-1/2}$, while for the uncoupled mode the most unstable wavelength is of order xPr^{-1}, where x is the distance downstream from the tip of the plate.

In an experimental study Jaluria and Gebhart (1974) studied the transition of the natural laminar convective boundary layer in water for a uniform heat flux from a flat vertical plate. They made combined temperature and velocity measurements using a copper-constantan thermocouple and a hot wire anemometer that traversed the boundary layer. The results show that the velocity and thermal boundary layers increase in thickness as both the distance from the tip and the heat flux increase. The changes in the transition region correlate with G^*/x^n where n is approximately 0.5. The factor of $1/x^n$ appears because the growth of the disturbances is probably related to the local values of the momentum and/or energy fluxes, quantities that do not correlate on G^*.

The authors suggest a new parameter, E, to characterize the transition to turbulence based on the boundary layer kinetic energy flux. E is defined as the nondimensional kinetic energy flux of the boundary layer based on the laminar flow:

$$E = G^*\left(\frac{\nu^2}{gx^3}\right)^{2/15} \quad . \tag{19}$$

Using the conversion given by the authors to convert from uniform flux to isothermal conditions, the value of E for my experiments is 18, with x equal to the length of the laminar regime. This value agrees remarkably well with values of E from 13 to 24 from experiments cited in Jaluria and Gebhart performed at Prandtl numbers 0.7 to 12. This suggests that the transition to turbulence does depend on the available kinetic energy from which the small disturbances can draw their energy.

These past studies show that the stability properties of a single species flow are quite well known and that similar stability characteristics exist for the bidirectional case. In the bidirectional case the inner saline layer, with its large buoyant forcing and high Schmidt number, dominates the stability of the flow while the outer thermal layer modifies the stability characteristics of the flow by changing the velocity distribution across the boundary layer. The effect of blowing at the wall on the stability has not been investigated and it may have a significant effect, especially at high Schmidt number.

Turbulent Studies

Studies of the turbulent convective boundary layer are scarce; the previous experimental studies do not represent the complexities of ice melting in seawater and the previous theoretical analyses use results from forced convection theory and experiments. Previous experiments had heat diffusing in air or water, for Pr = 0.73 or 10.0, where the resulting thermal anomaly creates the buoyancy. An electrically heated metal plate either produces a uniform heat flux to the ambient fluid or maintains a uniform wall temperature. Neither theory nor experiment

includes the effect of blowing at the solid boundary or opposing buoyancy forces.

Eckert and Jackson (1951) analyzed the turbulent boundary layer for a uniform wall temperature and no blowing by assuming shapes for the velocity and temperature profiles and then applying the integral techniques discussed previously. They modeled the turbulence by taking the wall stress from measurements in forced convection because the flow near the wall should have the same characteristics in each situation. The results give a boundary layer that grows as $x^{0.7}$ and a maximum velocity that increases as $x^{1/2}$, where x is the downstream coordinate. The average Nu-dependence on Gr and Pr was

$$Nu \propto (GrPr)^{2/5} \quad , \tag{20}$$

which agrees with the few previous experimental studies conducted in air.

Kato et al. (1968) also analyzed the turbulent free convection as a special form of forced convection. They took eddy diffusivities from forced convection results and assumed that the eddy diffusivity of heat equals that of momentum. The eddy diffusivity was zero at the wall, remained small over a viscous sublayer scale, then increased linearly over the entire boundary layer thickness. Equation (21) gives the eddy diffusivity

$$\varepsilon/\nu = .4y'[1-\exp(-.0017\ y'^2)] \quad , \tag{21}$$

where ε is the eddy diffusivity and y' is the dimensionless distance from the wall. For Pr = 1, $y' \simeq 10^3$ approximates the outer edge of the boundary layer and $\varepsilon/\nu \simeq 400$. The integral momentum and heat equations

are solved at several downstream positions, corresponding to Gr = 10^{10} to 10^{13}, by a trial and error method. At each Gr, an assumed temperature distribution determined a velocity profile; the new velocity profile then produced a new temperature distribution; this iterative process continued until no change occurred in the profiles. The velocity profiles agree with those of Eckert and Jackson and with the experimental data out to Gr x Pr equal to 10^{12}. At Pr equal to 10^{2} to 10^{4},

$$Nu_x \propto Gr_x^{0.31} , \tag{22}$$

where Nu_x is the local Nusselt number. This corresponds to a decrease in the heat flux to the wall as the downstream distance increases. The authors only give velocity and temperature profiles for Pr = 1 and omit the effects of blowing or suction at the wall and the opposing buoyancy forces, effects which the present study shows to be important.

Experimental studies of the turbulent boundary layer divide into two categories, uniform vertical wall temperature or uniform vertical heat flux at the wall. The results show that the associated convection is different for each category. In either case, the effects of blowing and opposing buoyancy forces are not present.

Cheesewright (1968) measured the mean velocity and temperature profiles and the local heat transfer rates in the turbulent flow produced by electrical heating of an aluminum plate 2.75 m high and 0.6 m wide. The apparatus maintained vertically uniform wall temperature on the plate. Platinum resistance thermometers measured both the temperature and the velocity fields; the instrument calibration took place in the laminar boundary layer at the bottom of the plate.

The transition from laminar to turbulent flow occurred at 2×10^9 to 10^{10} and the turbulent measurements were carried out to $Gr = 10^{11}$. The measured heat transfer agrees with the theory of Eckert and Jackson; however, the assumed shapes for velocity and temperature do not agree with the experiment. The assumed velocity profile is too narrow and too fast when compared to the measured velocity profile and the assumed temperature anomaly profile decreases too slowly as the distance from the wall increases when compared to measured profiles. When flow changes from laminar to turbulent, the turbulence steepens the temperature gradient near the wall and diffuses the temperature anomaly further from the wall. The data near the wall best correlate on

$$\eta = y/x \; Gr^{-1} \tag{23}$$

which indicates a different turbulent mechanism acting in each part of the boundary layer.

Vliet and Liu (1969) conducted an experiment in water with a vertical plate dissipating a vertically uniform heat flux. They measured the mean temperature and velocity profiles next to a 1.25 m long plate with a copper-constantan thermocouple and a hot film anemometer. The water temperature varied from 7°C to 50°C.

The wall temperature distributions as measured by a series of thermocouples on the surface of the plate show that the wall temperature is coldest at the bottom of the plate, increases in the laminar region and then rapidly decreases in the transition region.

In the turbulent region the wall temperature increased with distance up the plate, indicating a decrease in the heat transfer coefficient; the decrease was proportional to $x^{-.12}$. Also the wall temperatures in the turbulent region fluctuated with time, a phenomenon that was not observed in the ice interior in the present experiments.

A comparison of the laminar and turbulent heat fluxes shows that the local Nusselt number Nu_x dependence on the local modified Grashof number Gr_x^*, where Gr_x^* is Gr_x multiplied by Nu_x has almost the same power law dependence in each case, 0.2 versus 0.22. This indicates that the turbulent flow exhibits strong laminar characteristics. The transition to turbulence occurs in a range of Gr_x^* equivalent to Gr_x of 10^9 to 10^{10}, 1 to 2 orders of magnitude greater than the constant wall temperature case, which indicates that molecular diffusion processes remain important.

When compared to the data of Cheesewright, the measured velocity and temperature profiles are in good agreement; however, the transposed heat transfer data do not agree. The authors state that the disagreement results from the two modes of heating which produce slightly different fluid dynamics in each case. The velocity measurements found the maximum velocity within 7 mm of the wall and a sharp division between the outer quiescent fluid and the inner turbulent fluid that made it difficult to estimate an average boundary layer thickness. From their measurements the authors deduced that a one-parameter similarity may be applicable to the mean fields.

In summary this literature review shows that previous work on natural convection is not applicable to the convection generated by melting vertical ice walls in seawater because these studies, except for that of Sandstrom, took place at Gr and Sc of at least two orders of magnitude less than the expected values for oceanic situations and the effect of blowing is omitted. The theoretical laminar and turbulent studies suffer from the same drawbacks, although LaPadula did investigate the effect of blowing or suction at the wall for laminar single species convection. Also the theoretical turbulent studies use eddy diffusivities from forced convection experiments.

The Present Study

To investigate the convection that occurs when vertical ice walls melt in seawater, I performed a series of laboratory experiments to characterize the convective motions and determine the dependence of T_w, S_w and the melt rate on oceanic values of T_∞ and S_∞. The experiments show that the convection consists of both laminar and turbulent flows and oceanographically the most important flow is an upward flowing turbulent boundary layer driven by low salinity water.

I then numerically solved the equations of motion governing the turbulent convection under the assumption of self-similarity. A spatially varying eddy diffusivity parameterized the turbulent transport of momentum, heat, and salt and the experimental data determined the turbulent parameters. In solving these equations I retained the effect of opposing buoyancy forces and blowing or mass influx at the ice-water interface, and I found that these effects have a profound influence on the numerical solutions.

In an application of the laboratory and theoretical results, I conducted a field study adjacent to an iceberg in the North Atlantic Ocean in cooperation with the United States Coast Guard and the International Ice Patrol. The field study consisted of a series of STD casts around an iceberg and the results show that the ice melt modifies the salinity and temperature of the water in the upper 30 m within 200 m of the iceberg, which supports the concept of an upward flowing boundary layer adjacent to the ice.

The Laboratory Experiment

Apparatus

In my experimental study of the ablation of a vertical ice wall in seawater the important laboratory parameters are the salinity and temperature of the ambient water and the length of the ice wall. Oceanic temperature and salinity conditions, as well as 1 m vertical length scales, are easily modeled in the laboratory; these results may be extrapolated to vertical length scales greater than 1 m.

The experiments took place in a clear acrylic tank that measures 0.45 m wide, 1.2 m long, and 1.25 m deep which, when filled, contains approximately 650 kg of water. I produced water at oceanic salinities by mixing food grade NaCl into the water. I then determined the resultant salinity with either an American Optical or Endeco refractometer, respectively, accurate to 1.0 $^{o}/_{oo}$ or 0.2 $^{o}/_{oo}$. I obtained oceanic temperatures by placing the filled tank in one of the cold rooms of the Sea Ice Laboratory, Department of Oceanography, University of Washington, and setting the room temperature to the required value. The water than reached thermal equilibrium with the air; a process which took several days as a result of the large mass of water. The cold rooms are large walk-in freezers with controlled temperatures which range from -40°C to +5°C. The temperature within each room cycles around the set temperature with an amplitude of 1°C and a period of 40 minutes. For temperatures higher than 5°C, I shut off the refrigeration and let the room and water warm to the required temperature.

Before placing the ice in the tank, I insured homogeneous temperature and salinity conditions by using a stirring motor to vigorously

agitate the water and then letting the water come to rest. In addition, I removed the ice from cold storage and let it warm to a temperature of approximately -1°C to prevent thermal fracture of the ice slab when it was immersed in the water.

In the experiments I used sheets of bubble-free ice with an instrument array frozen within the ice to model the melting process. The ice sheets measured approximately 0.2 m wide, 0.1 m thick and varied in length from 0.5 m to 1.2 m. I grew bubble-free ice in an insulated tank, 0.4 m x 0.6 m x 0.4 m, that has a cold plate on the bottom and two laboratory stirring motors mounted on the top. As the ice grew, the air bubbles that formed at the ice-water interface were swept away by the water motion created by the stirring motors. When the ice thickness reached half the desired value or 50 mm, the array was placed in the tank and the ice froze around the array. When the ice reached the desired thickness, I set the temperature in the cold plate at +2°C; the subsequent small amount of melting freed the ice from the bottom of the tank so that it floated to the surface where it was easily removed. As the ice grown in this tank measured only 0.6 m long, to obtain 1.2 m long ice I joined two such lengths of ice by butting the ends together in a cold room at -15°C and seeping water into the joint. For these cases, the array lies only in the upper portion of the ice. I also performed two experiments using ice that had a CO_2 content of 5% or 1.5% by volume.

Before storing the ice or at the beginning of an experiment, I used a laboratory hot plate to smooth one side of the ice slab to a surface that was planar to within 2 mm/m. As Figure 3 shows, I also cut a bevel on the ice bottom to prevent bottom melting from interfering

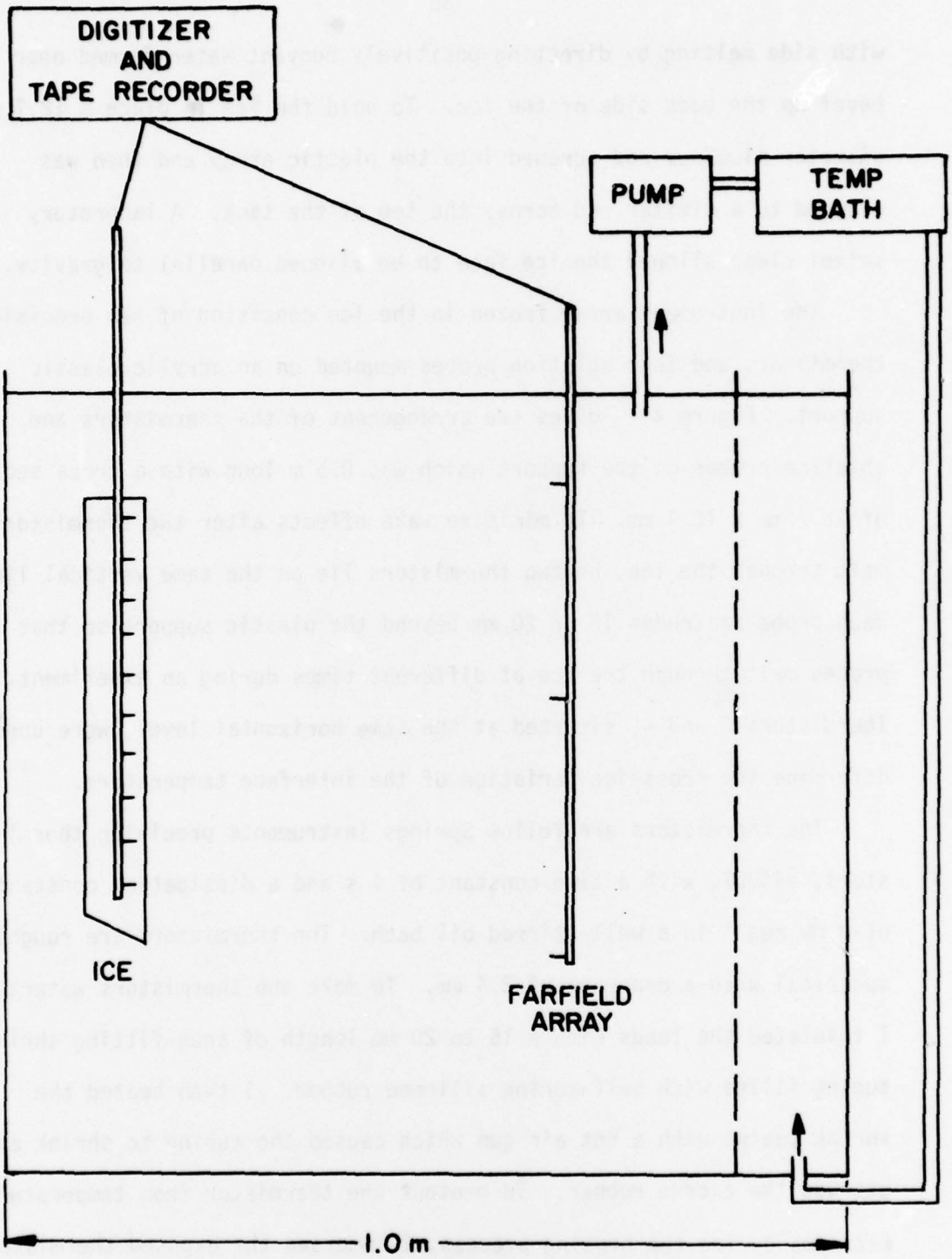


Figure 3. The experimental apparatus.

with side melting by directing positively buoyant water formed near the bevel up the back side of the ice. To hold the ice in place a 12.7 mm diameter aluminum rod screwed into the plastic array and then was clamped to a similar rod across the top of the tank. A laboratory swivel clamp allowed the ice face to be aligned parallel to gravity.

The instrument array frozen in the ice consisted of ten precision thermistors and four ablation probes mounted on an acrylic plastic support. Figure 4 gives the arrangement of the thermistors and ablation probes on the support which was 0.5 m long with a cross section of 12.7 mm x 12.7 mm. To minimize wake effects after the thermistors melt through the ice, no two thermistors lie on the same vertical line. Each probe protrudes 15 or 20 mm beyond the plastic support so that the probes melt through the ice at different times during an experiment. Thermistors 3 and 4, situated at the same horizontal level, were used to determine the cross-ice variation of the interface temperature.

The thermistors are Yellow Springs Instruments precision thermistors, #44007, with a time constant of 1 s and a dissipation constant of 8 mw deg^{-1} in a well-stirred oil bath. The thermistors are roughly spherical with a diameter of 2.4 mm. To make the thermistors watertight I insulated the leads with a 15 to 20 mm length of snug-fitting shrink tubing filled with self-curing silicone rubber. I then heated the shrink tubing with a hot air gun which caused the tubing to shrink and extrude the excess rubber. To protect the thermistor from temperature extremes during the heating process, I immersed the exposed thermistor tip to a depth of 1 mm in fresh water. After curing for several days the insulation became watertight. I then mounted each sensor on a 5 mm wide, 1 mm thick plastic strip of varying length and fastened this strip

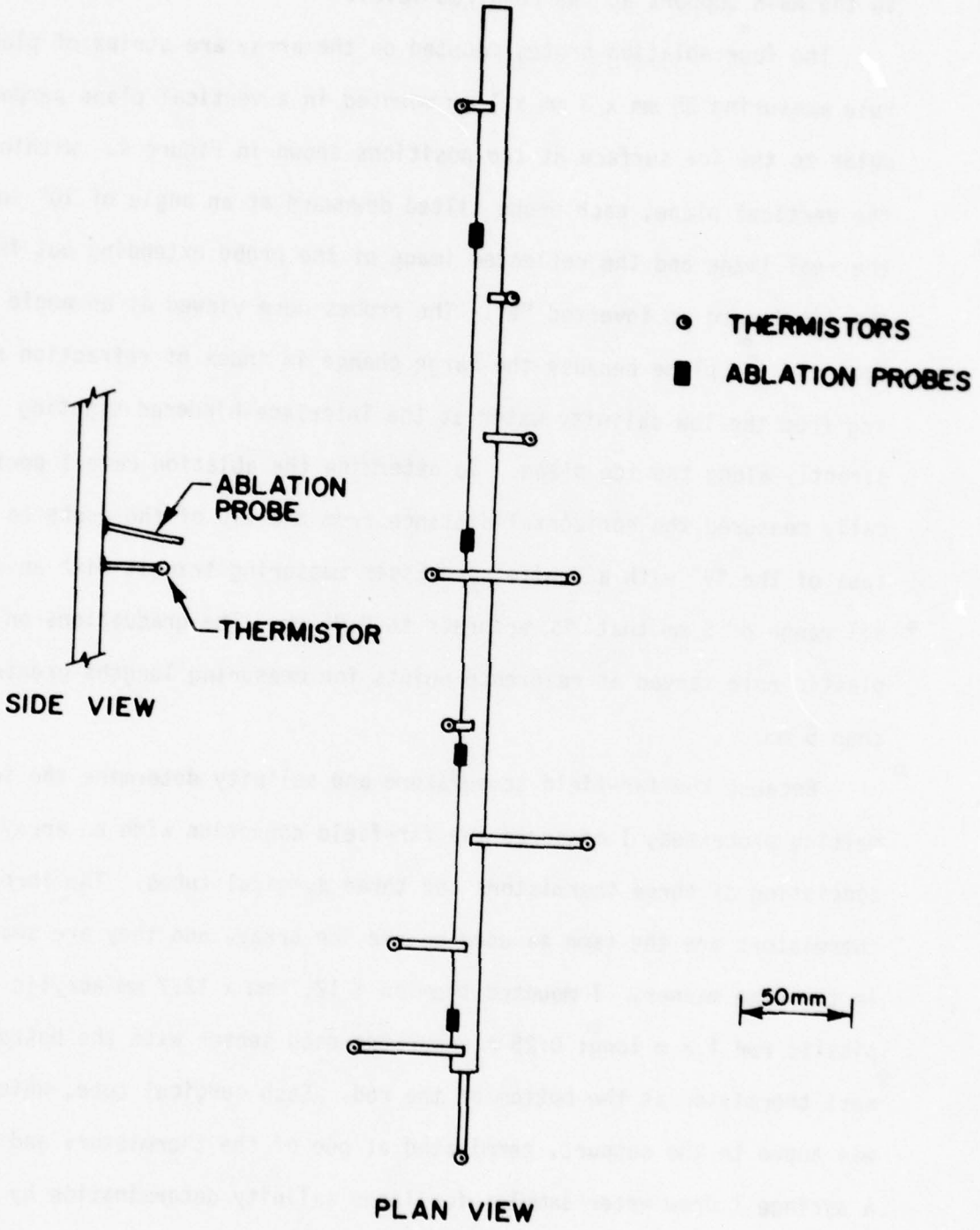


Figure 4. The thermistor array.

to the main support at the required level.

The four ablation probes mounted on the array are strips of plastic rule measuring 35 mm x 3 mm x 1 mm mounted in a vertical plane perpendicular to the ice surface at the positions shown in Figure 4. Within the vertical plane, each probe tilted downward at an angle of 10° so that the real image and the reflected image of the probe extending out from the ice formed an inverted "V". The probes were viewed at an angle of 5° from the ice plane because the large change in index of refraction resulting from the low salinity water at the interface hindered sighting directly along the ice plane. To determine the ablation rate I periodically measured the horizontal distance from the tip of the probe to the apex of the "V" with a Keuffel and Esser measuring transit with an overall range of 5 mm that is accurate to 0.05 mm. The graduations on the plastic rule served as reference points for measuring lengths greater than 5 mm.

Because the far-field temperature and salinity determine the ice melting processes, I measured the far-field condition with an array consisting of three thermistors and three surgical tubes. The three thermistors are the same as used on the ice array, and they are sealed in the same manner. I mounted them on a 12.7 mm x 12.7 mm acrylic plastic rod 1.2 m long; 0.25 m separates each sensor with the bottommost thermistor at the bottom of the rod. Each surgical tube, which was taped to the support, terminated at one of the thermistors and with a syringe I drew water samples for later salinity determination by either refractometer previously described. Figure 3 shows the placement of the ice and far-field array in the tank. I placed this array 0.5 m from the ice surface such that the far-field array and the array

within the ice spanned the same vertical distance inside the tank.

During an experiment I recorded the thermistor resistances with a Non-Linear Systems data acquisition system that scanned each of the thermistors once every minute, measured the resistances with a Keithly Model 160 Digital Multimeter and recorded the data on magnetic tape. The Keithly meter has an accuracy of ±0.01 k-Ohm, which corresponds to an accuracy in temperature of approximately ±0.01°C. Figure 5 gives a characteristic curve of the resistance data for a typical experiment. The flat section labeled "A" gives the ice-water interface temperature. The ice melted past the sensor at the point labeled "B" and the outer edge of boundary layer passed the sensor at the point labeled "C". The interval of time from the thermistor meltout to the outer edge of the boundary layer along with the melting rate gives an estimate of the thermal boundary layer thickness.

To visualize the convective motions generated by the melting ice I illuminated small reflecting flakes suspended in the salt water with a vertically oriented plane of light. The flakes are finely ground mother-of-pearl, obtained from the Mearl Corporation, 41 East 42nd Street, New York City, New York 10017, with the trade name "AA-Mearl Maid Flakes". The flakes are in paste form and 1 ml of paste emulsified in water insured a dense enough distribution of particles in the tank to trace the flow field. Because the settling time of the flakes is of order days, the flakes accurately followed the water motions. To prevent dissolution of these calcium carbonate flakes, I made the water slightly basic by the addition of 0.2 kg of sodium bicarbonate. To view the flakes, I illuminated them with a plane of light from a standard 2 inch by 2 inch slide projector. I generated a plane of light by

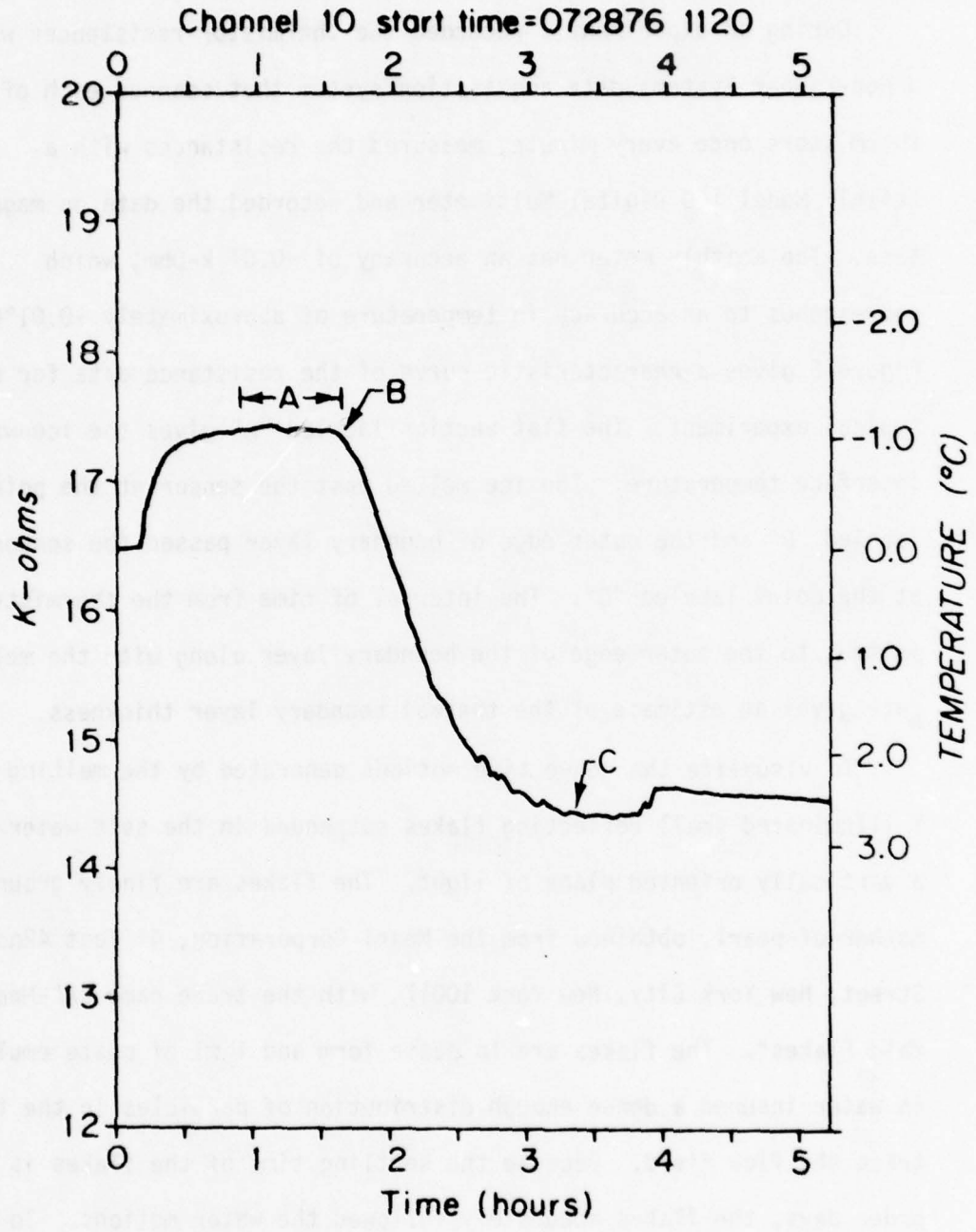


Figure 5. A representative thermistor record; A is the portion of the record averaged to obtain T_w, B is the time when the ice melted past the thermistor and C is the far-field temperature.

projecting the light through a slide mount which had two razor blades taped to the mount to form a slit 2 mm wide. The light entered the tank from the end near the ice slab and passed through the bubble-free ice to illuminate the convective boundary layer next to the ice. I viewed and photographed the flow field through the side of the tank normal to the light plane. I photographed the flow using a 35 mm Nikon camera with a 50 mm lens and Kodak Panatomic-X film; the exposures were usually at f-8 for a period of 30 s. Plate I is an example of a streak photograph; the particle motions appear on the photographs as white streaks against a black background. The streak photographs give only a qualitative picture of the flow because the flakes rotate during the exposure and thus may not be visible during the entire exposure.

To estimate the velocities associated with the convective motions, I injected a neutrally buoyant mixture of India ink and salt water into the boundary layer. I then measured with a stop watch the time it took for the leading edge of the dye to pass between thermistors in the ice. Also, the dispersion of the dye across the boundary layer gives an estimate of the boundary layer thickness. I obtained another estimate of the boundary layer thickness by viewing a Moiré grid through the boundary layer such that the line of sight was parallel to the ice surface. The large change in the index of refraction between the water near the ice and the ambient water distorts the Moiré grid and makes the outer limit of convective motions visible.

To maintain homogeneous far-field conditions, I relied on the large mass of water in the tank and a pumping and heating system. In the pumping system shown in Figure 3 the colder less saline water generated by the melting ice was pumped from the surface of the tank

through a constant temperature bath and returned to the bottom of the tank behind a perforated diffusing screen. This screen allowed the return flow to mix in the tank without affecting the convective motions generated by the melting ice. The pumping rate was of order 100 $mm^3 s^{-1}$ which produced an upward velocity in the tank of 0.15 mm s^{-1}, or much less than the 10 mm s^{-1} observed velocities.

To summarize, a typical experiment proceeded in the following fashion: I removed the ice from cold storage at -15°C and allowed the ice to warm to -1°C to prevent thermal fracture during placement in the tank. This procedure took approximately 30 minutes during which time the tank was vigorously stirred and allowed to come to rest to insure homogeneous far-field conditions. I then connected the thermistors to the data acquisition system and began recording just prior to submerging the ice. Once the ice was submerged, a plumb bob assured vertical alignment of the ice surface and the experiment began.

During the experiment I measured the lengths of the melt probes every 30 minutes and drew far-field salinity samples. I observed and photographed the flow using reflecting flakes and dye injections. Towards the end of an experiment, photographs recorded the final ice shape. The experiment ended when the ice melted past all of the thermistors frozen in the ice. After removing the array and any residual ice from the tank, I rinsed the array with fresh water and placed it in a crushed ice and water bath to determine the 0°C thermistor resistances. After this calibration, data recording stopped and the magnetic tape was read. I then determined the salinity of the far-field samples and reduced the melt rate data.

The Laboratory Observations

Introduction

This chapter presents and discusses the nature of the flow generated by a melting vertical ice wall, the vertical variation of the ice-water interface temperature, and the ice melt rates. To summarize, the laboratory experiments for ambient temperatures less than 20°C show that the flow next to the bottom portion of the ice consists of a laminar bidirectional flow with a vertical extent limited by a critical Grashof number of 1.6×10^8. Above this laminar region, I found an upward flowing turbulent boundary layer. Between the laminar and turbulent regions, a horizontal jet of ambient water flows towards the ice that melts a notch in the ice wall. Additional experiments show that high ambient temperatures, bubbles in the ice, and tilting the ice wall modify the flow, temperature and melt characteristics from those observed in the bubble-free case for $T_d < 20°C$.

In the laboratory study most of the experiments concentrate on the case of vertically oriented bubble-free ice at $T_d < 20°C$. The discussion continues with the specific cases of $T_d > 20°C$, bubbly ice and tilted walls.

The Case of Bubble-Free Ice, $T_d < 20°C$ and Vertical Wall.

The laminar bidirectional and unidirectional flow.

At the bottom portion of the ice I observe laminar flow, either bidirectional or upward, whose characteristics depend on the far-field conditions. When S_∞ and T_∞ lie in region II of Figure 1, the region where the salinity effect on density opposes the temperature effect, the flow is upward near the ice and downward away from the ice.

When S_∞ and T_∞ lie in region I of Figure 1, the region where the salinity and temperature effects reinforce, the flow is everywhere upward.

For the first case, the velocity field consists of a thin upward-flowing region next to the ice inside of a wider downward flowing region. Figure 6, a sketch of the observed flow, and Plates I and II illustrate the bidirectional nature. These two plates are 60 s streak photographs of the flow field for S_∞ = 33 $^{o}/_{oo}$ and T_∞ = -1.5°C; the top of Plate II joins Plate I at the level marked C. Immediately next to the ice Plates I and II show an upward-flowing region of order 1 mm thick which is thinnest at the bottom of the ice and increases in thickness with distance from the ice bottom; dye injections show the velocities in this region to be of order 1 mm s^{-1}. Two features on each plate mark the outer edge of the upward flowing layer: the apexes of the "V" shaped streak trajectories, and the region of short streaks and dots a few millimeters from the ice located between two regions of longer streaks. The arrows on the plates point to several of the "V" shaped trajectories and the arrow shafts lie along the region of short streaks and dots. The trajectories show a parcel of water moving out of the downward-flowing outer region, through a region of no vertical motion, and into the upward-flowing inner region.

The downward-flowing outer thermal region is of order 10 mm thick and grows in thickness as it flows downward until it approaches the bottom ice edge. As the outer flow approaches the bottom of the ice, the flow both constricts and curves slightly under the ice. Both the flow constriction and curvature below the ice bottom results from the

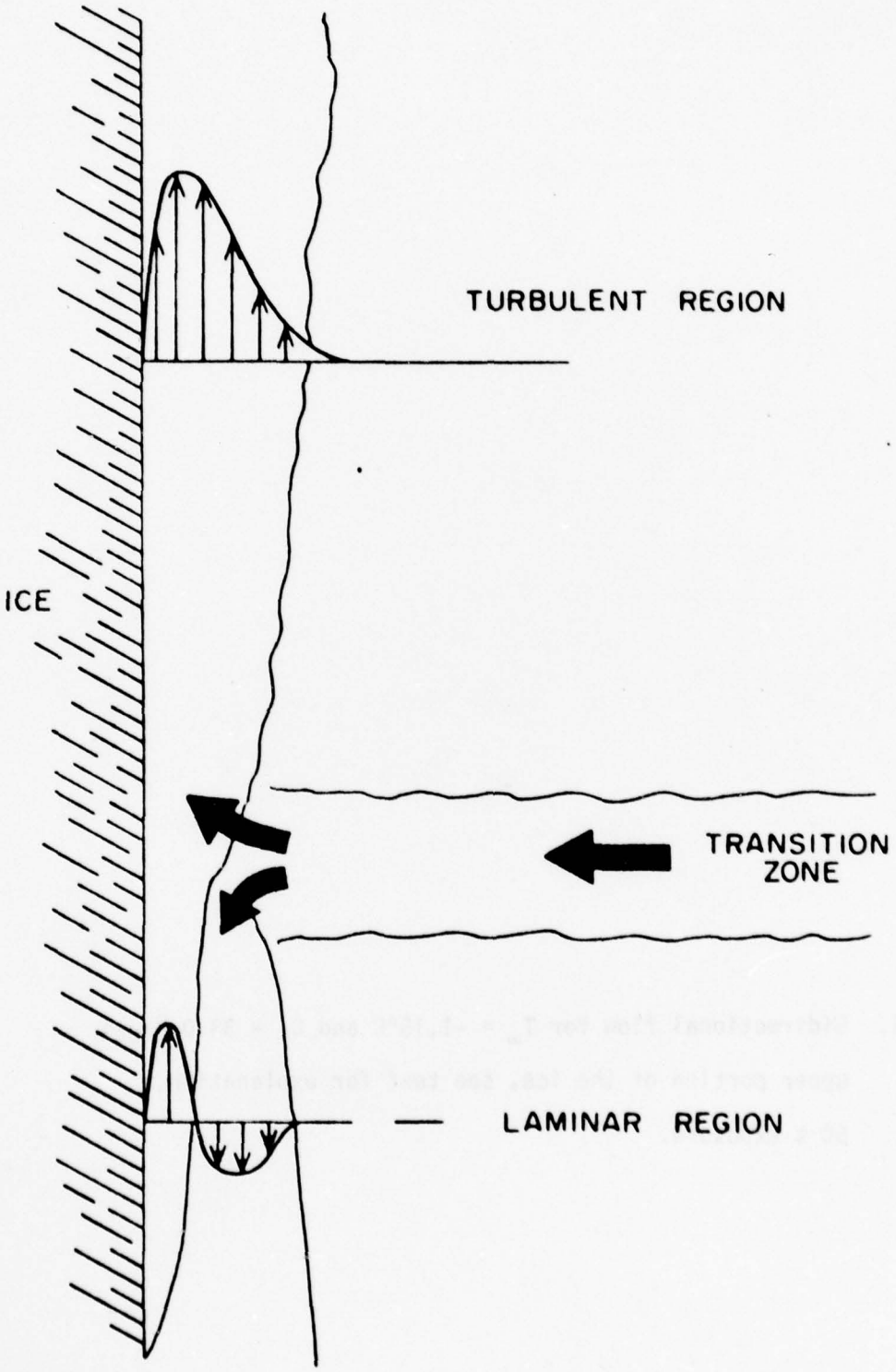
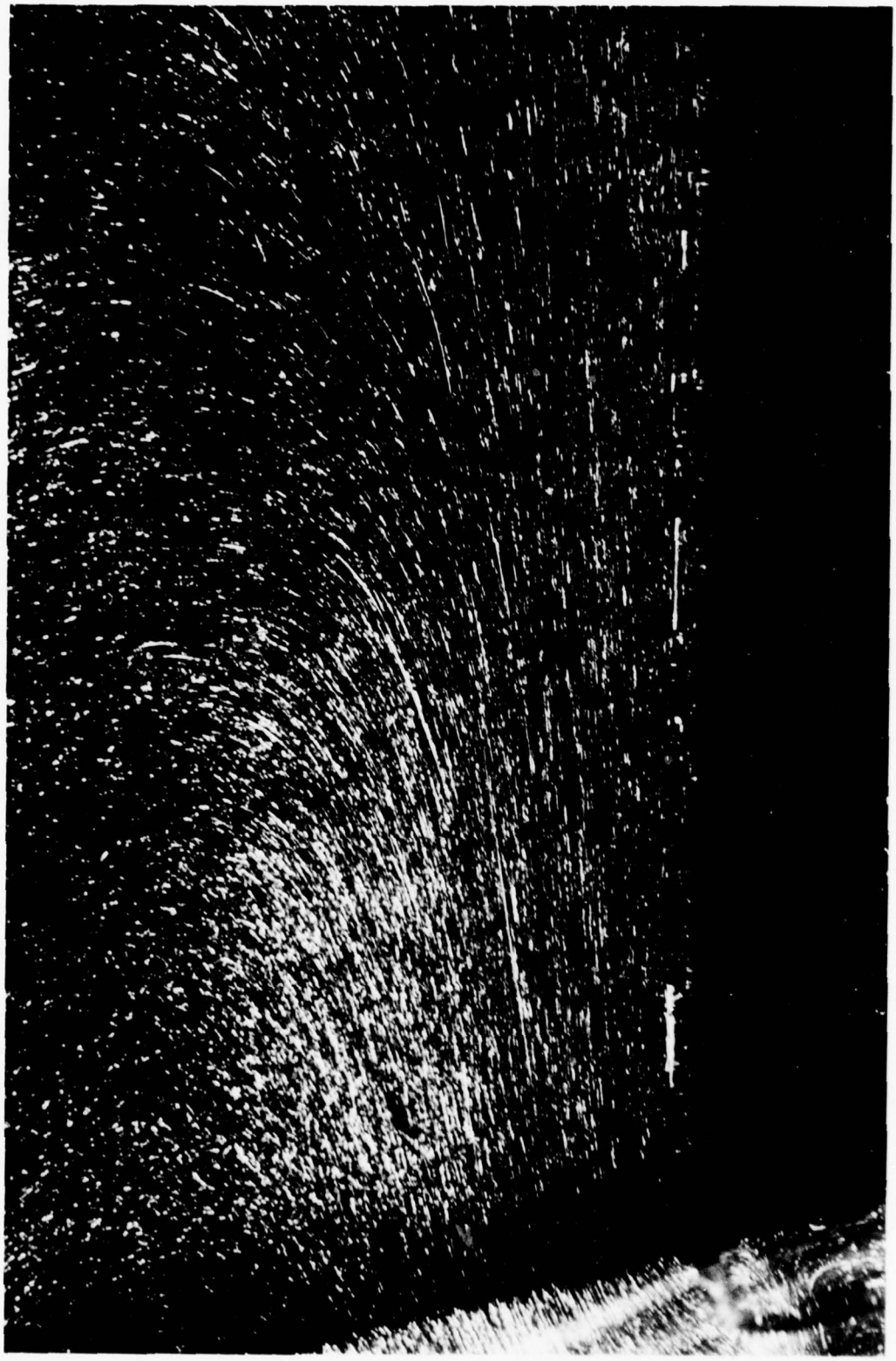


Figure 6. A sketch of the observed flow field next to the ice.

Plate I. Bidirectional flow for T_∞ = -1.15°C and S_∞ = 33.0 $^{o}/_{oo}$; upper portion of the ice, see text for explanation, 60 s exposure.

C

Plate II. Bidirectional flow next to lower portion of the ice, same experiment as Plate I, 60 s exposure.

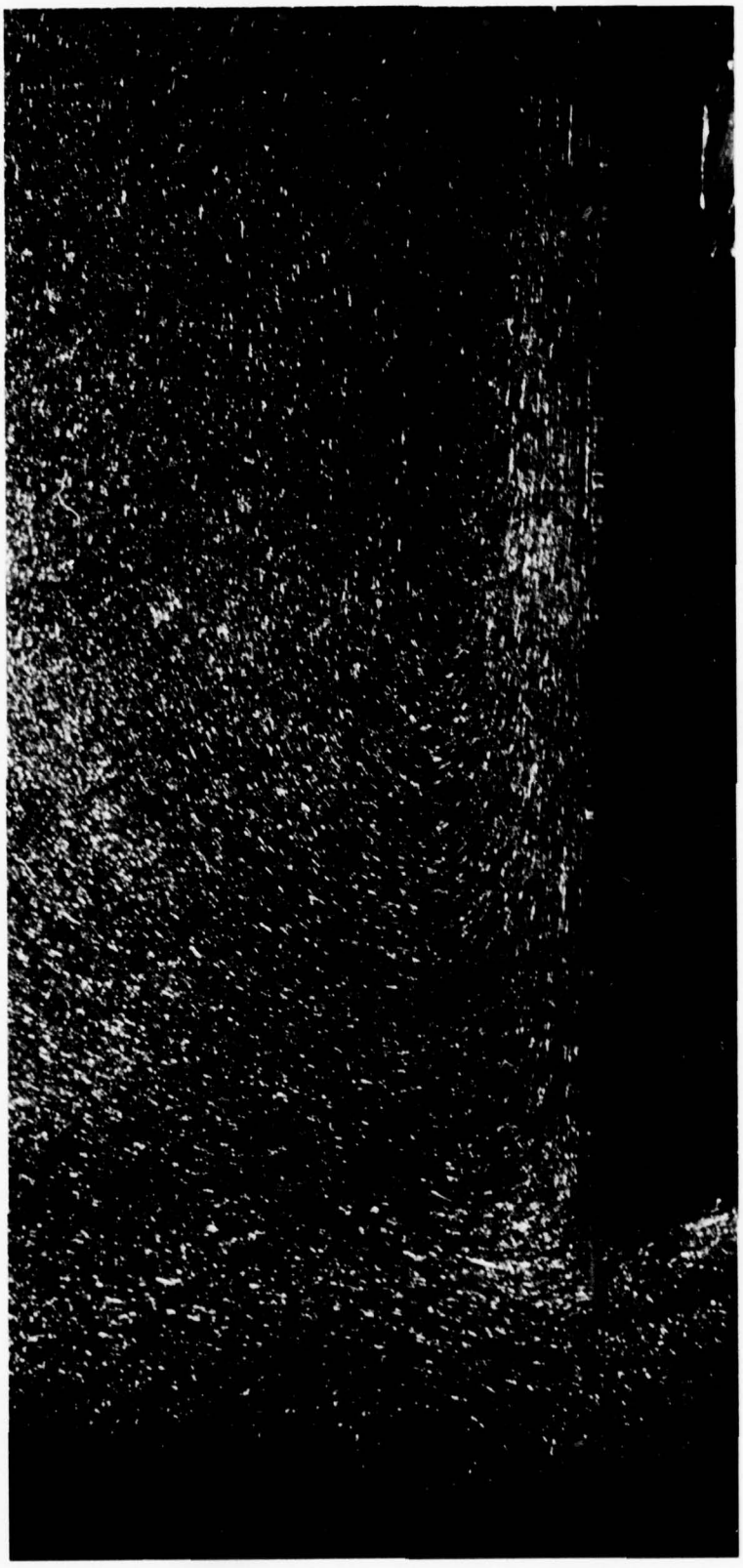


absence of the wall which causes the flow to accelerate; this acceleration, through Bernoulli's law, reduces the pressure within the boundary layer. Hence, the flow narrows and curves under the ice tip.

The large difference between the molecular diffusivities of heat and salt, characterized by Le = 200, produces the observed bidirectional flow. Adjacent to the ice, the melting dilutes and cools the salt water. As a result of the large difference in diffusivities, the dilution produces positively buoyant water near the ice that rises while the cooling produces negatively buoyant water farther from the ice that sinks. Even though the dilution buoyancy near the wall is much larger than the opposed buoyancy in the thermal layer, the frictional influence of the wall is largest near the wall so that the velocities in each region are of the same order.

For comparison when the far-field conditions lie between the freezing curve and the maximum density curve in Figure 1, I observe an upward-flowing unidirectional laminar boundary layer. In this case both dilution and cooling produce less dense water within the boundary layer; cooling decreases the density because the sign of α is positive in Region I of Figure 1. I performed two experiments with far-field conditions T = 0.05°C, S = 14.2 $^{o}/_{oo}$, and T = 1.8°C, S = 8.0 $^{o}/_{oo}$ to determine the characteristics of the flow in this situation. In both cases I observed an upward-flowing unidirectional boundary layer of order 10 mm thick. Plate III, a streak photograph from the first experiment, displays the unidirectional velocity field and a comparison with streak Plates I and II showing the bidirectional flow clearly illustrates the difference between the two cases.

Plate III. Unidirectional upward laminar flow, T_∞ = -0.4°C, S_∞ = 18 $^o/_{oo}$, 60 s exposure.



Transition to turbulence.

The turbulence studies concentrate on the case with opposing buoyancy forces because common oceanic salinities and temperatures lie in region II of Figure 1, or the region of opposing buoyancy forces. For the bidirectional case, the onset of turbulence in the inner saline layer determines the vertical extent of the laminar bidirectional flow. I observe the transition from laminar to turbulent flow in two ways; by viewing a Moiré grid through the boundary layer and by injecting dye into the boundary layer.

The use of both these techniques reveals small amplitude waves with horizontal crests parallel to the ice surface and perpendicular to gravity at the outer edge of the saline layer in the upper third of the laminar region. These waves propagate upward with a phase speed of order 1 mm s^{-1} and a wavelength of order 5 mm. The wave amplitude grows to approximately 3 mm at which point the waves "break"; about 30 mm above the point at which the waves break, the inner flow becomes turbulent. When compared to the theoretical stability study of Heiber and Gebhart (1971), these laboratory observations show that the stability of the inner saline layer is governed by a coupled buoyancy-momentum mechanism.

Vertical grooves which form in the ice in the upper third of the laminar region give indirect evidence of an additional transitional mechanism. These grooves have a width and depth of order 1 mm and a separation of order 25 mm. Gebhart (personal communication) attributes these grooves to a secondary flow feature consisting of longitudinal rolls that flow in a circular fashion perpendicular to the direction of

the mean flow. The increased melting results from the advection of heat towards the ice by these rolls in the flow.

When the inner flow becomes turbulent, the turbulence diffuses the dilute water near the ice further outward where the dilution buoyancy overwhelms the thermal buoyancy to produce an upward unidirectional flow. At the level of transition to turbulence, the divergence between the upward-flowing turbulent boundary layer and the downward-flowing laminar thermal boundary layer produces a horizontal jet of ambient water flowing towards the ice. Plates IV and V show the jet which appears as a broad band of horizontal streaks. The point labeled "B" at the ice-water interface on each photograph marks the stagnation stream line of the jet and will be called the bifurcation point. Water in the jet above the bifurcation point enters the upward-flowing boundary layer while water below this point enters the downward-flowing thermal boundary layer. Because the streaks in the jet are much longer than the horizontal streaks outside the jet, the velocities in the jet are much greater than the suction velocity associated with the boundary layer. The speeds in the jet are of order 1 mm s^{-1} and the jet has a thickness of approximately 100 mm.

As a result of the jet, the ice melts fastest in the region of the jet and a notch forms in the ice. Plate VI shows the ice after being immersed in water with a salinity of 29 $^{o}/_{oo}$ and a temperature of +1.5°C, T_d = 3.2°C, for a period of 5 hr. 17 min. Point B is the bifurcation point taken from Plate IV which shows the initial ice shape for this experiment. The experiment ended when the notch melted through the ice. Once the notch begins to form, it grows rapidly and stays at the same level.

Plate IV. Laminar bidirectional region and horizontal jet flowing towards the ice, T_∞ = 1.5°C, S_∞ = 29.0 $^{o}/_{oo}$, 60 s exposure.

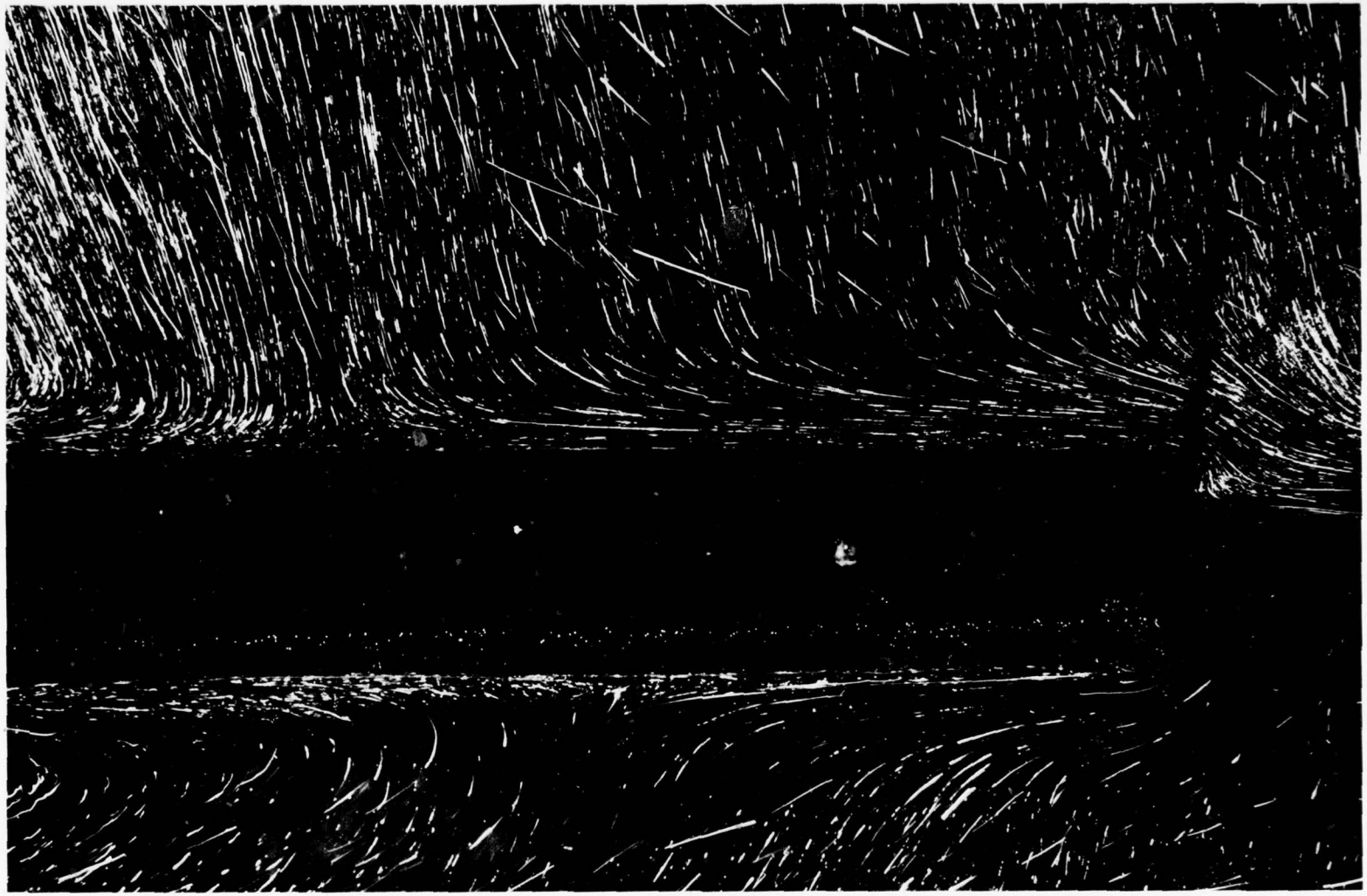


Plate V. Bidurcation of the horizontal jet; the arrow labeled B marks the bifurcation point; T_∞ = 2.2°C, S_∞ = 30.0 $^{o}/_{oo}$, 30 s exposure.

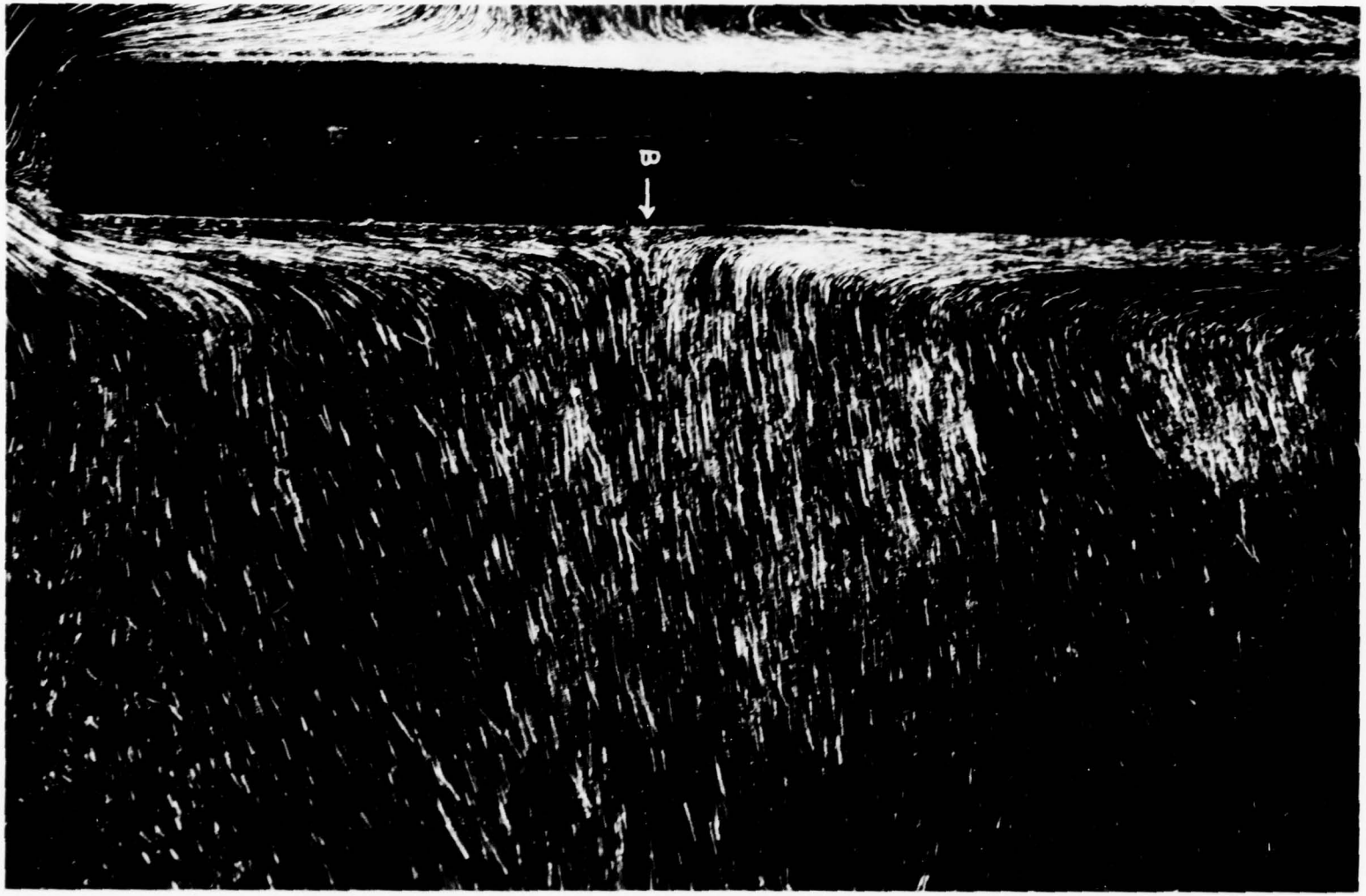
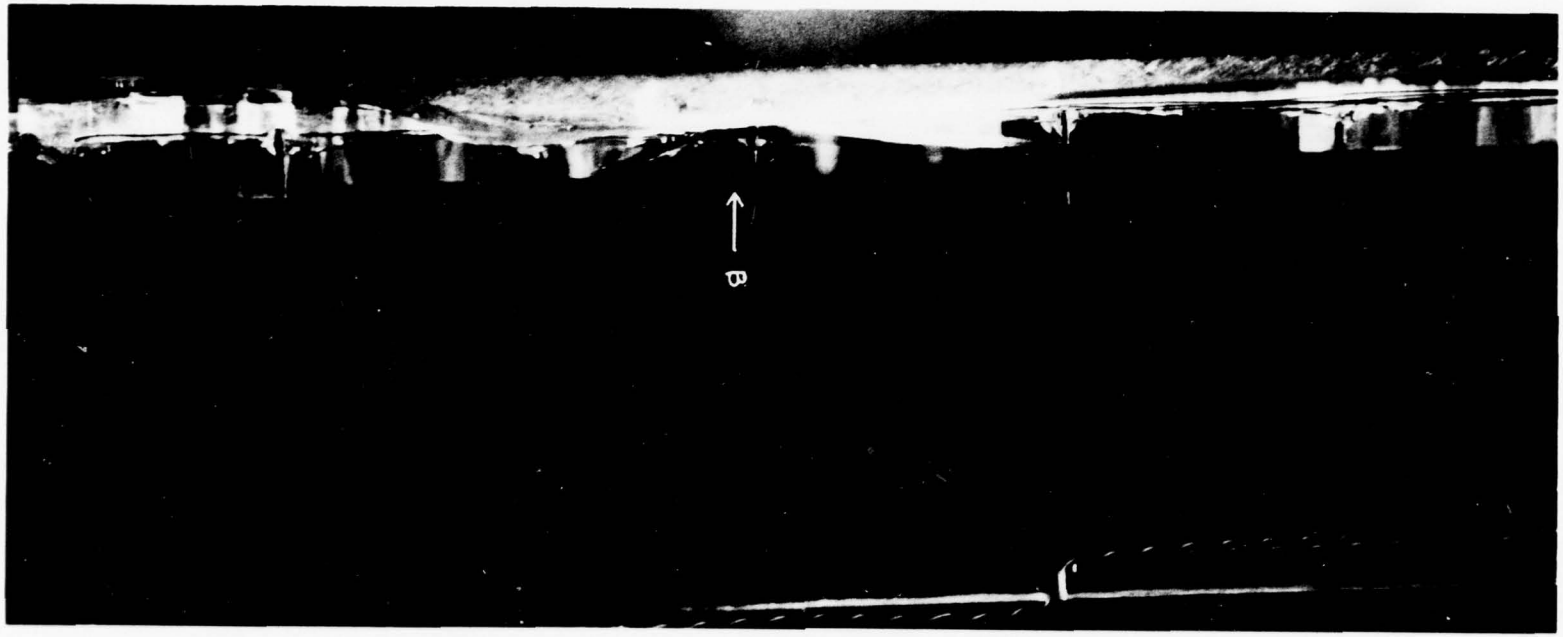

B

Plate VI. Increased melting at the bifurcation point, same experiment as Plate IV, after melting for 5 hr 17 min.


B

The length of the laminar regime, L_ℓ, is the distance from the bottom tip of the ice to the bifurcation point. Table 2 gives the observed values of L_ℓ, the average wall salinity and temperature, and the saline and thermal Grashof numbers for each of the laminar experiments. With increased thermal driving, L_ℓ decreases from 300 mm at T_d = 1.65°C to 110 mm at T_d = 8.71°C. The average G_S is 1.6 x 10^8, while the average G_T is 3.8 x 10^6. The coefficient of saline expansion used is 8.1 x 10^{-4} $^{o}/_{oo}{}^{-1}$ from Appendix I, while the coefficient of thermal expansion used to calculate G_T is evaluated at the far-field conditions. Because Gr_S is two orders of magnitude larger than Gr_T, the stability of the saline layer determines L_ℓ, which is a convenient length scale for the presentation of the laminar wall temperature data.

Laminar wall temperatures.

In the bidirectional case the average wall temperature, $\overline{T}_w$, decreases as T_d increases with the following vertical variation of T_w: T_w is coldest at the bottom of the ice and slowly warms with increasing distance from the ice tip. Figure 7 exhibits the vertical variation of T_w for the laminar experiments. The normalized interface temperature r is

$$r = \frac{T_w}{T_{fp}(S_\infty)} \quad .$$

Figure 7 shows r as a function of the distance from the bottom tip of the ice divided by the length of the laminar regime, L_ℓ. Where the L_ℓ was not measured directly, I computed it using a critical Gr_S = 1.6 x 10^8 and the measured salinity difference between the wall and the far field. The figure shows that r varies by as much as 20% over the

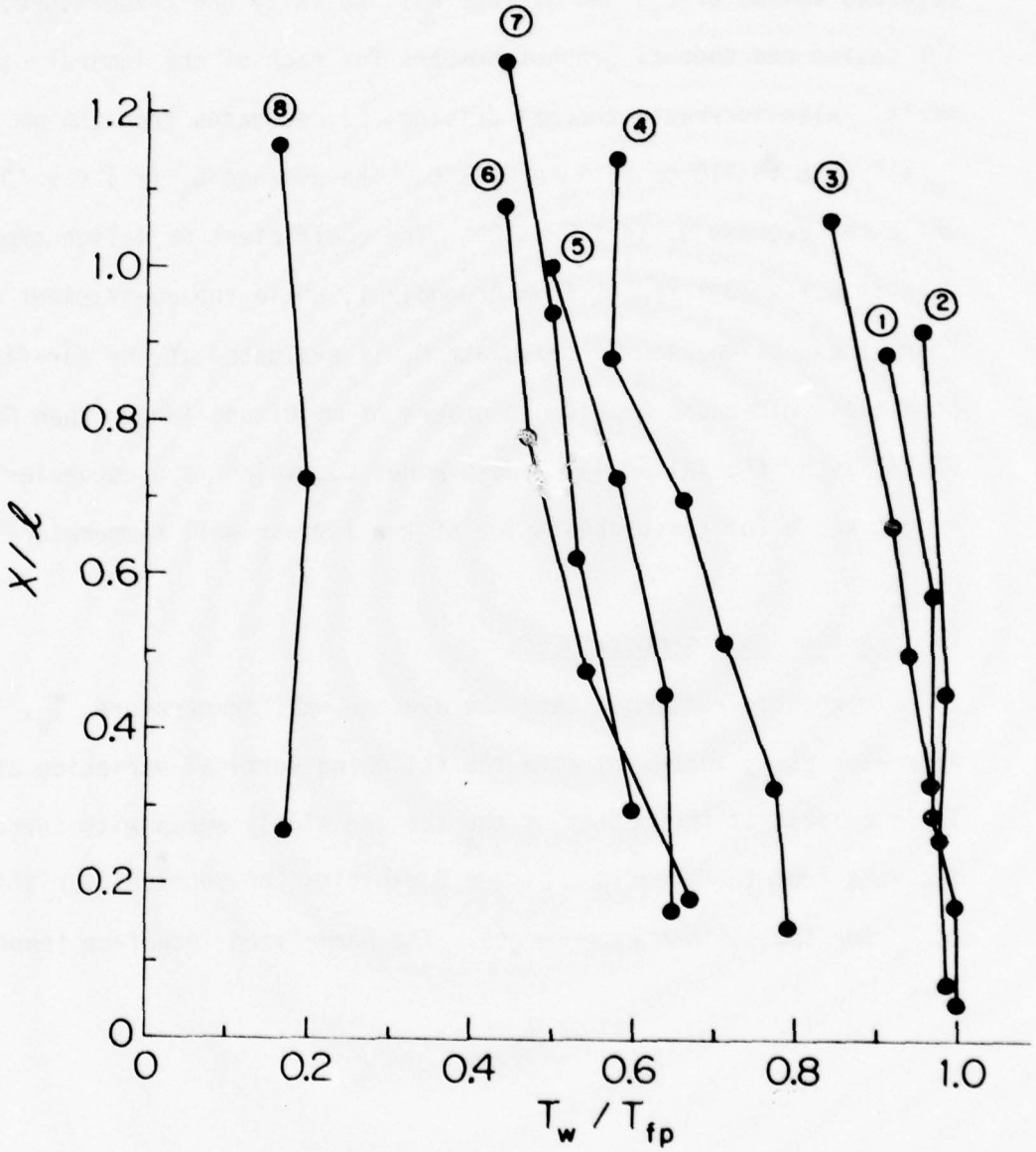


Figure 7. The vertical variation of T_w/T_{fp} in the laminar region. Each circled number is an experiment and Table 2 gives the far-field conditions of each experiment.

Table 2

Experiment number	T_∞ (°C)	S_∞ ($^o/_{oo}$)	T_d (°C)	ℓ (mm)	T_w (°C)
1	-0.5	29.0	1.08		-1.53
2	-0.72	33.7	1.13	260	-1.81
3	0.0	29.0	1.65	300	-1.49
4	1.55	29.0	3.13	270	-1.11
5	2.20	30.0	3.83	180	-0.97
6	2.70	29.0	4.28		-0.80
7	2.66	34.4	4.55	155	-1.03
8	6.85	34.0	8.71	110	-0.32

Summary of laminar bidirectional experiments, ℓ not observed for experiments 1 and 6.

Table 3

T_∞ (°C)	S_∞ ($^o/_{oo}$)	T_d (°C)	T_w (°C)	S_w ($^o/_{oo}$)	r
+0.05	14.2	0.78	-0.66	12.8	0.90
+1.80	8.0	2.50	-0.29	5.6	0.70

Far-field conditions for the two unidirectional experiments and the resulting interface conditions.

length of the laminar layer, which corresponds to a temperature change of approximately 0.35°C for the experimental conditions. The maximum variation occurs in the range of T_d from 3°C to 5°C. For $T_d > 5$°C the variation of r decreases because T_w at any level begins to approach the fresh water limit.

Figure 8 gives $\overline{T}_w$, obtained by averaging all of the temperature measurements in the laminar region from an experiment and then normalizing with $T_{fp}(S_\infty)$ for that experiment as a function of T_d. The normaized average interface temperature, $\overline{r}$, where

$$\overline{r} = \frac{\overline{T}_w}{T_{fp}(S_\infty)} \quad ,$$

gives a measure of the dilution occurring at the interface. $\overline{r}$ varies from 1, when the ice is in equilibrium with the far-field and no melting occurs, to 0 when the melt rate is great enough to prevent salt from reaching the interface. The interface temperature and hence the interface salinity both approach the fresh water limit, $T_w = 0$°C and $S_w = 0\ ^o/_{oo}$, as the thermal driving increases with 90% of the change occurring for $T_d \leq 10$°C. For $T_d > 10$°C the interface conditions asymptotically approach the fresh water limit.

For the unidirectional laminar case, I found vertically uniform wall conditions in each of the experiments. Table 3 gives the far-field conditions, T_d and T_w for the two experiments. The uniform S_w and T_w and unidirectional flow suggests that the analysis of Gebhart and Pera (1971) is applicable to this case; however, they do not include the effect of blowing at the interface.

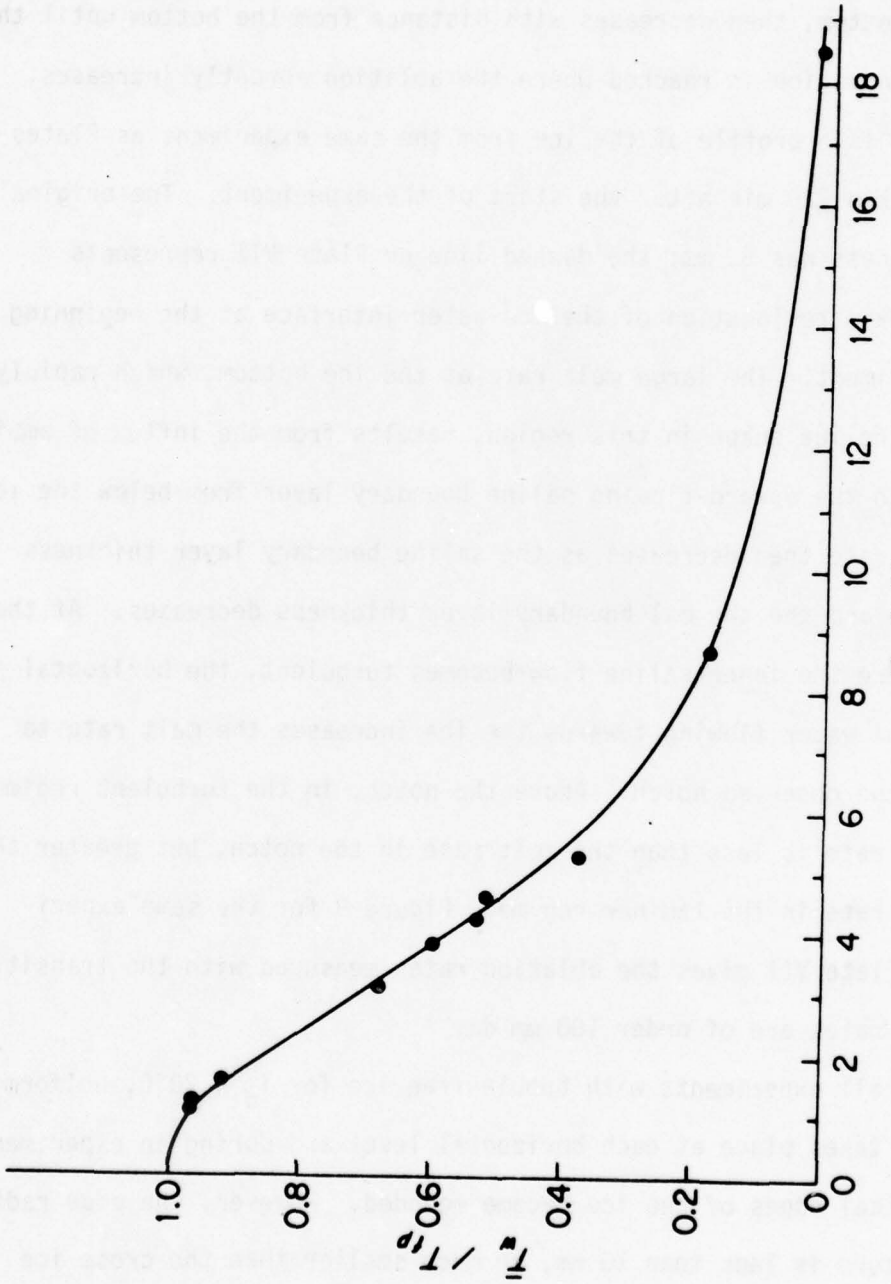


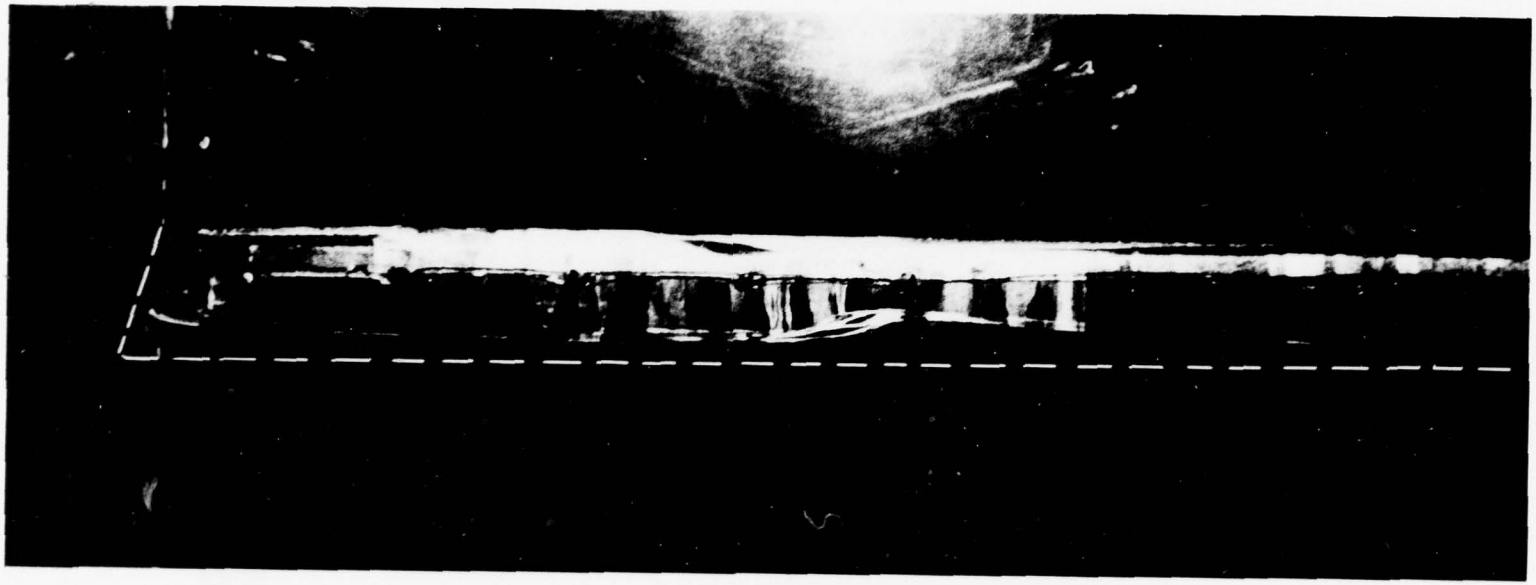
Figure 8. The dependence of $\bar{T}_w/T_{fp}$ in the laminar region on T_d.

Observations of melting in the laminar bidirectional region.

In the laminar bidirectional case, the ice ablation is greatest at the ice bottom, then decreases with distance from the bottom until the transition region is reached where the ablation abruptly increases. Plate VII is a profile of the ice from the same experiment as Plates IV and VI taken 220 min after the start of the experiment. The original ice thickness was 55 mm; the dashed line on Plate VII represents the approximate location of the ice-water interface at the beginning of the experiment. The large melt rate at the ice bottom, which rapidly changes the ice shape in this region, results from the influx of ambient water into the upward-flowing saline boundary layer from below the ice. The melt rate then decreases as the saline boundary layer thickness increases and the thermal boundary layer thickness decreases. At the level where the inner saline flow becomes turbulent, the horizontal jet of ambient water flowing towards the ice increases the melt rate to produce the observed notch. Above the notch, in the turbulent regime, the melt rate is less than the melt rate in the notch, but greater than the melt rate in the laminar regime. Figure 9 for the same experiment as Plate VII gives the ablation rates measured with the transit; the melt rates are of order 100 mm day^{-1}.

For all experiments with bubble-free ice for $T_d < 20°C$, uniform ice ablation takes place at each horizontal level and during an experiment the vertical edges of the ice become rounded. However, the edge radius of curvature is less than 10 mm, or much smaller than the cross ice dimension of 200 mm; therefore, edge rounding also has little effect on the overall flow and the observed melt rates.

Plate VII. Ice shape in the laminar region after melting for 3 hr 40 min, same experiment as Plate IV.



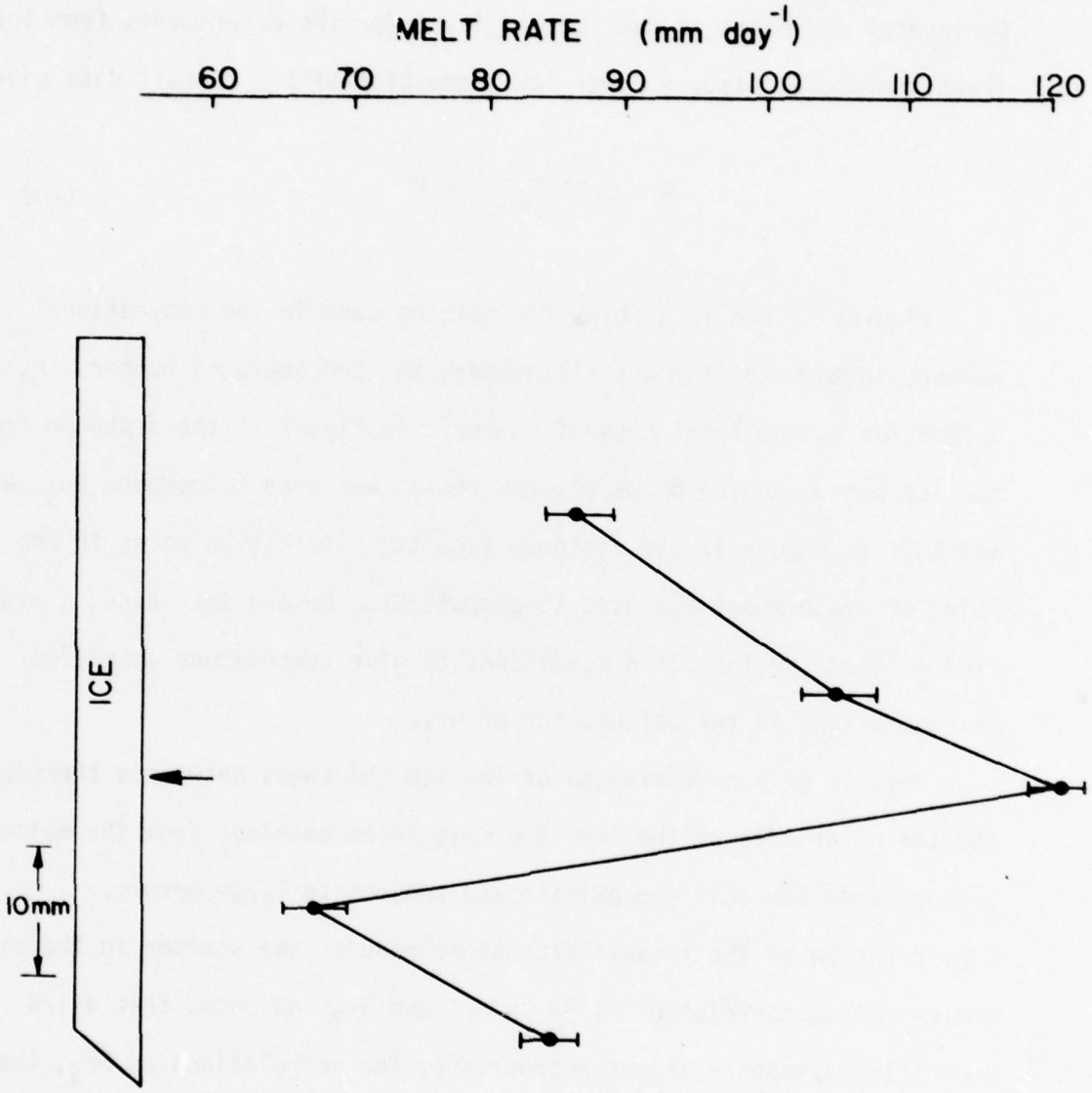


Figure 9. Representative melt rate distribution as measured by transit. The arrow locates the bifurcation point.

Figure 10 gives the melt rate measured at the vertical and horizontal mid-point of the laminar layer for the experiments from the transit measurements. A power law regression of the transit data gives

$$M = 0.34\ T_d^{2.0} \pm 1\% \quad . \tag{24}$$

Figures 11 and 12 display the melting data in the conventional manner; in terms of the Nusselt number, Nu, and Sherwood number, Sh, as a function of the local Grashof number. In Figure 11 the distance from the ice bottom to the point of measurement was used to compute Gr_S, Nu and Sh. In Figure 12 the distance from the bifurcation point to the point of measurement was used to compute Gr_T, Nu and Sh. Also, I evaluated $\frac{1}{\rho}\frac{\partial \rho}{\partial T}$ at the far-field conditions to give temperature anomalies maximum weight in the calculation of Gr_T.

Because of poor estimates of the ice thickness between a thermistor and the outer edge of the ice, the melt rates obtained from the melt-through time are only approximate and subject to large errors. Consideration of the transit data alone reduces the scatter in the data. The resulting correlation of Nu on Gr_S and Gr_T indicates that a 1/4 power law dependence is not appropriate; for correlations on Gr_S, the data indicate a 1/8 power law, while for correlations on Gr_T, the data indicate a 1/2 power law. The failure of a 1/4 power law for Sh results from the omission of blowing from previous studies that give the 1/4 power law correlation. LaPadula and Mueller (1970) show that the effect of blowing increases with increasing Pr or Sc which explains the observed correlation differences between Nu and Sh. The effect of blowing on the

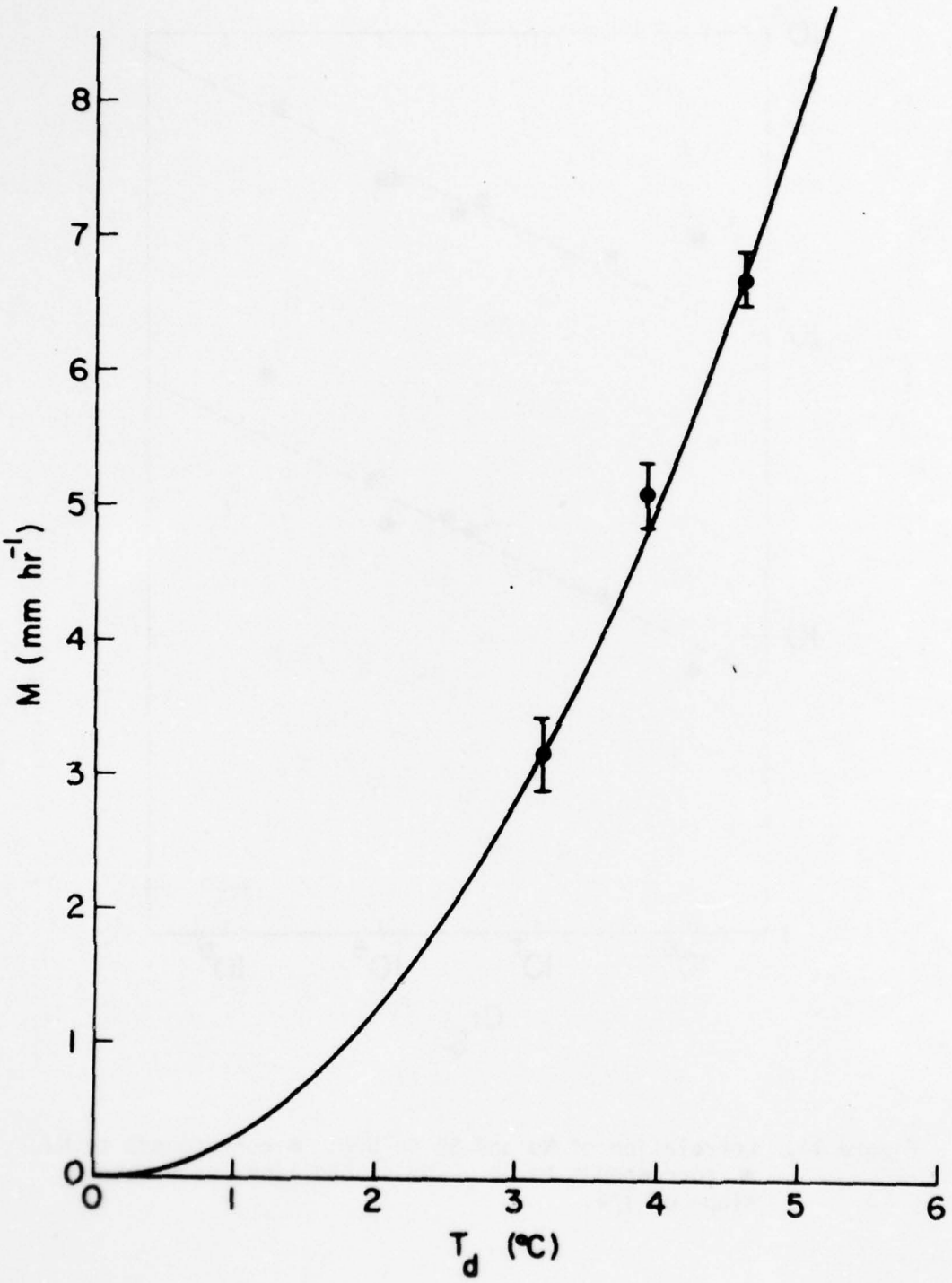


Figure 10. The dependence of the average melt rate, M, in the laminar region on T_d.

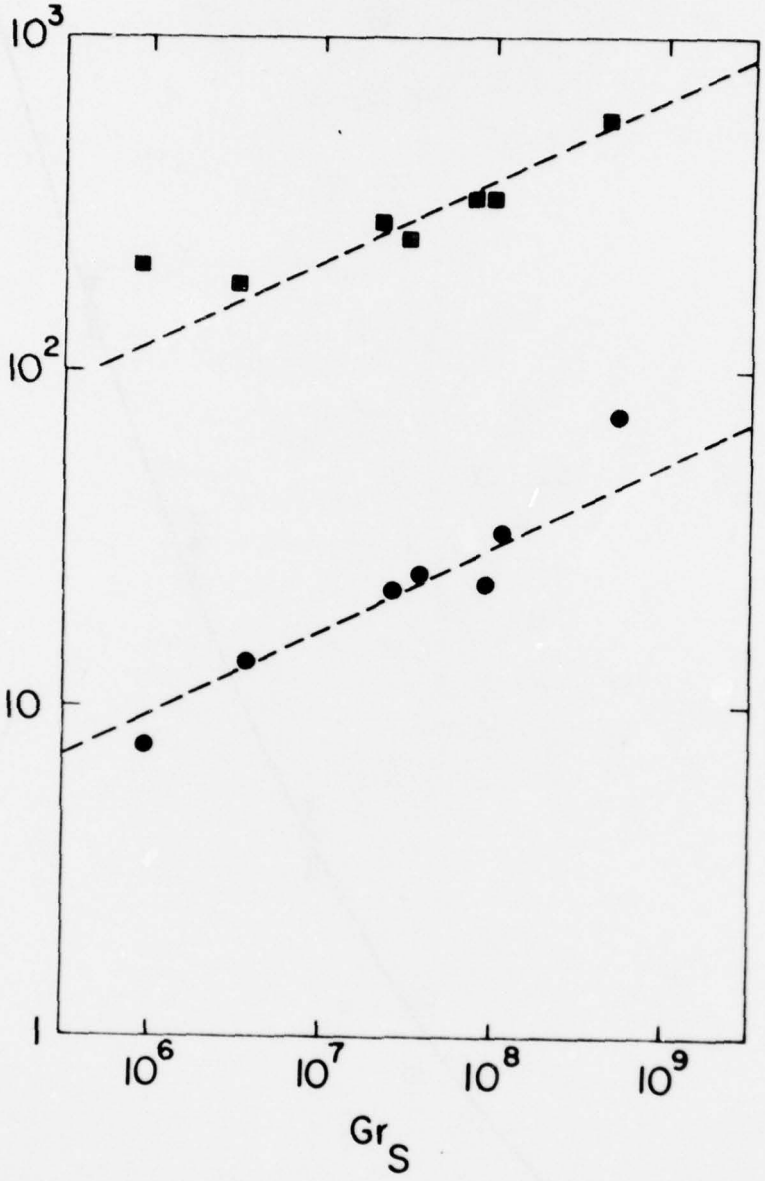


Figure 11. Correlation of Nu and Sh on Gr_S; ● corresponds to Nu, ■ corresponds to Sh. The dashed lines each have a slope of 1/4.

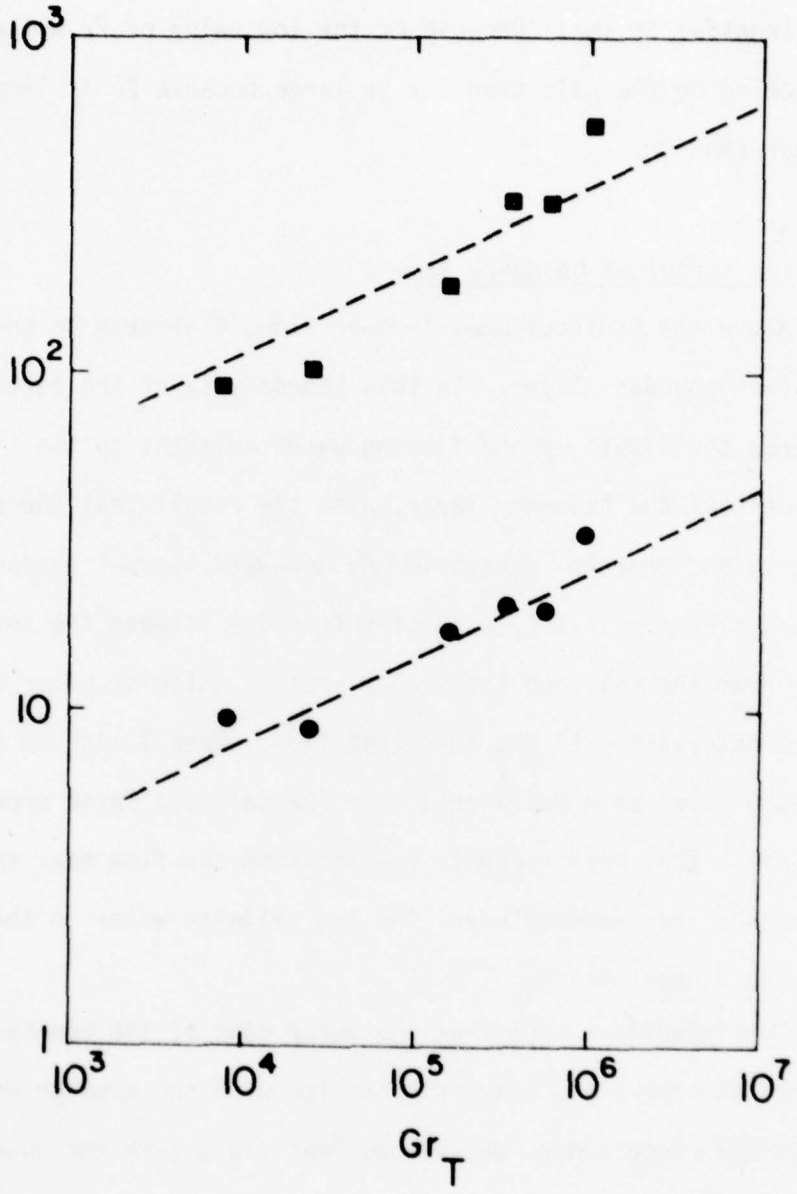


Figure 12. Correlation of Nu and Sh on Gr_T; ● corresponds to Nu, ■ corresponds to Sh. The dashed lines each have a slope of 1/4.

heat transfer is small because of the low value of Pr while the effect of blowing on the salt transfer is large because Sc is large, 200 times greater than Pr.

The turbulent boundary layer.

Above the bidirectional laminar flow, I observe an upward-flowing turbulent boundary layer. In this boundary layer the turbulent motions disperse the dilute upward-flowing water adjacent to the ice across the thickness of the boundary layer, with the result that the upward buoyancy and momentum overwhelm the downward thermal buoyancy. The large difference in the index-of-refraction between the low salinity water near the wall and the higher ambient salinity water allows for direct observation of the turbulent flow. When I sighted across the boundary layer at a Moiré grid, the low salinity water appeared as 1 mm wide wisps that were randomly ejected from the flow near the wall. The turbulence then rapidly mixes the low salinity water to the point where it is no longer visible.

Dye injections show that the outer edge of the boundary layer fluctuates toward and away from the ice with the passage of turbulent eddies and these eddies entrain ambient fluid into the boundary layer. Townsend (1976) shows that the boundary between a turbulent flow and the quiescent fluid remains sharp while wavering back and forth. The temperature records give further evidence of this phenomena. Figure 13 is an example of the temperature records from the turbulent region and these records are discussed fully below. The boundary layer thickness is approximately 10-30 mm and becomes thicker with increasing downstream

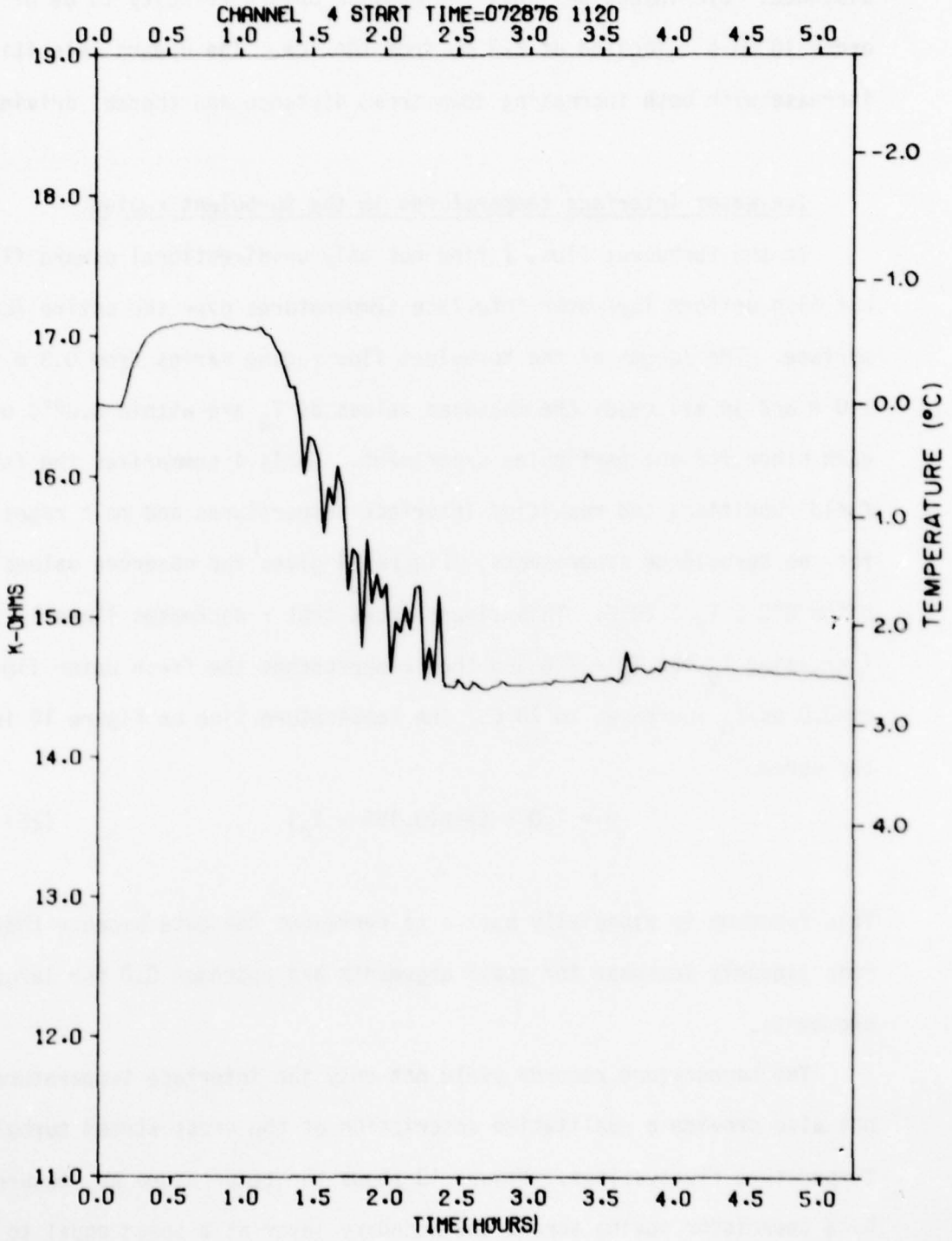


Figure 13. A representative thermistor record from the turbulent region. See text for explanation.

distance. Dye injections show the maximum upward velocity to be of order 10 mm s^{-1} located at 2-3 mm from the ice. The upward velocities increase with both increasing downstream distance and thermal driving.

Ice-water interface temperatures in the turbulent region.

In the turbulent flow, I find not only unidirectional upward flow, but also uniform ice-water interface temperatures over the entire ice surface. The length of the turbulent flow regime varies from 0.3 m to 1.0 m and in all cases the measured values of T_w are within 0.02°C of each other for any particular experiment. Table 4 summarizes the far-field conditions and resulting interface temperatures and melt rates for the turbulence experiments. Figure 14 gives the observed values of r for $0°C \leq T_d \leq 20°C$. This figure shows that r decreases linearly with increasing T_d for $T_d \approx 7°C$ and then r approaches the fresh water limit of 0.0 as T_d increases to 20°C. The temperature line on Figure 14 is the curve

$$r = 1.0 - \tanh(0.155 \times T_d) \quad . \tag{25}$$

This function is especially suited to represent the data because they both linearly decrease for small arguments and approach 0.0 for large arguments.

The temperature records yield not only the interface temperature, but also provide a qualitative description of the cross stream turbulent temperature fluctuations. Figure 13 shows the temperature as measured by a thermistor moving across the boundary layer at a speed equal to the ablation rate. In this case $T_w = -0.64°C$, $T_\infty = +2.7°C$, $T_d = 4.4°C$ and

Table 4

T_∞ (°C)	S_∞ ($^o/_{oo}$)	T_d (°C)	T_w (°C)	x (mm)	M x 10^{-3} mm s^{-1}
-0.10	29.9	1.53	-1.27	360	0.5
1.55	29.0	3.13	-0.92	100	1.02
				240	1.52
2.00	30.0	3.63	-0.76	390	1.56
				550	1.52
				840	1.54
2.20	30.0	3.83	-0.73	115	1.89
				240	2.03
2.66	34.4	4.55	-0.74	180	2.15
				330	2.20
3.42	30.0	5.05	-0.59	570	2.30
6.85	33.95	8.71	-0.20	220	6.27
				360	5.99
10.85	34.1	12.72	-0.06	370	9.47
16.31	35.2	18.24	-0.02	290	14.27

Table 4. Summary of turbulent experiments.

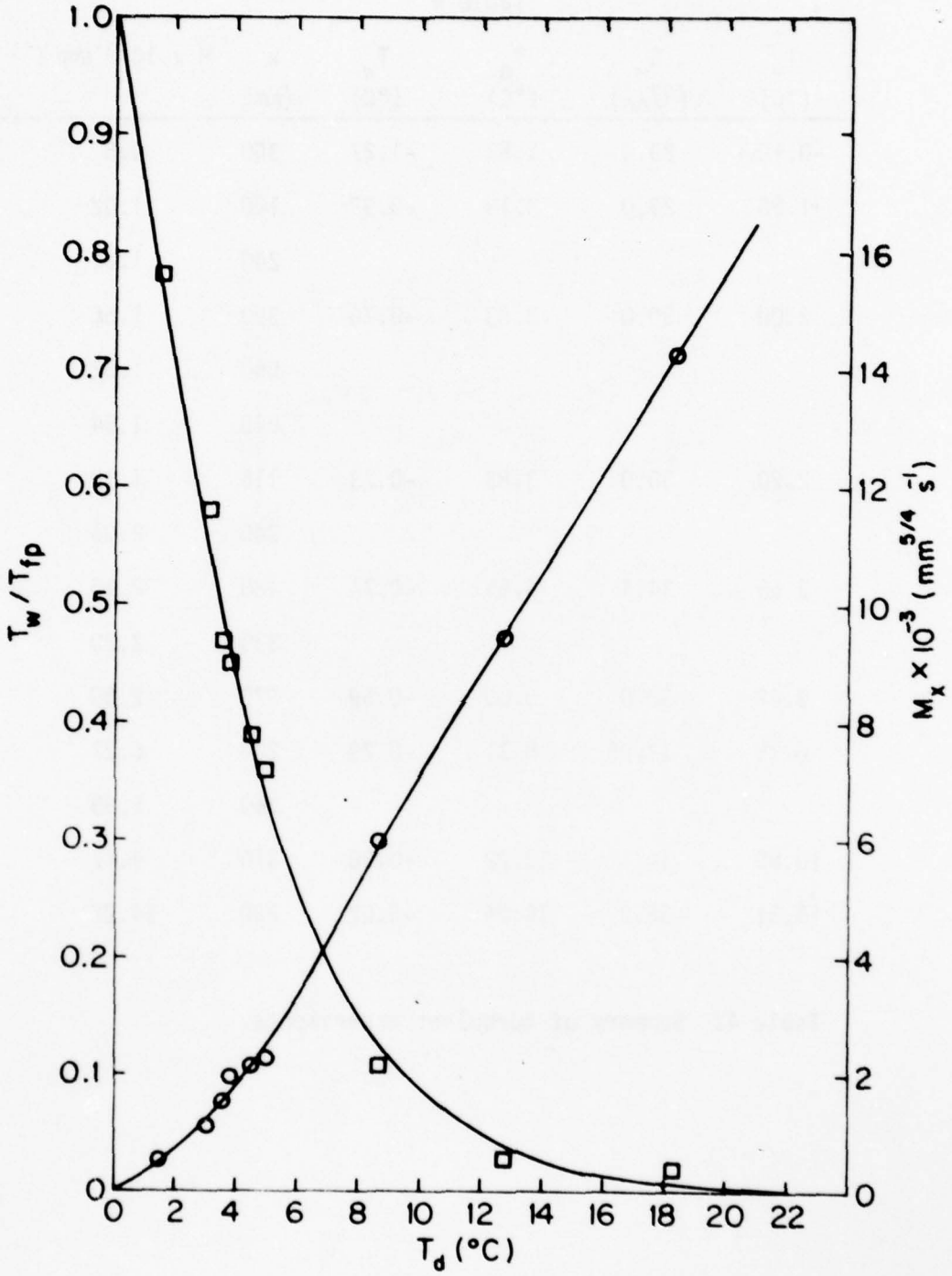


Figure 14. Experimental values of T_w/T_{fp}, □, and M_x, o, for the turbulent flow.

the melting rate, M, is 7.3 mm hr^{-1}. This record shows several features of the turbulent flow as the thermistor traverses the boundary layer. First, within 2 mm of the ice, no significant temperature fluctuations occur and the temperature increases monotonically. Second, in a region from 2 mm to 10 mm away from the ice, the temperature fluctuations occur as large as 0.5°C and the magnitude of the fluctuations increase with increasing distance from the ice. Third, the large temperature fluctuations at the outer edge of the boundary layer result from the wavering motion of the boundary between turbulent and quiescent fluid. Last, the thermal boundary layer thickness of 10 mm roughly equals the momentum boundary layer thickness observed by dye injections. The sampling rate of once-per-minute provides only a qualitative picture because fluctuations with frequencies greater than 0.02 s^{-1} remain undetected and both dye injections and the Moiré grid show fluctuations in the velocity field at frequencies of at least 1 s^{-1}.

Melt rates in the turbulent region.

For the ice adjacent to the turbulent flow, I found that the melt rate dependence on T_d changes from a power law dependence to a linear dependence at T_d = 9°C. Also, at a particular T_d, I found the melt rate to have the following vertical variation: The melt rate is highest at the bifurcation point and decreases with increasing distance from the bifurcation point. For all experiments at T_d < 20°C the ice melted in a smooth fashion; however, the wakes from the thermistors and melt probes produce 1 mm wide, 1 mm deep and 50 mm long perturbations on the ice surface.

Figure 14 gives the observed melt rates, M_x, for T_d up to 30°C, where M_x is the melt rate measured by transit at a distance x above the bifurcation point multiplied by $x^{1/4}$. For all cases, x lies between 0.2 m and 0.5 m. I chose this formulation for M_x because the uniform wall temperatures strongly suggest an $x^{1/4}$ similarity transformation where the melt rate decreases as $x^{-1/4}$. Therefore, M_x represents a characteristic melt rate for a given T_d that is independent of x; this convenient formulation aids in the similarity development discussed in the Similarity section.

Figure 15 gives the average observed melt rate $\overline{M}$ without the $x^{1/4}$ dependence and $\overline{M}$ is the average of all transit measured melt rates taken during each experiment. The solid line on Figure 15 is a power law regression fit of all the data given by

$$\overline{M} = 2.85 \times 10^{-4} T_d^{1.36} \text{ mm s}^{-1} \pm 2\% \quad . \tag{26}$$

However, as seen for M_x, a linear dependence best fits the data for $T_d < 9°C$.

Returning to Figure 14, the data show that the dependence of M_x on T_d changes in the vicinity of 9°C. For $T_d \leq 9°C$ a power law regression gives

$$M_x = 7.54 \; T_d^{1.63} \times 10^{-4} \text{ mm}^{5/4} \text{ s}^{-1} \tag{27}$$

while for $9°C \leq T_d \leq 20°C$ the data best fit a linear regression given by

$$M_x = [38.06 \; T_d - 7.29] \times 10^{-4} \text{ mm}^{5/4} \text{ s}^{-1} \quad . \tag{28}$$

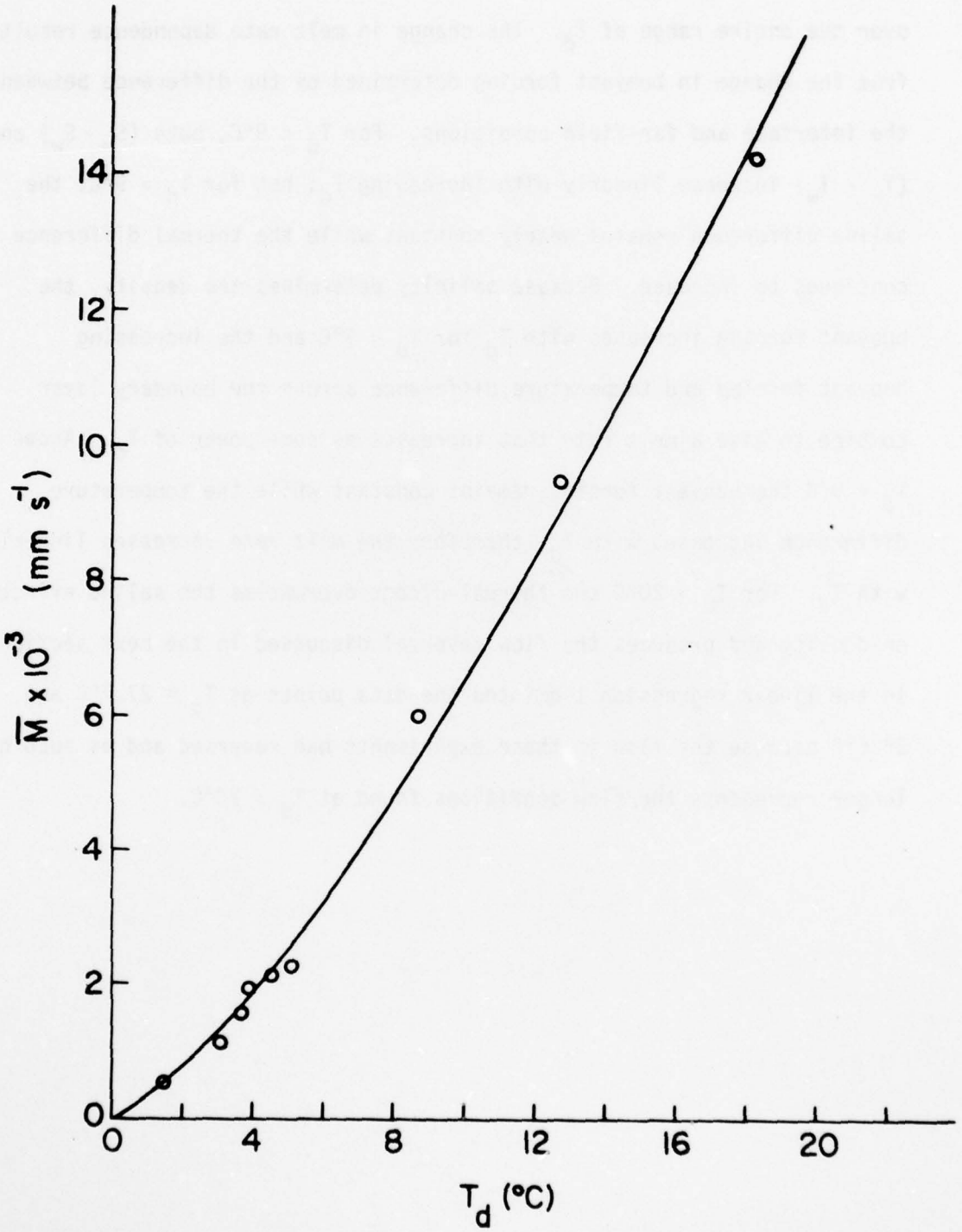


Figure 15. Experimental values of the vertically averaged melt rate, $\overline{M}$, for the turbulent flow.

Neither the linear nor the power law fit of the data is satisfactory over the entire range of T_d. The change in melt rate dependence results from the change in buoyant forcing determined by the difference between the interface and far-field conditions. For $T_d < 9°C$, both $(S_\infty - S_w)$ and $(T_\infty - T_w)$ increase linearly with increasing T_d; but for $T_d > 9°C$, the saline difference remains nearly constant while the thermal difference continues to increase. Because salinity determines the density, the buoyant forcing increases with T_d for $T_d < 9°C$ and the increasing buoyant forcing and temperature difference across the boundary layer combine to give a melt rate that increases as some power of T_d. Above $T_d \simeq 9°C$ the buoyant forcing remains constant while the temperature difference increases with T_d, therefore the melt rate increases linearly with T_d. For $T_d > 20°C$ the thermal effect overwhelms the saline effect on density and produces the flow reversal discussed in the next section. In the linear regression I omitted the data points at $T_d = 27.7°C$ and $26.6°C$ because the flow in these experiments had reversed and as such no longer represents the flow conditions found at $T_d < 20°C$.

The High Temperature Flow Reversal

Experiments at T_d > 25°C show that the flow next to the ice consists of a laminar bidirectional boundary layer at the top of the ice and a downward flowing turbulent boundary layer beneath the laminar flow. In addition, the ice ablates smoothly in the laminar region and irregularly in the turbulent region where the ablation produces cusps in the ice surface.

I performed two experiments at T_d > 25°C, T_d = 27.7°C, and 26.6°C and Figure 16, a sketch of the observed flow, illustrates the fluid motions and the resulting ice shape. At the top of the ice, I find a laminar bidirectional layer, 60 mm long, with the inner layer flowing up and the outer layer flowing down. The inner layer is 1-2 mm thick while the outer layer is 10-20 mm thick and the ice adjacent to this flow melted smoothly. Below this laminar flow I observe a 20-30 mm thick very turbulent downward flowing boundary layer that grows in thickness with distance down the ice. The ice next to this layer melts irregularly to produce cusps on the ice surface. Plate VIII shows the smooth region of the top of the ice and the cusped region over the rest of the ice. At the beginning of the experiment, this piece of ice was planed smooth; I took the photograph after the ice had been submerged in salt water at 24.8°C and 33.6 $^{o}/_{oo}$, T_d = 26.6°C, for 23 minutes.

The cusps have a downstream length scale that becomes longer as the experiment progresses. Plates IX and X taken 10 min and 23 min, respectively, after the start of the experiment, show the evolution of the cusps. Initially, well-ordered cusps form within 12 min from the beginning of an experiment with a downstream length of 10 mm and a cross

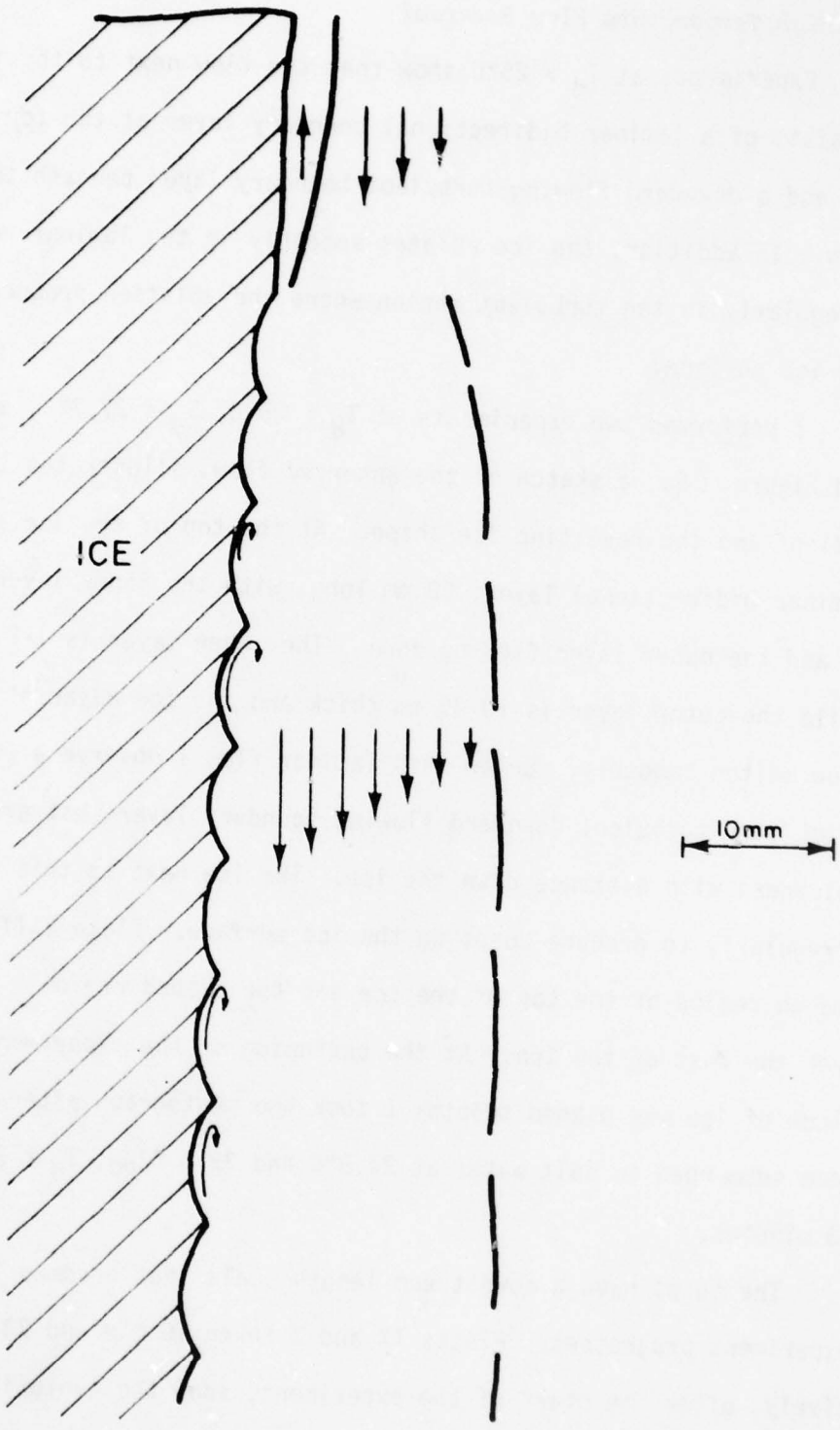
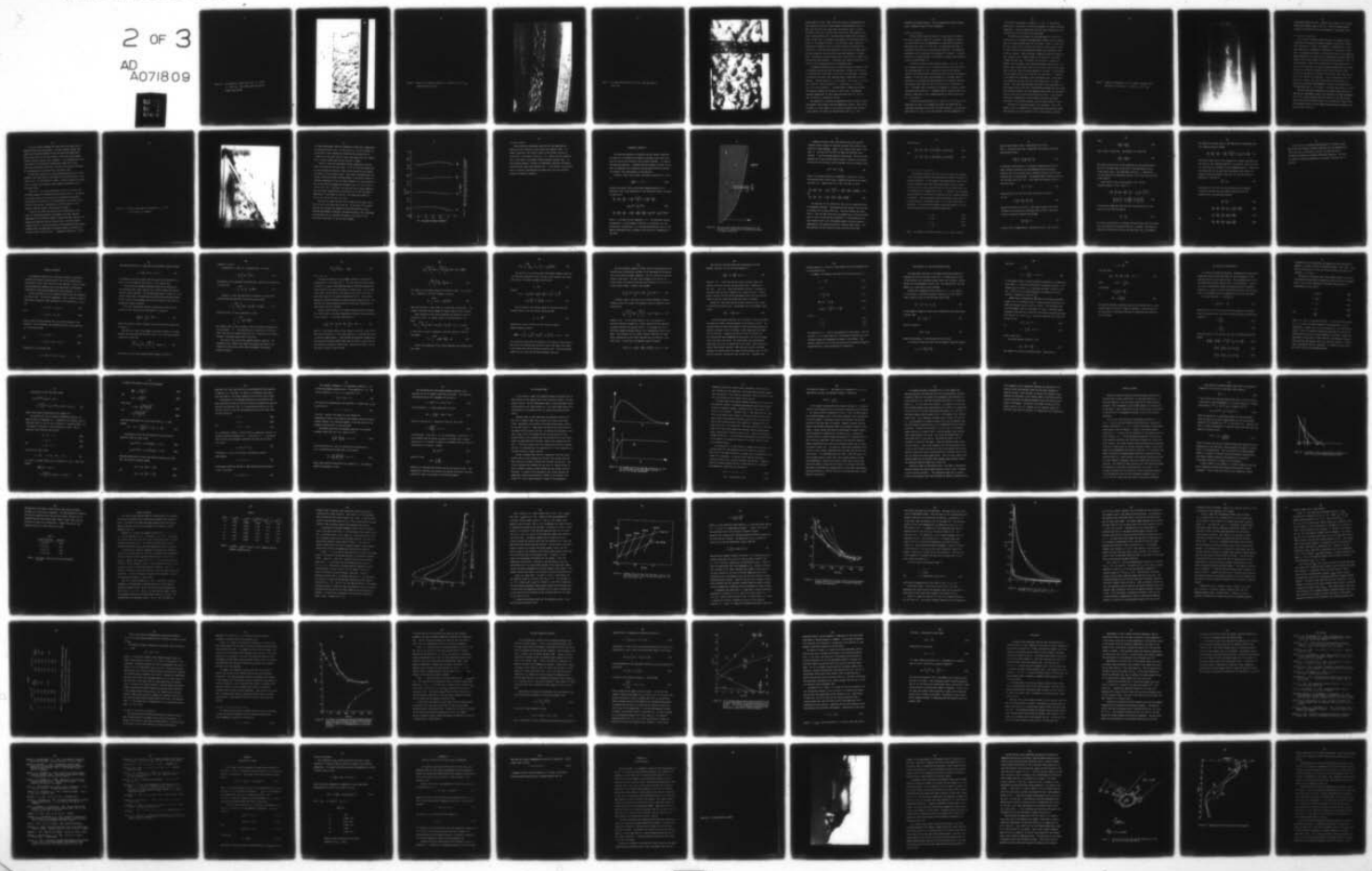


Figure 16. A sketch of the flow observed for $T_d > 25°C$.

AD-A071 809 WASHINGTON UNIV SEATTLE DEPT OF ATMOSPHERIC SCIENCES F/G 8/12
LAMINAR AND TURBULENT BOUNDARY LAYERS ADJACENT TO MELTING VERTI--ETC(U)
MAY 79 E G JOSBERGER N00014-76-C-0234
UNCLASSIFIED SCIENTIFIC-16 NL

2 OF 3
AD A071809



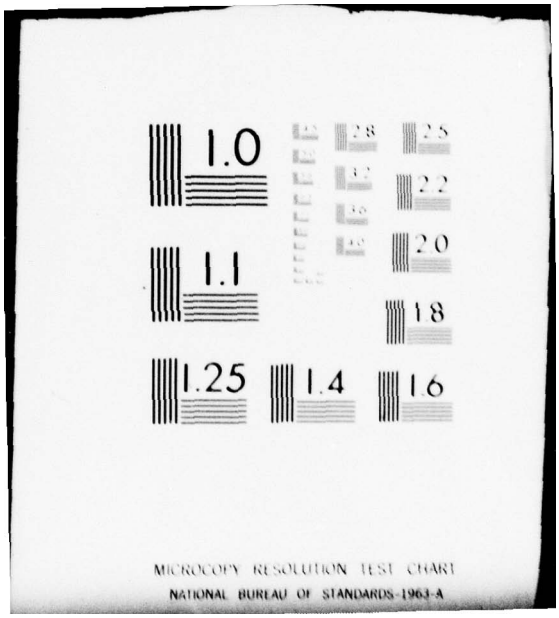

1.0
1.1
1.25
1.4
1.6
2.8
3.2
3.6
4.0
2.5
2.2
2.0
1.8
MICROCOPY RESOLUTION TEST CHART
NATIONAL BUREAU OF STANDARDS-1963-A

Plate VIII. Ice shape after melting for 23 min, T_∞ = 24.8°C, S_∞ = 33.6 $^{o}/_{oo}$. Note smooth upper portion and cusped lower portion.

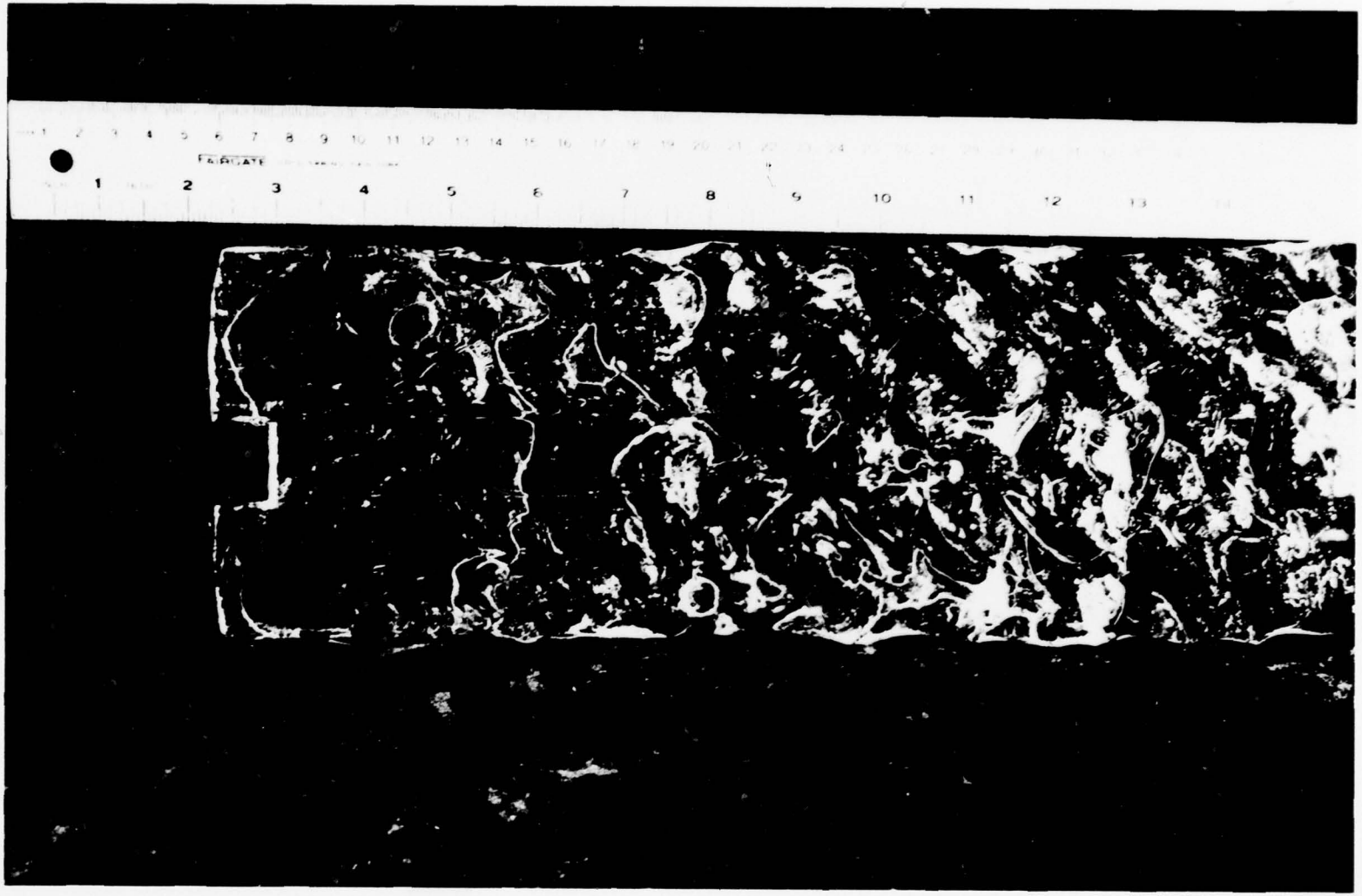


Plate IX. Cusps in ice surface formed for T_∞ = 26.0°C, S_∞ = 31.0 $^{o}/_{oo}$, after melting for 10 min.

Plate X. Ice shape after melting for 20 min, same experiment as Plate VIII.

4
5
6

stream length of 20 mm. After 30 min the cusps are disorganized with equal downstream and cross stream lengths of approximately 30 mm. In both cases the cusps are larger where the boundary layer is thicker. The depth of the cusps increases with time and the final depth of the cusps is approximately 5 mm. Dye observations showed that the physical effect of the cusps is to create a back eddy in the flow behind each ice crest, as illustrated in Figure 16 by the small arrows, where the buoyant water produced at the ice surface reinforces the upward flow near the ice. When dye was injected into a cusp, the dye flowed upward and then outward at the crest of the cusp, then downward in the mean flow. Occasionally, some dye flowed over a crest and into a higher cusp before being swept downward. I observed no net upward flow adjacent to the ice in the turbulent portion of the boundary layer.

I estimated the melting rates in these experiments by measuring the ice thickness before and after the experiment. Because the ice surface is cusped and the ice thickness at the end of the experiment is measured to the top of the cusps, this technique gives a lower bound to the ice ablation. The melt rate for T_∞ = 24.8°C and S_∞ = 33.6 $^{o}/_{oo}$, T_d = 26.6°C, was 175 mm hr^{-1}; the melt rate for T_∞ = 26.0°C and S_∞ = 31.0 $^{o}/_{oo}$, T_d = 27.7°C, was 114 mm hr^{-1}. The uncertainty in measuring the final ice thickness produces the disparity in melt rates. The measured interface temperatures for the second experiment were all -.02°C so that fresh water is produced at the wall.

The separation of salinity and temperature effect on density across the boundary layer produces the high temperature reversal. Next to the ice there is a small amount of very positively buoyant water inside of a large amount of slightly less buoyant water that at $T_d \approx$ 20°C

overwhelms the upward buoyancy. The high temperature reversal chapter gives a complete discussion of this phenomena.

Bubble Ice Experiments

Paterson (1975) shows that glacial ice, the source of icebergs, has an air content as high as 7% by volume. The formation of glacial ice, which results from the metamorphosis of snow under the weight of additional snow, traps air in the ice. To investigate the effect of released air from the ice on the convective processes, I performed two experiments with ice that had a CO_2 content of 1.5% and 5%. I used CO_2 because of its high solubility in cold water, a property that enabled me to easily produce bubble ice.

To produce ice with a suitable bubble content, I let 1 kg of dry ice sublimate in water at 0°C in the bubble-free ice tank, then lowered the room temperature to -20°C. Because the sides of the tank are insulated, the freezing takes place at the top of the tank and progresses downward. As the ice grows, the dissolved CO_2 is excluded from the crystalline ice structure and forms bubbles at the ice-water interface. These bubbles then freeze into the ice block as the ice continues to form. The bubbles have a characteristic diameter of 1 mm and a uniform distribution within the ice. I determine the CO_2 content of the ice by melting a known mass of ice in heated paraffin oil and collecting the CO_2 in a burrette.

I chose far-field conditions of $T_\infty = +2.6°C$, $S_\infty = 32.7\ ^o/_{oo}$ for the experiments so that I could compare the results to bubble-free ice experiments performed with similar far-field conditions. For the experiment with 5% CO_2 at $T_d = 4.06$, the turbulent interface temperature is

-1.35°C which corresponds to a value of r = 0.75. If the ice were bubble-free, r would equal 0.44 which corresponds to a warmer interface temperature. Interface temperatures from the other experiment are not available due to the failure of the data-logger.

The melting rate estimates for both experiments fall within 10% of the values of the bubble-free experiments; however, the ice ablation does not proceed uniformly over the ice surface. Plate XI, from the 5% CO_2 case, shows the ice form after melting for 3 hours; cusps, similar to those found in the high temperature bubble-free experiments, form on the ice surface. These cusps have a length of 30 mm and a depth of 5mm. Because of the irregular nature of the ablation, I could only estimate the melt rate. The melting ice continuously releases CO_2 bubbles into the boundary layer where these bubbles quickly rise. The bubbles always remain within 5 mm of the ice and as they rise they drag water with them, imparting upward momentum to the water. Dye injections show the upward velocity 30 cm from the tip to be 8 mm s^{-1}. Compared to the bubble-free experiments, these experiments give a colder interface temperature and show that the ice no longer melts in a smooth fashion. Also, many features remain the same for both experiments; at the bottom of the ice the flow is bidirectional and when the inner saline layer becomes turbulent, the flow becomes unidirectional but the characteristic notch at the transition point does not form. I also observe uniform wall temperatures in the turbulent regime and the upward velocities in the turbulent boundary layer are approximately 10 mm s^{-1}.

The effect of the bubbles appears to be threefold. First, the bubbles in the ice roughen the ice surface which previously was smooth which enhances the salt transport to the ice and lowers T_w from the

Plate XI. Bubble ice experiment, 5% CO_2 by volume, ice shape after melting for 2 hr 54 min; T_∞ = 2.26°C, S_∞ = 32.8 $^{o}/_{oo}$.



corresponding bubble-free case. Second, the ice melts in an irregular fashion that produces cusps in the ice. Third, the bubble release increases the production of positive momentum in the boundary layer.

The Tilted Wall Experiment

All ice walls in nature are not vertical; for example, pressure ridge keels are composed of randomly oriented ice blocks and icebergs have slanted walls. Usually, the seawater is underneath the ice but occasionally this configuration is reversed as in the case of iceberg rams. To determine the effect of tilting the ice wall on the convective motion generated by the melting ice, I performed an experiment where the angle of the ice with respect to the vertical varied from 0° to 60°. In this experiment I used a slab of bubble-free ice that measured 0.11 m thick, 0.6 m long, and 0.2 m wide which had the thermistor array frozen in the ice such that the thermistors were 18 mm from one ice face. Initially, I placed the ice vertically in the tank, then tilted the ice at 15°, 32°, and 60° to the vertical. The ice spent 40 min at 0°, 26 min at 15°, 34 min at 32°, and 30 min at 60°; the side of the ice nearest the thermistors faced downward. The far-field conditions for this experiment are T_∞ = 3.7°C and S_∞ = 29.5 $^{o}/_{oo}$ which gives T_d = 5.31°C.

The flow visualization methods are the same as those used in the vertical wall experiments; namely, dye injections and streak photographs. For 0° tilt, these techniques show that the flow is the same on each side of the ice and as before consists of a bidirectional laminar layer at the bottom of the ice and an upward-flowing turbulent boundary layer over the rest of the ice.

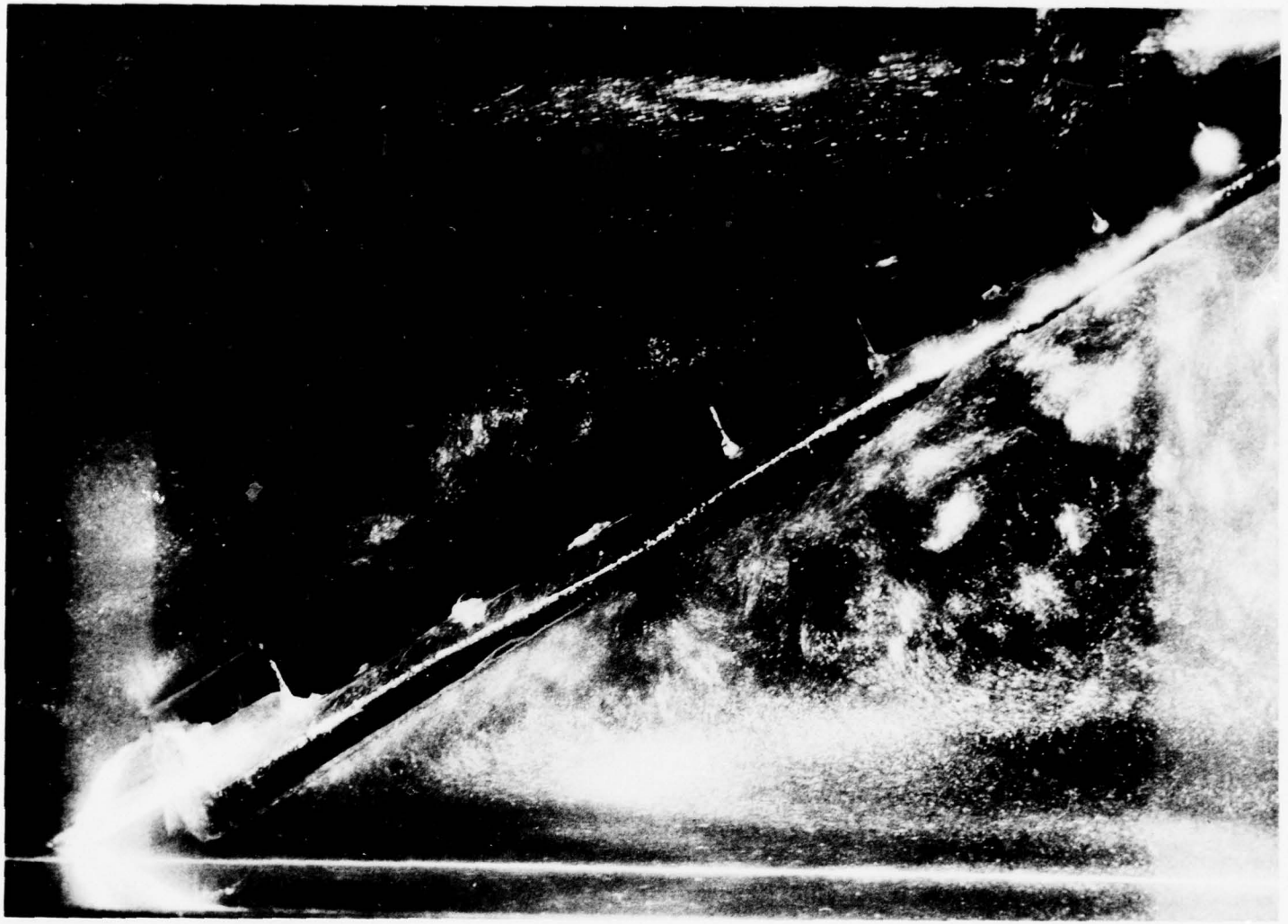
As the tilt angle increases the inner saline flow under the ice becomes thinner and less energetic. The outer laminar thermal flow under the ice becomes unsteady in that the colder more dense water forms plumes that sink into the interior of the tank and the upward flowing turbulent boundary layer disappears. The disappearance of this flow results from the density stratification under the ice that stabilizes the laminar saline flow. For 60° tilt the outer flow takes on the appearance of convection from a horizontal plate.

For the water above the ice, the convection above the ice is more energetic than that below the ice because the dilute melt water is now free to rise. For the three tilt angles, I found no laminar flow along the ice surface, only convection that resembles convection from a horizontal plate.

Plate XII, a 15 s streak photograph at a 60° tilt, depicts the difference between the convection on each side of the ice. The motions in the upper portion of the picture are disorganized and severely influenced by the proximity of the surface which is the white line at the top of the picture. Below the ice, the fluid motion is less dramatic; however, several sinking plumes are shown.

Plate XII also shows the proximity of the thermistors to the lower ice face which enabled me to determine the lower interface temperature for the different angles. Because the small amount of ice between the thermistor and the interface has an e-folding thermal response time of 7 min and each portion of the experiment lasts several response times, the thermistors accurately measure T_w provided T_w is the same on each side of the ice. I computed an accuracy of $\pm$ 0.07°C

Plate XII. Tilted ice experiment, tilt angle 60°, T_∞ = 3.8°C, S_∞ = 29.5 $^{o}/_{oo}$, 15 s exposure.



for these measurements under the assumption of equal wall temperatures by assuming the worst case. For this case, T_w = 0°C at the upper ice surface and a linear temperature gradient exists through the ice. I chose 0°C at the upper side as a worst case because the wall temperature is usually warmer when the melting rate is higher.

Figure 17 shows the distribution of wall temperature along the lower ice surface for the four cases. At 0° tilt the wall temperature has the expected distribution, coldest at the bottom and then warmest and uniform in the turbulent region. The pattern disappeared when the ice was tilted and the most striking feature is the overall decrease in interface temperature as the tilt angle increased. At the mid-point of the ice the interface temperature decreased from -.41°C at 0° tilt to -.82°C at 60° tilt. The spatial variation at a given angle changed to give the coldest temperatures at the ends of the ice and the warmest temperatures in the middle of the ice. This trend was evident at tilts of 15° and 60° but not at 32° tilt.

Plate XII also shows the melt rate is higher on the upper side of the ice than on the lower side of the ice. At the start of the experiment the ice thickness was symmetrical about the thermistor array. Detailed measurements of the melt rate were not made, as this experiment was undertaken only to determine the change in the nature of the convection as the angle of the ice block changed.

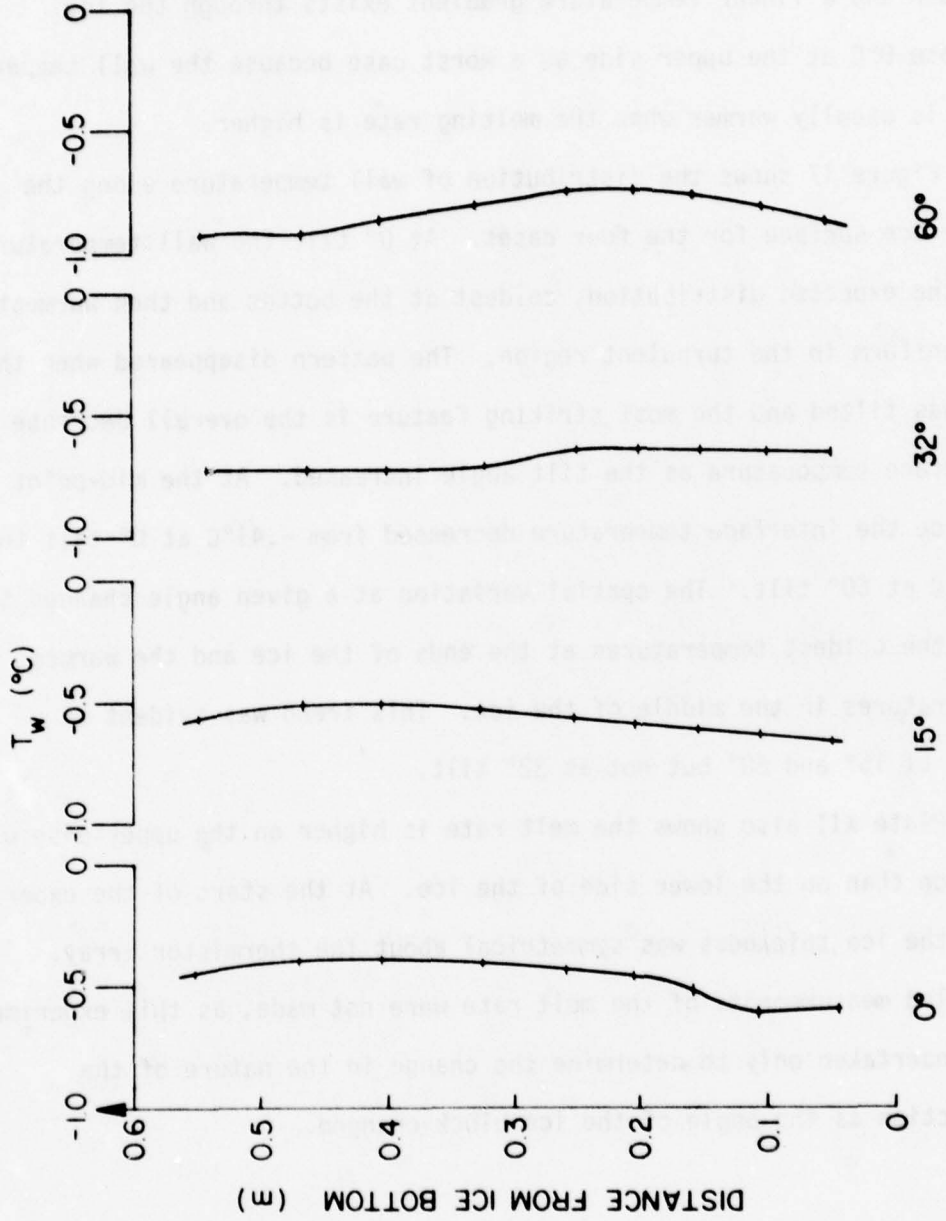


Figure 17. Measured values of T_w from the variable tilt experiment. The tick marks denote the location of the thermistors.

Concluding Remarks

These laboratory experiments show that the flow generated by a melting ice wall consists of both laminar and turbulent flows. For oceanic conditions, the vertical extent of the laminar flow next to an ice wall is less than 1.0 m for $T_d > 1°C$. Hence, the most important flow in the ocean is the upward flowing turbulent boundary layer. In the following chapters I develop the fundamental equations and boundary conditions that govern the turbulent flow. I then simplify the equations with a similarity transformation and numerically solve the resulting ordinary differential equations.

Fundamental Equations

The governing equations of turbulent vertical natural convection are those of a Boussinesq fluid subject to buoyancy forces that arise from the cooling and dilution at the ice-water interface. To simplify the governing equations, I parameterized the turbulent transfer of salt, heat, and momentum with a spatially varying eddy diffusivity and made the boundary layer approximation to the equations.

Batchelor (1967) gives the mass conservation equation for a fluid as

$$\frac{1}{\rho}\frac{D\rho}{Dt} + \nabla \cdot \vec{u} = 0 \quad . \tag{29a}$$

Tennekes and Lumley (1972) give the mean momentum equations of a Boussinesq fluid in two dimensions for the coordinate system illustrated in Figure 18 as

$$\frac{\partial u}{\partial t} + u\frac{\partial u}{\partial x} + v\frac{\partial u}{\partial y} = -\frac{1}{\rho}\frac{\partial p}{\partial x} + \frac{\left(\rho_o+\tilde{\rho}\right)}{\rho_o} g + \nu\left(\frac{\partial^2 u}{\partial x^2} + \frac{\partial^2 u}{\partial y^2}\right)$$

$$- \left(\frac{\partial}{\partial x}\overline{u'u'} + \frac{\partial}{\partial y}\overline{u'v'}\right) , \tag{29b}$$

$$\frac{\partial v}{\partial t} + u\frac{\partial v}{\partial x} + v\frac{\partial v}{\partial y} = -\frac{1}{\rho}\frac{\partial p}{\partial y} + \nu\left(\frac{\partial^2 v}{\partial x^2} + \frac{\partial^2 v}{\partial y^2}\right) - \left(\frac{\partial}{\partial x}\overline{v'u'} + \frac{\partial}{\partial y}\overline{v'v'}\right) \tag{29c}$$

where u, v are mean velocity components; u', v' are turbulent velocity fluctuations; ν is the kinematic viscosity; p is pressure; g is the gravitational acceleration, ρ_o is the undisturbed density; and $\tilde{\rho}$ is the density perturbation due to changes in the salinity or temperature of the fluid.

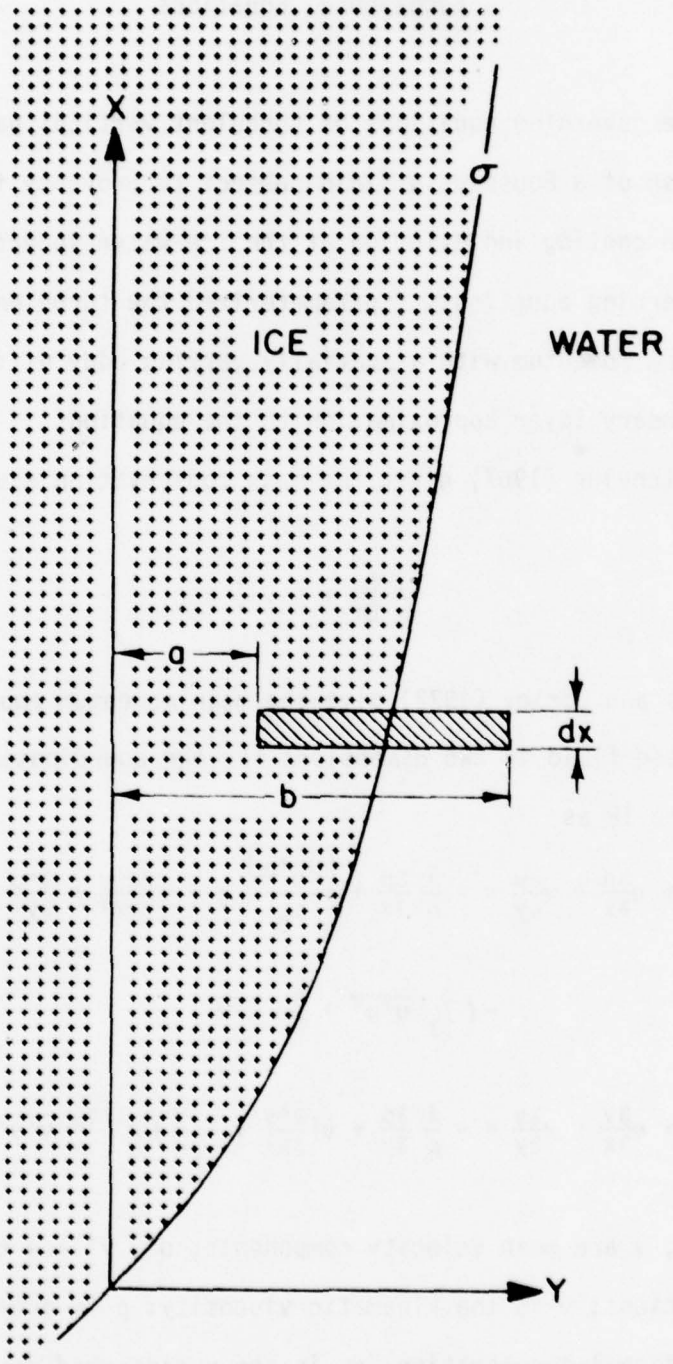


Figure 18. The coordinate system used in the analysis of the turbulent flow and the control volume used to derive the boundary conditions.

Tennekes and Lumley (1972) show that the terms $\overline{u'u'}$ and $\overline{v'v'}$ represent normal stresses or pressures and have little effect on the transport of mean momentum. Hence, I will neglect these terms in Eqs. (29b, c). The terms $\overline{u'v'}$ and $\overline{v'u'}$ are equal and represent shear stresses. I use the simplest model for these terms: The flux of mean momentum due to the turbulent motions equals a spatially varying eddy diffusivity times the mean velocity gradient across the boundary layer,

$$\overline{u'v'} = \overline{v'u'} = A \frac{\partial u}{\partial y} \tag{30}$$

where A is the eddy diffusivity of momentum, a function of x and y. The turbulent model section gives a complete discussion of the spatial variation of A. Substitution of Eq. (30) into (29b, c) gives

$$\frac{\partial u}{\partial t} + u\frac{\partial u}{\partial x} + v\frac{\partial u}{\partial y} = -\frac{1}{\rho}\frac{\partial p}{\partial x} + \frac{\left(\rho_o+\tilde{\rho}\right)}{\rho_o} g + \nu\left(\frac{\partial^2 u}{\partial x^2} + \frac{\partial^2 u}{\partial y^2}\right) + \frac{\partial}{\partial y}\left(A\frac{\partial u}{\partial y}\right) \tag{31a}$$

and

$$\frac{\partial v}{\partial t} + u\frac{\partial v}{\partial x} + v\frac{\partial v}{\partial y} = -\frac{1}{\rho}\frac{\partial p}{\partial y} + \nu\left(\frac{\partial^2 v}{\partial x^2} + \frac{\partial^2 v}{\partial y^2}\right) + \frac{\partial}{\partial x}\left(A\frac{\partial u}{\partial y}\right) . \tag{31b}$$

The equations for the diffusion of heat and salt complete the set of fundamental equations. These equations also contain flux terms that are modeled with an eddy diffusivity. Following Tennekes and Lumley (1972), I take the eddy diffusivity for momentum and a diffusing element (heat or salt) as equal because turbulence is a flow property and as such transports heat, salt, and momentum equally and the transport is independent of the respective molecular diffusion coefficients. The mean equations for the diffusion of heat and salt with an eddy

diffusivity are

$$\frac{\partial T}{\partial t} + u\frac{\partial T}{\partial x} + v\frac{\partial T}{\partial y} = \frac{\partial}{\partial x}\left[(\kappa+A)\frac{\partial T}{\partial x}\right] + \frac{\partial}{\partial y}\left[(\kappa+A)\frac{\partial T}{\partial y}\right] \qquad (32a)$$

and

$$\frac{\partial S}{\partial t} + u\frac{\partial S}{\partial x} + v\frac{\partial S}{\partial y} = \frac{\partial}{\partial x}\left[(D+A)\frac{\partial S}{\partial x}\right] + \frac{\partial}{\partial y}\left[(D+A)\frac{\partial S}{\partial y}\right] . \qquad (32b)$$

The Boundary Layer Approximation

The observed laboratory flows fall into the category of boundary layer flow and the boundary layer approximation further simplifies the governing equations. In the boundary layer approximation, scaling the governing equations shows that downstream gradient terms are always smaller than cross-stream gradient terms and are neglected unless they are multiplied by the downstream velocity. In addition, the u-momentum equation dominates the diffusion of momentum and the v-momentum equation is neglected. Also, the pressure within the boundary layer equals the pressure outside of the boundary layer; in this case the pressure is hydrostatic. To arrive at the boundary layer approximation, scale the continuity equation with the following relationships

$$u = u_{\star}\hat{u} \quad , \qquad (33a)$$

$$v = v_{\star}\hat{v} \quad , \qquad (33b)$$

$$x = \ell_x\hat{x} \quad , \qquad (33c)$$

$$y = \ell_y\hat{y} \quad , \qquad (33d)$$

where $\hat{}$ are quantities of order one and $u_{\star}$, $v_{\star}$, ℓ_x, and ℓ_y are the

velocity and distance scales. Substitution of (33) into (29a), eliminating the order 1 quantities, and omitting the partial time derivative gives

$$\frac{1}{\rho}\left(\frac{u_*}{\ell_x}\frac{\partial\rho}{\partial\hat{x}} + \frac{v_*}{\ell_y}\frac{\partial\rho}{\partial\hat{y}}\right) = \frac{u_*}{\ell_x} + \frac{v_*}{\ell_y} \quad . \tag{34}$$

A coordinate transformation to a reference frame moving with the ice-water interface eliminates the time dependence from the governing equations and a later section gives a complete discussion of the transformation and its ramifications. The maximum change in density affecting the left-hand side of Eq. (34) occurs when the interface salinity is zero which gives

$$\frac{\partial\rho}{\rho} \approx 2 \times 10^{-2} \quad . \tag{35}$$

Substitution of (35) into (34) scales the density variations to give

$$\frac{\partial\rho}{\rho}\left(\frac{u_*}{\ell_x} + \frac{v_*}{\ell_y}\right) = \frac{u_*}{\ell_x} + \frac{v_*}{\ell_y} \quad . \tag{36}$$

Because of the small value of $\frac{\partial\rho}{\rho}$, the change in density has little influence on the flow and the left-hand side of (29a) is neglected. The mass conservation equation then becomes

$$\frac{\partial u}{\partial x} + \frac{\partial v}{\partial y} = 0 \quad , \tag{37}$$

and the flow is incompressible. Substitution of Eqs. (33) into (37)

gives

$$o\left(\frac{u_*}{\ell_x}\right) = o\left(\frac{v_*}{\ell_y}\right) , \tag{38}$$

where o means of same order. Rearranging (37) shows that

$$o\left(\frac{\ell_x}{\ell_y}\right) = o\left(\frac{u_*}{v_*}\right) , \tag{39}$$

which means that the ratio of the downstream to cross-stream velocity must be of the same order as the ratio of the downstream to cross-stream length scales. The experiments show that $\ell_x \approx 1000$ mm and $\ell_y \approx 20$ mm; therefore the downstream velocity is 50 to 100 times the cross-stream velocity.

Substitution of the scaled variables, (33), into the x-momentum equation, (31a), results in

$$u_* \frac{\partial \hat{u}}{\partial t} + \frac{u_*^2}{\ell_x} \hat{u} \frac{\partial \hat{u}}{\partial \hat{x}} + \frac{u_* v_*}{\ell_y} \hat{v} \frac{\partial \hat{u}}{\partial \hat{y}} = - \frac{1}{\rho \ell_x} \frac{\partial p}{\partial \hat{x}} + \frac{\left(\rho_o + \tilde{\rho}\right)}{\rho_o} g$$

$$\nu \left[u_* \left(\frac{1}{\ell_x^2} \frac{\partial^2 \hat{u}}{\partial \hat{x}^2} + \frac{1}{\ell_y^2} \frac{\partial^2 \hat{u}}{\partial \hat{y}^2} \right) \right] + \frac{u_*}{\ell_y^2} \frac{\partial}{\partial \hat{y}} \left(A \frac{\partial \hat{u}}{\partial \hat{y}} \right) . \tag{40}$$

A term-by-term comparison shows that the frictional portion of the equation can be simplified because

$$\frac{1}{\ell_x^2} << \frac{1}{\ell_y^2} \tag{41}$$

but neither the molecular nor turbulent diffusive terms can be eliminated since the magnitude of the eddy diffusivity is unknown. Both advective terms must be retained as they are the same order, u_*^2/ℓ_x, and keeping

all terms of this order, which is the same order as the buoyant term, the x-momentum equation becomes

$$\frac{\partial u}{\partial t} + u\frac{\partial u}{\partial x} + v\frac{\partial u}{\partial y} = -\frac{1}{\rho}\frac{\partial p}{\partial x} + \frac{\left(\rho_o+\tilde{\rho}\right)}{\rho_o} g + \frac{\partial}{\partial y}\left[(\nu+A)\frac{\partial u}{\partial y}\right] . \quad (42)$$

Schlichting (1960) carries this procedure out in detail and shows that the scale for the v-momentum equation is $v_\star/\ell_y^2$ which is much less than $u_\star/\ell_y^2$ allowing for the neglect of the v-momentum equation. Schlichting also shows that the pressure within the boundary layer equals the pressure outside the boundary layer; for this case the pressure is hydrostatic, and given by

$$\frac{\partial p}{\partial x} = \rho_o g \quad . \quad (43)$$

Substitution of (43) into (42) and using the scaling arguments to simplify the heat and salt diffusion equations gives the simplest form of the governing equations

$$\frac{\partial u}{\partial x} + \frac{\partial v}{\partial y} = 0 \quad , \quad (44a)$$

$$\frac{\partial u}{\partial t} + u\frac{\partial u}{\partial x} + v\frac{\partial u}{\partial y} = \frac{-\tilde{\rho}}{\rho_o} g + \frac{\partial}{\partial y}\left[(\nu+A)\frac{\partial u}{\partial y}\right] , \quad (44b)$$

$$\frac{\partial T}{\partial t} + u\frac{\partial T}{\partial x} + v\frac{\partial T}{\partial y} = \frac{\partial}{\partial y}\left[(\kappa+A)\frac{\partial T}{\partial y}\right] \quad (44c)$$

and

$$\frac{\partial S}{\partial t} + u\frac{\partial S}{\partial x} + v\frac{\partial S}{\partial y} = \frac{\partial}{\partial y}\left[(\kappa+A)\frac{\partial S}{\partial y}\right] \quad . \quad (44d)$$

In this study, a coordinate transformation to a reference frame moving with the ice-water interface eliminates the time dependence and then a similarity transformation converts the governing partial differential equations to ordinary differential equations. But first, to complete the governing equations, the boundary conditions must be derived.

Boundary Conditions

The boundary conditions for a melting or freezing liquid-solid interface follow from the application of the no-slip condition and conservation of mass, heat, and salt at the interface. Figure 18 shows the two-dimensional geometry used in the derivation of the boundary conditions for a melting two-dimensional curved boundary, $\sigma(x, t)$.

At the interface the no-slip condition requires that the tangential velocity be zero. The velocity components, u and v, written in terms of the velocity components normal and parallel to the interface, u_r and v_r, are

$$u = u_r \cos \gamma - v_r \sin \gamma \quad , \tag{45a}$$

and

$$v = u_r \sin \gamma + v_r \cos \gamma \quad , \tag{45b}$$

where γ equals the angle between the x-axis and the tangent to the interface. At the interface, the component parallel to the interface, u_r, is zero which gives

$$u = -v_r \sin \gamma \quad , \tag{46a}$$

and

$$v = v_r \cos \gamma \text{ at } y = \sigma(x, t) \quad . \tag{46b}$$

Elimination of v_r from (46) gives

$$u + v \tan \gamma = 0 \text{ at } y = \sigma(x, t) \quad , \tag{47}$$

and recognizing that $\tan \gamma = \frac{\partial \sigma}{\partial x}$, the no-slip boundary condition becomes

$$u + v \frac{\partial \sigma}{\partial x} = 0 \text{ at } y = \sigma(x, t) \quad . \tag{48}$$

An alternative derivation states that the sum of the projections of u and v on to the tangent of the curve $y = \sigma(x,t)$ must be zero.

I next derive the boundary conditions which follow respectively from conserving mass, heat, and salt for a control volume that contains the solid liquid interface. The cross-hatched region in Figure 18 is the control volume used in the derivations and letting the horizontal bounds of this control volume approach the interface from each side gives the appropriate boundary condition.

First, mass conservation provides an additional condition on the velocity at the interface; mass conservation is written as

$$\frac{\partial}{\partial t}\iiint_V \rho dV + \iint_A \rho \vec{u} \cdot \hat{n} dA = 0 \quad , \tag{49}$$

where the volume and surface integrals are over the control volume shown in Figure A.

Application of Gauss's law changes the surface integral to a volume integral and noting that the choice of x and x + dx is arbitrary and not a function of time gives

$$\int_x^{x+dx} dx' \frac{\partial}{\partial t} \int_a^b \rho dy + \int_x^{x+dy} dx' \int_a^b \nabla \cdot (\rho \vec{u}) dy = 0 \; . \tag{50}$$

For brevity, the first and second multiple integrals in (50) are

denoted as I and II.

Integration of I from a to σ and then from σ to b gives

$$I = \frac{\partial}{\partial t}\left(\int_a^{\sigma} \rho dy + \int_{\sigma}^{b} \rho dy\right) \quad . \tag{51}$$

Performance of the integration and noting that a and b are not functions of time yields

$$I = \int_x^{x+dx} \left(\rho_i \frac{\partial \sigma}{\partial t} - \rho_w \frac{\partial \sigma}{\partial t}\right) dx \quad . \tag{52}$$

Integral II, after the application of Leibnitz's rule with the condition that the velocities in the ice are zero yields

$$II = \int_x^{x+dx} \left[\frac{\partial}{\partial x} \int_a^b \rho u dy - (\rho u)_b \frac{\partial b}{\partial x} + (\rho v)|_b\right] dx \quad . \tag{53}$$

Taking the limit of a and b approaching σ gives

$$II = \int_x^{x+dx} \rho_w \left(v - u \frac{\partial \sigma}{\partial x}\right) dx \quad . \tag{54}$$

The integral term, $\int_a^b \rho u dy$, vanishes in the limit because a decomposition of the integral into two parts, one on each side of the interface, shows that the integral within the ice is identically zero and the integral in the water equals zero in the limit.

The sum of I and II gives the complete boundary condition. The integrand of this integral must equal zero because the bounds of the integral are arbitrary and after some rearrangement the boundary condition becomes

$$\frac{\left(\rho_w - \rho_i\right)}{\rho_w} \frac{\partial \sigma}{\partial t} = v - u \frac{\partial \sigma}{\partial x} \qquad (55)$$

at $y = \sigma(x, t)$.

The physical meaning of this boundary condition is most easily understood for a flat plate, $\frac{\partial \sigma}{\partial x} = 0$. For this case the velocity normal to the wall is equal to the normalized density difference between the liquid and the solid times the melting or freezing rate. For an ablating ice wall, the melting of a unit mass of ice yields a unit mass of water that occupies a 10% smaller volume than the ice. This volume decrease is exactly balanced by a suction velocity toward the ice. For freezing, the volume expansion caused by liquid water changing to ice expels water from the interface.

Second, the derivation of the thermal boundary condition proceeds in a similar manner using heat conservation instead of mass conservation at the interface. I write heat conservation as

$$\frac{\partial}{\partial t} \iiint_V \rho e dV + \iint_A \rho e \vec{u} \cdot \vec{n} dA + \iint_A \vec{F}_h \cdot \vec{n} dA = 0 \quad , \qquad (56)$$

where e is the internal energy of the liquid or solid, $\vec{F}_h$ is the flux of heat due to diffusion, $\vec{u}$ is the vector velocity, ρ is the density, and $\vec{n}$ is the unit outward normal. I have omitted the mechanical production of heat because Schlichting (1960) shows that this effect is small for the slow velocities observed in these flows. Application of Gauss's law to the control volume in Figure A gives

$$\frac{\partial}{\partial t}\int_{x}^{x+dx} dx \int_{a}^{b} \rho e dy + \int_{x}^{x+dx} dx \int_{a}^{b} \left[\frac{\partial}{\partial x}(\rho eu) + \frac{\partial}{\partial y}(\rho ev)\right] dy$$

$$+ \int_{x}^{x+dx} dx \int_{a}^{b} \left(\frac{\partial F_x}{\partial x} + \frac{\partial F_y}{\partial y}\right) dy = 0 \quad . \tag{57}$$

For simplicity, the three integrals are called in order: I_h, II_h, and III_h. Expansion of the first integral, I_h, gives

$$I_h = \int_{x}^{x+dx} \left(\rho_i e_i - \rho_w e_w\right) \frac{\partial \sigma}{\partial t} dx \quad . \tag{58}$$

where the subscripts i and w refer to ice and water, respectively. This integral represents the net change of internal energy as the ice melts.

Next, expansion of II_h, which represents the advection of heat by the velocity field, in a manner similar to the derivation of (53) gives

$$II_h = \int_{x}^{x+dx} \left(\frac{\partial}{\partial x}\int_{a}^{b} \rho eu dy + \rho eu|_a \frac{\partial u}{\partial x} - \rho eu|_b \frac{\partial b}{\partial x} + \rho ev|_b - \rho ev|_a\right) dx \quad . \tag{59}$$

In the limit of a and b approaching σ with zero velocity in the ice, II_h becomes

$$II_h = \int_{x}^{x+dx} \rho_w e_w \left(v - u \frac{\partial \sigma}{\partial x}\right)_{y=\sigma} dx \quad . \tag{60}$$

Finally, the expansion of III_h, which represents the diffusive heat flux, gives

$$III_h = \int_x^{x+dx} \left[F_{y_w} - F_{y_i} + \left(F_{x_i} - F_{x_w} \right) \frac{\partial \sigma}{\partial x} \right] dx' \quad . \tag{61}$$

The sum of I_h, II_h, and III_h gives the thermal boundary condition; with arbitrary integration limits the sum of the integrands must equal zero; hence, the thermal boundary condition with

$$\vec{F} = -K \nabla T \tag{62}$$

becomes

$$\left(\rho_i e_i - \rho_w e_w \right) \frac{\partial \sigma}{\partial t} + \rho_w e_w \left(v - u \frac{\partial \sigma}{\partial x} \right) + K_i \frac{\partial T_i}{\partial y} - K_w \frac{\partial T_w}{\partial y}$$

$$+ \left(K_w \frac{\partial T_w}{\partial x} - K_i \frac{\partial T_i}{\partial x} \right) \frac{\partial \sigma}{\partial x} = 0 \quad \text{at } y = \sigma \ . \tag{63}$$

At the interface, the internal energy of the water equals the internal energy of the ice plus the latent heat, $\mathcal{L}$,

$$e_w = e_i + \mathcal{L} \ . \tag{64}$$

Substitution of (55) and (64) into (63) gives the complete thermal boundary condition

$$- \rho_i \mathcal{L} \frac{\partial \sigma}{\partial t} + K_i \frac{\partial T_i}{\partial y} - K_w \frac{\partial T_w}{\partial y} + \left(K_w \frac{\partial T_w}{\partial x} - K_i \frac{\partial T_i}{\partial x} \right) \frac{\partial \sigma}{\partial x} = 0 \text{ at } y = \sigma \ . \tag{65}$$

This condition states that the difference in the amount of heat entering one side of the interface and leaving the other side equals the product of the latent heat and the freezing or melting rate. Carslaw and Jaeger (1959) call this condition the Stefan boundary condition.

The third boundary condition follows from salt conservation at the interface and the derivation proceeds in the same manner as the derivation of the thermal boundary condition. The salt conservation equation contains three terms: the time rate-of-change of salt within the control volume, and both the advection and diffusion of salt in or out of the control volume. Formally, this becomes

$$\frac{\partial}{\partial t}\iiint_V \rho S dV + \iint_A S\rho\vec{u}\cdot\vec{n}dA + \iint_A \vec{F}_S\cdot\vec{n}dA = 0 \quad . \qquad (66)$$

As before, Gauss's law converts the surface integrals to volume integrals, then the integrals are expanded using the identical control volume giving

$$\frac{\partial}{\partial t}\int_x^{x+dx} dx \int_a^b \rho S dy + \int_x^{x+dx} dx \int_a^b \nabla\cdot\left(\rho S\vec{u} + \vec{F}_S\right)dy = 0 \quad . \qquad (67)$$

Equation (67) is the saline analog to (57), the expansion of the three integrals proceeds in a similar fashion with the additional assumption that the ice contains no salt. For icebergs this is an excellent assumption because glacier ice is metamorphosed snow or pure water. For multiyear sea ice, either pressure ridge keels or large floes, observations by Cox (1974) show that the ice salinity is less than 4 $^{o}/_{oo}$. In the limit, the boundary condition becomes

$$-S\frac{\partial\sigma}{\partial t} + Sv - Su\frac{\partial\sigma}{\partial x} - D\frac{\partial S}{\partial y} + D\frac{\partial S}{\partial x}\frac{\partial\sigma}{\partial x} = 0 \text{ at } y = \sigma. \qquad (68)$$

The flat wall case facilitates the interpretation of this boundary condition; in this case the condition is

$$S\left(\frac{\partial \sigma}{\partial t} - v\right) + D\frac{\partial S}{\partial y} = 0 \text{ at } y = \sigma \quad . \tag{69}$$

Equation (69) states that the salt flux to the wall equals the product of the wall salinity and the melting rate. Comparison of Eqs. (69) and (65) shows that the wall salinity is analogous to the latent heat and can be thought of as a latent salinity. Unfortunately, the wall salinity varies and depends both on the salt and heat fluxes to the ice, unlike the latent heat which is constant.

Because Eq. (55) shows that the suction velocity at the ice wall is one-tenth the melting rate, I approximate the saline boundary condition as

$$S\,\frac{\partial \sigma}{\partial t} = -\,D\,\frac{\partial S}{\partial y} \text{ at } y = \sigma \quad . \tag{70}$$

I used the boundary conditions for a flat wall to discuss and model the convective motions observed adjacent to the melting ice wall. The curvature does not affect the dynamics of the fluid motions because the radius of curvature of the ice surface is much larger than the length scale of the flow. Inspection of Plate VII which illustrates the ice surface after being submerged for 220 minutes, verifies the assumption of an almost flat plate. Two regions where this approximation breaks down are at the ice bottom and in the 'notch' region where the laminar layer becomes turbulent. Both the notch and the ice bottom represent the leading edge of an upward flowing boundary layer; in this case the turbulent flow and the inner laminar flow. Therefore, the

following analysis is invalid in these regions but valid everywhere else in the turbulent flow.

In summary, the boundary conditions for a flat wall are at $y = \sigma$

$$T_w = - mS_w \quad , \tag{71a}$$

$$u = 0 \quad , \tag{71b}$$

$$v = \frac{\rho_w - \rho_i}{\rho_w} \frac{\partial \sigma}{\partial t} \quad , \tag{71c}$$

$$\rho_i \frac{\partial \sigma}{\partial t} = - K_w \frac{\partial T}{\partial y} \quad , \tag{71d}$$

$$S_w \frac{\partial \sigma}{\partial t} \left(1 - \frac{\rho_w - \rho_i}{\rho_w} \right) = - D \frac{\partial S}{\partial y} \quad , \tag{71e}$$

and at $y = \infty$

$$u = 0 \quad , \tag{71f}$$

$$S = S_\infty \quad , \tag{71g}$$

$$T = T_\infty \quad . \tag{71h}$$

The conditions at $y = \sigma$ add to the complexity of the problem. Only the condition $u = 0$ is known explicitly, the remaining conditions are relationships between the independent variables of the problem. With boundary conditions of this form the solution of the governing equations becomes difficult, either analytically or numerically.

Transformation to a Moving Coordinate System

The experiments show that at any height the melting proceeds at a constant rate and the flow next to the ice is in steady state so that a transformation to a coordinate system fixed to the ice-water interface removes the time dependence from Eq. (44). The constant melt rate then appears as a fluid source at the interface.

Writing the v-component of the velocity as $v = v_r + v_t$, where v_r is the velocity in the moving reference frame and v_t is the translational velocity, gives for the left-hand side of (44b)

$$\frac{\partial}{\partial t} + u \frac{\partial}{\partial x} + (v_r + v_t) \frac{\partial}{\partial y} \quad . \tag{72}$$

If the temporal changes are solely due to advection by the translational velocity, then

$$\frac{\partial}{\partial t} + v_t \frac{\partial}{\partial y} = 0 \quad , \tag{73}$$

and (72) reduces to

$$u \frac{\partial}{\partial x} + v_r \frac{\partial}{\partial y} \quad , \tag{74}$$

where the coordinate y is the distance from the ice wall.

In the moving frame the normal velocity boundary conditions becomes

$$v_r + v_t = \frac{\rho_w - \rho_i}{\rho_w} \frac{\partial \sigma}{\partial t} \quad , \tag{75}$$

and since

$$v_t = \frac{\partial \sigma}{\partial t} \quad ,$$

$$v_r = - \frac{\rho_i}{\rho_w} \frac{\partial \sigma}{\partial t} \qquad \text{at } y = 0. \tag{76}$$

In the geometry shown in Figure 18 melting corresponds to a negative $\frac{\partial \sigma}{\partial t}$ which means v_r is positive, so that there is blowing at the wall. For freezing, $\frac{\partial \sigma}{\partial t}$ is positive, v_r is negative, and there is suction at the wall. Since ice is less dense than water, the blowing or suction velocity is reduced by a factor of $\frac{\rho_i}{\rho_w}$.

Another way to conceptualize the effect of the moving coordinate system is to fix the boundary layer in space and then translate the ice toward the boundary layer as fast as it melts. This introduces mass into the boundary layer at a rate equal to $\rho_i \frac{\partial \sigma}{\partial t}$. Since mass cannot accumulate, there must be a velocity at the interface carrying mass away from the wall at a rate of $\rho_w v_r$. The sum of these two mass fluxes must be zero so that

$$\rho_i \frac{\partial \sigma}{\partial t} + \rho_w v_r = 0 \quad , \tag{77a}$$

or

$$v_r = - \frac{\rho_i}{\rho_w} \frac{\partial \sigma}{\partial t} \quad \text{at } y = 0 \quad , \tag{77b}$$

which is again (76).

The saline boundary condition, (71e),

$$S_w \left(v - \frac{\partial \sigma}{\partial t} \right) = D \frac{\partial S}{\partial y} \quad , \tag{78}$$

also changes in the moving coordinate system. Substitution of

$$v = v_r + \frac{\partial \sigma}{\partial t}$$

into (78) gives

$$S_w\left(v_r + \frac{\partial \sigma}{\partial t} - \frac{\partial \sigma}{\partial t}\right) = D \frac{\partial S}{\partial y} , \quad \text{at } y = 0 . \tag{79}$$

Since $$v_r(0) = - \frac{\rho_i}{\rho_w} \frac{\partial \sigma}{\partial t} ,$$

(79) becomes

$$-S_w \frac{\rho_i}{\rho_w} \frac{\partial \sigma}{\partial t} = D \frac{\partial S}{\partial y} ,$$

or

$$\frac{\partial \sigma}{\partial t} = - \frac{\rho_w}{\rho_i} \frac{D}{S_w} \frac{\partial S}{\partial y} . \tag{80}$$

The remaining boundary conditions, both at the interface and at a large distance away from the wall, transform unchanged. Further discussion will take place in the moving frame and for convenience the subscript r will be dropped.

The Similarity Transformation

To simplify the governing equations, incompressibility and the two-dimensional nature of the flow allows for the replacement of u and v with derivatives of the stream function. Then, nondimensional salinity and temperature variables replace S and T in the equations. Finally, a similarity transformation reduces the governing partial differential equations to a system of ordinary differential equations and transformation of the boundary conditions completes the similarity development.

The stream function, ψ, is defined as

$$u = \frac{\partial \psi}{\partial y} \text{ and } v = -\frac{\partial \psi}{\partial x} \quad . \tag{81}$$

Normalization of T and S on the salinity and temperature differences across the boundary layer gives the following convenient nondimensional formulation:

$$\phi = \frac{S-S_\infty}{S_w-S_\infty} \quad , \tag{82a}$$

$$\theta = \frac{T-T_\infty}{T_\infty-T_w} \quad . \tag{82b}$$

Upon substitution of (81) and (82) into (44), the governing equations become

$$\frac{\partial \psi}{\partial y}\frac{\partial^2 \psi}{\partial x \partial y} - \frac{\partial \psi}{\partial x}\frac{\partial^2 \psi}{\partial y^2} = -g\frac{(\rho-\rho_o)}{\rho_o} + \frac{\partial}{\partial y}\left[(\nu+A)\frac{\partial^2 \psi}{\partial y^2}\right] \quad , \tag{83a}$$

$$\frac{\partial \psi}{\partial y}\frac{\partial \phi}{\partial x} - \frac{\partial \psi}{\partial x}\frac{\partial \phi}{\partial y} = \frac{\partial}{\partial y}\left[(D+A)\frac{\partial \phi}{\partial y}\right] \tag{83b}$$

$$\frac{\partial \psi}{\partial y}\frac{\partial \theta}{\partial x} - \frac{\partial \psi}{\partial x}\frac{\partial \theta}{\partial y} = \frac{\partial}{\partial y}\left[(\kappa+A)\frac{\partial \theta}{\partial y}\right] \quad . \tag{83c}$$

To complete the set of equations, the equation of state, described in Appendix I, provides the final relationship between ρ and ϕ and θ. Thus, (83) and the equation of state are the four equations that govern the variables ψ, ϕ, θ and ρ.

The analysis of boundary layer flows commonly employs a similarity transformation that assumes the downstream variation of the flow depends only on a scale factor determined by the downstream coordinate. A transformation in this case is

$$\psi = ax^p f(\eta) \tag{84a}$$

$$A = x^r N(\eta) \tag{84b}$$

$$\phi = \phi(\eta) \tag{84c}$$

$$\theta = \theta(\eta) \tag{84d}$$

and

$$\eta = \frac{by}{x^q} \tag{84e}$$

where f, N, ϕ and θ are unknown functions, η is the similarity variable, a, b, p, q, and r are unknown constants to be determined. In this formulation, I assume ϕ and θ are only functions of η for the following reasons: First, my laboratory observations show that for uniform far-field conditions S_w and T_w have no measurable x-variation. Second, the experiments of Vliet and Liu (1969) show that the temperature distribution across the flow depends only on the similarity variable. Finally, other investigators make this assumption [cf. Gebhart and Pera (1971) and Turner (1973)] with reasonable success.

Substitution of (84) into (83a) yields

$$a^2b^2x^{2p-2q-1}[(p-q)f'^2 - pff''] = -g\frac{\rho(\phi,\theta)-\rho_o}{\rho_o} + ab^3x^{p-3q}[(\nu+x^rN)f''' + x^rN'f''] \qquad (85)$$

where primes denote differentiation with respect to η.

To transform (85) into an ordinary differential equation, the equation must be independent of x. Inspection of the buoyancy term in (85) shows that this term is only a function of η because neither ϕ nor θ are explicit functions of x by the equation of state. Thus by inspection three conditions must be met:

$$2p - 2q - 1 = 0 \ , \qquad (86a)$$

$$p - 3q = 0 \ , \qquad (86b)$$

and

$$p - 3q + r = 0 \ . \qquad (86c)$$

The solution of (86) yields

$$p = 3/4, \quad q = 1/4, \quad \text{and} \quad r = 0; \qquad (87)$$

as a result, the eddy diffusivity is a function of η only. Then, (85) becomes

$$\frac{a^2b^2}{4}[2f'^2 - 3ff''] = g\frac{\rho(\phi,\theta)-\rho_o}{\rho_o} + ab^3[f''A' + (\nu+A)f'''] \ . \qquad (88)$$

To simplify (88) define a and b by the equations

$$\frac{a^2b^2}{4} = -g\,\frac{(\rho_w-\rho_\infty)}{\rho_\infty}\ , \tag{89a}$$

and

$$\nu b^3 a = -g\,\frac{(\rho_w-\rho_\infty)}{\rho_\infty}\ , \tag{89b}$$

which gives

$$a = 4\nu b = 4\nu\left[\frac{-g(\rho_w-\rho_\infty)}{4\nu^2}\right]^{1/4}\ , \tag{90a}$$

and

$$b = \left[\frac{-g(\rho_w-\rho_\infty)}{4\nu^2}\right]^{1/4}\ . \tag{90b}$$

With these formulations for a and b and letting $\rho_o = \rho_\infty$ (88) becomes

$$2f'^2 - 3ff'' = \frac{\rho(\phi,\theta)-\rho_\infty}{\rho_w-\rho_\infty} + f''\frac{A'}{\nu} + (1+\frac{A}{\nu})f'''\ . \tag{91}$$

Substitution of (84) into the thermal and saline diffusion equations, (83b) and (83c) yields

$$-\,pab\,x^{p-q-1}f\phi' = b^2x^{-2q}[(D+A)\phi'' + \phi'A'] \tag{92a}$$

$$-\,pab\,x^{p-q-1}f\theta' = b^2\,x^{-2q}[(\kappa+A)\theta'' + \theta'A']. \tag{92b}$$

Using the definitions of a and b from (90) and taking p and q from (87), the diffusion equations become

$$-3f\phi' = (S_c + \frac{A}{\nu})\phi'' + \phi'\frac{A'}{\nu} \tag{93a}$$

and

$$-3f\theta' = (P_r + \frac{A}{\nu})\theta'' + \theta'\frac{A'}{\nu}\ . \tag{93b}$$

Equations (91), (93a) and (93b) are the transformed diffusion equations of momentum, salt, and heat. If there is no turbulence, then these equations reduce to the laminar equations given by Schlichting (1960).

Transformation of the boundary conditions and confirmation that these conditions satisfy the similarity functions completes the equations governing the turbulent flow. At a large distance from the ice, the vertical velocity is zero and the temperature and salinity equal their far-field values, or

$$u = 0 \quad , \tag{94a}$$

$$S = S_\infty \quad , \tag{94b}$$

and

$$T = T_\infty \qquad \text{at } y = \infty \quad . \tag{94c}$$

In η coordinates, because x is held fixed as y approaches infinity, the boundary conditions evaluated at $y = \infty$ also hold at $\eta = \infty$. Transformation of the far-field boundary conditions (94) gives the following: First since

$$u = 4\nu b^2 \, x^{1/2} \, f'(\eta) \tag{95}$$

and because ν, b, and x are non-zero, the boundary condition (94a) becomes

$$f' = 0 \quad \text{at} \quad \eta = \infty \quad . \tag{96}$$

The boundary conditions (94b and c) when used with the definitions of ϕ and θ, (82) yield

$$\phi = \theta = 0 \text{ at } \eta = \infty \quad . \tag{97}$$

The ice-water interface, $y = 0$, transforms by (84e) to $\eta = 0$; so that the boundary conditions at $y = 0$ are applied at $\eta = 0$. The no-slip condition, $u = 0$ at $y = 0$, using (95), gives

$$f'(0) = 0 \text{ at } \eta = 0 \quad . \tag{98}$$

The salinity and temperature at the interface is, respectively, S_w and T_w which gives

$$\phi = \theta = 1 \quad \text{at } \eta = 0 \tag{99}$$

from (82). Equation (99) appears to have removed the indeterminant nature of the freezing curve boundary condition from the problem; however, this condition reappears in the heat and salt flux boundary condition which is discussed next.

The thermal and saline flux boundary conditions in the moving reference frame, (80) and (71d), combine to give

$$\frac{D}{S_w}\frac{\partial S}{\partial y} = \frac{K_w}{L\rho_w}\frac{\partial T}{\partial y} \quad , \quad \text{at } y = 0 \; . \tag{100}$$

Use of definitions Eqs. (82) and changing the y-differentiation to an η-differentiation through (84e), (100) becomes

$$\frac{\phi'}{\theta'} = \frac{K_w}{DL\rho_w}\frac{S_w(T_w - T_\infty)}{(S_w - S_\infty)} \quad \text{at } y = 0 \; , \tag{101}$$

where primes denote differentiation with respect to η. The freezing condition now appears as (101).

The transformation of the blowing boundary condition, (76), completes the set of boundary conditions at the wall. The similarity transformation gives the v-component of velocity as

$$v = -3\nu b x^{-1/4} f + \nu b^2 x^{-1/2} y f' \quad ; \tag{102}$$

at the interface $y = 0$, which along with (76) gives

$$v(0) = -\frac{\rho_i}{\rho_w}\frac{\partial \sigma}{\partial t} = -3\nu b x^{-1/4} f(0) \ , \tag{103}$$

which is a function of x. Solution of (103) for f(0) yields

$$f = \frac{\rho_i \frac{\partial \sigma}{\partial t} x^{1/4}}{3\nu b \rho_w} \quad \text{at } \eta = 0 \ . \tag{104}$$

For melting $\frac{\partial \sigma}{\partial t} < 0$ and f(0) is < 0; for freezing $\frac{\partial \sigma}{\partial t} > 0$ and f(0) is > 0. The assumption that the spatial variation of the melt rate is proportional to $x^{-1/4}$ is required to remove the x-dependence and the similarity transformation is complete. Letting

$$\frac{\partial \sigma}{\partial t} = M_o x^{-1/4} \tag{105}$$

gives for (104)

$$f(0) = \frac{\rho_i}{\rho_w}\frac{M_o}{3\nu b} \ , \tag{106}$$

where M_o is a characteristic melting rate for the entire ice wall. This formulation of the melt rate restricts the spatial variation of the eddy diffusivity, which is discussed in the following chapter.

The Turbulent Model

In this section I model the turbulent transports processes with an eddy diffusivity that depends both on the similarity variable η and the buoyant forcing. The bulk measurements made in these experiments permit the evaluation of this eddy diffusivity. This simple model permits the investigation of the complex effects of blowing and opposed buoyancy forces.

Townsend (1976, p. 259) shows that the turbulent structure of a wall jet, a boundary layer flow, consists of an inner and an outer region, separated by the location of the mean maximum upward velocity. For my case, Figure 19 shows these two regions and the variation of the eddy diffusivity across the flow. By analogy with Townsend, in the inner region, which lies between the wall and the position of the maximum velocity, the turbulence has the characteristics of wall turbulence; the eddy diffusivity increases linearly with distance from the wall. In the outer region, which lies outside the position of maximum velocity, the turbulence has the characteristics of free turbulence and the eddy diffusivity remains constant.

Further, Townsend shows that for a smooth wall the inner region divides into a viscous sublayer near the wall and a region where the eddy diffusivity increases linearly with distance from the wall. The viscous sublayer exists because the ice melts in a smooth fashion; if the ice melted to produce a rough surface then the sublayer would be destroyed. In support of the existence of the viscous sublayer the temperature records from thermistors located in the turbulent flow (Figure 13) show a smooth monotonic increase in the temperature

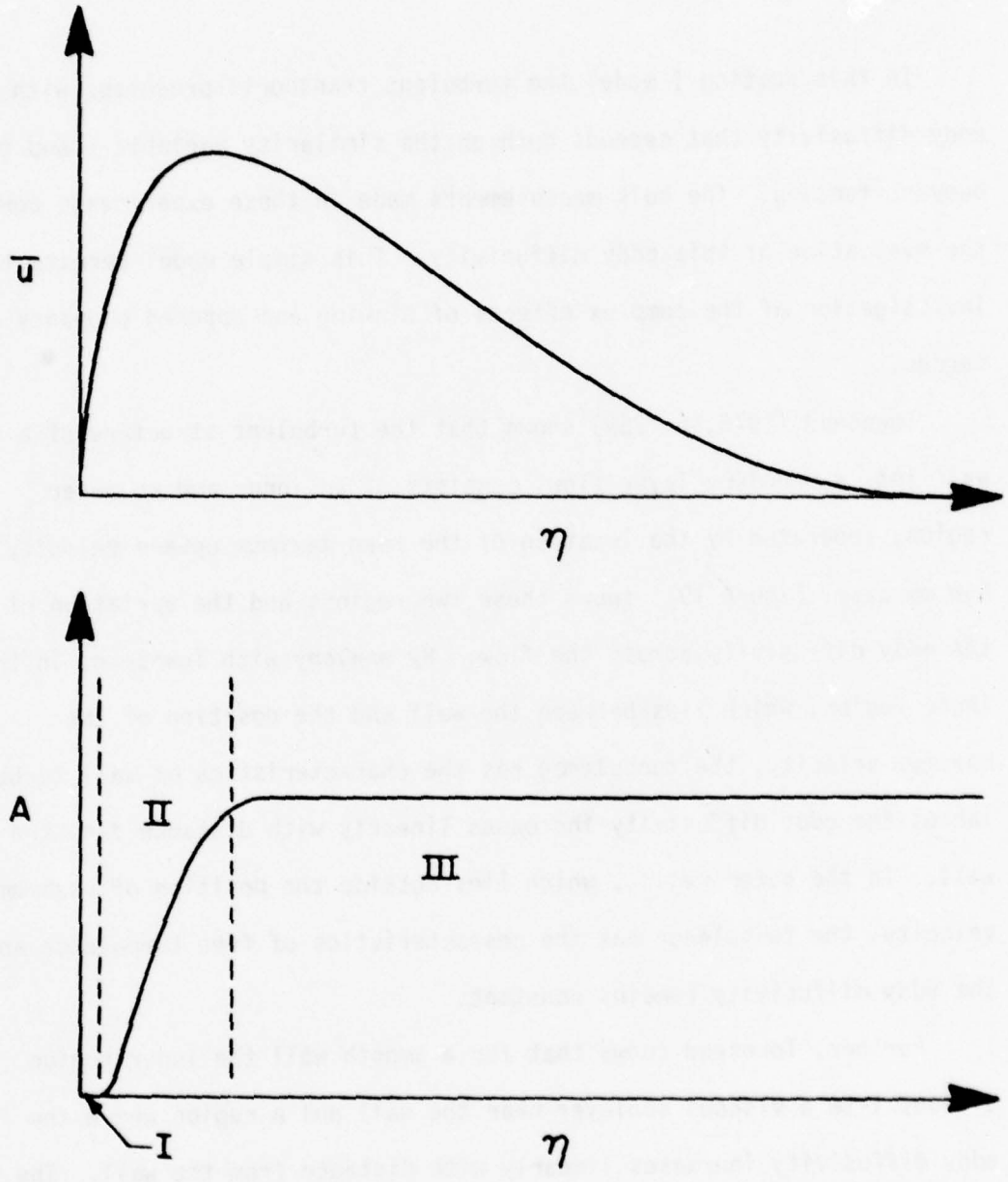


Figure 19. The assumed variation of the eddy diffusivity, A, and its relationship to the mean upward velocity, $\bar{u}$. See text for further explanation.

immediately after the ice melts past a thermistor, then as the ice melts further past the thermistor, the record shows turbulent temperature fluctuations. Also, particle trajectories and dye injections show very low turbulent activity within 2 mm of the ice.

The outer edge of the viscous sublayer represents the region where the turbulent transfer of momentum approximately equals the molecular transfer of momentum; however, turbulent velocity fluctuations still persist in the sublayer. Townsend (1976, p. 354) shows that for large Pr or Sc the heat or salt transfer in the outer region of the viscous layer results from turbulent convection, while close to the wall the heat or salt transfer results from conduction. Townsend calls this inner region the 'visco-conductive' layer and the position of the outer edge of this layer occurs where the turbulent transfer approximately equals the molecular transfer of heat or salt. Because the molecular thermal diffusivity, κ, is much larger than molecular saline diffusivity, D, the thermal visco-conductive layer will be larger than the saline visco-conductive layer.

To incorporate all of these effects, I modeled the turbulence with an eddy diffusivity that depends only on the similarity variable η. Near the wall the eddy diffusivity, A, equals zero, corresponding to the region of no turbulence. In the wall layer the eddy diffusivity increases linearly with increasing distance from the wall. Beyond the point of the mean maximum velocity, an eddy diffusivity is constant. The mathematical formulation of this model is

$$A(\eta) = 0 \quad \text{for} \quad 0 \leq \eta \leq \Delta\eta \quad , \tag{107a}$$

$$A(\eta) = A_0[1-\text{sech}(\alpha(\eta-\Delta\eta))] \tag{107b}$$

illustrated by Figure 19. The region of no turbulence is $\Delta\eta$, α is a shape factor and sech, the hyperbolic secant, is defined as

$$\text{sech}(\gamma) = \frac{2}{e^{\gamma}-e^{-\gamma}} \quad . \tag{108}$$

In this model the eddy diffusivity remains constant as η increases; ideally A should approach zero as the velocity decreases with increasing η. Two factors allow this ambiguity to exist: First, the outer edge of the turbulent boundary layer is not clearly defined; visual observations of the entrainment of quiescent fluid by the turbulent flow show the position of the outer edge to fluctuate. Keeping A constant over the region of entrainment accurately models the turbulent processes in this region. Second, outside the region of entrainment the upward velocity and the gradients of momentum salt and heat are zero. Because the diffusive flux of a quantity equals the product of its gradient and its total diffusion coefficient, the solution to the governing equations remains unaffected by the value of the diffusion coefficient as long as the gradient equals zero. The numerical scheme takes advantage of this result by using a larger integration step size away from the wall than near the wall. If A approached zero for large η, then the large Sc of the flow would require a small step size to prevent numerical errors from accumulating. Betchov and Criminale (1964) used a similar eddy diffusivity model to study the oscillations of a turbulent flow which they state as applicable to turbulent jets; in their model they reduced the eddy diffusivity in the far field to 1/3 its maximum value to avoid numerical difficulties.

To estimate the order of magnitude of A, I next compare the observed turbulent flow characteristics with the theoretical solutions of Ostrach (1954) for the laminar flow generated by the diffusion of a single species at Sc = 1000 and the results show that A is of the same order as ν. For the laminar case taking $S_\infty - S_w$ equal to 15 $^0/_{00}$ gives the following boundary layer characteristics at a point 0.3 m downstream from the origin of the flow; the melting rate equals 1.03×10^{-3} mm s^{-1}, the maximum upward velocity equals 6 mm s^{-1} and boundary layer thickness equals 30 mm. In my laboratory turbulent case, a value of 15 $^0/_{00}$ for $S_\infty - S_w$ corresponds to a thermal driving of 4°C, and the boundary layer has the following characteristics at 0.3 m downstream from the bifurcation point: The melting rate equals 1.74×10^{-3} mm s^{-1}, the maximum upward velocity is of order 10 mm s^{-1} and the boundary layer thickness equals approximately 20 to 30 mm. The similarity between these two cases shows that A is the same as ν and molecular effects must be included in a realistic flow model. These low turbulent levels result from the large Sc. Even in the turbulent case the low molecular diffusivity of salt contains the majority of the saline anomaly near the ice wall well within the viscous sublayer where the frictional effect of the wall can counter the large buoyant forces. Also, the small value of the Reynolds number for the observed flows suggests weak turbulent mixing; the laboratory Reynolds number was of order 10^2.

Because of these low turbulence levels, in my model I retained the molecular effects and used an eddy diffusivity which is only a function of the similarity variable η. This formulation means that at similar points in the boundary layer the turbulence has identical characteristics.

This assumption may not adequately represent the turbulence at all points, but the low turbulent levels and the large influence of molecular effects allows the model to simulate the laboratory flow. Modeling the turbulence in this fashion admits a similarity solution in which the effects of opposing buoyancy forces and blowing can be readily investigated. The results of the model are then valid for large Sc and Gr up to 10^{13}; however, for an iceberg Gr equals 10^{18} and direct application of the model to icebergs may not be appropriate.

Numerical Scheme

Because the governing equations and the boundary conditions are nonlinear with variable coefficients, I solved them numerically. To solve the equations I used the quasi-linearization scheme of Radbill and McCue (1970) programmed on the CDC 6400 computer at the University of Washington. Quasi-linearization allows for the linear superposition of the particular and homogeneous solutions to satisfy the boundary conditions.

In this case, specification of the boundary conditions at $\eta = 0$ and $\eta = \infty$ gives a two point boundary value problem and I applied the boundary conditions at $\eta = \infty$ at $\eta = 20$ which correspond to approximately three boundary layer thicknesses. A guess of the unknown boundary conditions at $\eta = 0$ allows for the integration of the equations over the entire interval. At $\eta = 20$ the difference between the calculated and given boundary conditions gives the disparity between the iterated and exact solution. With linear equations these differences would determine a new set of coefficients for the next iteration through a linear combination of the homogeneous and particular solutions. In a nonlinear case Radbill and McCue use a Newton-Raphson algorithm to generate the next iteration which is a linear function of the previous iteration and then use linear methods to generate a new set of coefficients for the next iteration. The iteration process continues until the difference between the iterations is less than a specified value, in my case 5×10^{-3}. To check the sensitivity of the solution to the convergence parameter, I ran two duplicate cases with the convergence parameters equal to 5×10^{-3} and 10^{-3} respectively and found no discernable differences.

I next describe the Newton-Raphson method used in the numerical integration for the case of a nonlinear scalar equation

$$g(x) = 0 \quad . \tag{109}$$

If the function g(x) decreases monotonically and is strictly convex in a sufficiently large neighborhood of x, the exact root g(x) is linearly approximated at $x^{(o)}$ by $g[x^{(o)}]$ and its tangent $g'[x^{(o)}]$,

$$g(x) \cong g[x^{(o)}] + [x-x^{(o)}]g'[x^{(o)}] \quad , \tag{110}$$

where the superscript in parentheses denotes the iteration number. Figure 20 shows the successive approximations of g(x) and the rapid approach of the iterated root, $x^{(n)}$, to the actual root. Equation (110) gives a further approximation to r when g(x) equals zero which gives the general recurrence relation:

$$x^{(n+1)} = x^{(n)} - \frac{g[x^{(n)}]}{g'[x^{(n)}]} \quad . \tag{111}$$

Radbill and McCue show that this method converges both quadratically and asymptotically; each additional iteration doubles the number of correct digits in the approximation. They also generalize the Newton-Raphson method to a system of n nonlinear ordinary differential equations and give several detailed examples of the application of the quasi-linearization technique to problems in fluid mechanics.

A useful feature of this scheme is a variable integration step size which I adjusted to minimize the computing time required to obtain convergence. Table 5 gives the division of the integration interval

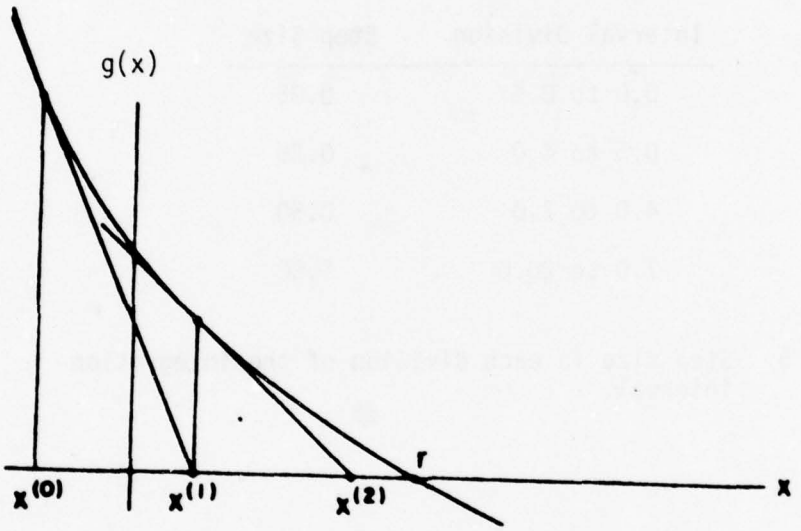


Figure 20. A sequence of linear approximations converging to a root, illustrating the Newton-Raphson method.

and the size of the steps in each division; each step was further divided by 15 in the actual integration. The high gradients of velocity, salinity and temperature near the wall which result from the lack of turbulence and the high Schmidt number require a small step size near the wall to prevent error accumulation. Further from the wall the gradients relax and a larger step size is used.

Table 5

Interval Division	Step Size
0.0 to 0.5	0.05
0.5 to 4.0	0.25
4.0 to 7.0	0.50
7.0 to 20.0	1.00

Table 5. Step size in each division of the integration interval.

Numerical Results

This section shows how the numerical scheme permits me to evaluate the turbulent parameters which determine the boundary layer characteristics. The results also show that both blowing at the interface and opposing buoyancy forces must be included in the analysis to model adequately the flow.

Appendix IV contains the computer printouts of f'', f', f, ϕ', ϕ, θ', θ and the buoyancy for $0 \leq \eta \leq 20$ and $2°C \leq T_d \leq 12°C$. This appendix contains three cases; the first case includes the effect of blowing and opposed buoyancy forces. The second case omits blowing at the interface and the third case omits the temperature effects on density.

I evaluated the turbulent parameters by varying these parameters until the calculated values of $\phi'(0)$ and $\theta'(0)$ equaled the experimental values calculated from the smoothed laboratory data. Table 6 gives $\phi'_{lab}(0)$, $\theta'_{lab}(0)$, and $f'_{lab}(0)$ for $2°C \leq T_d \leq 12°C$, where the subscript lab refers to the laboratory results. The calculations at each T_d used $f'_{lab}(0)$ at that T_d for the blowing boundary condition. Also, the resulting flow had to satisfy two other less exact but equally important conditions: The entire flow must be upward and the boundary layer must be approximately 20 mm or 5 η units thick.

Once this method succeeded at $T_d = 4°C$, I found that a parabolic dependence of the magnitude of the eddy diffusivity on the density difference between the wall and the far-field accurately modeled the flow from $2°C \leq T_d \leq 12°C$. For $T_d = 14°C$ the solution showed a significant downward velocity and the calculated values of $\phi'(0)$ and $\theta'(0)$ disagreed with the laboratory values. For $T_d \geq 16°C$ the numerical

Table 6

T_d(°C)	$\phi'_{lab}(0)$	$\theta'_{lab}(0)$	$f'_{lab}(0)\times10^{-3}$	a ($mm^{5/4}\ s^{-1}$)	b ($mm^{-3/4}$)
2	-5.02	-0.556	-0.26	11.0	1.53
4	-4.67	-0.720	-0.68	12.8	1.78
6	-3.83	-0.837	-1.24	13.7	1.90
8	-2.93	-0.937	-1.92	14.2	1.97
10	-2.04	-0.982	-2.59	14.4	2.00
12	-1.33	-0.989	-3.22	14.5	2.02

Table 6. $\phi'_{lab}(0)$, $\theta'_{lab}(0)$, $f'_{lab}(0)$, a and b computed from the smoothed laboratory data.

scheme failed to converge, which shows that at high T_d the flow characteristics change radically. This result is in fair agreement with the observed flow reversal found at $T_d > 20°C$. In the following section I use the model results at $T_d = 12°C$ to form zero net buoyancy condition that accurately predicts the turbulent flow reversal.

To evaluate the turbulent parameters, which are A, the maximum value of the eddy diffusivity; $\Delta\eta$, the thickness of the laminar region; and α, the shape factor, I set α equal to 1.5 and then varied A and $\Delta\eta$ in a systematic fashion until the calculate values of $\phi'(0)$ and $\theta'(0)$ equaled the laboratory values shown in Table 6. This technique rapidly yielded values for A and $\Delta\eta$ because changes in each parameter affected the salinity and temperature distributions differently.

I chose $\alpha = 1.5$ to allow the eddy diffusivity to reach its maximum value in the region of the maximum velocity, as required by Townsend (1976). Figure 21 gives the f' profiles from the final turbulent model with $\alpha = 1.5$ and shows that the maximum velocity occurs for $0.7 \leq \eta \leq 2.0$. The position of maximum velocity remained virtually unaffected when I varied α from 0.5 to 2.0, however I could not satisfy the thermal and saline boundary conditions. The eddy diffusivity attains 90% of its maximum value when $\alpha\eta = 3.0$; therefore, this value of α places the maximum eddy diffusivity at the required location for $T_d > 2°C$. For $T_d = 2°C$, the eddy diffusivity in the region of maximum velocity is much less than the molecular viscosity and hence, the eddy diffusivity has little direct effect on the distribution of momentum. To simplify the calculations over the entire temperature range, I kept α constant for all T_d.

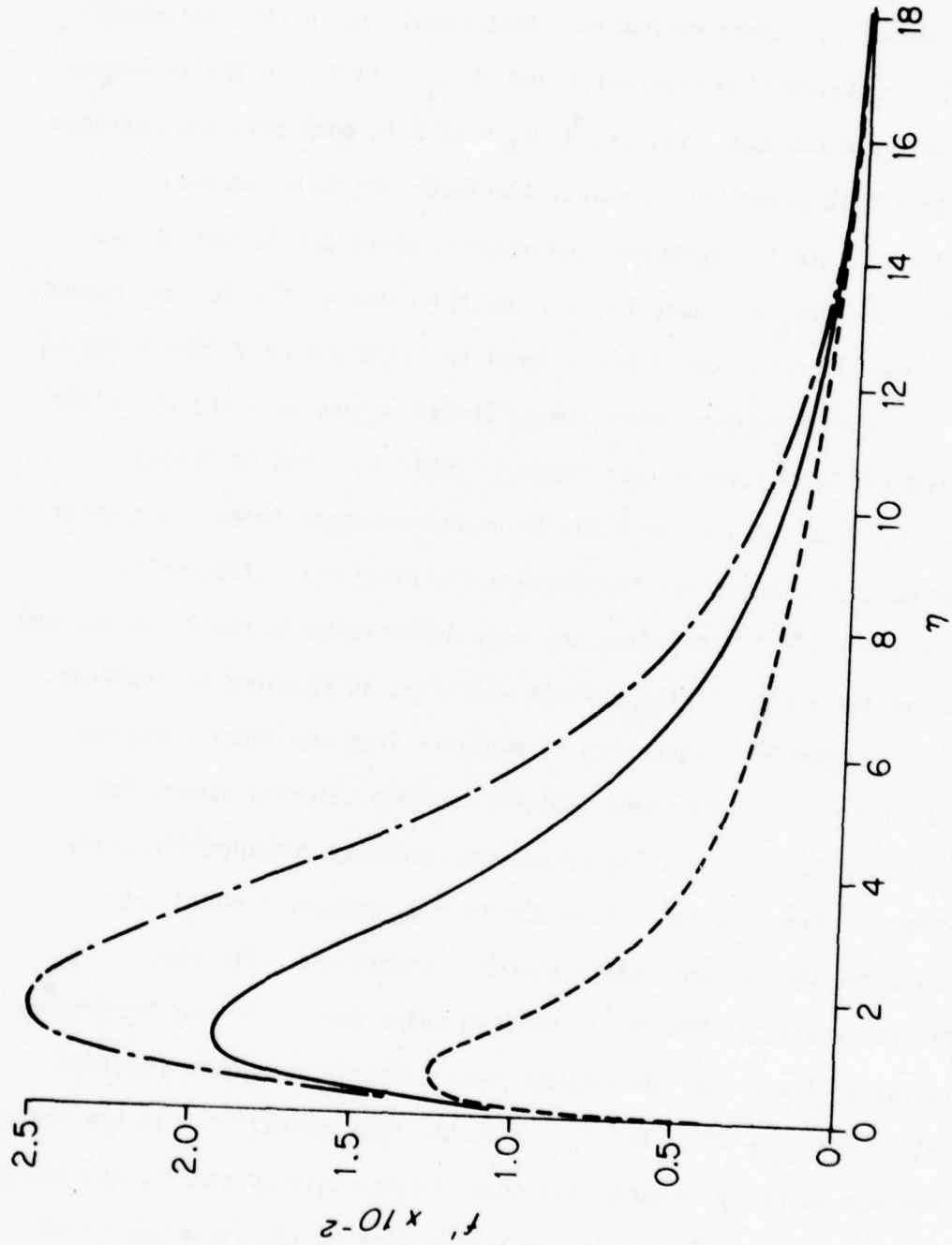


Figure 21. Computed profiles of f' for T_d = 2°C ----, T_d = 4°C ——, and T_d = 8°C - ——— -.

With α fixed at 1.5, I then varied A and $\Delta\eta$ until $\phi'(0) = \phi'_{lab}(0)$ and $\theta'(0) = \theta'_{lab}(0)$ at $T_d = 4°C$. Figure 22 shows the dependence of $\phi'(0)$ and $\theta'(0)$ on A and $\Delta\eta$ with $\alpha = 1.5$ at $T_d = 4°C$, where a more negative value of either $\phi'(0)$ or $\theta'(0)$ corresponds to a higher salinity or temperature gradient at the interface. Variations of A have a larger effect on $\theta'(0)$ than on $\phi'(0)$ while the opposite holds true for variations of $\Delta\eta$; this is a result of the large Lewis number that characterizes these flows. The thermal anomaly with its high diffusivity, diffuses through the laminar region into the turbulent region where the eddy diffusivity affects the heat transfer. The low value of the saline molecular diffusivity contains the saline anomaly close to the ice; hence, changes in the thickness of the laminar region greatly affect the salt distribution within the boundary layer. A change in $\Delta\eta$ also affects the temperature distribution for two reasons: First, the temperature distribution is affected in the same manner as the salt distribution only to a lesser extent because of the large Lewis number. Second, the density dependence on salinity produces large changes in the buoyant forcing which affect the flow and its transfer characteristics.

Figure 22 shows that $A = 0.3$ mm^2 s^{-1} and $\Delta\eta = 0.08$ almost give the required values of $\phi'(0)$ and $\theta'(0)$ for $T_d = 4°C$. For the model at $T_d = 4°C$ I chose A and $\Delta\eta$ equal to 0.28 mm^2 s^{-1} and 0.078, respectively, for the turbulent parameters because these values gave an average error in the salinity and temperature gradients of 2.5%, and an average error of less than 5% for an extension of the turbulent model over the range of T_d from 2°C to 12°C.

To extend the turbulent model over the temperature range, I took the following formulation for A:

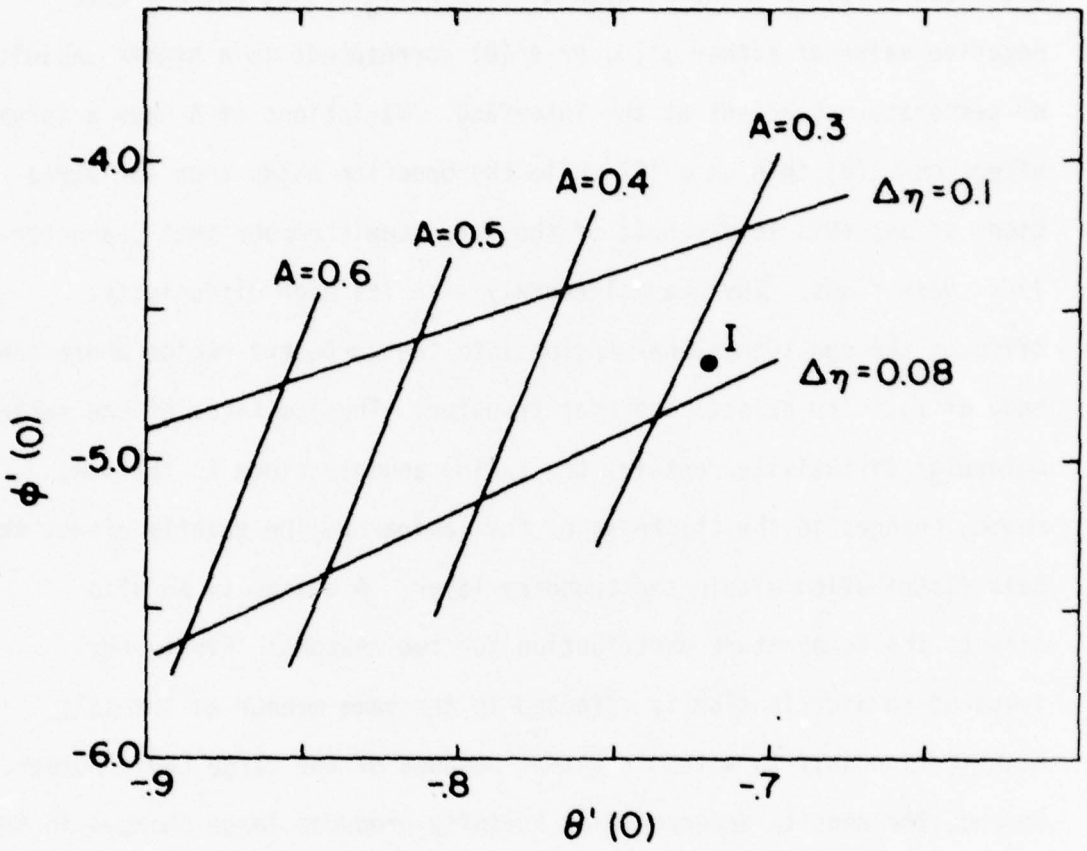


Figure 22. Dependence of $\phi'(0)$ and $\theta'(0)$ on A and $\Delta\eta$ at T_d = 4°C; the point labeled I gives the required values of $\phi'(0)$ and $\theta'(0)$ at T_d = 4°C.

$$A = A_o\left(\frac{\rho_\infty - \rho_w}{\rho_\infty - \rho_f}\right)^n \qquad (112)$$

where ρ_w is the interfacial water density, ρ_f is the fresh water density at T = 0, and n is an undetermined exponent. I choose (112) because the experimental melt rates indicate a turbulent transfer mechanism that increases with increasing density difference between the far-field and the interface. The dependence of ρ_w on T_d makes A a function of T_d and the experimental results show that

$$\frac{\rho_\infty - \rho_w}{\rho_\infty - \rho_f} = \tanh(0.15\ T_d) \qquad (113)$$

because density depends linearly on salinity. This formulation gives a rapidly increasing A for T_d up to 9°C and an almost constant A for T_d > 9°C, a variation suggested by the observed melt rates. Figure 14 gives the experimental melt rate dependence on T_d. Below 9°C the melt rate increases as $T_d^{1.6}$ which indicates that transfer of heat and salt not only increases as the result of higher temperature and saline differences across the boundary layer, but also the turbulent transfer mechanism becomes stronger. Above 9°C the melt rate increases linearly which indicates that the turbulent transfer mechanism remains constant while the temperature difference across the boundary increases linearly.

To determine the coefficient n, I numerically solved the governing equations at T_d equal to 2°C, 4°C, and 8°C for three values of n: 1, 1.5, and 2. with $\Delta\eta$ held constant at 0.09. For each value of n, I held $\Delta\eta$ constant at 0.09 and I adjusted A_o to give A at 4°C equal to 0.28 $mm^2\ s^{-1}$. Figure 23 compares the smoothed experimental data with

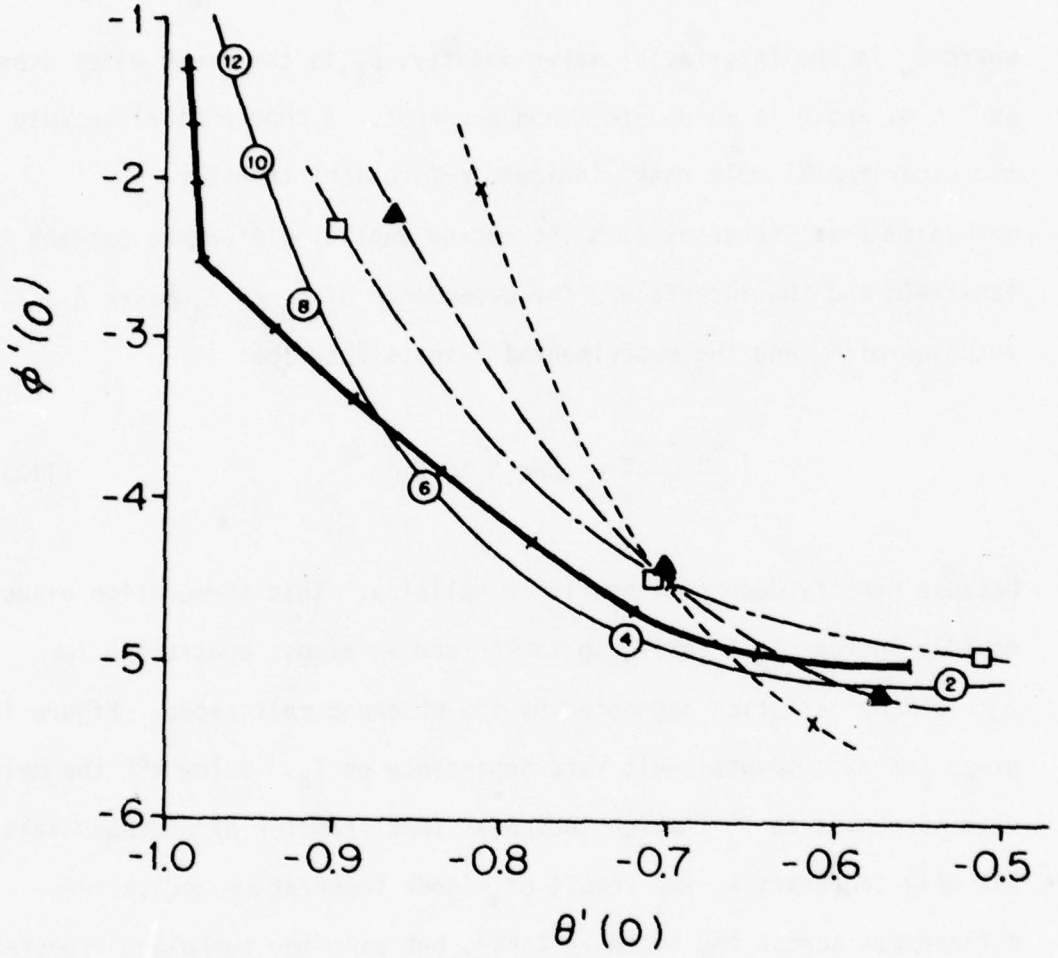


Figure 23. Locus of points for $\phi'(0)$ and $\theta'(0)$ from the experiments, ———, and from four models of the eddy diffusivity; see text for discussion.

the results from each set of calculations. The heavy solid line is the locus of experimental points. Each tick mark on this line represents the boundary conditions for consecutively increasing T_d, beginning at 2°C at the lower right and ending at 12°C at the upper left. The arbitrary division of melt rate dependence on T_d produces the kink at T_d = 9°C. The solutions for n = 1, denoted by x, give temperature and salinity gradients that are too low at T_d = 8°C and too high at 2°C. The solutions for n = 3/2, denoted by Δ, are in better agreement with the laboratory results. The solutions for n = 2, denoted by □, give results that all lie above the experimental line which indicates a change in $\Delta\eta$ would give better overall agreement. Values of 0.078 for $\Delta\eta$ and 0.922 $mm^2\ s^{-1}$ for A_o give the results denoted by 0 where the numbers inside the 0's are the T_d for each calculation. These are the final parameters of the model and they give an average error of less than 5% over the range of T_d.

The final form of the turbulent model is

$$\alpha = 1.5 \ ,$$

$$\Delta\eta = 0.078 \ ,$$

and

$$A = 0.922[\tanh(0.15\ T_d)]^2\ mm^2\ s^{-1} \qquad (114)$$

which gives an average error of less than 5% for 2°C ≤ T_d ≤ 12°C.

Using these values, I next discuss the profiles of salinity, temperature and velocity across the boundary layer and the variations in these profiles that result from a change in the thermal driving.

Figure 24 gives the profiles of ϕ and θ for a thermal driving of 4°C, 8°C, and 12°C. The two most important features are the difference in

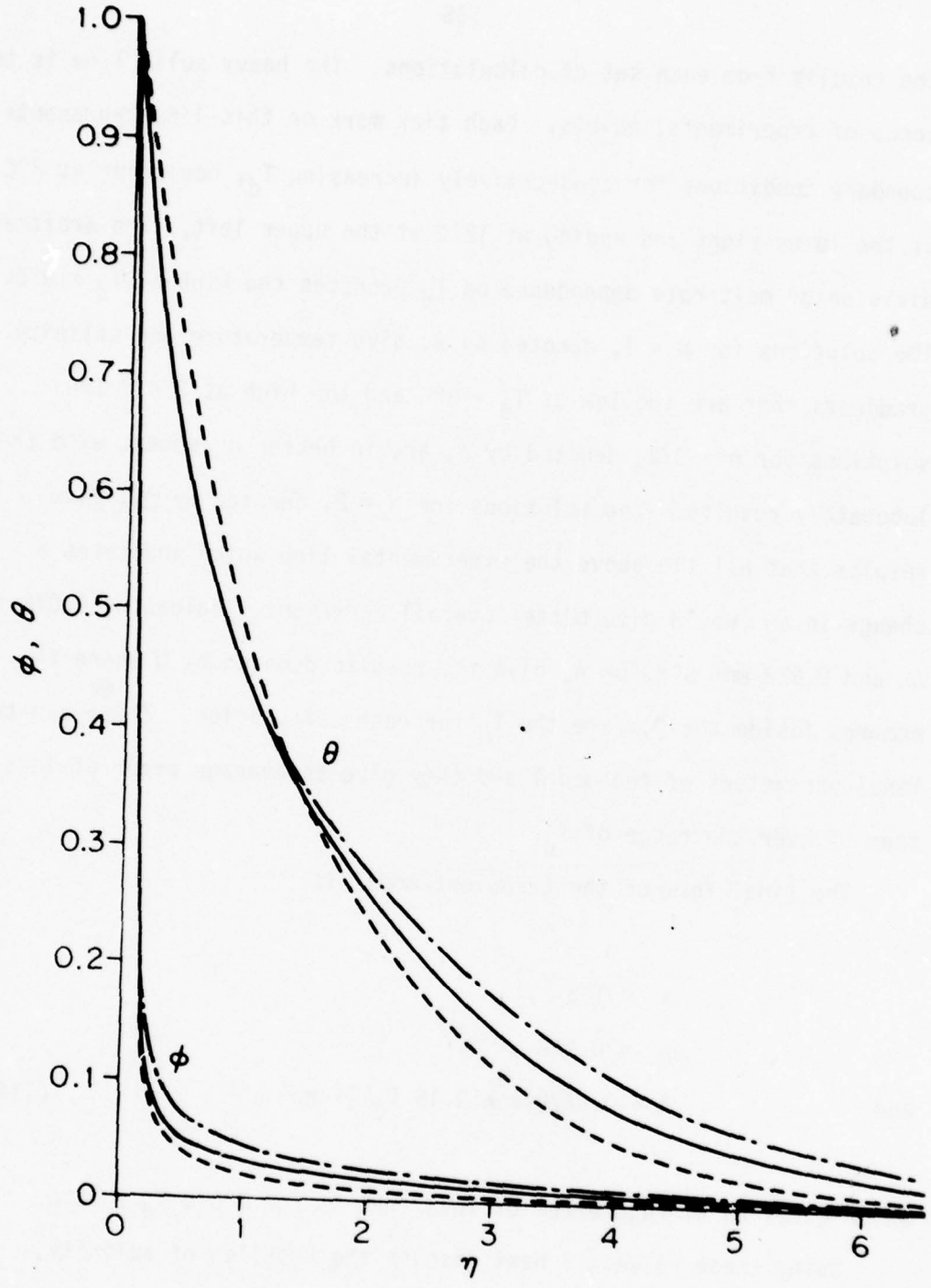


Figure 24. Computed profiles of ϕ and θ for T_d = 4°C, ----; T_d = 8°C, ———, and T_d = 12°C, - ——— -.

the saline and thermal boundary layer thicknesses and the thickening of each boundary layer as the thermal driving increases. The difference in the boundary layer thicknesses results from the low turbulence levels and the large Lewis number. The laminar region adjacent to the ice and the small value of D act to contain 95% of the saline anomaly to within 1 η unit of the ice wall. Although most of the saline anomaly is contained near the ice, the eddy diffusivity, which increases with distance from the wall, allows the dilution effect to diffuse out to 4 or 5 η. The eddy diffusivity reaches the same order of magnitude as D at a distance of approximately 0.01 η from the ice and this effect produces the sharp bend in the ϕ profiles at 0.5 η. The thermal boundary layer thickness is 4 to 5 η units and the θ profiles do not exhibit the same sharp bend found in the ϕ profiles. This behavior results from a maximum eddy diffusivity that is less than or of the same order as the molecular thermal diffusivity.

Next, Figure 21 gives the nondimensional velocity or f' profiles for T_d = 2°C, 4°C, and 8°C. The profile for T_d = 12°C, which is almost identical to that of T_d = 8°C, has been omitted but Appendix IV contains values of $f'(\eta)$ for T_d = 12°C. The similarity in profiles results from the almost identical buoyant forcing in each case. The difference between the far-field and interfacial conditions determines the overall buoyant forcing at each T_d. When T_d increases from 8°C to 12°C, the laboratory results show that the saline difference across the boundary layer increases by 10% while the thermal difference increases by 50%. This large change in temperature difference along with the increasing effect of temperature on density creates enough downward buoyancy to counter the increased upward buoyancy that results from

increased salinity difference. Hence, as T_d increases from 8°C to 12°C, the velocity profile undergoes little change.

Figure 21 shows that the momentum boundary layer thickness, δ_m, is constant for all T_d. Definition of δ_m as the distance from the ice where f' drops to 90% of its maximum value gives δ_m approximately 11 η. This value for δ_m of 11 η corresponds to approximately 25 mm which agrees with the laboratory observations; however, the long tails of the f'-profiles make determination of the boundary layer thickness arbitrary. The constant δ_m for varying T_d results from the low values of A which are always less than the molecular diffusivity, ν. At all T_d ν determines the boundary layer thickness and the turbulence has only an indirect effect on the distribution of momentum. The turbulence acts to transport the dilute water near the ice away from the ice where this buoyant water generates upward momentum away from the strong frictional effect of the wall. This dilute water is approximately 0.5 $^{o}/_{oo}$ less saline than the ambient water but the large effect of salinity on density produces enough buoyancy to overwhelm the negative thermally-produced buoyancy. The numerical solutions, given in Appendix IV show that cooling produces negative buoyancy of order 10^{-2} mm s^{-2}. Because the velocity or f' profiles show no reversal, the combined molecular and turbulent diffusion of positive momentum into the region of negative buoyancy overwhelms this small amount of negative buoyancy.

A comparison of the f' profiles, given in Figure 21, to either the ϕ profiles or θ profiles, given in Figure 24 shows that the momentum boundary layer is always thicker. Unlike δ_m, δ_h, and δ_S increase in thickness for increasing T_d and this thickening manifests

itself as longer tails in each profile.

Figure 21 also shows that the maximum value of f', f'_{max}, increases with increasing T_d up to T_d = 8°C. Above T_d = 8°C, f'_{max} remains almost constant at 2.5×10^{-2}. Table 7 gives f'_{max} for $2°C \leq T_d \leq 12°C$ for three cases; namely, density as a function of both S and T; density is only a function of S, and density is a function of S and T with no blowing at the interface. In the case of no blowing, for $T_d \geq 10°C$, the numerical scheme failed to converge. The values of f'_{max} for $\rho(S, T)$ increase rapidly with T_d up to 8°C where they reach an almost constant value and then slightly decrease at 12°C. The increase results from greater buoyancy at increasing T_d but the available buoyancy reaches a maximum as S_w approaches zero. Figure 14 from the laboratory results, shows that S_w approaches zero in the neighborhood of T_d = 10°C; therefore, f'_{max} should approach a constant value near 10°C. Above T_d = 10°C, the increasing thermal effect on density causes the slight decrease of f'_{max} at T_d = 12°C.

The increase of f'_{max} is not linearly related to the available buoyancy because the increased mixing at higher T_d also increases the upward mass transport. A comparison of the first two columns of Table 7 shows that the disproportionate increase in f'_{max} results from the increased mixing and not the increasing production of downward thermal buoyancy. The second column shows the case with the density is only a function of salinity and the same disproportionate increase is observed in addition to higher values of f'_{max}. These higher values result from the elimination of the downward thermally produced buoyancy force and a later section of this chapter discusses the effect of both thermal buoyancy and blowing at the interface of the turbulent boundary layer.

Table 7

T_d(°C)	$f'_{max} \times 10^{-2}$			$f(\infty) \times 10^{-2}$		
	$\rho(S,T)$	$\rho(S)$	No Blowing	$\rho(S,T)$	$\rho(S)$	No Blowing
2	1.26	1.45	1.13	5.50	8.04	4.30
4	1.93	2.31	1.55	10.8	11.9	8.60
6	2.30	2.88		12.3	14.7	
8	2.50	3.39	1.26	13.6	17.6	3.34
10	2.57	3.69		13.8	18.2	
12	2.52	4.02		13.2	19.7	

Table 7. Values of f'_{max} and $f(\infty)$ for three cases: Opposing buoyancy forces with blowing, $\rho(S,T)$; density only a function of S with blowing, $\rho(S)$; and opposing buoyancy forces without blowing.

Table 7 also gives the nondimensional upward mass transport, $f(\infty)$, for the same three situations and $f(\infty)$ exhibits the same variation as f'_{max}.

To compute the upward transport per unit width, (84a) evaluated at $y = \infty$ gives

$$\psi(\infty) = ax^{1/4} f(\infty)$$

where x is the vertical length of the turbulent boundary layer and Table 6 gives values of a for $2°C \leq T_d \leq 12°C$. As an example, in the laboratory, the upward transport by a 0.5 m long boundary layer next to a block of ice 0.2 m wide after 1 hour is 0.13 m^3. During an experiment there are two sides of the ice block melting at the same rate; therefore, the transport must be doubled to give 0.26 m^3. Because the experimental tank has a horizontal cross sectional area of 1.2 m x 0.45 m, after one hour the water in the upper 0.48 m is water upwelled by the boundary layer. To counter this vigorous upflow, I used the pumping and heating systems previously described to maintain uniform far-field conditions. A final example applies these results to an iceberg with a 100 meter vertical length scale floating in seawater at a thermal driving of 2°C. The resulting upward volume transport equals 294 m^2 day^{-1} per waterline meter. If the iceberg has a circumference of 1 km, the upwelling would equal 2.9×10^5 m^3 day.

The Effect of Blowing at the Interface

The following section discusses the effects of blowing at the ice-water interface which are greatest on the salinity distribution. To determine the blowing or melt water injection effects, I set the blowing or f(0) equal to zero, then numerically solved the differential

equations (91, 92a,b) at T_d = 2, 4, and 8°C with the turbulent parameters previously used at the respective T_d's.

Figure 25 displays the effect of no blowing on $\phi'(0)$ and $\theta'(0)$; the circled numbers are the results from each calculation and the broken line connects the points. For comparison, the solid line connects the points from the calculations with blowing at the interface. The results show that as T_d increases, $\phi'(0)$ and $\theta'(0)$ become more negative which corresponds to both higher salinity and heat fluxes to the ice; however, the experiments show that with increasing T_d the heat flux increases while the salt flux decreases.

In summary, the reduction in both S_w and salt flux to the ice results from blowing at the interface and the low saline molecular diffusivity. The blowing indirectly effects the momentum distribution in the boundary layer and the heat transfer through the large effect of salinity on density. As an interesting note, Radbill and McCue (1970) show that blowing is used to protect space vehicles from thermal extremes during re-entry into the atmosphere. These vehicles are coated with a substance that vaporizes upon heating which creates a blowing velocity that is large enough to inhibit the flow of heat toward the vehicle.

The Effect of Opposing Buoyancy Forces

To investigate the effect of opposing buoyancy forces on the model, I solved the governing equations with the buoyancy determined by a linear dependence of density on salinity only

$$\rho = \rho_\infty - \beta(S_\infty - S) \quad . \tag{115}$$

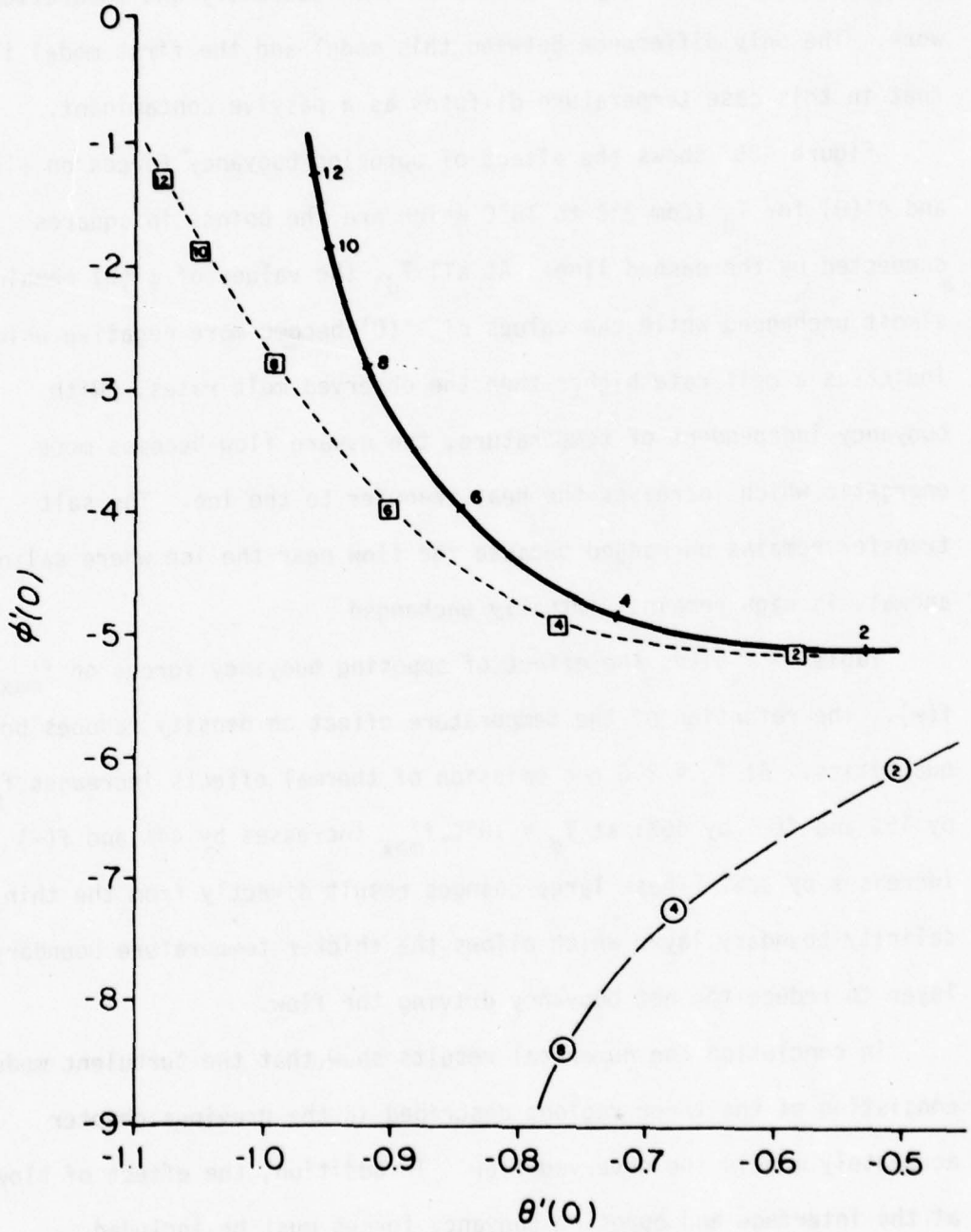


Figure 25. The effects of blowing and opposing buoyancy forces on $\phi'(0)$ and $\theta'(0)$ at various T_d; results including both blowing and opposing buoyancy forces, ————————; no blowing, ——— ———; and density only a function of salinity, -----.

I retained blowing at the interface and used the same turbulent parameters that gave agreement between the laboratory and theoretical work. The only difference between this model and the first model is that in this case temperature diffuses as a passive contaminant.

Figure 25 shows the effect of opposing buoyancy forces on $\phi'(0)$ and $\theta'(0)$ for T_d from 2°C to 10°C which are the points in squares connected by the dashed line. At all T_d, the values of $\phi'(0)$ remain almost unchanged while the values of $\theta'(0)$ become more negative which indicates a melt rate higher than the observed melt rates. With buoyancy independent of temperature, the upward flow becomes more energetic which increases the heat transfer to the ice. The salt transfer remains unchanged because the flow near the ice where saline anomaly is high remains virtually unchanged.

Table 7 gives the effect of opposing buoyancy forces on f'_{max} and $f(\infty)$. The retention of the temperature effect on density reduces both quantities. At T_d = 2°C the omission of thermal effects increases f'_{max} by 15% and $f(\infty)$ by 46%; at T_d = 10°C, f'_{max} increases by 44% and $f(\infty)$ increases by 32%. These large changes result directly from the thin salinity boundary layer which allows the thicker temperature boundary layer to reduce the net buoyancy driving the flow.

In conclusion the numerical results show that the turbulent model consisting of the three regions described in the previous chapter accurately models the observed flow. In addition, the effect of blowing at the interface and opposing buoyancy forces must be included. Previous turbulent studies, either experimental or theoretical, have not included either of these effects.

The High Temperature Reversal

The high temperature reversal of the turbulent boundary layer results from three factors. First, in the turbulent boundary layer the model shows that the difference in molecular diffusivities and the lack of turbulent mixing near the wall produces a saline boundary layer that is thinner than the thermal boundary layer. Second, the large temperature difference across the boundary layer produces more dense water in the thermal layer. Finally, the effect of temperature on density increases as the temperature increases. These factors combine to produce a small amount of much less dense fluid inside of a large amount of slightly more dense fluid. For T_∞ less than the reversal temperature, T_r, enough low salinity and positive momentum water diffuses away from the ice to overwhelm the thermal effect on density; as T_∞ increases past T_r, the cooling produces a large amount of slightly more dense water that overwhelms the small amount of very less dense water.

Integration of the density distribution across the boundary layer gives the net density anomaly, B, within the boundary layer,

$$B = \int_0^\infty \frac{[\rho_\infty - \rho(x)]}{\rho_\infty} dy \quad . \tag{116}$$

The use of a linear equation of state,

$$\rho = \rho_\infty[1 + \beta(S-S_\infty) + \alpha(T - T_\infty)] \ , \tag{117}$$

with α evaluated at T_∞ and S_∞ simplifies the calculations and gives the

maximum effect of temperature on density and results in

$$B = \int_0^\infty [\beta(S-S_\infty) + \alpha(T-T_\infty)]\, dy \ . \qquad (118)$$

Elimination of T and S from (118) through substitution of (82a,b), the definition of ϕ and θ, into (138) and setting B equal to zero yields

$$\beta(S_w-S_\infty) \int_0^\infty \phi dy = -\alpha(T_w-T_\infty) \int_0^\infty \theta dy \ . \qquad (119)$$

At high temperatures the experiments show that S_w and T_w approach zero, which gives

$$\beta S_\infty \int_0^\infty \phi dy = -\alpha T_\infty \int_0^\infty \theta dy \ . \qquad (120)$$

In terms of the similarity variable, η, (120) becomes

$$\beta S_\infty \frac{\int_0^\infty \phi d\eta}{\int_0^\infty \theta d\eta} = -\alpha(S_\infty, T_\infty) T_\infty \ . \qquad (121)$$

after eliminating the common similarity scales. The ratio of two integrals taken from the model at T_d = 10°C and 12°C is 0.145 and 0.157. Because the buoyant driving is constant above 10°C T_d, the profiles remain unchanged except for the effect of the increased blowing which is greatest near the wall; so I took 0.157 as a typical value of the ratio to use in the computations. I also used the equation of state of Gebhart and Mollendorf (1977) to calculate $\alpha(S_\infty, T_\infty)$ which resulted in a transcendental equation in T_∞ for a given S_∞. An iterative technique solved (121) for S_∞ up to 40 $^0/_{00}$ and Figure 26 shows the position of the zero net buoyancy curve, labeled Z. For far-field

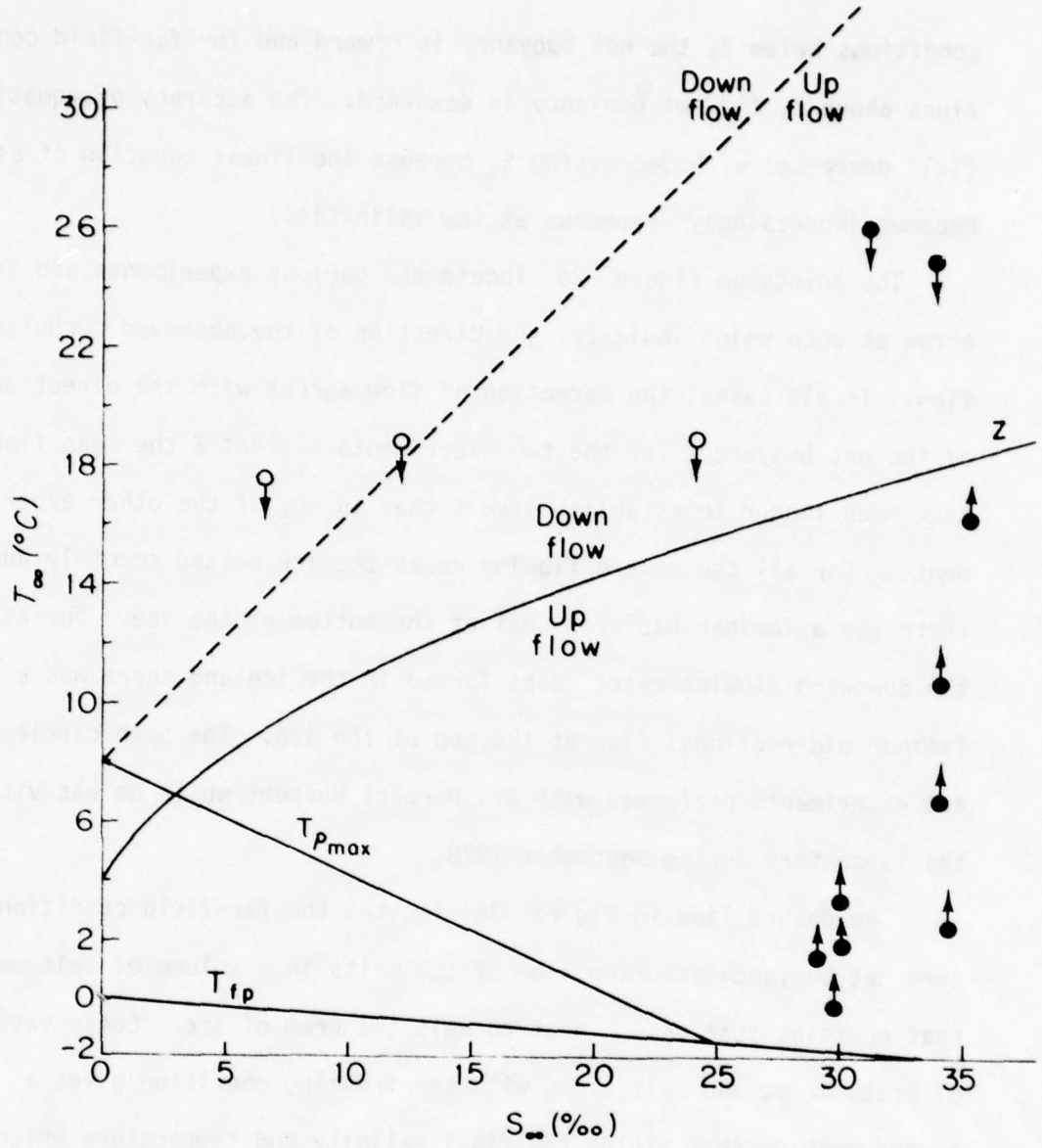


Figure 26. A T-S diagram showing the far-field conditions of the turbulent experiments; the arrows indicate direction of flow. Flow reversal predicted by a simple mixing model, ------, and by the buoyancy integrated across the boundary layer which is the curve label z.

conditions below Z, the net buoyancy is upward and for far-field conditions above Z, the net buoyancy is downward. The accuracy of equation (121) decreases with decreasing S_∞ because the linear equation of state becomes increasingly erroneous at low salinities.

The points on Figure 26 locate the various experiments and the arrow at each point indicates the direction of the observed turbulent flow. In all cases, the direction of flow agrees with the direction of the net buoyancy; for the two experiments nearest Z the mean flow took much longer to establish itself than in any of the other experiments. For all the upward flowing cases the ice melted smoothly and there was a laminar bidirectional at the bottom of the ice. For all of the downward flowing cases cusps formed in the ice and there was a laminar bidirectional flow at the top of the ice. The open circle points are experiments performed with Dr. Herbert Huppert while he was visiting the laboratory during September 1978.

The dashed line in Figure 26 locates the far-field conditions for zero net buoyancy assuming 1 gm of ice melts in a volume of salt water that contains just enough heat to melt the gram of ice. Conservation of heat, mass, and salt along with the freezing condition gives a closed problem that yields the final salinity and temperature which determines the final density. Comparison of the initial density to the final density then determines the buoyancy. Conservation of heat gives

$$L' = (T_\infty - T_f)V_\infty \qquad (122)$$

where $L' = L/c_{pw}\rho_\infty$, and the subscripts f, ∞ refer to final and initial

conditions. Conservation of salt gives

$$S_f V_f = V_\infty S_\infty \quad . \tag{123}$$

Conservation of mass gives

$$V_f = 1 + V_\infty \quad . \tag{124}$$

The linear freezing condition is $T_f = -mS_f$ where m is a constant equal to 0.057. Solving for S_f gives the quadratic

$$S_f^2 + \frac{(T_\infty + L')}{m} S_f - \frac{L'S_\infty}{m} = 0 \quad . \tag{125}$$

The solution to equation (125) is the dashed line on Figure 26 which does not fit the data. This discrepancy results from the assumption that all of the cooling and diluting takes place in one parcel of water and the effect of the large Lewis number is neglected. In this case, the large Lewis number allows one parcel of water to be diluted and another parcel of water to be cooled. The relative sizes of these parcels becomes important in determining the net buoyancy across the boundary layer.

Conclusions

In summary these experiments show that the flow generated by a melting vertical ice wall immersed in salt water of oceanic temperatures and salinities consists of a laminar bidirectional boundary layer flow adjacent to the bottom portion of the ice which becomes a turbulent upward flow further up the ice. The bidirectional laminar flow results from the high Lewis number, Le $\simeq$ 200, which separates the cooling and dilution effects within the boundary layer. The low value of D, $\sim 10^{-9}$ m^2 s^{-1}, contains the saline anomaly within 3 mm of the ice where it generates an upward flowing boundary layer. The comparatively high value of κ, $\sim 10^{-7}$ m^2 s^{-1}, allows the thermal anomaly to diffuse past the saline anomaly where it generates a downward flowing boundary layer 10 mm-20 mm thick.

The large effect of salinity on density allows the inner saline layer to determine the length of the laminar regime. The inner layer becomes turbulent when the Grashof number reached a critical value of 10^8 which, for oceanic cases, corresponds to a maximum laminar length scale of 0.5 m.

When the inner layer becomes turbulent, the low salinity water near the ice diffuses further out where it overwhelms the thermal effect on density and results in a unidirectional upward flowing turbulent boundary layer. The divergence between the downward flowing laminar thermal layer and the upward flowing turbulent boundary layer produces a horizontal jet of ambient water flowing towards the ice. The jet marks the top of the laminar region and the origin of the turbulent flow.

Measurements of the ice-water interface temperature, made by thermistors frozen in the ice, show a vertically varying temperature in the laminar region and a uniform temperature in the turbulent region. In the laminar region the interface temperatures are coldest at the bottom of the ice and slowly increase with height until the turbulent region is reached. In the turbulent region the interface temperatures are uniform over the ice face. For both regions, the interface temperature approaches 0°C as the thermal driving increases past 10°C.

Measurements of the melt rate in the turbulent region by a measuring transit show the ablation rate increases as the thermal driving to the 3/2 power below T_d = 10°C, while above T_d = 10°C the ablation rate increases linearly with thermal driving. In the region between the laminar and turbulent flow, the ice ablates the fastest because of the jet of ambient water flowing towards the ice at this level.

To analyze the turbulent flow, I solved the boundary layer equations of motion for a turbulent flow under the assumption of a self-similarity. I modeled the turbulent transfer of salt, heat, and momentum with an eddy diffusivity that varies across the boundary layer in the following fashion: Near the ice the eddy diffusivity equals zero then increases to a constant value.

I numerically solved the similarity equations and used the smoothed laboratory data to determine the turbulent parameters. The numerical results show that the maximum value of the eddy diffusivity is of order 10^{-6} m^2 s^{-1}. The turbulent diffusion and this low value for the eddy diffusivity further supports the similarity assumption. The main direct effect of the turbulence is the increased diffusivity of salt that,

through the large effect of salt on density, indirectly affects the distribution of momentum within the boundary layer.

The numerical results also show that the blowing at the interface and the opposing buoyancy forces have an important effect on the turbulent flow. The blowing reduces S_w which increases the buoyant driving of the boundary layer as T_d increases. The downward thermal buoyancy remains important because the high Le allows for the production of a small amount of positively buoyant water and a large amount of negatively buoyant water within the boundary layer. In addition, the increasing effect of temperature on density at higher temperature combines with the Lewis number effect to reduce the upward velocities and transports and eventually produces the flow reversal at a T_d of 25°C.

Bibliography

Adams, J. A., and McFadden, P. W. 1966. Simultaneous heat and mass transfer in free convection with opposing body forces. *A.I.Ch.E. Journal*, Vol. 12, no. 4, p. 642-47.

Bajzak, D. 1974. Thermal mapping of water envelopes surrounding icebergs. *Second Canadian Symposium on Remote Sensing, University of Guelph, Ontario, April 29-May 2, 1974.* p. 573-79.

Batchelor, G. K. 1967. *An Introduction to Fluid Dynamics.* Cambridge University Press.

Bendell, M. S., and Gebhart, B. 1976. Heat transfer and ice melting in ambient water near its density extremum. *Intl. J. Heat and Mass Transfer*, Vol. 19, p. 1081-87.

Betchov, R., and Criminale, W. O. 1964. Oscillations of a turbulent flow. *The Physics of Fluids*, Vol. 7, no. 12.

Caldwell, D. R. 1974. The effect of pressure on thermal and Fickian diffusion of sodium chloride. *Deep-Sea Research*, Vol. 21, p. 369-75.

Carslaw, H. S., and Jaeger, J. C. 1959. *Conduction of Heat in Solids*, 2nd Edition. Oxford University Press.

Cheesewright, R. 1968. Turbulent natural convection from a vertical plane surface. *J. Heat Transfer, Trans. ASME*, Series C, Vol. 90, no. 1, p. 1-8.

Cox, G. F. 1974. Brine drainage in sodium chloride ice. Ph.D. thesis, Dartmouth College, Hanover, NH.

Cox, G. F., and Weeks, W. F. 1974. Salinity variations in sea ice. *J. Glaciology*, Vol. 13, no. 67, p. 109-120.

Den Bouter, DeLeeuw, J. A., De Munnik, B., and Heertjes, P. M. 1968. Simultaneous heat and mass transfer in laminar free convection from a vertical plate. *Chemical Engineering Science*, Vol. 23, p. 1185-90.

Eckert, E.R.G., and Jackson, T. W. 1951. Analysis of turbulent free-convection boundary layer on flat plate. *NACA Technical Report 1015*, p. 255-61.

Fujino, K., Lewis, E. L., and Perkin, R. G. 1974. The freezing point of seawater at pressures up to 100 bars. *J. Geophysical Research*, Vol. 79, no. 12, p. 1792-97.

Gebhart, B. 1973. Instability, transition and turbulence in buoyancy induced flows. *Ann. Rev. Fluid Mechanics*, Vol. 5, p. 213-46.

Gebhart, B., and Mollendorf, J. C. 1977. A new density relation for pure and saline water. *Deep-Sea Research*, Vol. 24, p. 831-48.

Gebhart, B., and Pera, L. 1971. The nature of vertical natural convection flows resulting from the combined buoyancy effects of thermal and mass diffusion. *Intl. J. Heat and Mass Transfer*, Vol. 14, p. 2025-50.

Hieber, C. A., and Gebhart, B. 1971A. Stability of vertical natural convection boundary layers: Expansions at large Prandtl numbers. *J. Fluid Mechanics*, Vol. 49, pt. 3, p. 577-91.

Hieber, C. A., and Gebhart, B. 1971B. Stability of vertical natural convection boundary layers: Some numerical solutions. *J. Fluid Mechanics*, Vol. 48, pt. 4, p. 625-46.

Hult, J. L., and Ostrander, N. C. 1973. *Antarctic Icebergs as a Global Fresh Water Resource*. The RAND Corporation, R-1255-NSF.

Huppert, H. E., and Turner, J. S. 1978. On melting icebergs. *Nature*, Vol. 271, no. 5640, p. 46-8.

Husseiny, A. A. 1978. *Iceberg Utilization*. Pergamon Press.

Jaluria, Y., and Gebhart, B. 1974. On transition mechanisms in vertical natural convection flow. *J. Fluid Mechanics*, Vol. 66, pt. 2, p. 309-37.

Kato, H., Nishiwaki, N., and Hirata, M. 1968. On the turbulent heat transfer by free convection from a vertical plate. *Intl. J. Heat and Mass Transfer*, Vol. 11, 1117-25.

Kaufman, D. W. (ed.) 1960. *Sodium Chloride*. Reinhold.

LaPadula, C. A., and Mueller, W. K. 1970. The effect of buoyancy on the formation of a solid deposit freezing onto a vertical surface. *Intl. J. Heat and Mass Transfer*, Vol. 13, p. 13-26.

Lord, W. 1976. *A Night to Remember*. Holt, Reinhart and Winston,

McClain, E. P. 1978. Eleven year chronicle of one of the world's most gigantic icebergs. *Mariners Weather Log*, Vol. 22, no. 5, p. 328-33.

Neshyba, S. 1977. Upwelling by icebergs. *Nature*, Vol. 267, p. 507-8.

Neumann, G., and Pierson, W. J. Jr. 1966. *Principles of Physical Oceanography*. Prentice Hall.

Ostrach, S. 1953. An analysis of laminar free-convection flow and heat transfer about a flat plate parallel to the direction of the generating body force. *NACA Technical Report 1111*, p. 1-17.

Parmerter, R., and Coon, M. D. 1972. Model of pressure ridge formation in sea ice. *J. Geophysical Research*, Vol. 77, no. 33, p. 6565-75.

Paterson, W.S.B. 1975. *The Physics of Glaciers*. Pergamon Press.

Phillips, O. M. 1969. *The Dynamics of the Upper Ocean*. Cambridge University Press.

Radbill, J. R., and McCue, G. A. 1970. *Quasilinearization and Nonlinear Problems in Fluid and Orbital Mechanics*. American Elsevier Publishing Company, Inc.

Ruffman, A. 1976. Of bergy bits and growlers. *Science*, Vol. 192, no. 4234, p. 7.

Sandstrom, W. J. 1919. The hydrodynamics of the Canadian Atlantic waters. (*In* J. Hjort *ed.*, *Canadian Fisheries Expedition, 1914-1915, in the Gulf of St. Lawrence and Atlantic Waters of Canada*, Department of the Naval Service, Ottawa, Canada.) U.W. Fisheries Library #591.92C16lc.

Schlichting, H. 1960. *Boundary Layer Theory*. Fourth edition. McGraw-Hill.

Tennekes, H., and Lumley, J. L. 1972. *A First Course in Turbulence*. The MIT Press.

Townsend, A. A. 1976. *The Structure of Turbulent Shear Flow*. Second edition. Cambridge University Press.

Turner, J. S. 1973. *Buoyancy Effects in Fluids*. Cambridge University Press.

Vliet, G. C., and Liu, C. K. 1969. An experimental study of turbulent natural convection boundary layers. *J. Heat Transfer, Trans. ASME*, Series C, Vol. 91, p. 517-31.

APPENDIX I

The Equation of State

In this study I used the equation of state given by Gebhart and Mollendorf (1977) at 1 atmosphere of pressure because of its compactness and ease of manipulation. The authors fitted the experimental density data to

$$\rho(S, T) = \rho_m(S)\{1 - \gamma(S)|T-T_m(S)|^q\} \qquad (I\text{-}1)$$

where $\rho(S,T)$ represents density, $\rho_m(S)$ is the maximum density at a given salinity, $\gamma(S)$ is the thermal coefficient, $T_m(S)$ is the temperature of maximum density, and q is an unknown coefficient. They took both a linear and a quadratic for the dependence of ρ_m, γ, and T_m on salinity and retained pressure effects in each case.

I used the linear version of ρ_m, γ, and T_m at 1 atmosphere to compute $\rho(S, T)$ and $\alpha(S, T)$ in the numerical calculations. The linear forms are

$$\rho_m(S) = a_1 + a_2S \quad , \qquad (I\text{-}2a)$$

$$\gamma(S) = a_3 + a_4S \quad , \qquad (I\text{-}2b)$$

and

$$T_m(S) = a_5 + a_6S \quad . \qquad (I\text{-}2c)$$

In this case

$$q = 1.894 \qquad (I\text{-}2d)$$

and Table A-1 gives the values of the coefficients a_1 through a_6 for S

in parts per thousand.

This formulation gives accurate densities and allows for easy computation of $\frac{1}{\rho}\frac{\partial\rho}{\partial T}$ and $\frac{1}{\rho}\frac{\partial\rho}{\partial S}$, two quantities needed in the numerical computations. For oceanic conditions, the density dependence on salinity is nearly linear so that

$$\beta = \frac{1}{\rho}\frac{\partial\rho}{\partial S} = 8.05 \times 10^{-4}\ {}^{o}/_{oo}{}^{-1}\ , \qquad \text{(I-3)}$$

while the density dependence on temperature is more complicated. Differentiation of (A-1) with respect to T gives

$$\alpha(S, T) = \frac{1}{\rho}\frac{\partial\rho}{\partial T} \simeq \pm\gamma(S)q|T-T_m(s)|^{q-1}\ ; \qquad \text{(I-4)}$$

for $T > T_m$, $\alpha < 0$ and for $T < T_m$, $\alpha > 0$.

TABLE A-1

a_1	1.00
a_2	8.046×10^{-4}
a_3	9.30×10^{-6}
a_4	-2.646×10^{-8}
a_5	4.007
a_6	-2.124×10^{-1}

Values for the coefficients of the linear equations for ρ_m, γ, and T_m.

APPENDIX II

Molecular Diffusivities of Salt, Heat, and Momentum

In seawater the molecular diffusivities of salt, heat, and momentum differ by three orders-of-magnitude; the large difference between the thermal and saline diffusivities produces a bidirectional flow in the laminar case and retains a strong influence in the turbulent case.

Caldwell (1974) gives the dependence of the saline diffusivity, D, on temperature, T, as

$$D = 10^{-11}(62.5 + 3.63T)m^2\ s^{-1} \quad . \tag{II-1}$$

Neumann and Pierson (1966) show that the thermal diffusivity, κ, has only a slight variation with temperature such that κ can be taken as constant:

$$\kappa = 1.44 \times 10^{-7}\ m^2\ s^{-1} \quad . \tag{II-2}$$

The ratio of κ to D defines the Lewis number, Le,

$$Le = \frac{\kappa}{D} \quad . \tag{II-3}$$

For seawater Le varies from 245 to 170 as the temperature changes from -1°C to +6°C. This study shows that the large Le produces the bidirectionality of the laminar flow and it is partially responsible for the high temperature reversal of the turbulent flow.

Neumann and Pierson (1966) values of the kinematic viscosity of momentum, ν, in seawater for a temperature range of 0°C to 20°C; they

show that the viscosity dependence on salinity is negligible. In this study I took ν at 0°C,

$$\nu = 1.8 \times 10^{-6} \text{ m}^2 \text{ s}^{-1} \quad . \tag{II-4}$$

I assumed a constant viscosity because ice is found in cold water and the convective motions occur in water cooled by the ice.

APPENDIX III

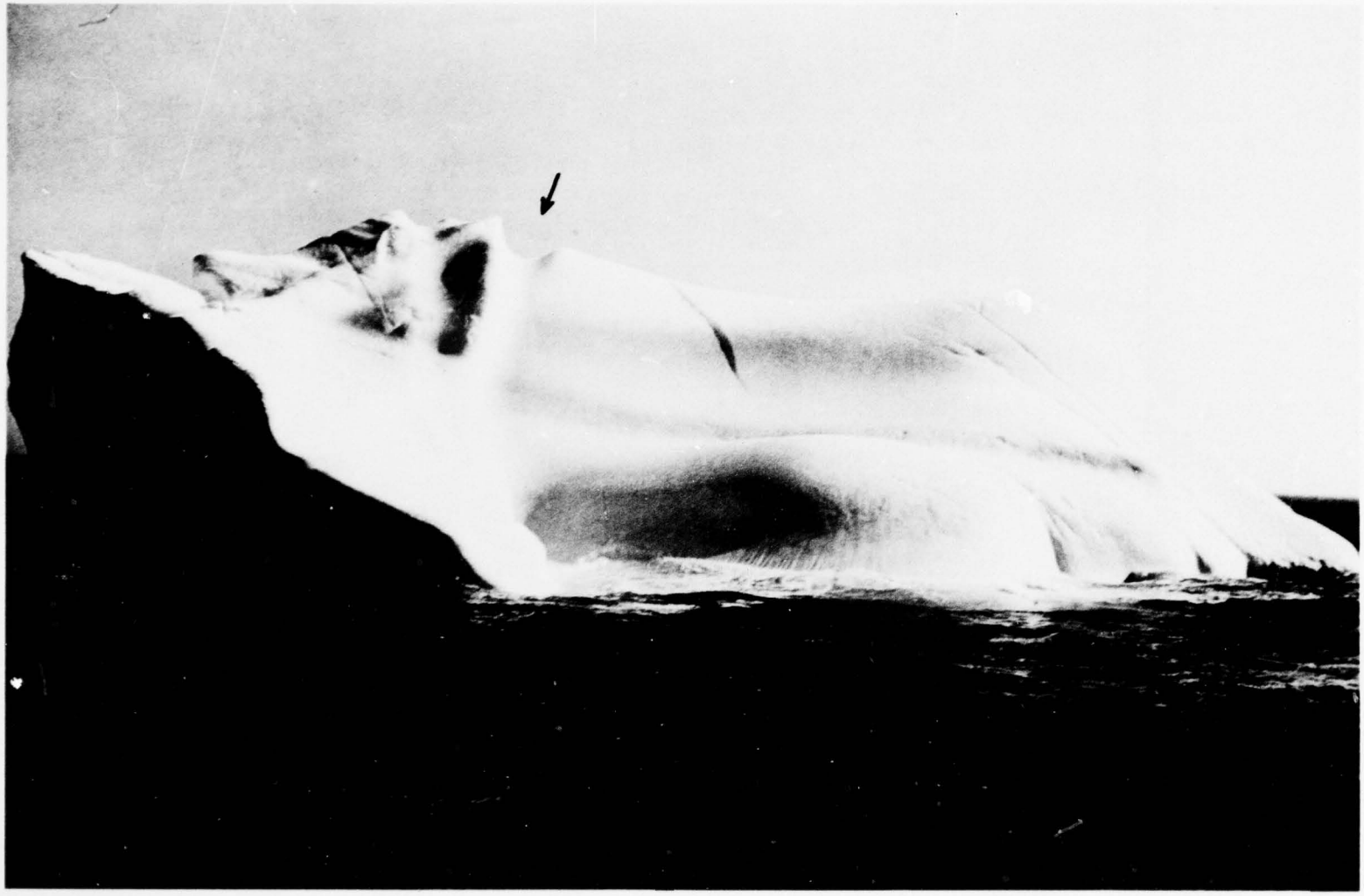
The Field Study

During June 1977, in a cooperative study with the International Ice Patrol, I investigated iceberg melting processes at an iceberg in the Labrador Sea at 50° 49'N, 52° 21'W aboard the USCG Cutter *Evergreen*. Plate XIII shows the iceberg; it had a waterline length of 100 m, a height of 30 m and a draft of 100 m. The draft was determined by side-scanning sonar. The arrow A in Plate XIII indicates one of many old waterlines on the iceberg; these features are a result of increased melting due to the action of surface waves on the side of the iceberg. To the right of this waterline the subsurface portion of the iceberg has been exposed to view by rolling of the iceberg. The iceberg probably rolled to this position in the previous two or three days because the present waterline has not been deeply eroded. Comparison of the ice above and below the old waterline indicates that the ice melts faster in the water than in the air and the features that were underwater are more rounded and polished than the aerial features.

The water surrounding the iceberg was well mixed and turbulent as a result of surface waves breaking against the iceberg. This effect was especially pronounced if the waves were incident on one of the many sloping ice beaches. The presence of a swell with a period of approximately 5 s and an amplitude of 1 m made extended observations next to the iceberg impossible. I observed numerous seabirds and small blocks of ice near the iceberg.

Because the laboratory and theoretical results show that the upward flowing turbulent boundary layer is only a few meters thick for this

Plate XIII. A North Atlantic iceberg.



iceberg, direct measurements in the boundary layer are impractical in the field. Therefore, I measured the salinity and temperature of the surrounding water to determine the alteration of these properties that results from melting ice. The field program consisted of one synoptic surface survey of the temperature and salinity around the iceberg and two STD sections taken radially out from the iceberg.

The synoptic survey consisted of continuously measuring the temperature and salinity at a depth of 2 m while the ship steamed in a circle around the iceberg. The ship made two circuits around the iceberg, one at a range of 100 m to 200 m and the other at a range of 500 m to 600 m. The wind during the surveys blew from a direction of 196°T with a speed of 10 m s^{-1}. The inner survey showed that the temperature dropped from 4.2°C to 3.4°C in a 150 meter wide plume centered at 17° to the right of the downwind direction. I found no comparable salinity plume in this survey. The outer survey did not show any changes that could be attributed to the presence of a melt plume. Although this melt plume did not extend from the iceberg more than 0.5 km, Bajzak (1974) found a melt plume from a 300 m long iceberg in the Labrador Sea extending for a distance of over 1 km.

As a result of the Coriolis force the melt plume is not found directly downwind of the iceberg. Neuman and Pierson (1966) show that the surface current is at an angle of 45° to the right of the wind and the current veers to the right with increasing depth. Therefore, the iceberg moves to the right of the wind at an angle determined by the depth-integrated water drag while the surface waters move to the right at an angle of 45° to give a melt plume location of approximately 17° for this case.

The STD sections, which determined the spatial distribution of temperature and salinity with depth, indicate upwelling may occur as a result of the turbulent natural convection next to a melting iceberg. Figure 27 shows the positions of the 11 STD casts taken around the iceberg (the location of the surface melt plume), and the direction of the wind, which had a speed of 5 m s^{-1}. The first section, taken on 10 June 1977, consists of casts 2 through 6; cast 4 determined the undisturbed water column properties 3.3 km upwind of the iceberg. The second section, taken on 11 June 1977, consists of casts 7 through 12; cast 7 determined the undisturbed water column properties 3.3 km upwind of the iceberg. I took casts 2, 6, and 12 within 2 m of the iceberg from the bow of the ship using a portable Inter-Ocean STD that I hand-lowered to depths of 20 m. I used the shipboard Bisset-Berman CTD for the rest of the casts. At each cast, I used deep-sea reversing thermometers and a Nansen bottle to obtain calibration values of temperature and salinity for the CTD; I took these measurements at the greatest depth of each cast, usually 200 m. I then calibrated the Inter-Ocean STD against the shipboard CTD by taking simultaneous readings during cast 4.

Figure 28 shows the temperature field for section 1 to a depth of 100 m, the level of the bottom of the iceberg. Below 100 m I found no significant differences in either the salinity or the temperature for all of the casts. Casts within 100 m of the iceberg showed water colder by 1°C than the water 3.3 km upwind. Casts 2 and 3 showed isothermal water of 3.0°C to a depth of 15 m out to 100 m downwind of the iceberg. Casts 5 and 6 showed an unexpected result: The water next to the iceberg is generally warmer than the water 30 m away. This results from the advection of warm surface water towards the iceberg by the turbulent

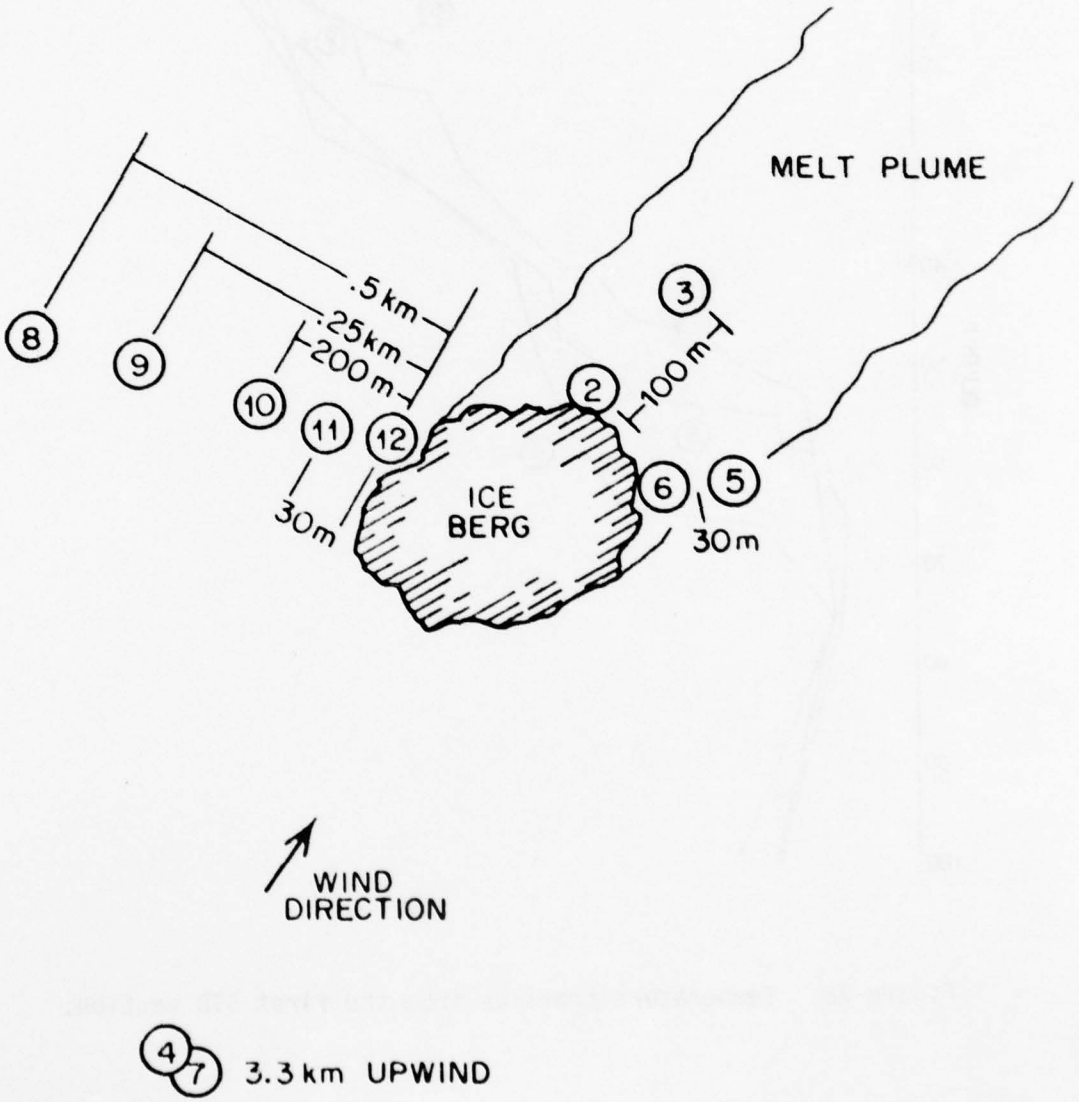


Figure 27. Location of the STD casts and the observed melt plume. See text for further explanation.

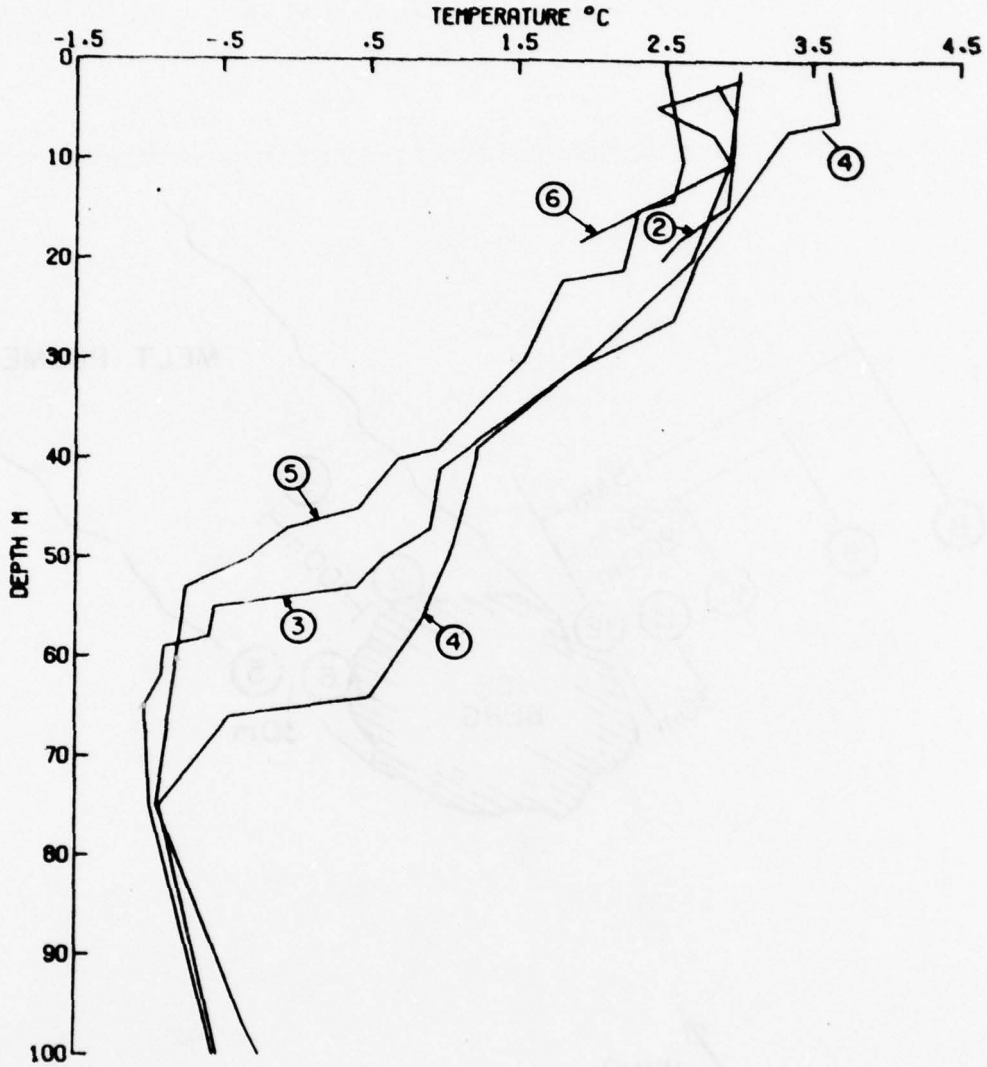


Figure 28. Temperature profiles from the first STD section.

motions generated by the incident surface waves. Casts 3 and 5 showed colder water between 40 m and 70 m that may also be the result of ice melting.

Figure 29a shows the salinity field for the first section. The salinity at the iceberg is lowered by 0.5 $^{o}/_{oo}$ at the surface and then increases to the far-field value of 33.1 $^{o}/_{oo}$ at 5 m. Cast 6 shows the salinity decreases by 0.3 $^{o}/_{oo}$ at 18 m; this corresponds to the 1.0°C decrease in temperature at this depth. These changes occurred when the handline of the portable STD went slack, indicating that the STD was in contact with an underwater prow of ice.

Figures 29b and 30 illustrate the temperature and salinity fields for section 2. Near the iceberg the surface water was 2.9°C colder than the surface water at 3.3 km. The water temperature to 20 m deep was 2.0°C colder than those found in the far-field. At 30 m away from the iceberg the water temperature is 2.1°C colder than the far-field water at 4 m depth; this difference decreases to zero at the 40 m level. Figure 29b shows the salinity for section 2 and the far-field salinity distribution for this section was identical to the distribution found in section 1. In the upper 20 m, at distances of 2 m and 30 m, the salinity had perturbations of 0.6 $^{o}/_{oo}$.

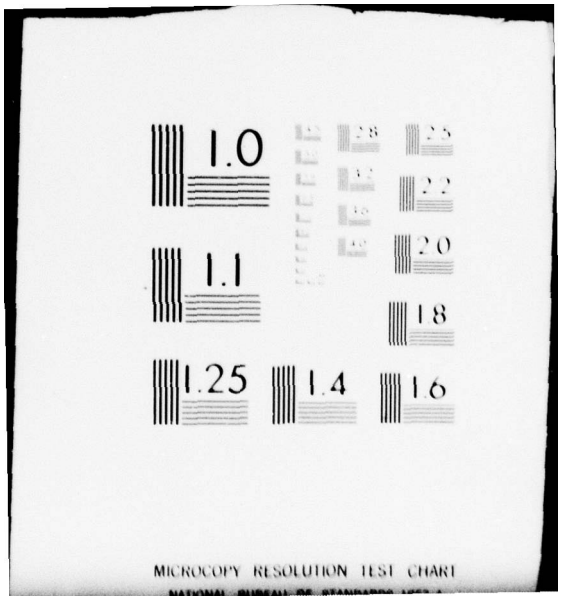
The two STD sections suggest that upwelling occurs as a result of subsurface ice melting. The temperature gradient in the upper 75 m makes the advection of cold water from depth visible in the upper layers. In a 100 m region surrounding the iceberg, anomalously cold water is found down to 40 m. This colder water results from the combination of cooling due to melting and advection of cold water from below, through the action of the convective boundary layer next to the ice. As the

AD-A071 809 WASHINGTON UNIV SEATTLE DEPT OF ATMOSPHERIC SCIENCES F/G 8/12
LAMINAR AND TURBULENT BOUNDARY LAYERS ADJACENT TO MELTING VERTI--ETC(U)
MAY 79 E G JOSBERGER N00014-76-C-0234
UNCLASSIFIED SCIENTIFIC-16 NL

3 OF 3
AD A071809



END
DATE FILMED
8-79
DDC


1.0
1.1
1.25
1.4
1.6
2.0
2.2
2.5
1.8
MICROCOPY RESOLUTION TEST CHART

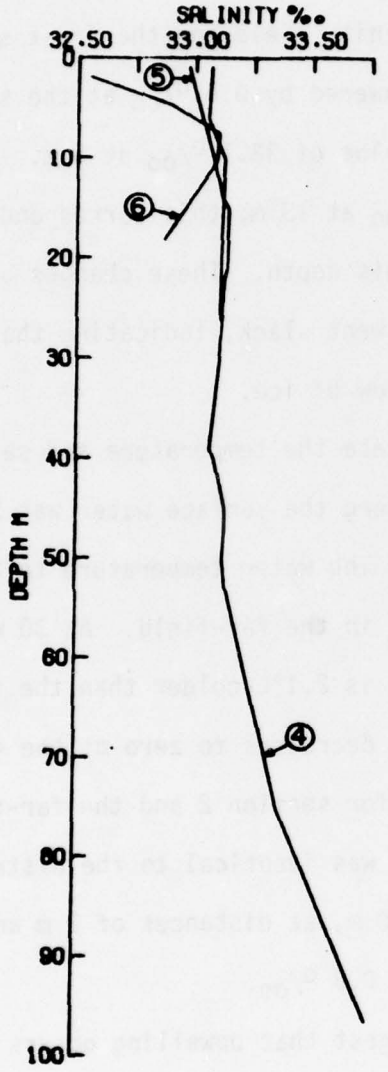


Fig. 29a. Salinity profiles from the first STD section.

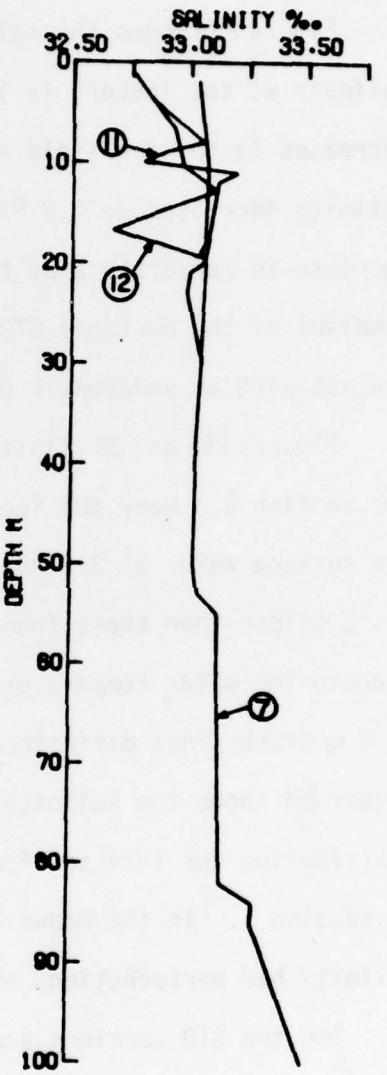


Fig. 29b. Salinity profiles from the second STD section.

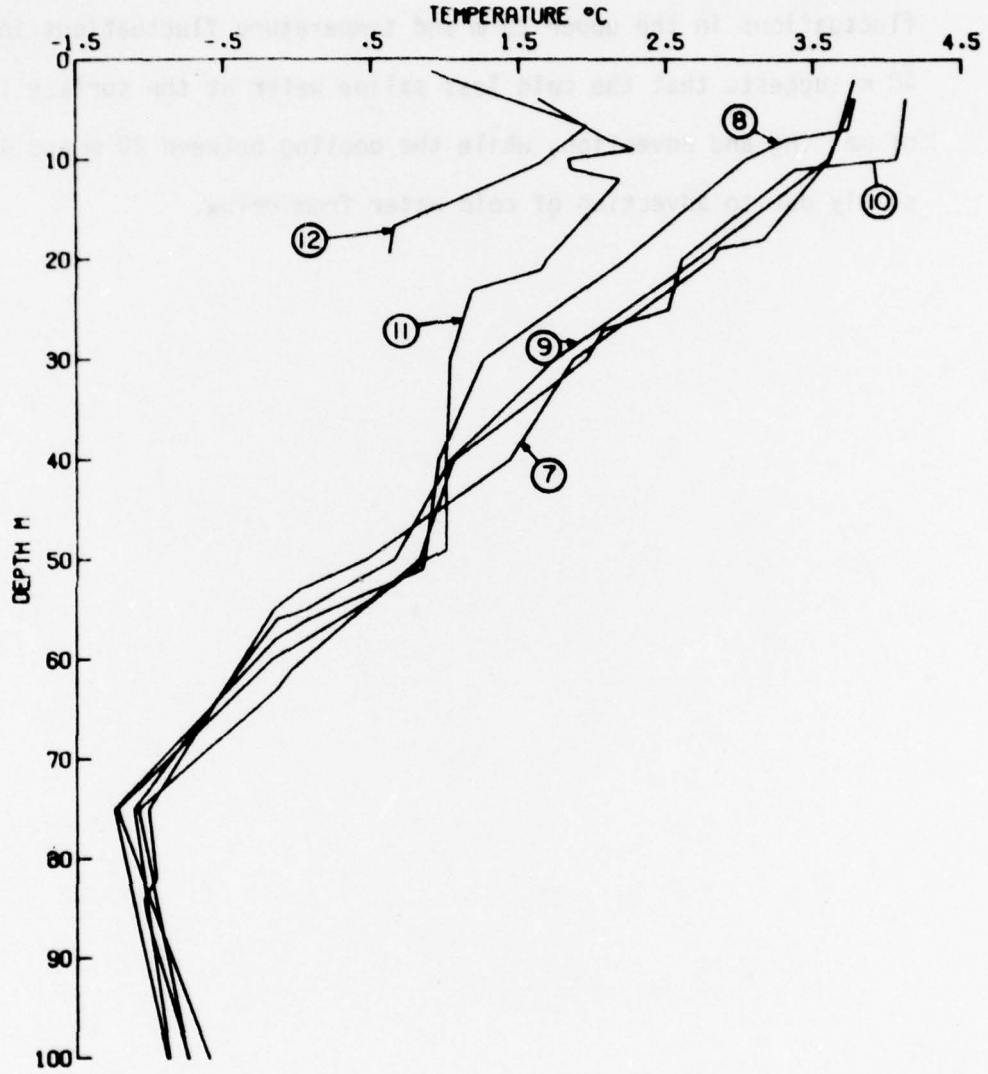


Figure 30. Temperature profiles from the second STD section.

salinity is uniformly almost distributed with depth, upward advection cannot be seen in the salinity sections; therefore, any salinity changes must be due to dilution by ice melting. The observation of salinity fluctuations in the upper 20 m and temperature fluctuations in the upper 40 m suggests that the cold less saline water at the surface is a result of melting and advection, while the cooling between 20 m and 40 m is solely due to advection of cold water from below.

APPENDIX IV

This appendix contains the tables of f'', f', f, ϕ', ϕ, θ' and θ generated by the numerical solution of the governing equations with the turbulent parameters determined by (114). Tables IV-1 through IV-6 contain the solutions for T_d from 2°C to 12°C in 2°C increments respectively. These solution retain both blowing at the interface and opposing buoyancy forces.

Tables IV-7 through IV-12 contain the solutions for T_d from 2°C to 12°C in 2°C increments respectively. These solutions retain blowing at the interface but density is only a function of salinity.

Tables IV-13, 14 and 15 contain the solutions for T_d = 2, 4, and 8°C with opposing buoyancy forces but no blowing at the interface.

Table IV-1

ETA	FZP	FP	F	PHIP	PHI	THETAP	THETA	BUOY
.0000	1.1755E-01	.0	-2.550E-04	-5.125E+00	1.000E+00	-5.301E-01	1.000E+00	6.881E+00
.0500	7.181E-02	4.579E-03	-1.314E-04	-5.594E+00	7.310E-01	-5.303E-01	9.735E-01	5.012E+00
.1000	4.355E-02	7.406E-03	1.737E-04	-5.214E+00	4.514E-01	-5.302E-01	9.470E-01	3.076E+00
.1500	2.719E-02	9.139E-03	5.906E-04	-2.859E+00	2.494E-01	-5.282E-01	9.205E-01	1.681E+00
.2000	1.838E-02	1.026E-02	1.079E-03	-1.384E+00	1.481E-01	-5.241E-01	8.942E-01	9.820E-01
.2500	1.284E-02	1.103E-02	1.611E-03	-7.301E-01	9.740E-02	-5.181E-01	8.681E-01	6.332E-01
.3000	9.151E-03	1.158E-02	2.177E-03	-4.264E-01	6.937E-02	-5.104E-01	8.424E-01	4.407E-01
.3500	6.515E-03	1.197E-02	2.766E-03	-2.714E-01	5.231E-02	-5.011E-01	8.171E-01	3.239E-01
.4000	4.545E-03	1.224E-02	3.372E-03	-1.843E-01	4.111E-02	-4.907E-01	7.923E-01	2.475E-01
.4500	3.024E-03	1.243E-02	3.989E-03	-1.317E-01	3.332E-02	-4.793E-01	7.681E-01	1.966E-01
.5000	1.822E-03	1.255E-02	4.613E-03	-9.806E-02	2.763E-02	-4.673E-01	7.444E-01	1.563E-01
.5500	-1.518E-03	1.262E-02	7.763E-03	-3.193E-02	1.340E-02	-4.049E-01	6.354E-01	6.221E-02
1.0000	-2.274E-03	1.194E-02	1.083E-02	-1.552E-02	7.825E-03	-3.490E-01	5.413E-01	2.749E-02
1.0500	-3.380E-03	1.115E-02	1.372E-02	-8.494E-03	4.817E-03	-3.021E-01	4.601E-01	1.061E-02
1.5000	-3.443E-03	1.029E-02	1.640E-02	-5.524E-03	3.116E-03	-2.623E-01	3.897E-01	1.604E-03
1.5500	-3.326E-03	9.436E-03	1.885E-02	-3.553E-03	2.001E-03	-2.277E-01	3.285E-01	-3.241E-03
2.0000	-3.078E-03	8.634E-03	2.112E-02	-2.312E-03	1.279E-03	-1.971E-01	2.755E-01	-5.670E-03
2.0500	-2.784E-03	7.900E-03	2.319E-02	-1.502E-03	8.092E-04	-1.697E-01	2.297E-01	-6.647E-03
2.5000	-2.492E-03	7.242E-03	2.508E-02	-9.671E-04	5.051E-04	-1.452E-01	1.904E-01	-6.754E-03
2.5500	-2.192E-03	6.659E-03	2.681E-02	-6.141E-04	3.105E-04	-1.234E-01	1.569E-01	-6.365E-03
3.0000	-1.928E-03	6.144E-03	2.841E-02	-3.938E-04	1.879E-04	-1.041E-01	1.285E-01	-5.722E-03
3.0500	-1.694E-03	5.692E-03	2.989E-02	-2.354E-04	1.118E-04	-8.716E-02	1.046E-01	-4.978E-03
3.5000	-1.498E-03	5.295E-03	3.125E-02	-1.423E-04	6.547E-05	-7.246E-02	8.473E-02	-4.227E-03
3.5500	-1.316E-03	4.945E-03	3.254E-02	-8.439E-05	3.772E-05	-5.983E-02	6.824E-02	-3.523E-03
4.0000	-1.168E-03	4.635E-03	3.374E-02	-4.919E-05	2.139E-05	-4.906E-02	5.466E-02	-2.893E-03
4.0500	-9.395E-04	4.111E-03	3.592E-02	-1.590E-05	6.577E-06	-3.235E-02	3.456E-02	-1.886E-03
5.0000	-7.784E-04	3.684E-03	3.784E-02	-4.826E-06	1.911E-06	-2.085E-02	2.144E-02	-1.189E-03
5.5000	-6.636E-04	3.325E-03	3.961E-02	-1.384E-06	5.472E-07	-1.315E-02	1.308E-02	-7.713E-04
6.0000	-5.797E-04	3.015E-03	4.120E-02	-3.763E-07	1.388E-07	-8.131E-03	7.848E-03	-4.407E-04
6.5000	-5.159E-04	2.742E-03	4.264E-02	-9.758E-08	3.520E-08	-4.940E-03	4.642E-03	-2.612E-04
7.0000	-4.654E-04	2.497E-03	4.394E-02	-2.420E-08	8.793E-09	-2.953E-03	2.708E-03	-1.526E-04
8.0000	-3.881E-04	2.073E-03	4.622E-02	-1.916E-09	6.263E-10	-1.011E-03	8.891E-04	-5.012E-05
9.0000	-3.289E-04	1.715E-03	4.811E-02	-8.831E-11	2.787E-11	-3.289E-04	2.796E-04	-1.577E-05
10.0000	-2.804E-04	1.411E-03	4.967E-02	-3.474E-12	1.059E-12	-1.027E-04	8.470E-05	-4.774E-06
11.0000	-2.395E-04	1.152E-03	5.095E-02	-1.177E-13	3.467E-14	-3.094E-05	2.474E-05	-1.395E-06
12.0000	-2.046E-04	9.302E-04	5.199E-02	-3.321E-15	9.252E-16	-9.035E-06	6.897E-06	-3.889E-07
13.0000	-1.748E-04	7.409E-04	5.282E-02	-6.864E-17	2.910E-18	-2.551E-06	1.754E-06	-9.888E-08
14.0000	-1.493E-04	5.792E-04	5.348E-02	-2.419E-19	-1.608E-17	-6.797E-07	3.291E-07	-1.856E-08
15.0000	-1.275E-04	4.411E-04	5.399E-02	7.160E-20	-1.301E-17	-1.522E-07	-3.212E-08	1.809E-09
16.0000	-1.089E-04	3.231E-04	5.437E-02	5.350E-21	-9.922E-18	-8.422E-09	-9.695E-08	5.467E-09
17.0000	-9.302E-05	2.224E-04	5.464E-02	2.803E-22	-7.965E-18	2.694E-08	-8.334E-08	4.698E-09
18.0000	-7.945E-05	1.363E-04	5.482E-02	1.271E-23	-6.008E-18	3.152E-08	-5.287E-08	2.978E-09
19.0000	-6.787E-05	6.279E-05	5.491E-02	5.751E-25	-4.051E-18	2.684E-08	-2.331E-08	1.312E-09
20.0000	-5.798E-05	2.598E-16	5.495E-02	2.981E-26	-1.877E-18	1.447E-08	3.123E-17	.0

Table IV-2

ETA	F2D	FD	F	PHIP	PHI	THETAP	THETA	BUOY
.0000	1.140E-01	.[illegible]	-5.83[illegible]E-04	-4.8[illegible]E+00	1.000E+00	-7.253E-01	1.000E+00	1.260E+01
.0500	7.252E-02	4.[illegible]E-03	-5.592E-04	-5.[illegible]E+00	7.[illegible]3E-01	-7.261E-01	9.637E-01	9.033E+00
.1000	4.825E-02	7.507E-03	-2.508E-04	-5.[illegible]E+00	3.840E-01	-7.259E-01	9.274E-01	4.736E+00
.1500	3.364E-02	9.467E-03	1.761E-04	-2.176E+00	1.914E-01	-7.197E-01	8.912E-01	2.296E+00
.2000	2.581E-02	1.096E-02	5.883E-04	-9.102E-01	1.204E-01	-7.036E-01	8.557E-01	1.400E+00
.2500	2.232E-02	1.219E-02	1.268E-03	-4.767E-01	8.[illegible]0E-02	-6.820E-01	8.210E-01	9.853E-01
.3000	1.901E-02	1.322E-02	1.904E-03	-2.890E-01	6.883E-02	-6.554E-01	7.875E-01	7.536E-01
.3500	1.640E-02	1.410E-02	2.597E-03	-1.932E-01	5.701E-02	-6.256E-01	7.555E-01	6.075E-01
.4000	1.427E-02	1.486E-02	3.312E-03	-1.383E-01	4.884E-02	-5.941E-01	7.250E-01	5.074E-01
.4500	1.246E-02	1.553E-02	4.072E-03	-1.042E-01	4.284E-02	-5.623E-01	6.961E-01	4.347E-01
.5000	1.091E-02	1.611E-02	4.863E-03	-8.165E-02	3.823E-02	-5.311E-01	6.688E-01	3.795E-01
.7500	5.495E-03	1.810E-02	9.168E-03	-3.447E-02	2.506E-02	-4.004E-01	5.533E-01	2.271E-01
1.0000	2.181E-03	1.903E-02	1.383E-02	-2.057E-02	1.845E-02	-3.156E-01	4.646E-01	1.555E-01
1.2500	1.475E-05	1.928E-02	1.868E-02	-1.438E-02	1.417E-02	-2.600E-01	3.931E-01	1.114E-01
1.5000	-1.438E-03	1.909E-02	2.343E-02	-1.088E-02	1.106E-02	-2.206E-01	3.332E-01	8.140E-02
1.7500	-2.403E-03	1.861E-02	2.815E-02	-8.493E-03	8.657E-03	-1.901E-01	2.820E-01	5.922E-02
2.0000	-3.035E-03	1.792E-02	3.272E-02	-6.766E-03	6.759E-03	-1.648E-01	2.378E-01	4.252E-02
2.2500	-3.410E-03	1.711E-02	3.710E-02	-5.411E-03	5.243E-03	-1.428E-01	1.994E-01	2.987E-02
2.5000	-3.600E-03	1.623E-02	4.127E-02	-4.312E-03	4.032E-03	-1.233E-01	1.662E-01	2.033E-02
2.7500	-3.656E-03	1.532E-02	4.521E-02	-3.410E-03	3.071E-03	-1.058E-01	1.376E-01	1.375E-02
3.0000	-3.616E-03	1.441E-02	4.893E-02	-2.686E-03	2.314E-03	-9.011E-02	1.131E-01	8.888E-03
3.2500	-3.512E-03	1.352E-02	5.242E-02	-2.064E-03	1.725E-03	-7.611E-02	9.235E-02	4.432E-03
3.5000	-3.398E-03	1.266E-02	5.569E-02	-1.576E-03	1.273E-03	-6.374E-02	7.490E-02	1.931E-03
3.7500	-3.193E-03	1.184E-02	5.875E-02	-1.184E-03	9.288E-04	-5.293E-02	6.035E-02	2.950E-04
4.0000	-3.009E-03	1.106E-02	6.161E-02	-8.863E-04	6.710E-04	-4.359E-02	4.832E-02	-7.077E-04
4.2500	-2.841E-03	1.669E-03	6.674E-02	-6.745E-04	3.400E-04	-2.884E-02	3.041E-02	-1.507E-03
5.0000	-2.298E-03	8.416E-03	7.129E-02	-2.435E-04	1.603E-04	-1.855E-02	1.873E-02	-1.479E-03
5.2500	-1.998E-03	7.344E-03	7.522E-02	-1.201E-04	7.878E-05	-1.162E-02	1.130E-02	-1.186E-03
6.0000	-1.736E-03	6.413E-03	7.865E-02	-5.723E-05	3.626E-05	-7.114E-03	6.702E-03	-8.253E-04
6.2500	-1.613E-03	5.902E-03	8.165E-02	-2.445E-05	1.627E-05	-4.269E-03	3.912E-03	-5.436E-04
7.0000	-1.323E-03	4.894E-03	8.427E-02	-1.190E-05	7.144E-06	-2.516E-03	2.252E-03	-3.409E-04
8.0000	-1.016E-03	3.732E-03	8.654E-02	-2.277E-06	1.305E-06	-9.363E-04	7.205E-04	-1.214E-04
9.0000	-7.831E-04	2.439E-03	9.183E-02	-3.983E-07	2.213E-07	-2.64AE-04	2.219E-04	-3.966E-05
10.0000	-6.042E-04	2.148E-03	9.430E-02	-6.541E-08	3.578E-08	-8.089E-05	6.643E-05	-1.225E-05
11.0000	-4.881E-04	1.916E-03	9.617E-02	-1.045E-08	5.573E-09	-2.407E-05	1.940E-05	-3.652E-06
12.0000	-3.563E-04	1.205E-03	9.754E-02	-1.602E-09	8.440E-10	-7.017E-06	5.608E-06	-1.062E-06
13.0000	-2.748E-04	8.890E-04	9.862E-02	-2.394E-10	1.252E-10	-2.014E-06	1.595E-06	-3.035E-07
14.0000	-2.132E-04	6.453E-04	9.938E-02	-3.527E-11	1.867E-11	-5.711E-07	4.493E-07	-8.570E-08
15.0000	-1.641E-04	4.577E-04	9.993E-02	-5.117E-12	2.698E-12	-1.605E-07	1.256E-07	-2.398E-08
16.0000	-1.243E-04	3.133E-04	1.003E-01	-7.356E-13	3.779E-13	-4.483E-08	3.480E-08	-6.657E-09
17.0000	-9.725E-05	2.021E-04	1.006E-01	-1.051E-13	5.372E-14	-1.244E-08	9.501E-09	-1.822E-09
18.0000	-7.495E-05	1.186E-04	1.007E-01	-1.494E-14	7.502E-15	-3.453E-09	2.480E-09	-4.740E-10
19.0000	-5.761E-05	5.[illegible]94E-05	1.008E-01	-2.120E-15	9.333E-16	-9.544E-10	5.367E-10	-1.088E-10
20.0000	-4.435E-05	-5.551E-17	1.008E-01	-3.000E-16	7.454E-19	-2.632E-10	.0	.0

Table IV-3

ETA	F2P	FP	F	DMIP	PHI	THETAP	THETA	MUOY
.0000	1.[illegible]E+01	.0	-1.[illegible]E-04	-3.[illegible]E+00	1.000E+00	-8.450E-01	1.000E+00	1.462E+01
.0500	7.[illegible]E-02	+.[illegible]E-03	-1.[illegible]E-03	-8.[illegible]E+00	7.450E-01	-8.469E-01	9.577E-01	1.228E+01
.1000	4.[illegible]E-02	1.[illegible]E-03	-3.[illegible]E-04	-8.701E+00	3.676E-01	-8.468E-01	9.153E-01	5.900E+00
.1500	3.[illegible]E-02	9.[illegible]E-03	-3.[illegible]E-04	-1.[illegible]E+00	1.706E-01	-8.328E-01	8.733E-01	2.499E+00
.2000	2.[illegible]E-02	1.[illegible]E-02	1.[illegible]E-04	-7.[illegible]E-01	1.147E-01	-8.041E-01	8.323E-01	1.468E+00
.2500	2.[illegible]E-02	1.[illegible]E-02	7.[illegible]E-04	-4.[illegible]E-01	8.637E-02	-7.647E-01	7.930E-01	1.201E+00
.3000	2.[illegible]E-02	1.[illegible]E-02	1.[illegible]E-03	-2.507E-01	7.035E-02	-7.174E-01	7.560E-01	9.405E-01
.3500	2.[illegible]E-02	1.[illegible]E-02	2.[illegible]E-03	-1.[illegible]E-01	6.005E-02	-6.675E-01	7.213E-01	7.752E-01
.4000	1.[illegible]E-02	1.[illegible]E-02	2.[illegible]E-03	-1.[illegible]E-01	5.204E-02	-6.177E-01	6.892E-01	6.415E-01
.4500	1.[illegible]E-02	1.[illegible]E-02	3.[illegible]E-03	-9.[illegible]E-02	4.[illegible]E-02	-5.700E-01	6.595E-01	5.[illegible]E-01
.5000	1.[illegible]E-02	1.[illegible]E-02	4.[illegible]E-03	-7.[illegible]E-02	4.331E-02	-5.258E-01	6.322E-01	5.153E-01
.5500	8.[illegible]E-03	2.[illegible]E-02	9.[illegible]E-03	-3.[illegible]E-02	3.104E-02	-3.632E-01	5.230E-01	3.780E-01
1.0000	[illegible]	[illegible]	1.[illegible]E-02	-2.[illegible]E-02	2.[illegible]E-02	-2.[illegible]E-01	4.[illegible]E-01	2.513E-01
1.5000	1.[illegible]E-03	2.[illegible]E-02	2.[illegible]E-02	-1.[illegible]E-02	2.[illegible]E-02	-2.[illegible]E-01	3.827E-01	1.959E-01
2.0000	3.[illegible]E-05	2.[illegible]E-02	2.[illegible]E-02	-1.[illegible]E-02	1.670E-02	-1.[illegible]E-01	3.314E-01	1.555E-01
2.5000	-1.[illegible]E-03	2.[illegible]E-02	3.[illegible]E-02	-1.[illegible]E-02	1.394E-02	-1.651E-01	2.872E-01	1.241E-01
3.0000	-2.[illegible]E-03	2.[illegible]E-02	3.[illegible]E-02	-[illegible]E-03	1.102E-02	-1.456E-01	2.484E-01	9.878E-02
3.5000	-3.[illegible]E-03	2.[illegible]E-02	4.[illegible]E-02	-7.[illegible]E-03	9.656E-03	-1.291E-01	2.141E-01	7.810E-02
4.0000	-3.[illegible]E-03	2.[illegible]E-02	4.[illegible]E-02	-[illegible]E-03	7.[illegible]E-03	-1.144E-01	1.837E-01	6.114E-02
4.5000	-3.[illegible]E-03	1.[illegible]E-02	5.[illegible]E-02	-5.[illegible]E-03	6.[illegible]E-03	-1.010E-01	1.568E-01	4.727E-02
5.0000	-4.[illegible]E-03	1.[illegible]E-02	5.[illegible]E-02	-4.[illegible]E-03	5.[illegible]E-03	-[illegible]E-02	1.332E-01	3.601E-02
5.5000	-4.[illegible]E-03	1.[illegible]E-02	5.[illegible]E-02	-3.[illegible]E-03	4.[illegible]E-03	-7.735E-02	1.124E-01	2.697E-02
6.0000	-4.[illegible]E-03	1.[illegible]E-02	5.[illegible]E-02	-3.[illegible]E-03	3.[illegible]E-03	-[illegible]E-02	9.439E-02	1.980E-02
6.5000	-4.[illegible]E-03	1.[illegible]E-02	7.[illegible]E-02	-2.[illegible]E-03	2.705E-03	-5.766E-02	7.883E-02	1.419E-02
7.0000	-3.[illegible]E-03	1.[illegible]E-02	7.[illegible]E-02	-2.[illegible]E-03	2.[illegible]E-03	-4.926E-02	6.548E-02	9.879E-03
7.5000	-3.[illegible]E-03	1.[illegible]E-02	8.[illegible]E-02	-1.[illegible]E-03	1.[illegible]E-03	-3.519E-02	4.452E-02	4.207E-03
8.0000	-3.[illegible]E-03	1.[illegible]E-02	8.[illegible]E-02	-[illegible]E-04	8.[illegible]E-04	-2.[illegible]E-02	2.972E-02	1.228E-03
8.5000	-2.[illegible]E-03	[illegible]	[illegible]	-5.[illegible]E-04	4.[illegible]E-04	-1.671E-02	1.952E-02	-1.[illegible]E-04
9.0000	-2.[illegible]E-03	[illegible]	[illegible]	-3.[illegible]E-04	2.[illegible]E-04	-1.[illegible]E-02	1.264E-02	-6.[illegible]E-04
9.5000	-2.[illegible]E-03	7.[illegible]E-03	1.[illegible]E-01	-1.[illegible]E-04	1.[illegible]E-04	-7.[illegible]E-03	8.077E-03	-7.[illegible]E-04
10.0000	-1.[illegible]E-03	[illegible]	1.[illegible]E-01	-1.[illegible]E-04	[illegible]	-4.[illegible]E-03	5.[illegible]E-03	-6.[illegible]E-04
10.5000	-1.[illegible]E-03	[illegible]	1.[illegible]E-01	-[illegible]E-05	2.[illegible]E-05	-1.[illegible]E-03	1.[illegible]E-03	-3.[illegible]E-04
11.0000	-1.[illegible]E-03	[illegible]	1.[illegible]E-01	-[illegible]E-05	[illegible]	-7.[illegible]E-04	7.[illegible]E-04	-1.[illegible]E-04
11.5000	-7.[illegible]E-04	[illegible]	1.[illegible]E-01	-2.[illegible]E-05	2.[illegible]E-05	-2.[illegible]E-04	2.[illegible]E-04	-8.[illegible]E-05
12.0000	-5.[illegible]E-04	[illegible]	1.[illegible]E-01	-[illegible]E-07	5.[illegible]E-07	-1.[illegible]E-04	1.[illegible]E-04	-3.[illegible]E-05
12.5000	-4.[illegible]E-04	1.[illegible]E-03	1.[illegible]E-01	-1.[illegible]E-07	1.[illegible]E-07	-3.[illegible]E-05	3.702E-05	-1.[illegible]E-05
13.0000	-3.[illegible]E-04	[illegible]	1.[illegible]E-01	-[illegible]E-08	[illegible]	-1.[illegible]E-05	1.337E-05	-4.[illegible]E-06
14.0000	-2.[illegible]E-04	[illegible]	1.[illegible]E-01	-[illegible]E-08	[illegible]	-4.[illegible]E-06	4.813E-06	-1.[illegible]E-06
15.0000	-1.[illegible]E-04	[illegible]	1.[illegible]E-01	-[illegible]E-09	[illegible]	-1.[illegible]E-06	1.727E-06	-6.[illegible]E-07
16.0000	-1.[illegible]E-04	[illegible]	1.[illegible]E-01	-[illegible]E-10	[illegible]	-[illegible]E-07	[illegible]	-2.[illegible]E-07
17.0000	-[illegible]E-05	[illegible]	1.[illegible]E-01	-2.[illegible]E-10	1.[illegible]E-10	-2.[illegible]E-07	2.155E-07	-[illegible]E-08
18.0000	-7.[illegible]E-05	[illegible]	1.[illegible]E-01	-[illegible]E-11	[illegible]	-[illegible]E-08	7.[illegible]	-2.[illegible]E-08
19.0000	-5.[illegible]E-05	[illegible]	1.[illegible]E-01	-1.[illegible]E-11	[illegible]	-[illegible]E-08	1.[illegible]	-7.[illegible]E-09
20.0000	-4.[illegible]E-05	1.[illegible]E-17	1.[illegible]E-01	-[illegible]E-12	-2.711E-19	-[illegible]E-08	-5.[illegible]	.0

Table IV-4

ETA	F2P	FP	F	PHIP	PHI	THETAP	THETA	BUOY
.0000	1.206E-01	.0	-1.920E-03	-2.776E+00	1.000E+00	-3.201E-01	1.000E+00	1.913E+01
.0300	7.768E-02	4.214E-03	-1.788E-03	-6.044E+00	7.889E-01	-9.233E-01	9.539E-01	1.495E+01
.1000	4.984E-02	8.018E-03	-1.453E-03	-7.384E+00	3.874E-01	-1.239E-01	9.077E-01	7.076E+00
.1300	3.815E-02	1.018E-02	-1.002E-03	-1.277E+00	1.856E-01	-9.042E-01	8.614E-01	3.162E+00
.2000	3.193E-02	1.192E-02	-4.479E-04	-7.897E-01	1.229E-01	-4.641E-01	8.176E-01	1.957E+00
.2300	2.770E-02	1.340E-02	1.486E-04	-4.153E-01	9.424E-02	-8.094E-01	7.757E-01	1.414E+00
.3000	2.446E-02	1.471E-02	8.894E-04	-2.555E-01	7.796E-02	-7.474E-01	7.368E-01	1.111E+00
.3300	2.183E-02	1.586E-02	1.655E-03	-1.736E-01	6.743E-02	-6.835E-01	7.010E-01	9.200E-01
.4000	1.959E-02	1.689E-02	2.473E-03	-1.264E-01	6.093E-02	-6.219E-01	6.684E-01	7.886E-01
.4300	1.765E-02	1.782E-02	3.342E-03	-9.681E-02	5.630E-02	-5.649E-01	6.387E-01	6.930E-01
.5000	1.594E-02	1.866E-02	4.254E-03	-7.706E-02	5.019E-02	-5.137E-01	6.118E-01	6.203E-01
.5300	9.624E-03	2.180E-02	9.345E-03	-3.513E-02	3.734E-02	-3.384E-01	5.078E-01	4.171E-01
1.0000	5.501E-03	2.365E-02	1.505E-02	-2.245E-02	3.038E-02	-2.508E-01	4.353E-01	3.174E-01
1.0300	2.641E-03	2.465E-02	2.110E-02	-1.478E-02	2.556E-02	-2.026E-01	3.792E-01	2.535E-01
1.1000	5.496E-04	2.504E-02	2.732E-02	-1.359E-02	2.180E-02	-1.724E-01	3.325E-01	2.062E-01
1.1300	-9.722E-04	2.498E-02	3.354E-02	-1.150E-02	1.808E-02	-1.512E-01	2.922E-01	1.689E-01
2.0000	-2.126E-03	2.458E-02	3.974E-02	-9.950E-03	1.600E-02	-1.347E-01	2.566E-01	1.383E-01
2.0300	-2.983E-03	2.394E-02	4.585E-02	-8.595E-03	1.368E-02	-1.208E-01	2.247E-01	1.128E-01
2.1000	-3.604E-03	2.311E-02	5.174E-02	-7.413E-03	1.184E-02	-1.085E-01	1.960E-01	9.130E-02
2.1300	-4.033E-03	2.215E-02	5.740E-02	-6.654E-03	9.453E-03	-9.727E-02	1.703E-01	7.327E-02
3.0000	-4.307E-03	2.111E-02	6.281E-02	-5.803E-03	8.302E-03	-8.687E-02	1.473E-01	5.819E-02
3.0300	-4.455E-03	2.001E-02	6.795E-02	-5.022E-03	6.930E-03	-7.714E-02	1.268E-01	4.584E-02
3.1000	-4.502E-03	1.889E-02	7.281E-02	-4.317E-03	5.794E-03	-6.818E-02	1.087E-01	3.578E-02
3.1300	-4.470E-03	1.777E-02	7.734E-02	-3.688E-03	4.786E-03	-5.985E-02	9.270E-02	2.698E-02
4.0000	-4.378E-03	1.666E-02	8.170E-02	-3.113E-03	3.937E-03	-5.222E-02	7.871E-02	2.020E-02
4.0300	-4.048E-03	1.454E-02	8.944E-02	-2.134E-03	2.621E-03	-4.401E-02	5.601E-02	1.061E-02
5.0000	-3.684E-03	1.260E-02	9.624E-02	-1.492E-03	1.711E-03	-2.851E-02	3.924E-02	4.374E-03
5.0300	-3.260E-03	1.088E-02	1.021E-01	-9.938E-04	1.076E-03	-2.041E-02	2.710E-02	1.664E-03
6.0000	-2.847E-03	9.334E-03	1.072E-01	-6.474E-04	6.917E-04	-1.435E-02	1.849E-02	6.425E-05
6.0300	-2.445E-03	8.007E-03	1.115E-01	-4.139E-04	4.303E-04	-9.939E-03	1.248E-02	-5.332E-04
7.0000	-2.124E-03	6.861E-03	1.152E-01	-2.604E-04	2.545E-04	-6.791E-03	8.340E-03	-9.114E-04
8.0000	-1.669E-03	5.028E-03	1.211E-01	-9.899E-05	9.679E-05	-3.066E-03	3.640E-03	-7.527E-04
9.0000	-1.154E-03	3.477E-03	1.254E-01	-3.604E-05	3.447E-05	-1.339E-03	1.551E-03	-4.513E-04
0.0000	-8.499E-04	2.583E-03	1.284E-01	-1.277E-05	1.178E-05	-5.700E-04	6.488E-04	-2.754E-04
1.0000	-6.274E-04	1.950E-03	1.303E-01	-4.414E-06	4.079E-06	-2.383E-04	2.680E-04	-1.174E-04
2.0000	-4.640E-04	1.494E-03	1.315E-01	-1.505E-06	1.391E-06	-9.435E-05	1.047E-04	-5.185E-05
3.0000	-3.437E-04	1.108E-03	1.323E-01	-5.137E-07	4.728E-07	-4.021E-05	4.455E-05	-2.288E-05
4.0000	-2.546E-04	7.112E-04	1.328E-01	-1.708E-07	1.637E-07	-1.635E-05	1.813E-05	-9.328E-06
5.0000	-1.890E-04	4.409E-04	1.332E-01	-5.817E-08	5.960E-08	-5.631E-06	7.362E-06	-4.128E-06
6.0000	-1.402E-04	3.276E-04	1.334E-01	-2.056E-08	2.323E-08	-2.698E-06	2.991E-06	-1.693E-06
7.0000	-1.041E-04	2.063E-04	1.335E-01	-8.094E-09	9.900E-09	-1.111E-06	1.205E-06	-6.704E-07
8.0000	-7.723E-05	1.163E-04	1.336E-01	-3.744E-09	4.403E-09	-4.584E-07	4.827E-07	-2.665E-07
9.0000	-5.732E-05	4.956E-05	1.336E-01	-2.061E-09	1.814E-09	-2.067E-07	1.434E-07	-7.137E-08
0.0000	-4.254E-05	3.990E-17	1.336E-01	-1.249E-09	-1.220E-19	-4.643E-08	.0	.0

Table IV-5

ETA	F2P	FP	F	PHIP	PHI	THETAP	THETA	BUOY
.0000	1.2578E-01	.0	-2.5901E-03	-1.8654E+00	1.0000E+00	-9.5008E-01	1.0000E+00	2.0488E+01
.0500	8.2055E-02	5.1598E-03	-2.4525E-03	-5.3755E+00	8.3326E-01	-9.5455E-01	9.5246E-01	1.6906E+01
.1000	5.2325E-02	7.4335E-03	-2.1045E-03	-8.0116E+00	4.6234E-01	-9.5596E-01	9.0465E-01	8.2496E+00
.1500	3.9746E-02	1.0698E-02	-1.6255E-03	-2.1415E+00	2.0696E-01	-9.3366E-01	8.5725E-01	3.4706E+00
.2000	3.3054E-02	1.2508E-02	-1.0446E-03	-8.4602E-01	1.3688E-01	-9.8746E-01	8.1165E-01	2.2616E+00
.2500	2.8573E-02	1.4037E-02	-3.7985E-04	-4.5478E-01	1.0758E-01	-9.2536E-01	7.6888E-01	1.6256E+00
.3000	2.5086E-02	1.5376E-02	3.5556E-04	-2.8045E-01	8.9078E-02	-7.5556E-01	7.2926E-01	1.2716E+00
.3500	2.2295E-02	1.6556E-02	1.1546E-03	-1.9146E-01	7.8096E-02	-6.8506E-01	6.9326E-01	1.0476E+00
.4000	1.9938E-02	1.7615E-02	2.0096E-03	-1.3976E-01	6.9926E-02	-6.1816E-01	6.6076E-01	8.9406E-01
.4500	1.7895E-02	1.8555E-02	2.9136E-03	-1.0726E-01	6.3806E-02	-5.5736E-01	6.3136E-01	7.8316E-01
.5000	1.6106E-02	1.9405E-02	3.8626E-03	-8.5526E-02	5.9026E-02	-5.0356E-01	6.0486E-01	6.9916E-01
.5500	1.4538E-02	2.0253E-02	9.1336E-03	-3.9346E-02	4.4706E-02	-3.6496E-01	5.0406E-01	4.6676E-01
1.0000	5.3396E-03	2.4436E-02	1.5026E-02	-2.5326E-02	3.6896E-02	-2.3896E-01	4.3476E-01	3.5446E-01
1.0500	2.4406E-03	2.6316E-02	2.1256E-02	-1.9056E-02	3.1436E-02	-1.9266E-01	3.8136E-01	2.9286E-01
1.1000	3.9256E-04	2.7646E-02	2.7636E-02	-1.5576E-02	2.7136E-02	-1.6426E-01	3.3696E-01	2.3006E-01
1.1500	-1.1376E-03	2.8556E-02	3.4046E-02	-1.3246E-02	2.3346E-02	-1.4456E-01	2.9856E-01	1.8856E-01
2.0000	-2.2796E-03	2.9126E-02	4.0346E-02	-1.1626E-02	2.0446E-02	-1.2936E-01	2.6436E-01	1.5456E-01
2.0500	-3.1276E-03	2.9446E-02	4.6546E-02	-1.0266E-02	1.7716E-02	-1.1676E-01	2.3366E-01	1.2626E-01
2.1000	-3.7416E-03	2.9586E-02	5.2546E-02	-9.0946E-03	1.5296E-02	-1.0566E-01	2.0586E-01	1.0236E-01
2.1500	-4.1566E-03	2.9586E-02	5.8356E-02	-8.0626E-03	1.3156E-02	-9.5496E-02	1.8076E-01	8.2156E-02
3.0000	-4.4376E-03	2.9516E-02	6.3976E-02	-7.1206E-03	1.1256E-02	-8.6046E-02	1.5806E-01	6.5266E-02
3.0500	-4.5826E-03	2.9386E-02	6.9406E-02	-6.2546E-03	9.5026E-03	-7.7226E-02	1.3766E-01	5.1166E-02
3.1000	-4.6276E-03	2.9226E-02	7.4656E-02	-5.4656E-03	8.1196E-03	-6.8946E-02	1.1946E-01	3.9506E-02
3.1500	-4.5976E-03	2.9036E-02	7.9716E-02	-4.7436E-03	6.8446E-03	-6.1226E-02	1.0316E-01	2.9956E-02
4.0000	-4.4976E-03	2.8936E-02	8.3096E-02	-4.0906E-03	5.7416E-03	-5.4066E-02	8.8736E-02	2.2216E-02
4.0000	-4.2036E-03	2.8756E-02	9.1006E-02	-2.3826E-03	3.9846E-03	-4.1456E-02	6.4946E-02	1.1146E-02
5.0000	-3.7886E-03	2.8256E-02	9.7876E-02	-2.1236E-03	2.7146E-03	-3.1146E-02	4.6886E-02	4.4456E-03
5.5000	-3.3456E-03	2.8976E-02	1.0386E-01	-1.4776E-03	1.8656E-03	-2.3906E-02	3.3436E-02	8.8486E-04
6.0000	-2.9146E-03	2.9406E-02	1.0896E-01	-1.0116E-03	1.2106E-03	-1.6706E-02	2.3586E-02	-1.2036E-03
6.5000	-2.5156E-03	2.9516E-02	1.1326E-01	-6.7936E-04	7.9206E-04	-1.1966E-02	1.6476E-02	-1.9706E-03
7.0000	-2.1596E-03	2.9446E-02	1.1706E-01	-4.5016E-04	5.1326E-04	-8.4626E-03	1.1416E-02	-2.1126E-03
8.0000	-1.5956E-03	2.9276E-02	1.2296E-01	-1.9046E-04	2.1016E-04	-4.1046E-03	5.3606E-03	-1.6446E-03
9.0000	-1.1566E-03	2.8966E-02	1.2726E-01	-7.7946E-05	8.3036E-05	-1.9376E-03	2.4726E-03	-1.0256E-03
10.0000	-8.6456E-04	2.8756E-02	1.3036E-01	-3.1046E-05	3.2806E-05	-8.9346E-04	1.1216E-03	-5.7176E-04
11.0000	-6.2286E-04	2.8476E-02	1.3266E-01	-1.2136E-05	1.2056E-05	-4.0556E-04	5.0236E-04	-2.9826E-04
12.0000	-4.6036E-04	2.8096E-02	1.3436E-01	-4.5716E-06	4.4676E-06	-1.8196E-04	2.2326E-04	-1.4876E-04
13.0000	-3.4146E-04	2.7616E-02	1.3556E-01	-1.7816E-06	1.6686E-06	-8.0896E-05	9.8476E-05	-7.1766E-05
14.0000	-2.5386E-04	2.7016E-02	1.3636E-01	-6.7446E-07	6.8776E-07	-3.5756E-05	4.3176E-05	-3.3786E-05
15.0000	-1.8916E-04	2.6336E-02	1.3696E-01	-2.5406E-07	2.5716E-07	-1.5736E-05	1.8776E-05	-1.5556E-05
15.0000	-1.4106E-04	2.5596E-02	1.3746E-01	-9.5346E-08	9.5166E-08	-6.9046E-06	8.0516E-06	-6.9756E-06
17.0000	-1.0526E-04	2.4826E-02	1.3776E-01	-3.5716E-08	3.4436E-08	-3.0246E-06	3.5506E-06	-3.0086E-06
18.0000	-7.9556E-05	2.4046E-02	1.3796E-01	-1.3356E-08	1.2696E-08	-1.3236E-06	1.2936E-06	-1.1946E-06
19.0000	-5.9476E-05	2.3286E-02	1.3796E-01	-5.0026E-09	3.1876E-09	-5.7836E-07	3.9346E-07	-3.7076E-07
20.0000	-4.4736E-05	.0	1.3796E-01	-1.8766E-09	-5.4216E-10	-2.5296E-07	-6.9396E-10	.0

Table IV-6

ETA	F2P	FP	F	PHIP	PHI	THETAP	THETA	MUOY
.0000	1.2[illegible]E-01	.0	-3.2205E-03	-1.3615E+00	1.0000E+00	-7.8138E-01	1.0000E+00	2.1122E+01
.0200	8.4568E-02	5.2495E-03	-3.0778E-03	-4.7116E+00	8.8846E-01	-9.6708E-01	9.5188E-01	1.8168E+01
.0400	5.[illegible]E-02	[illegible]E-03	-2.7238E-03	-8.5148E+00	6.6108E-01	-1.0937E+00	9.0338E-01	9.1398E+00
.0600	4.[illegible]E-02	1.[illegible]E-02	-2.2305E-03	-2.2908E+00	2.2062E-01	-1.4498E-01	8.5538E-01	4.0508E+00
.0800	3.2455E-02	1.2765E-02	-1.6356E-03	-4.2556E-01	1.5531E-01	-8.9437E-01	8.0938E-01	2.4788E+00
.0900	2.5215E-02	1.4288E-02	-1.5458E-04	-4.9146E-01	1.2146E-01	-1.2667E-01	7.6628E-01	1.7688E+00
.1000	2.0454E-02	1.5805E-02	-2.1056E-04	-5.0658E-01	1.0621E-01	-7.5156E-01	7.2678E-01	1.3728E+00
.1200	2.1745E-02	1.6745E-02	5.9945E-04	-2.0381E-01	8.9531E-02	-5.7691E-01	6.9108E-01	1.1238E+00
.1400	1.[illegible]E-02	1.7745E-02	1.4635E-03	-1.5227E-01	8.0026E-02	-5.0649E-01	6.5908E-01	9.5378E-01
.1500	1.7245E-02	1.8205E-02	2.3735E-03	-1.1715E-01	7.3955E-02	-5.4405E-01	6.3026E-01	8.3178E-01
.1700	1.5425E-02	1.8515E-02	3.3315E-03	-9.1546E-02	6.8726E-02	-4.8916E-01	6.0446E-01	7.3906E-01
.1900	8.2715E-03	2.2485E-02	8.6115E-03	-4.1435E-02	5.3016E-02	-3.1106E-01	5.0736E-01	4.8676E-01
1.0000	4.7565E-03	2.4145E-02	1.4465E-02	-2.4106E-02	4.4376E-02	-2.2726E-01	4.4116E-01	3.6616E-01
1.0200	1.3245E-03	2.4965E-02	2.0615E-02	-2.1245E-02	3.8629E-02	-1.8356E-01	3.9036E-01	2.9016E-01
1.0300	1.5646E-05	2.5205E-02	2.5405E-02	-1.7536E-02	3.3476E-02	-1.5646E-01	3.4806E-01	2.3476E-01
1.0500	-1.4275E-03	2.5025E-02	3.3135E-02	-1.5046E-02	2.9426E-02	-1.3866E-01	3.1116E-01	1.9136E-01
2.0000	-2.4465E-03	2.4525E-02	3.9145E-02	-1.1316E-02	2.5086E-02	-1.2646E-01	2.7836E-01	1.5596E-01
2.0200	-3.2965E-03	2.3795E-02	4.5625E-02	-1.1886E-02	2.2736E-02	-1.1346E-01	2.4856E-01	1.2646E-01
2.0300	-3.6496E-03	2.2485E-02	5.1256E-02	-1.0656E-02	1.9926E-02	-1.0356E-01	2.2146E-01	1.0166E-01
2.0500	-4.2356E-03	2.1885E-02	5.6456E-02	-9.5576E-03	1.7406E-02	-9.4396E-02	1.9676E-01	8.0756E-02
3.0000	-4.4746E-03	2.0175E-02	5.2136E-02	-8.5586E-03	1.5146E-02	-8.5906E-02	1.7426E-01	6.3236E-02
3.0200	-4.5946E-03	1.8655E-02	5.7256E-02	-7.8396E-03	1.3116E-02	-7.7436E-02	1.5376E-01	4.9616E-02
3.0300	-4.6136E-03	1.8505E-02	7.2026E-02	-6.7726E-03	1.1316E-02	-7.0396E-02	1.3526E-01	3.8516E-02
3.0500	-4.5676E-03	1.8355E-02	7.6506E-02	-5.8706E-03	9.7226E-03	-6.3306E-02	1.1856E-01	2.9616E-02
4.0000	-4.4596E-03	1.8225E-02	8.0706E-02	-5.2646E-03	8.3206E-03	-5.6656E-02	1.0356E-01	1.8596E-02
4.0200	-4.1406E-03	1.8065E-02	8.4826E-02	-3.3746E-03	6.0246E-03	-4.4716E-02	7.8256E-02	7.1636E-03
5.0000	-3.7286E-03	1.7045E-02	9.4726E-02	-2.0556E-03	4.3016E-03	-3.4696E-02	5.8486E-02	3.5806E-04
5.0200	-3.2716E-03	1.6345E-02	1.0046E-01	-2.1556E-03	3.0326E-03	-2.6506E-02	4.3256E-02	-3.7116E-03
5.0400	-2.[illegible]E-03	1.[illegible]E-02	1.0526E-01	-1.5946E-03	2.1146E-03	-1.9946E-02	3.1706E-02	-4.9546E-03
5.0500	-2.4216E-03	1.5065E-02	1.0926E-01	-1.0946E-03	1.4596E-03	-1.4856E-02	2.3066E-02	-5.7756E-03
7.0000	-2.[illegible]E-03	5.[illegible]E-03	1.1276E-01	-7.4476E-04	9.9926E-04	-1.0946E-02	1.6856E-02	-5.1116E-03
8.0000	-1.6956E-03	4.4276E-03	1.1426E-01	-3.6206E-04	4.5896E-04	-5.7776E-03	8.5446E-03	-3.8026E-03
9.0000	-1.[illegible]E-03	3.[illegible]E-03	1.1516E-01	-1.6576E-04	2.0966E-04	-2.9796E-03	4.3116E-03	-2.6606E-03
10.0000	-7.7246E-04	2.6446E-03	1.1566E-01	-7.5046E-05	9.1356E-05	-1.5096E-03	2.1486E-03	-1.6496E-03
11.0000	-5.[illegible]E-04	1.7926E-03	1.1596E-01	-3.3246E-05	4.0116E-05	-7.5246E-04	1.0606E-03	-8.3236E-04
12.0000	-4.1476E-04	1.2476E-03	1.1606E-01	-1.4546E-05	1.7436E-05	-3.7226E-04	5.1896E-04	-4.5646E-04
13.0000	-3.[illegible]E-04	9.[illegible]E-04	1.1616E-01	-5.3406E-06	7.5286E-06	-1.8276E-04	2.5256E-04	-2.4146E-04
14.0000	-2.3146E-04	6.7046E-04	1.1626E-01	-2.7406E-06	3.6356E-06	-8.9206E-05	1.2216E-04	-1.2576E-04
15.0000	-1.7396E-04	4.7006E-04	1.1636E-01	-1.1806E-06	1.5836E-06	-4.3416E-05	5.8476E-05	-6.7546E-05
16.0000	-1.4176E-04	3.1846E-04	1.1646E-01	-5.0816E-07	5.8546E-07	-2.1086E-05	2.7586E-05	-3.1756E-05
17.0000	-9.[illegible]E-05	2.[illegible]E-04	1.1656E-01	-2.1926E-07	2.4196E-07	-1.0236E-05	1.2556E-05	-1.4406E-05
18.0000	-7.5476E-05	1.1676E-04	1.1666E-01	-9.5156E-08	9.3356E-08	-4.9686E-06	5.2636E-06	-6.3796E-06
19.0000	-5.[illegible]E-05	5.[illegible]E-05	1.1676E-01	-4.1756E-08	2.8506E-08	-2.4176E-06	1.7246E-06	-2.1316E-06
20.0000	-4.[illegible]E-05	.0	1.1686E-01	-1.8616E-08	.0	-1.1796E-06	-2.7766E-17	.0

Table IV-7

ETA	F2P	FP	F	PHIP	PHI	THETAP	THETA	BUOY
.0000	1.177E-01	.0	-2.550E-04	-5.194E+00	1.000E+00	-5.852E-01	1.000E+00	6.975E+00
.0500	7.549E-02	4.775E-03	-1.269E-04	-5.669E+00	7.274E-01	-5.854E-01	9.707E-01	5.073E+00
.1000	4.693E-02	7.778E-03	1.930E-04	-5.256E+00	4.448E-01	-5.852E-01	9.415E-01	3.102E+00
.1500	3.067E-02	9.677E-03	5.327E-04	-2.856E+00	2.419E-01	-5.830E-01	9.122E-01	1.687E+00
.2000	2.142E-02	1.096E-02	1.151E-03	-1.364E+00	1.412E-01	-5.785E-01	8.832E-01	9.947E-01
.2500	1.607E-02	1.190E-02	1.723E-03	-7.153E-01	9.129E-02	-5.718E-01	8.544E-01	6.367E-01
.3000	1.235E-02	1.260E-02	2.334E-03	-4.145E-01	6.394E-02	-5.631E-01	8.261E-01	4.460E-01
.3500	9.670E-03	1.315E-02	2.981E-03	-2.614E-01	4.744E-02	-5.527E-01	7.982E-01	3.309E-01
.4000	7.644E-03	1.358E-02	3.649E-03	-1.761E-01	3.670E-02	-5.409E-01	7.708E-01	2.560E-01
.4500	6.058E-03	1.392E-02	4.337E-03	-1.249E-01	2.928E-02	-5.281E-01	7.441E-01	2.042E-01
.5000	4.783E-03	1.419E-02	5.040E-03	-9.224E-02	2.391E-02	-5.145E-01	7.180E-01	1.667E-01
.5500	1.002E-03	1.485E-02	8.689E-03	-2.863E-02	1.076E-02	-4.433E-01	5.983E-01	7.503E-02
1.0000	-8.022E-04	1.485E-02	1.241E-02	-1.331E-02	5.847E-03	-3.786E-01	4.957E-01	4.078E-02
1.0500	-1.741E-03	1.452E-02	1.609E-02	-7.242E-03	3.376E-03	-3.232E-01	4.082E-01	2.355E-02
1.1000	-2.226E-03	1.401E-02	1.965E-02	-4.224E-03	1.981E-03	-2.755E-01	3.335E-01	1.382E-02
1.1500	-2.452E-03	1.342E-02	2.309E-02	-2.522E-03	1.157E-03	-2.336E-01	2.699E-01	8.070E-03
1.2000	-2.528E-03	1.280E-02	2.635E-02	-1.503E-03	6.645E-04	-1.963E-01	2.163E-01	4.735E-03
1.2500	-2.517E-03	1.217E-02	2.944E-02	-8.916E-04	3.728E-04	-1.631E-01	1.714E-01	2.800E-03
1.3000	-2.457E-03	1.154E-02	3.245E-02	-5.046E-04	2.035E-04	-1.339E-01	1.344E-01	1.619E-03
1.3500	-2.372E-03	1.094E-02	3.524E-02	-2.805E-04	1.078E-04	-1.085E-01	1.042E-01	7.522E-04
1.4000	-2.274E-03	1.036E-02	3.792E-02	-1.510E-04	5.543E-05	-8.668E-02	7.986E-02	3.864E-04
1.4500	-2.171E-03	9.804E-03	4.044E-02	-7.866E-05	2.762E-05	-6.835E-02	6.055E-02	1.927E-04
1.5000	-2.068E-03	9.274E-03	4.282E-02	-3.963E-05	1.335E-05	-5.320E-02	4.542E-02	9.311E-05
1.5500	-1.968E-03	8.770E-03	4.508E-02	-1.932E-05	6.263E-06	-4.087E-02	3.372E-02	4.368E-05
1.6000	-1.870E-03	8.290E-03	4.721E-02	-9.121E-06	2.857E-06	-3.102E-02	2.478E-02	1.992E-05
1.6500	-1.687E-03	7.401E-03	5.113E-02	-1.886E-06	5.498E-07	-1.723E-02	1.301E-02	3.835E-06
1.7000	-1.518E-03	6.601E-03	5.463E-02	-3.415E-07	9.407E-08	-9.177E-03	6.595E-03	6.561E-07
1.7500	-1.365E-03	5.881E-03	5.774E-02	-5.574E-08	1.463E-08	-4.703E-03	3.238E-03	1.021E-07
1.8000	-1.226E-03	5.233E-03	6.052E-02	-8.285E-09	2.097E-09	-2.328E-03	1.545E-03	1.463E-08
1.8500	-1.100E-03	4.653E-03	6.299E-02	-1.133E-09	2.891E-10	-1.117E-03	7.188E-04	2.019E-09
1.9000	-9.855E-04	4.132E-03	6.519E-02	-1.438E-10	4.826E-11	-5.214E-04	3.271E-04	3.399E-10
1.9500	-7.897E-04	3.247E-03	6.885E-02	-2.245E-11	4.869E-12	-1.075E-04	6.410E-05	3.399E-11
2.0000	-6.311E-04	2.540E-03	7.174E-02	-2.373E-13	4.968E-14	-2.018E-05	1.162E-05	.0
2.0500	-5.034E-04	1.975E-03	7.399E-02	-1.367E-15	2.930E-16	-3.564E-06	1.998E-06	.0
2.1000	-4.009E-04	1.525E-03	7.572E-02	-1.173E-17	8.348E-18	-5.998E-07	3.294E-07	.0
2.1500	-3.199E-04	1.166E-03	7.706E-02	-1.827E-19	4.879E-18	-9.720E-08	5.243E-08	.0
2.2000	-2.535E-04	8.814E-04	7.809E-02	-2.791E-21	4.662E-18	-1.524E-08	8.082E-09	.0
2.2500	-2.015E-04	6.549E-04	7.884E-02	-3.365E-23	4.120E-18	-2.295E-09	1.218E-09	.0
2.3000	-1.600E-04	4.750E-04	7.941E-02	-3.196E-25	3.361E-18	-3.242E-10	2.038E-10	.0
2.3500	-1.271E-04	3.320E-04	7.981E-02	-2.325E-27	2.602E-18	-4.501E-11	6.233E-11	.0
2.4000	-1.009E-04	2.185E-04	8.009E-02	-9.149E-30	2.060E-18	-1.392E-11	3.774E-11	.0
2.4500	-8.014E-05	1.284E-04	8.025E-02	8.622E-32	1.301E-18	-1.312E-11	2.378E-11	.0
2.5000	-6.364E-05	5.684E-05	8.034E-02	2.850E-33	7.589E-19	-1.224E-11	1.030E-11	.0
2.5500	-5.054E-05	2.082E-17	8.037E-02	7.356E-35	.0	-7.962E-12	-6.668E-19	.0

Table IV-8

ETA	F2P	FP	F	PHIP	PHI	THETAP	THETA	BUOY
.0000	1.207E-01	.0	-6.830E-04	-4.907E+00	1.000E+00	-7.711E-01	1.000E+00	1.281E+01
.0500	7.647E-02	4.922E-03	-5.511E-04	-6.395E+00	7.178E-01	-7.720E-01	9.614E-01	9.195E+00
.1000	5.171E-02	4.106E-03	-2.199E-04	-6.087E+00	3.776E-01	-7.719E-01	9.228E-01	4.837E+00
.1500	3.477E-02	1.033E-02	2.437E-04	-2.164E+00	1.850E-01	-7.540E-01	8.844E-01	2.370E+00
.2000	3.166E-02	1.209E-02	8.053E-04	-8.093E-01	1.146E-01	-7.478E-01	8.466E-01	1.468E+00
.2500	2.891E-02	1.353E-02	1.446E-03	-4.685E-01	8.204E-02	-7.247E-01	8.097E-01	1.051E+00
.3000	2.336E-02	1.479E-02	2.155E-03	-2.927E-01	6.303E-02	-6.962E-01	7.742E-01	8.177E-01
.3500	2.048E-02	1.588E-02	2.922E-03	-1.881E-01	5.230E-02	-6.642E-01	7.402E-01	6.700E-01
.4000	1.810E-02	1.684E-02	3.741E-03	-1.342E-01	4.436E-02	-6.304E-01	7.078E-01	5.682E-01
.4500	1.606E-02	1.770E-02	4.605E-03	-1.007E-01	3.855E-02	-5.962E-01	6.771E-01	4.938E-01
.5000	1.428E-02	1.845E-02	5.509E-03	-7.864E-02	3.410E-02	-5.627E-01	6.482E-01	4.368E-01
.5500	7.821E-03	2.115E-02	1.049E-02	-3.255E-02	2.152E-02	-4.215E-01	5.262E-01	2.756E-01
1.0000	3.706E-03	2.255E-02	1.598E-02	-1.907E-02	1.532E-02	-3.294E-01	4.331E-01	1.983E-01
1.5000	9.143E-04	2.311E-02	2.170E-02	-1.303E-02	1.139E-02	-2.684E-01	3.589E-01	1.459E-01
1.5000	-1.019E-03	2.308E-02	2.748E-02	-9.604E-03	8.597E-03	-2.245E-01	2.976E-01	1.101E-01
1.5500	-2.341E-03	2.265E-02	3.320E-02	-7.324E-03	6.497E-03	-1.907E-01	2.459E-01	8.323E-02
2.0000	-3.271E-03	2.194E-02	3.878E-02	-5.659E-03	4.884E-03	-1.618E-01	2.019E-01	6.256E-02
2.5000	-3.859E-03	2.104E-02	4.415E-02	-4.371E-03	3.637E-03	-1.371E-01	1.647E-01	4.659E-02
2.5000	-4.206E-03	2.003E-02	4.923E-02	-3.351E-03	2.676E-03	-1.155E-01	1.331E-01	3.428E-02
2.5500	-4.372E-03	1.895E-02	5.415E-02	-2.534E-03	1.944E-03	-9.635E-02	1.067E-01	2.490E-02
3.0000	-4.407E-03	1.785E-02	5.877E-02	-1.896E-03	1.393E-03	-7.959E-02	8.476E-02	1.784E-02
3.5000	-4.348E-03	1.676E-02	6.309E-02	-1.394E-03	9.841E-04	-6.503E-02	6.673E-02	1.281E-02
3.5000	-4.224E-03	1.568E-02	6.714E-02	-1.009E-03	6.859E-04	-5.255E-02	5.207E-02	8.786E-03
3.5500	-4.057E-03	1.465E-02	7.093E-02	-7.190E-04	4.716E-04	-4.202E-02	4.029E-02	6.041E-03
4.0000	-3.866E-03	1.366E-02	7.447E-02	-5.044E-04	3.201E-04	-3.324E-02	3.092E-02	4.100E-03
4.5000	-3.446E-03	1.183E-02	8.083E-02	-2.370E-04	1.421E-04	-2.019E-02	1.779E-02	1.821E-03
5.0000	-3.030E-03	1.021E-02	8.633E-02	-1.054E-04	6.046E-05	-1.183E-02	9.948E-03	7.745E-04
5.5000	-2.642E-03	8.793E-03	9.108E-02	-4.510E-05	2.473E-05	-5.710E-03	5.422E-03	3.168E-04
6.0000	-2.293E-03	7.561E-03	9.515E-02	-1.845E-05	9.773E-06	-3.701E-03	2.888E-03	1.252E-04
6.5000	-1.985E-03	6.493E-03	9.867E-02	-7.293E-06	3.746E-06	-1.990E-03	1.506E-03	4.799E-05
7.0000	-1.714E-03	5.570E-03	1.017E-01	-2.795E-06	1.396E-06	-1.047E-03	7.707E-04	1.788E-05
8.0000	-1.274E-03	4.086E-03	1.065E-01	-3.772E-07	1.793E-07	-2.762E-04	1.900E-04	2.297E-06
9.0000	-9.435E-04	2.985E-03	1.100E-01	-4.543E-08	2.117E-08	-6.596E-05	4.216E-05	2.712E-07
10.0000	-6.970E-04	2.171E-03	1.125E-01	-5.280E-09	2.411E-09	-1.414E-05	8.142E-06	3.089E-08
11.0000	-5.140E-04	1.570E-03	1.144E-01	-5.885E-10	2.639E-10	-2.549E-06	1.263E-06	3.379E-09
12.0000	-3.786E-04	1.127E-03	1.157E-01	-6.297E-11	2.804E-11	-3.528E-07	1.229E-07	3.403E-10
13.0000	-2.786E-04	8.009E-04	1.167E-01	-6.600E-12	2.918E-12	-2.424E-08	-1.261E-09	4.079E-11
14.0000	-2.050E-04	5.810E-04	1.174E-01	-6.807E-13	2.994E-13	8.678E-09	-1.275E-09	6.798E-12
15.0000	-1.507E-04	3.946E-04	1.178E-01	-6.938E-14	3.040E-14	5.357E-09	-5.205E-09	.0
16.0000	-1.109E-04	2.548E-04	1.181E-01	-7.014E-15	3.049E-15	2.001E-09	-1.703E-09	.0
17.0000	-8.144E-05	1.595E-04	1.183E-01	-7.050E-16	2.888E-16	6.326E-10	-4.978E-10	.0
18.0000	-5.986E-05	8.939E-05	1.185E-01	-7.056E-17	1.945E-17	1.834E-10	-1.315E-10	.0
19.0000	-4.400E-05	3.787E-05	1.185E-01	-7.034E-18	2.602E-18	5.041E-11	-2.774E-11	.0
20.0000	-3.234E-05	-5.551E-17	1.185E-01	-6.624E-19	8.674E-19	1.287E-11	.0	.0

Table IV-9

ETA	F2P	FP	F	PHIP	PHI	THETAP	THETA	BUOY
.0000	1.2[illegible]E-01	.0	-1.240E-03	-3.985E+00	1.000E+00	-9.064E-01	1.000E+00	1.497E+01
.0200	8.30[illegible]E-02	5.177E-03	-1.102E-03	-6.534E+00	7.409E-01	-9.084E-01	9.546E-01	1.257E+01
.1000	5.5[illegible]E-02	8.575E-03	-7.522E-04	-8.726E+00	3.597E-01	-9.083E-01	9.092E-01	6.105E+00
.1200	4.4045E-02	1.104E-02	-2.593E-04	-1.926E+00	1.690E-01	-8.931E-01	8.641E-01	2.368E+00
.2000	3.74[illegible]E-02	1.306E-02	3.444E-04	-7.70[illegible]E-01	1.077E-01	-8.622E-01	8.201E-01	1.927E+00
.2200	3.2[illegible]E-02	1.481E-02	1.043E-03	-4.014E-01	7.980E-02	-8.191E-01	7.781E-01	1.754E+00
.3000	2.9[illegible]E-02	1.636E-02	1.823E-03	-2.650E-01	5.411E-02	-7.695E-01	7.383E-01	1.688E+00
.3200	2.624E-02	1.775E-02	2.678E-03	-1.950E-01	5.406E-02	-7.145E-01	7.013E-01	9.174E-01
.4000	2.3[illegible]E-02	1.[illegible]E-02	3.534E-03	-1.192E-01	4.705E-02	-6.606E-01	6.669E-01	7.985E-01
.4200	2.142E-02	2.012E-02	4.573E-03	-9.053E-02	4.106E-02	-6.090E-01	6.352E-01	7.104E-01
.5000	1.940E-02	2.114E-02	5.605E-03	-7.151E-02	3.704E-02	-5.611E-01	6.059E-01	6.421E-01
.5200	1.175E-02	2.498E-02	1.141E-02	-3.144E-02	2.610E-02	-3.844E-01	4.898E-01	4.430E-01
1.0000	6.622E-03	2.722E-02	1.734E-02	-1.934E-02	1.998E-02	-2.879E-01	4.069E-01	3.391E-01
1.0200	2.[illegible]E-03	2.[illegible]E-02	2.447E-02	-1.[illegible]E-02	1.588E-02	-2.310E-01	3.426E-01	2.694E-01
1.5000	3.[illegible]E-04	2.[illegible]E-02	3.204E-02	-1.[illegible]E-02	1.281E-02	-1.934E-01	2.898E-01	2.177E-01
1.5200	-1.[illegible]E-03	2.[illegible]E-02	3.924E-02	-8.[illegible]E-01	1.010E-02	-1.656E-01	2.451E-01	1.758E-01
2.0000	-3.[illegible]E-03	2.[illegible]E-02	4.637E-02	-7.[illegible]E-03	8.358E-03	-1.437E-01	2.066E-01	1.419E-01
2.0200	-4.[illegible]E-03	2.[illegible]E-02	5.332E-02	-6.010E-03	6.704E-03	-1.242E-01	1.732E-01	1.138E-01
2.5000	-4.[illegible]E-03	2.[illegible]E-02	5.999E-02	-4.[illegible]E-03	5.336E-03	-1.073E-01	1.443E-01	9.056E-02
2.5200	-5.[illegible]E-03	2.[illegible]E-02	6.633E-02	-4.071E-03	4.210E-03	-9.219E-02	1.194E-01	7.145E-02
3.0000	-5.471E-03	2.[illegible]E-02	7.233E-02	-3.307E-03	3.290E-03	-7.859E-02	9.806E-02	5.584E-02
3.0200	-5.570E-03	2.[illegible]E-02	7.802E-02	-2.654E-03	2.547E-03	-6.641E-02	7.997E-02	4.322E-02
3.5000	-5.[illegible]E-03	2.[illegible]E-02	8.337E-02	-2.113E-03	1.952E-03	-5.561E-02	6.474E-02	3.313E-02
3.5200	-5.[illegible]E-03	1.[illegible]E-02	8.837E-02	-1.654E-03	1.483E-03	-4.614E-02	5.205E-02	2.514E-02
4.0000	-5.[illegible]E-03	1.[illegible]E-02	9.303E-02	-1.284E-03	1.116E-03	-3.795E-02	4.157E-02	1.893E-02
4.0200	-4.[illegible]E-03	1.[illegible]E-02	1.014E-01	-7.514E-04	5.158E-04	-2.499E-02	2.601E-02	1.045E-02
5.0000	-4.[illegible]E-03	1.[illegible]E-02	1.044E-01	-4.214E-04	3.297E-04	-1.597E-02	1.591E-02	5.595E-03
5.0200	-3.[illegible]E-03	1.[illegible]E-02	1.145E-01	-2.282E-04	1.717E-04	-9.975E-03	9.539E-03	2.715E-03
6.0000	-3.1[illegible]E-03	9.[illegible]E-03	1.194E-01	-1.194E-04	8.738E-05	-5.035E-03	5.620E-03	1.483E-03
6.5000	-2.[illegible]E-03	8.[illegible]E-03	1.242E-01	-6.143E-05	4.357E-05	-3.594E-03	3.262E-03	7.395E-04
7.0000	-2.[illegible]E-03	8.[illegible]E-03	1.273E-01	-3.07[illegible]E-05	2.136E-05	-2.104E-03	1.869E-03	3.624E-04
8.0000	-1.[illegible]E-03	6.[illegible]E-03	1.335E-01	-7.341E-06	4.962E-06	-6.933E-04	5.939E-04	8.360E-05
9.0000	-1.1[illegible]E-03	3.[illegible]E-03	1.377E-01	-1.661E-06	1.090E-06	-2.181E-04	1.816E-04	1.951E-05
10.0000	-8.45[illegible]E-04	2.[illegible]E-03	1.405E-01	-3.624E-07	2.349E-07	-6.630E-05	5.381E-05	3.986E-06
11.0000	-6.[illegible]E-04	1.[illegible]E-03	1.425E-01	-7.74[illegible]E-08	4.974E-08	-1.954E-05	1.544E-05	8.442E-07
12.0000	-4.241E-04	1.157E-03	1.438E-01	-1.63[illegible]E-08	1.044E-08	-5.575E-06	4.277E-06	1.773E-07
13.0000	-3.[illegible]E-04	7.[illegible]E-04	1.446E-01	-3.417E-09	2.189E-09	-1.536E-06	1.134E-06	3.714E-08
14.0000	-2.1[illegible]E-04	5.413E-04	1.456E-01	-7.161E-10	4.610E-10	-4.047E-07	2.826E-07	7.825E-09
15.0000	-1.5[illegible]E-04	3.[illegible]E-04	1.460E-01	-1.511E-10	9.808E-11	-9.992E-08	6.332E-08	1.644E-09
16.0000	-1.[illegible]E-04	2.[illegible]E-04	1.463E-01	-3.22[illegible]E-11	2.117E-11	-2.196E-08	1.123E-08	3.503E-10
17.0000	-7.5[illegible]E-05	1.[illegible]E-04	1.465E-01	-7.021E-12	4.630E-12	-1.637E-09	8.847E-10	8.158E-11
18.0000	-5.3[illegible]E-05	7.[illegible]E-05	1.466E-01	-1.562E-12	1.002E-12	-1.379E-11	-6.184E-10	2.039E-11
19.0000	-3.[illegible]E-05	5.[illegible]E-05	1.466E-01	-3.565E-13	1.871E-13	3.880E-10	-3.305E-10	8.798E-12
20.0000	-2.[illegible]E-05	.0	1.467E-01	-5.20[illegible]E-14	1.084E-19	2.542E-10	6.934E-10	.0

Table IV-10

ETA	F2P	FP	F	PHIP	PHI	THETAP	THETA	RHOV
.0000	1.3405E-01	.0	-1.9205E-03	-2.8135E+00	1.0000E+00	-4.4346E-01	1.0000E+00	1.9646E+01
.0200	9.1795E-02	2.4525E-03	-1.7645E-03	-8.1127E+00	7.8038E-01	-4.4691E-01	9.5026E-01	1.5465E+01
.0400	6.2745E-02	4.4305E-03	-1.3446E-03	-7.4315E+00	3.8427E-01	-4.4755E-01	9.0035E-01	7.5246E+00
.0600	5.0055E-02	1.2215E-02	-8.4276E-04	-2.0015E+00	1.7095E-01	-4.7685E-01	8.5085E-01	3.5176E+00
.0800	4.2985E-02	1.4525E-02	-1.7235E-04	-7.9545E-01	1.1355E-01	-4.9465E-01	8.0305E-01	2.2705E+00
.1000	3.7955E-02	1.6545E-02	5.0405E-04	-4.1655E-01	8.5005E-02	-4.7445E-01	7.5775E-01	1.7045E+00
.1200	3.3985E-02	1.8345E-02	1.0475E-03	-2.5305E-01	7.0375E-02	-4.1045E-01	7.1555E-01	1.3435E+00
.1400	3.0435E-02	1.9955E-02	2.0435E-03	-1.7265E-01	5.9085E-02	-3.4125E-01	6.7675E-01	1.1775E+00
.1600	2.7775E-02	2.1415E-02	3.4705E-03	-1.2515E-01	5.0235E-02	-2.7505E-01	6.4135E-01	1.0335E+00
.1800	2.5155E-02	2.2735E-02	4.5725E-03	-9.5305E-02	4.3705E-02	-2.1405E-01	6.0915E-01	9.2565E-01
.2000	2.2945E-02	2.3935E-02	5.7115E-03	-7.5045E-02	3.8235E-02	-1.6065E-01	5.7995E-01	8.4225E-01
.2200	2.1035E-02	2.5045E-02	6.8335E-03	-6.1105E-02	3.3625E-02	-1.1625E-01	5.5365E-01	7.8455E-01
.2400	1.9335E-02	2.6065E-02	7.9225E-03	-5.1115E-02	2.9715E-02	-8.0875E-02	5.2985E-01	7.4625E-01
.2600	1.7815E-02	2.7015E-02	8.9715E-03	-4.3415E-02	2.6425E-02	-5.3995E-02	5.0845E-01	7.1775E-01
.2800	1.6445E-02	2.7905E-02	9.9815E-03	-3.7615E-02	2.3615E-02	-3.1395E-02	4.8905E-01	6.9605E-01
.3000	1.5205E-02	2.8735E-02	1.0955E-02	-3.2815E-02	2.1185E-02	-1.2805E-02	4.7145E-01	6.7945E-01
.3200	1.4075E-02	2.9515E-02	1.1895E-02	-2.8815E-02	1.9045E-02	2.9505E-03	4.5545E-01	6.6705E-01
.3400	1.3035E-02	3.0245E-02	1.2805E-02	-2.5415E-02	1.7135E-02	1.7115E-02	4.4085E-01	6.5805E-01
.3600	1.2075E-02	3.0935E-02	1.3685E-02	-2.2515E-02	1.5415E-02	2.9875E-02	4.2755E-01	6.5205E-01
.3800	1.1185E-02	3.1585E-02	1.4545E-02	-2.0015E-02	1.3855E-02	4.1395E-02	4.1535E-01	6.4905E-01
.4000	1.0355E-02	3.2205E-02	1.5375E-02	-1.7915E-02	1.2435E-02	5.1405E-02	4.0415E-01	6.4905E-01
.4200	9.5805E-03	3.2795E-02	1.6185E-02	-1.6115E-02	1.1135E-02	6.0405E-02	3.9385E-01	6.5205E-01
.4400	8.8615E-03	3.3355E-02	1.6965E-02	-1.4575E-02	9.9355E-03	6.8485E-02	3.8435E-01	6.5805E-01
.4600	8.1945E-03	3.3895E-02	1.7725E-02	-1.3245E-02	8.8255E-03	7.5765E-02	3.7555E-01	6.6705E-01
.4800	7.5765E-03	3.4405E-02	1.8465E-02	-1.2095E-02	7.8005E-03	8.2335E-02	3.6745E-01	6.7945E-01
.5000	7.0045E-03	3.4895E-02	1.9185E-02	-1.1095E-02	6.8555E-03	8.8275E-02	3.5995E-01	6.9605E-01
.5200	6.4755E-03	3.5365E-02	1.9885E-02	-1.0225E-02	6.0005E-03	9.3665E-02	3.5305E-01	7.1775E-01
.5400	5.9865E-03	3.5815E-02	2.0565E-02	-9.4615E-03	5.2075E-03	9.8575E-02	3.4665E-01	7.4625E-01
.5600	5.5345E-03	3.6245E-02	2.1225E-02	-8.7805E-03	4.4795E-03	1.0305E-01	3.4075E-01	7.8455E-01
.5800	5.1165E-03	3.6655E-02	2.1865E-02	-8.1705E-03	3.8105E-03	1.0715E-01	3.3525E-01	8.4225E-01
.6000	4.7295E-03	3.7045E-02	2.2485E-02	-7.6225E-03	3.1955E-03	1.1095E-01	3.3015E-01	9.2565E-01
.6200	4.3715E-03	3.7425E-02	2.3085E-02	-7.1295E-03	2.6295E-03	1.1445E-01	3.2535E-01	1.0335E+00
.6400	4.0405E-03	3.7785E-02	2.3665E-02	-6.6855E-03	2.1075E-03	1.1775E-01	3.2085E-01	1.1775E+00
.6600	3.7345E-03	3.8125E-02	2.4225E-02	-6.2855E-03	1.6255E-03	1.2085E-01	3.1665E-01	1.3435E+00
.6800	3.4515E-03	3.8455E-02	2.4765E-02	-5.9245E-03	1.1795E-03	1.2375E-01	3.1265E-01	1.5465E+00
.7000	3.1895E-03	3.8765E-02	2.5285E-02	-5.5985E-03	7.6555E-04	1.2655E-01	3.0885E-01	1.7045E+00
.7200	2.9465E-03	3.9065E-02	2.5785E-02	-5.3045E-03	3.8105E-04	1.2915E-01	3.0525E-01	2.2705E+00
.7400	2.7215E-03	3.9345E-02	2.6265E-02	-5.0385E-03	2.1005E-05	1.3165E-01	3.0185E-01	3.5175E+00
.7600	2.5125E-03	3.9615E-02	2.6725E-02	-4.7985E-03	-3.4195E-04	1.3405E-01	2.9865E-01	8.5085E-01
.7800	2.3185E-03	3.9865E-02	2.7165E-02	-4.5815E-03	-6.9005E-04	1.3635E-01	2.9565E-01	3.5175E+00
.8000	2.1385E-03	4.0105E-02	2.7585E-02	-4.3855E-03	-1.0295E-03	1.3855E-01	2.9285E-01	1.0335E+00
.8200	1.9715E-03	4.0335E-02	2.7985E-02	-4.2085E-03	-1.3615E-03	1.4065E-01	2.9025E-01	1.3435E+00
.8400	1.8165E-03	4.0545E-02	2.8365E-02	-4.0495E-03	-1.6865E-03	1.4265E-01	2.8785E-01	1.7045E+00
.8600	1.6725E-03	4.0745E-02	2.8725E-02	-3.9075E-03	-2.0045E-03	1.4455E-01	2.8565E-01	2.2705E+00
.8800	1.5385E-03	4.0935E-02	2.9065E-02	-3.7815E-03	-2.3165E-03	1.4635E-01	2.8365E-01	3.5175E+00
.9000	1.4135E-03	4.1105E-02	2.9385E-02	-3.6705E-03	-2.6225E-03	1.4805E-01	2.8185E-01	8.5085E-01
.9200	1.2975E-03	4.1255E-02	2.9685E-02	-3.5745E-03	-2.9225E-03	1.4965E-01	2.8025E-01	3.5175E+00
.9400	1.1895E-03	4.1385E-02	2.9965E-02	-3.4935E-03	-3.2165E-03	1.5115E-01	2.7885E-01	1.0335E+00
.9600	1.0895E-03	4.1495E-02	3.0225E-02	-3.4275E-03	-3.5045E-03	1.5255E-01	2.7765E-01	1.3435E+00
.9800	9.9675E-04	4.1585E-02	3.0465E-02	-3.3765E-03	-3.7865E-03	1.5385E-01	2.7665E-01	1.7045E+00
1.0000	9.1105E-04	4.1655E-02	3.0685E-02	-3.3405E-03	-4.0625E-03	1.5505E-01	2.7585E-01	2.2705E+00
1.0200	8.3195E-04	4.1705E-02	3.0885E-02	-3.3195E-03	-4.3325E-03	1.5615E-01	2.7525E-01	3.5175E+00
1.0400	7.5945E-04	4.1735E-02	3.1065E-02	-3.3135E-03	-4.5965E-03	1.5715E-01	2.7485E-01	8.5085E-01
1.0600	6.9355E-04	4.1745E-02	3.1225E-02	-3.3225E-03	-4.8545E-03	1.5805E-01	2.7465E-01	3.5175E+00
1.0800	6.3425E-04	4.1735E-02	3.1365E-02	-3.3465E-03	-5.1065E-03	1.5885E-01	2.7465E-01	1.0335E+00
1.1000	5.8155E-04	4.1705E-02	3.1485E-02	-3.3855E-03	-5.3525E-03	1.5955E-01	2.7485E-01	1.3435E+00
1.1200	5.3545E-04	4.1655E-02	3.1585E-02	-3.4395E-03	-5.5925E-03	1.6015E-01	2.7525E-01	1.7045E+00
1.1400	4.9595E-04	4.1585E-02	3.1665E-02	-3.5085E-03	-5.8265E-03	1.6065E-01	2.7585E-01	2.2705E+00
1.1600	4.6305E-04	4.1495E-02	3.1725E-02	-3.5925E-03	-6.0545E-03	1.6105E-01	2.7665E-01	3.5175E+00
1.1800	4.3675E-04	4.1385E-02	3.1765E-02	-3.6915E-03	-6.2765E-03	1.6135E-01	2.7765E-01	8.5085E-01
1.2000	4.1705E-04	4.1255E-02	3.1785E-02	-3.8055E-03	-6.4925E-03	1.6155E-01	2.7885E-01	3.5175E+00
1.2200	4.0395E-04	4.1105E-02	3.1785E-02	-3.9345E-03	-6.7025E-03	1.6165E-01	2.8025E-01	1.0335E+00
1.2400	3.9745E-04	4.0935E-02	3.1765E-02	-4.0785E-03	-6.9065E-03	1.6165E-01	2.8185E-01	1.3435E+00
1.2600	3.9755E-04	4.0745E-02	3.1725E-02	-4.2375E-03	-7.1045E-03	1.6155E-01	2.8365E-01	1.7045E+00
1.2800	4.0425E-04	4.0545E-02	3.1665E-02	-4.4115E-03	-7.2965E-03	1.6135E-01	2.8565E-01	2.2705E+00
1.3000	4.1755E-04	4.0335E-02	3.1585E-02	-4.6005E-03	-7.4825E-03	1.6105E-01	2.8785E-01	3.5175E+00
1.3200	4.3745E-04	4.0105E-02	3.1485E-02	-4.8045E-03	-7.6625E-03	1.6065E-01	2.9025E-01	8.5085E-01
1.3400	4.6395E-04	3.9865E-02	3.1365E-02	-5.0235E-03	-7.8365E-03	1.6015E-01	2.9285E-01	3.5175E+00
1.3600	4.9705E-04	3.9615E-02	3.1225E-02	-5.2575E-03	-8.0045E-03	1.5955E-01	2.9565E-01	1.0335E+00
1.3800	5.3675E-04	3.9345E-02	3.1065E-02	-5.5065E-03	-8.1665E-03	1.5885E-01	2.9865E-01	1.3435E+00
1.4000	5.8305E-04	3.9065E-02	3.0885E-02	-5.7705E-03	-8.3225E-03	1.5805E-01	3.0185E-01	1.7045E+00
1.4200	6.3595E-04	3.8765E-02	3.0685E-02	-6.0495E-03	-8.4725E-03	1.5715E-01	3.0525E-01	2.2705E+00
1.4400	6.9545E-04	3.8455E-02	3.0465E-02	-6.3435E-03	-8.6165E-03	1.5615E-01	3.0885E-01	3.5175E+00
1.4600	7.6155E-04	3.8125E-02	3.0225E-02	-6.6525E-03	-8.7545E-03	1.5505E-01	3.1265E-01	8.5085E-01
1.4800	8.3425E-04	3.7785E-02	2.9965E-02	-6.9765E-03	-8.8865E-03	1.5385E-01	3.1665E-01	3.5175E+00
1.5000	9.1355E-04	3.7425E-02	2.9685E-02	-7.3155E-03	-9.0125E-03	1.5255E-01	3.2085E-01	1.0335E+00
1.5200	9.9945E-04	3.7045E-02	2.9385E-02	-7.6695E-03	-9.1325E-03	1.5115E-01	3.2535E-01	1.3435E+00
1.5400	1.0919E-03	3.6655E-02	2.9065E-02	-8.0385E-03	-9.2465E-03	1.4965E-01	3.3015E-01	1.7045E+00
1.5600	1.1911E-03	3.6245E-02	2.8725E-02	-8.4225E-03	-9.3545E-03	1.4805E-01	3.3525E-01	2.2705E+00
1.5800	1.2971E-03	3.5815E-02	2.8365E-02	-8.8215E-03	-9.4565E-03	1.4635E-01	3.4075E-01	3.5175E+00
1.6000	1.4099E-03	3.5365E-02	2.7985E-02	-9.2355E-03	-9.5525E-03	1.4455E-01	3.4665E-01	8.5085E-01
1.6200	1.5295E-03	3.4895E-02	2.7585E-02	-9.6645E-03	-9.6425E-03	1.4265E-01	3.5305E-01	3.5175E+00
1.6400	1.6559E-03	3.4405E-02	2.7165E-02	-1.0109E-02	-9.7265E-03	1.4065E-01	3.5995E-01	1.0335E+00
1.6600	1.7891E-03	3.3895E-02	2.6725E-02	-1.0569E-02	-9.8045E-03	1.3855E-01	3.6745E-01	1.3435E+00
1.6800	1.9291E-03	3.3355E-02	2.6265E-02	-1.1045E-02	-9.8765E-03	1.3635E-01	3.7555E-01	1.7045E+00
1.7000	2.0759E-03	3.2795E-02	2.5785E-02	-1.1535E-02	-9.9425E-03	1.3405E-01	3.8435E-01	2.2705E+00
1.7200	2.2295E-03	3.2205E-02	2.5285E-02	-1.2041E-02	-1.0003E-02	1.3165E-01	3.9385E-01	3.5175E+00
1.7400	2.3899E-03	3.1585E-02	2.4765E-02	-1.2565E-02	-1.0055E-02	1.2915E-01	4.0415E-01	8.5085E-01
1.7600	2.5571E-03	3.0935E-02	2.4225E-02	-1.3105E-02	-1.0101E-02	1.2655E-01	4.1535E-01	3.5175E+00
1.7800	2.7311E-03	3.0245E-02	2.3665E-02	-1.3665E-02	-1.0140E-02	1.2375E-01	4.2755E-01	1.0335E+00
1.8000	2.9119E-03	2.9515E-02	2.3085E-02	-1.4245E-02	-1.0173E-02	1.2085E-01	4.4085E-01	1.3435E+00
1.8200	3.0995E-03	2.8735E-02	2.2485E-02	-1.4845E-02	-1.0199E-02	1.1775E-01	4.5545E-01	1.7045E+00
1.8400	3.2939E-03	2.7905E-02	2.1865E-02	-1.5465E-02	-1.0219E-02	1.1445E-01	4.7145E-01	2.2705E+00
1.8600	3.4951E-03	2.7015E-02	2.1225E-02	-1.6105E-02	-1.0233E-02	1.1095E-01	4.8905E-01	3.5175E+00
1.8800	3.7031E-03	2.6065E-02	2.0565E-02	-1.6765E-02	-1.0241E-02	1.0715E-01	5.0845E-01	8.5085E-01
1.9000	3.9179E-03	2.5045E-02	1.9885E-02	-1.7445E-02	-1.0243E-02	1.0305E-01	5.2985E-01	3.5175E+00
1.9200	4.1395E-03	2.3935E-02	1.9185E-02	-1.8145E-02	-1.0241E-02	9.8575E-02	5.5365E-01	1.0335E+00
1.9400	4.3679E-03	2.2735E-02	1.8465E-02	-1.8865E-02	-1.0233E-02	9.3665E-02	5.7995E-01	1.3435E+00
1.9600	4.6031E-03	2.1415E-02	1.7725E-02	-1.9605E-02	-1.0219E-02	8.8275E-02	6.0915E-01	1.7045E+00
1.9800	4.8451E-03	1.9955E-02	1.6965E-02	-2.0365E-02	-1.0199E-02	8.2335E-02	6.4135E-01	2.2705E+00
2.0000	5.0939E-03	1.8345E-02	1.6185E-02	-2.1145E-02	-1.0173E-02	7.5765E-02	6.7675E-01	3.5175E+00
2.0200	5.3495E-03	1.6545E-02	1.5375E-02	-2.1945E-02	-1.0140E-02	6.8485E-02	7.1555E-01	8.5085E-01
2.0400	5.6119E-03	1.4525E-02	1.4545E-02	-2.2765E-02	-1.0101E-02	6.0405E-02	7.5775E-01	3.5175E+00
2.0600	5.8811E-03	1.2215E-02	1.3685E-02	-2.3605E-02	-1.0055E-02	5.1405E-02	8.0305E-01	1.0335E+00
2.0800	6.1571E-03	9.4275E-03	1.2805E-02	-2.4465E-02	-1.0003E-02	4.1395E-02	8.5085E-01	1.3435E+00
2.1000	6.4399E-03	6.2715E-03	1.1895E-02	-2.5345E-02	-9.9425E-03	2.9505E-02	9.0035E-01	1.7045E+00
2.1200	6.7295E-03	2.4525E-03	1.0955E-02	-2.6245E-02	-9.8765E-03	1.7115E-02	9.5025E-01	2.2705E+00
2.1400	7.0259E-03	-1.9205E-03	9.9815E-03	-2.7165E-02	-9.8045E-03	3.8105E-04	1.0000E+00	3.5175E+00

Table IV-11

ETA	F2P	FP	F	PHIP	PHI	THETAP	THETA	RHOV
.0000	1.[illegible]E-01	.0	-2.[illegible]E-13	-1.[illegible]E+00	1.0000E+00	-1.0551E+00	1.0000E+00	2.1246E+01
.0100	1.[illegible]E-01	2.[illegible]E-03	-2.[illegible]E-04	-5.[illegible]E+00	8.6746E-01	-1.0546E+00	9.4736E-01	1.7626E+01
.0200	8.[illegible]E-02	1.[illegible]E-02	-2.[illegible]E-03	-4.[illegible]E+00	4.1006E-01	-1.0557E+00	8.9456E-01	8.8506E+00
.0300	5.[illegible]E-02	1.[illegible]E-02	-1.[illegible]E-03	-2.[illegible]E+00	1.9246E-01	-1.0337E+00	8.6216E-01	4.1616E+00
.0400	4.[illegible]E-02	1.[illegible]E-02	-6.[illegible]E-04	-9.[illegible]E-01	1.2746E-01	-1.0256E-01	7.9106E-01	2.7056E+00
.0500	4.[illegible]E-02	1.[illegible]E-02	1.[illegible]E-04	-4.[illegible]E-01	9.0106E-02	-1.1456E-01	7.4426E-01	2.0416E+00
.0600	3.[illegible]E-02	2.[illegible]E-02	1.[illegible]E-03	-2.[illegible]E-01	7.0356E-02	-1.1376E-01	7.0036E-01	1.6646E+00
.0700	3.[illegible]E-02	2.[illegible]E-02	2.[illegible]E-03	-1.[illegible]E-01	5.6706E-02	-1.0006E-01	6.6046E-01	1.4216E+00
.0800	3.[illegible]E-02	2.[illegible]E-02	3.[illegible]E-03	-1.[illegible]E-01	5.4876E-02	-1.0506E-01	6.2436E-01	1.2516E+00
.0900	2.[illegible]E-02	2.[illegible]E-02	4.[illegible]E-03	-1.[illegible]E-01	5.6346E-02	-1.1036E-01	5.9176E-01	1.1236E+00
.1000	2.[illegible]E-02	2.[illegible]E-02	5.[illegible]E-03	-4.[illegible]E-02	4.8626E-02	-1.0936E-01	5.6236E-01	1.0246E+00
.1200	1.[illegible]E-02	3.[illegible]E-02	1.[illegible]E-02	-1.[illegible]E-02	3.4456E-02	-1.0726E-01	4.5086E-01	7.7196E-01
1.0000	8.[illegible]E-03	3.[illegible]E-02	2.[illegible]E-02	-2.[illegible]E-02	2.7116E-02	-1.0596E-01	3.7516E-01	5.7596E-01
1.0200	6.[illegible]E-03	3.[illegible]E-02	3.[illegible]E-02	-1.[illegible]E-02	2.2116E-02	-1.0526E-01	3.1776E-01	4.4976E-01
1.0400	7.[illegible]E-04	3.[illegible]E-02	3.[illegible]E-02	-1.[illegible]E-02	1.8286E-02	-1.7126E-01	2.7096E-01	3.8836E-01
1.0600	-1.[illegible]E-03	3.[illegible]E-02	4.[illegible]E-02	-1.[illegible]E-02	1.5176E-02	-1.4706E-01	2.3136E-01	3.3236E-01
2.0000	-3.[illegible]E-03	3.[illegible]E-02	5.[illegible]E-02	-4.[illegible]E-03	1.0376E-02	-1.2746E-01	1.9706E-01	2.6716E-01
2.0200	-3.[illegible]E-03	3.[illegible]E-02	5.[illegible]E-02	-4.[illegible]E-03	1.0386E-02	-1.1176E-01	1.6716E-01	2.2046E-01
2.0400	-3.[illegible]E-03	3.[illegible]E-02	6.[illegible]E-02	-3.[illegible]E-03	8.5096E-03	-9.7456E-02	1.4106E-01	1.8086E-01
2.0600	-3.[illegible]E-03	3.[illegible]E-02	7.[illegible]E-02	-3.[illegible]E-03	7.0646E-03	-8.4676E-02	1.1836E-01	1.4726E-01
3.0000	-7.[illegible]E-03	3.[illegible]E-02	9.[illegible]E-02	-4.[illegible]E-03	5.0006E-03	-7.3096E-02	9.8576E-02	1.1906E-01
3.0200	-7.[illegible]E-03	3.[illegible]E-02	9.[illegible]E-02	-4.[illegible]E-03	4.4706E-03	-6.2426E-02	8.1036E-02	9.5396E-02
3.0400	-7.[illegible]E-03	3.[illegible]E-02	1.[illegible]E-01	-3.[illegible]E-03	3.5726E-03	-5.3236E-02	6.7186E-02	7.5896E-02
3.0600	-7.[illegible]E-03	3.[illegible]E-02	1.[illegible]E-01	-2.[illegible]E-03	2.8616E-03	-4.4866E-02	5.6446E-02	5.9926E-02
4.0000	-7.[illegible]E-03	3.[illegible]E-02	1.[illegible]E-01	-2.[illegible]E-03	2.2116E-03	-3.7516E-02	4.6806E-02	4.6966E-02
4.0200	-6.[illegible]E-03	3.[illegible]E-02	1.[illegible]E-01	-1.[illegible]E-03	1.3306E-03	-2.5606E-02	2.9036E-02	2.8246E-02
5.0000	-5.[illegible]E-03	3.[illegible]E-02	1.[illegible]E-01	-4.[illegible]E-04	7.8126E-04	-1.7016E-02	1.8516E-02	1.4596E-02
5.0200	-4.[illegible]E-03	3.[illegible]E-02	1.[illegible]E-01	-5.[illegible]E-04	4.4046E-04	-1.1026E-02	1.1546E-02	9.5366E-03
6.0000	-4.[illegible]E-03	3.[illegible]E-02	1.[illegible]E-01	-2.[illegible]E-04	2.5336E-04	-6.9936E-03	7.1506E-03	5.7816E-03
6.0200	-3.[illegible]E-03	3.[illegible]E-02	1.[illegible]E-01	-1.[illegible]E-04	1.4076E-04	-4.3476E-03	4.3626E-03	2.8896E-03
7.0000	-2.[illegible]E-03	3.[illegible]E-02	1.[illegible]E-01	-9.[illegible]E-05	7.7156E-05	-2.6856E-03	2.6316E-03	1.4796E-03
8.0000	-2.[illegible]E-03	3.[illegible]E-02	1.[illegible]E-01	-5.[illegible]E-05	2.2496E-05	-9.4006E-04	9.3376E-04	4.7776E-04
9.0000	-1.[illegible]E-03	3.[illegible]E-02	1.[illegible]E-01	-2.[illegible]E-05	6.3256E-06	-2.4406E-04	3.2346E-04	1.7506E-04
10.0000	-9.[illegible]E-04	3.[illegible]E-02	1.[illegible]E-01	-2.[illegible]E-06	1.7346E-06	-1.1946E-04	1.1026E-04	5.7346E-05
11.0000	-6.[illegible]E-04	3.[illegible]E-02	1.[illegible]E-01	-9.[illegible]E-07	4.7496E-07	-4.0546E-05	3.7106E-05	1.9196E-05
12.0000	-4.[illegible]E-04	3.[illegible]E-02	1.[illegible]E-01	-1.[illegible]E-07	1.2476E-07	-1.3476E-05	1.2406E-05	6.7556E-06
13.0000	-3.[illegible]E-04	3.[illegible]E-02	1.[illegible]E-01	-4.[illegible]E-08	3.4026E-08	-4.5646E-06	4.1216E-06	2.3946E-06
14.0000	-2.[illegible]E-04	3.[illegible]E-02	1.[illegible]E-01	-1.[illegible]E-08	9.3076E-09	-1.5116E-06	1.3646E-06	1.2776E-06
15.0000	-1.[illegible]E-04	3.[illegible]E-02	1.[illegible]E-01	-4.[illegible]E-09	2.4796E-09	-5.0036E-07	4.4996E-07	5.2476E-07
16.0000	-9.[illegible]E-05	3.[illegible]E-02	1.[illegible]E-01	-8.[illegible]E-10	6.5746E-10	-1.6576E-07	1.4746E-07	1.3966E-06
17.0000	-5.[illegible]E-05	3.[illegible]E-02	1.[illegible]E-01	-2.[illegible]E-10	1.7646E-10	-5.4596E-08	4.7446E-08	3.6466E-09
18.0000	-4.[illegible]E-05	3.[illegible]E-02	1.[illegible]E-01	-5.[illegible]E-11	4.3346E-11	-1.8006E-08	1.6206E-08	9.2456E-10
19.0000	-3.[illegible]E-05	3.[illegible]E-02	1.[illegible]E-01	-1.[illegible]E-11	9.1066E-12	-5.4356E-09	3.5436E-09	1.3076E-10
20.0000	-2.[illegible]E-05	4.[illegible]E-02	1.[illegible]E-01	-4.[illegible]E-12	.0	-1.4576E-09	2.7116-09	.0

Table IV-12

ETA	FZP	FP	F	DHIP	DHI	THETAH	THETA	HUUY
.0000	1.-44E-01	.0	-3.217E-03	-1.2H-E+00	1.000E+00	-1.0H4E+00	1.000E+00	2.215E+01
.0300	1.1336-01	5.541E-03	-3.041E-03	-4.702E+00	8.660E-01	-1.090E+00	9.456E-01	1.918E+01
.1000	7.AH5E-02	1.123E-02	-2.547E-03	-8.436E+00	4.502E-01	-1.093E+00	8.910E-01	1.810E+01
.1300	6.159E-02	1.465E-02	-1.937E-03	-2.30HE+00	2.172E-01	-1.057E+00	8.304E-01	4.911E+00
.2000	5.291E-02	1.750E-02	-1.132E-03	-4.533E-01	1.41HE-01	-1.012E+00	7.H48E-01	3.140E+00
.2300	4.669E-02	1.998E-02	-1.937E-04	-5.024E-01	1.071E-01	-4.390E-01	7.359E-01	2.373E+00
.3000	4.171E-02	2.219E-02	5.A14E-04	-3.094E-01	A.741E-02	-A.567E-01	6.910E-01	1.936E+00
.3300	3.751E-02	2.416E-02	2.021E-03	-2.103E-01	7.405E-02	-7.734E-01	6.503E-01	1.653E+00
.4000	3.395E-02	2.594E-02	3.274E-03	-1.524E-01	6.509E-02	-6.953E-01	6.136E-01	1.455E+00
.4300	3.0A9E-02	2.755E-02	4.613E-03	-1.184E-01	5.991E-02	-6.243E-01	5.806E-01	1.307E+00
.5000	2.747E-02	2.901E-02	5.927E-03	-9.29HE-02	5.380E-02	-5.A19E-01	5.510E-01	1.192E+00
.5300	1.455E-02	3.043E-02	1.402E-02	-4.174E-02	3.441E-02	-3.551E-01	4.390E-01	A.507E-01
1.0000	9.144E-03	3.159E-02	2.304E-02	-2.62HE-02	3.020E-02	-2.559E-01	3.A48E-01	6.A89E-01
1.0300	4.075E-03	3.A21E-02	3.259E-02	-1.92HE-02	2.400E-02	-2.014E-01	3.079E-01	5.450E-01
1.1000	3.1A0E-04	3.475E-02	4.2H5E-02	-1.52HE-02	2.033E-02	-1.679E-01	2.A20E-01	4.502E-01
1.1300	-2.322E-03	3.549E-02	5.24HE-02	-1.26HE-02	1.A06E-02	-1.437E-01	2.232E-01	3.733E-01
2.0000	-4.337E-03	3.A64E-02	6.227E-02	-1.05HE-02	1.396E-02	-1.247E-01	1.A97E-01	3.091E-01
2.0300	-5.A00E-03	3.736E-02	7.17HE-02	-4.014E-03	1.171E-02	-1.087E-01	1.606E-01	2.549E-01
2.1000	-6.429E-03	3.578E-02	A.092E-02	-7.43HE-03	9.A31E-03	-A.A40E-02	1.352E-01	2.088E-01
2.1300	-7.5A4E-03	3.398E-02	A.96EE-02	-6.441E-03	7.A74E-03	-A.199E-02	1.132E-01	1.700E-01
3.0000	-7.400E-03	3.205E-02	9.790E-02	-5.39HE-03	6.179E-03	-7.059E-02	9.413E-0	1.377E-01
3.0300	-8.066E-03	3.005E-02	1.057E-01	-4.67HE-03	4.A07E-03	-5.033E-02	7.77AE-0	1.109E-01
3.1000	-8.A54E-03	2.803E-02	1.129E-01	-4.07HE-03	3.450E-03	-5.114E-02	6.3A7E-0	A.749E-02
3.1300	-7.6A3E-03	2.603E-02	1.197E-01	-2.99AE-03	3.11AE-03	-4.299E-02	5.213E-0	6.204E-02
4.0000	-7.A49E-03	2.409E-02	1.253E-01	-2.41HE-03	2.443E-03	-3.5A6E-02	4.229E-0	5.411E-02
4.0300	-6.963E-03	2.A43E-02	1.371E-01	-1.53HE-03	1.A70E-03	-2.A36E-02	2.734E-0	3.257E-02
5.0000	-6.115E-03	1.716E-02	1.A64E-01	-9.37HE-04	8.641E-04	-1.61HE-02	1.734E-0	1.A14E-02
5.0300	-5.274E-03	1.A32E-02	1.543E-01	-5.589E-04	4.97AE-04	-1.039E-02	1.088E-0	1.101E-02
6.0000	-4.A81E-03	1.1HAE-02	1.609E-01	-3.251E-04	2.A12E-04	-A.574E-03	A.AA3E-0	A.227E-03
6.0300	-3.749E-03	9.A23E-03	1.A52E-01	-1.A53E-04	1.506E-04	-4.0A7E-03	4.064E-0	3.A40E-03
7.0000	-3.144E-03	8.09AE-03	1.707E-01	-1.034E-04	A.616E-05	-2.505E-03	2.A46E-0	1.988E-03
8.0000	-2.142E-03	5.471E-03	1.774E-01	-3.149E-05	2.533E-05	-1.104E-04	8.650E-0	5.511E-04
9.0000	-1.470E-03	3.677E-03	1.A13E-01	-4.144E-06	7.236E-06	-3.205E-04	2.992E-0	1.503E-04
10.0000	-9.A36E-04	2.A50E-03	1.A50E-01	-2.595E-06	2.067E-06	-1.104E-04	1.018E-0	A.A99E-05
11.0000	-6.A36E-04	1.A34E-03	1.A70E-01	-7.23AE-07	5.606E-07	-3.744E-05	3.A28E-0	1.A2AE-05
12.0000	-4.506E-04	1.2A5E-03	1.AA3E-01	-1.995E-07	1.535E-07	-1.259E-05	1.140E-0	5.099E-06
13.0000	-3.029E-04	7.145E-04	1.A92E-01	-5.454E-08	4.170E-08	-4.207E-06	3.A07E-0	A.237E-07
14.0000	-2.034E-04	A.A45E-04	1.A98E-01	-1.481E-08	1.141E-08	-1.394E-06	1.250E-0	2.A35E-07
15.0000	-1.367E-04	2.A66E-04	1.900E-01	-3.98AE-09	2.A32E-09	-4.623E-07	A.145E-0	A.534E-08
16.0000	-9.14AE-05	1.A38E-04	1.900E-01	-1.072E-09	7.412E-10	-1.525E-07	1.350E-0	1.A23E-08
17.0000	-6.142E-05	1.A08E-04	1.900E-01	-2.A70E-10	1.A40E-10	-5.009E-08	A.700E-0	1.A19E-08
18.0000	-4.12AE-05	7.711E-05	1.900E-01	-7.421E-11	2.A17E-11	-1.653E-08	1.285E-0	3.371E-10
19.0000	-2.7A2E-05	5.A95E-05	1.900E-01	-1.5A4E-12	-1.052E-12	-5.230E-09	3.0AA-0	-1.392E-11
20.0000	-1.A49E-05	.0	1.900E-01	-2.AA0E-12	5.A21E-20	-1.614E-09	1.735E-1	.0

Table IV-13

ETA	F2P	FP	F	PHIP	PHI	THETAP	THETA	BUOY
.0000	1.7598E-01	.0	.0	-6.086E+00	1.000E+00	-5.022E-01	1.000E+00	6.881E+00
.0500	6.5078E-02	4.211E-03	1.139E-04	-5.987E+00	6.970E-01	-5.022E-01	9.749E-01	4.777E+00
.1000	3.4708E-02	6.748E-03	3.932E-04	-5.066E+00	4.121E-01	-5.019E-01	9.498E-01	2.805E+00
.1500	2.4178E-02	8.281E-03	7.720E-04	-2.606E+00	2.261E-01	-4.998E-01	9.247E-01	1.492E+00
.2000	1.8198E-02	9.272E-03	1.212E-03	-1.225E+00	1.311E-01	-4.958E-01	8.998E-01	8.667E-01
.2500	1.1338E-02	9.951E-03	1.696E-03	-6.390E-01	8.649E-02	-4.900E-01	8.752E-01	5.578E-01
.3000	8.0688E-03	1.043E-02	2.206E-03	-3.721E-01	6.202E-02	-4.826E-01	8.509E-01	3.898E-01
.3500	5.7308E-03	1.077E-02	2.735E-03	-2.366E-01	4.715E-02	-4.739E-01	8.270E-01	2.880E-01
.4000	3.9728E-03	1.101E-02	3.280E-03	-1.410E-01	3.738E-02	-4.640E-01	8.035E-01	2.215E-01
.4500	2.6068E-03	1.118E-02	3.835E-03	-1.154E-01	3.055E-02	-4.534E-01	7.806E-01	1.752E-01
.5000	1.5198E-03	1.129E-02	4.394E-03	-8.625E-02	2.556E-02	-4.422E-01	7.582E-01	1.416E-01
.5500	-1.5578E-03	1.121E-02	7.224E-03	-2.887E-02	1.293E-02	-3.843E-01	6.549E-01	5.820E-02
1.0000	-2.9568E-03	1.064E-02	9.962E-03	-1.439E-02	7.828E-03	-3.330E-01	5.654E-01	2.655E-02
1.0500	-3.7468E-03	9.450E-03	1.253E-02	-8.479E-03	5.061E-03	-2.903E-01	4.877E-01	1.070E-02
1.1000	-4.1738E-03	8.989E-03	1.488E-02	-5.426E-03	3.359E-03	-2.543E-01	4.197E-01	1.939E-03
1.1500	-4.3418E-03	8.132E-03	1.702E-02	-3.609E-03	2.248E-03	-2.232E-01	3.601E-01	-3.012E-03
2.0000	-4.1328E-03	7.318E-03	1.895E-02	-2.438E-03	1.502E-03	-1.956E-01	3.078E-01	-5.690E-03
2.0500	-2.9468E-03	6.571E-03	2.063E-02	-1.651E-03	9.973E-04	-1.709E-01	2.621E-01	-6.951E-03
2.1000	-2.5428E-03	5.497E-03	2.224E-02	-1.112E-03	6.562E-04	-1.488E-01	2.222E-01	-7.721E-03
2.1500	-2.2428E-03	5.299E-03	2.364E-02	-7.429E-04	4.272E-04	-1.286E-01	1.876E-01	-7.165E-03
3.0000	-1.9608E-03	4.775E-03	2.490E-02	-4.907E-04	2.750E-04	-1.107E-01	1.577E-01	-6.652E-03
3.0500	-1.7048E-03	4.317E-03	2.603E-02	-3.203E-04	1.750E-04	-9.473E-02	1.321E-01	-5.999E-03
3.1000	-1.4748E-03	3.920E-03	2.704E-02	-2.065E-04	1.101E-04	-8.067E-02	1.102E-01	-5.285E-03
3.1500	-1.2778E-03	3.576E-03	2.800E-02	-1.315E-04	6.855E-05	-6.836E-02	9.160E-02	-4.576E-03
4.0000	-1.1088E-03	3.279E-03	2.895E-02	-8.272E-05	4.222E-05	-5.784E-02	7.588E-02	-3.987E-03
4.0500	-8.744E-04	2.798E-03	3.037E-02	-3.163E-05	1.555E-05	-4.047E-02	5.156E-02	-2.763E-03
5.0000	-6.407E-04	2.432E-03	3.167E-02	-1.162E-05	5.524E-06	-2.797E-02	3.462E-02	-1.898E-03
5.0500	-5.044E-04	2.148E-03	3.281E-02	-4.114E-06	1.899E-06	-1.905E-02	2.300E-02	-1.276E-03
6.0000	-4.087E-04	1.921E-03	3.383E-02	-1.409E-06	6.336E-07	-1.282E-02	1.513E-02	-8.454E-04
6.0500	-3.410E-04	1.734E-03	3.474E-02	-4.487E-07	2.054E-07	-8.525E-03	9.859E-03	-5.531E-04
7.0000	-2.924E-04	1.577E-03	3.557E-02	-1.516E-07	6.405E-08	-5.612E-03	6.372E-03	-3.583E-04
8.0000	-2.293E-04	1.318E-03	3.701E-02	-1.431E-08	5.904E-09	-2.368E-03	2.602E-03	-1.466E-04
9.0000	-1.916E-04	1.109E-03	3.822E-02	-1.237E-09	4.934E-10	-9.668E-04	1.034E-03	-5.829E-05
10.0000	-1.642E-04	9.315E-04	3.924E-02	-9.710E-11	3.770E-11	-3.842E-04	4.015E-04	-2.264E-05
11.0000	-1.440E-04	7.774E-04	4.009E-02	-7.014E-12	2.661E-12	-1.492E-04	1.526E-04	-8.607E-06
12.0000	-1.286E-04	6.424E-04	4.080E-02	-4.885E-13	1.743E-13	-5.678E-05	5.684E-05	-3.205E-06
13.0000	-1.117E-04	5.233E-04	4.134E-02	-2.901E-14	1.062E-14	-2.123E-05	2.064E-05	-1.164E-06
14.0000	-9.847E-05	4.183E-04	4.185E-02	-1.463E-15	6.058E-16	-7.784E-06	7.220E-06	-4.071E-07
15.0000	-8.720E-05	3.255E-04	4.222E-02	-8.737E-17	3.464E-17	-2.776E-06	2.349E-06	-1.324E-07
16.0000	-7.708E-05	2.434E-04	4.250E-02	-4.085E-18	3.381E-18	-9.361E-07	6.445E-07	-3.636E-08
17.0000	-6.814E-05	1.704E-04	4.271E-02	-1.564E-19	1.491E-18	-2.720E-07	9.660E-08	-5.446E-09
18.0000	-6.025E-05	1.056E-04	4.285E-02	-2.495E-21	-2.135E-19	-4.145E-08	-3.951E-08	2.230E-09
19.0000	-5.327E-05	5.013E-05	4.293E-02	2.437E-22	-1.094E-18	2.917E-08	-3.802E-08	2.142E-09
20.0000	-4.711E-05	0.429E-16	4.295E-02	1.162E-22	-1.037E-18	4.107E-08	6.245E-17	.0

Table IV-14

ETA	F2P	FP	F	PHIP	PHI	THETAP	THETA	BUOY
.0000	9.6565E-02	.0	.0	-7.252E+00	1.000E+00	-6.792E-01	1.000E+00	1.260E+01
.0500	5.7365E-02	3.775E-03	1.025E-04	-7.146E+00	6.387E-01	-6.791E-01	9.660E-01	7.979E+00
.1000	3.537E-02	6.024E-03	3.521E-04	-5.705E+00	3.042E-01	-6.781E-01	9.321E-01	3.723E+00
.1500	2.573E-02	7.521E-03	6.937E-04	-1.689E+00	1.456E-01	-6.706E-01	8.983E-01	1.716E+00
.2000	2.065E-02	8.670E-03	1.098E-03	-6.910E-01	9.153E-02	-6.560E-01	8.652E-01	1.034E+00
.2500	1.733E-02	9.614E-03	1.554E-03	-3.514E-01	6.700E-02	-6.355E-01	8.328E-01	7.266E-01
.3000	1.448E-02	1.042E-02	2.054E-03	-2.123E-01	5.333E-02	-6.105E-01	8.017E-01	5.567E-01
.3500	1.295E-02	1.111E-02	2.594E-03	-1.417E-01	4.466E-02	-5.826E-01	7.718E-01	4.500E-01
.4000	1.136E-02	1.172E-02	3.167E-03	-1.015E-01	3.866E-02	-5.534E-01	7.434E-01	3.771E-01
.4500	1.001E-02	1.225E-02	3.767E-03	-7.662E-02	3.425E-02	-5.239E-01	7.165E-01	3.243E-01
.5000	8.543E-03	1.272E-02	4.391E-03	-6.019E-02	3.086E-02	-4.951E-01	6.910E-01	2.842E-01
.5500	4.719E-03	1.437E-02	7.799E-03	-2.590E-02	2.108E-02	-3.755E-01	5.831E-01	1.737E-01
1.0000	2.135E-03	1.520E-02	1.151E-02	-1.577E-02	1.607E-02	-2.987E-01	4.996E-01	1.208E-01
1.2500	4.018E-04	1.551E-02	1.534E-02	-1.125E-02	1.276E-02	-2.491E-01	4.315E-01	8.941E-02
1.5000	-7.952E-04	1.545E-02	1.927E-02	-8.705E-03	1.029E-02	-2.144E-01	3.738E-01	6.568E-02
1.7500	-1.624E-03	1.514E-02	2.304E-02	-7.015E-03	8.335E-03	-1.879E-01	3.236E-01	4.869E-02
2.0000	-2.184E-03	1.466E-02	2.679E-02	-5.763E-03	6.745E-03	-1.661E-01	2.795E-01	3.562E-02
2.2500	-2.544E-03	1.407E-02	3.039E-02	-4.766E-03	5.433E-03	-1.471E-01	2.404E-01	2.545E-02
2.5000	-2.751E-03	1.340E-02	3.382E-02	-3.939E-03	4.347E-03	-1.300E-01	2.058E-01	1.756E-02
2.7500	-2.844E-03	1.270E-02	3.708E-02	-3.239E-03	3.452E-03	-1.145E-01	1.752E-01	1.150E-02
3.0000	-2.852E-03	1.199E-02	4.015E-02	-2.643E-03	2.719E-03	-1.002E-01	1.484E-01	6.936E-03
3.2500	-2.799E-03	1.128E-02	4.307E-02	-2.137E-03	2.123E-03	-8.713E-02	1.250E-01	3.574E-03
3.5000	-2.703E-03	1.059E-02	4.580E-02	-1.711E-03	1.644E-03	-7.526E-02	1.048E-01	1.175E-03
3.7500	-2.579E-03	9.929E-03	4.837E-02	-1.356E-03	1.262E-03	-6.455E-02	8.732E-02	-4.652E-04
4.0000	-2.440E-03	9.301E-03	5.077E-02	-1.064E-03	9.604E-04	-5.499E-02	7.240E-02	-1.522E-03
4.2500	-2.148E-03	8.154E-03	5.513E-02	-6.351E-04	5.434E-04	-3.911E-02	4.905E-02	-2.440E-03
5.0000	-1.845E-03	7.152E-03	5.895E-02	-3.654E-04	2.986E-04	-2.715E-02	3.263E-02	-2.442E-03
5.2500	-1.516E-03	6.284E-03	6.230E-02	-2.038E-04	1.598E-04	-1.844E-02	2.135E-02	-2.058E-03
6.0000	-1.398E-03	5.532E-03	6.525E-02	-1.103E-04	8.343E-05	-1.228E-02	1.377E-02	-1.578E-03
6.2500	-1.216E-03	4.880E-03	6.785E-02	-5.904E-05	4.265E-05	-8.034E-03	8.758E-03	-1.137E-03
7.0000	-1.044E-03	4.311E-03	7.015E-02	-2.989E-05	2.139E-05	-5.176E-03	5.504E-03	-7.830E-04
8.0000	-8.262E-04	3.373E-03	7.397E-02	-7.497E-06	5.122E-06	-2.065E-03	2.105E-03	-3.381E-04
9.0000	-6.507E-04	2.638E-03	7.696E-02	-1.748E-06	1.135E-06	-7.880E-04	7.749E-04	-1.337E-04
10.0000	-5.147E-04	2.059E-03	7.930E-02	-3.866E-07	2.489E-07	-2.899E-04	2.754E-04	-4.953E-05
11.0000	-4.120E-04	1.595E-03	8.112E-02	-8.207E-08	5.183E-08	-1.031E-04	9.416E-05	-1.736E-05
12.0000	-3.291E-04	1.226E-03	8.252E-02	-1.688E-08	1.051E-08	-3.532E-05	3.067E-05	-5.733E-06
13.0000	-2.631E-04	9.315E-04	8.359E-02	-3.391E-09	2.094E-09	-1.154E-05	9.316E-06	-1.755E-06
14.0000	-2.104E-04	6.958E-04	8.440E-02	-6.713E-10	4.131E-10	-3.518E-06	2.516E-06	-4.759E-07
15.0000	-1.693E-04	5.072E-04	8.500E-02	-1.320E-10	8.134E-11	-9.554E-07	5.251E-07	-9.940E-08
16.0000	-1.365E-04	3.563E-04	8.543E-02	-2.599E-11	1.612E-11	-2.002E-07	2.607E-08	-4.794E-09
17.0000	-1.077E-04	2.357E-04	8.572E-02	-5.176E-12	3.229E-12	-8.146E-09	-5.476E-08	1.051E-08
18.0000	-8.419E-05	1.391E-04	8.591E-02	-1.052E-12	6.439E-13	2.481E-08	-4.041E-08	7.725E-09
19.0000	-6.998E-05	6.184E-05	8.601E-02	-2.207E-13	1.125E-13	2.078E-08	-1.653E-08	3.162E-09
20.0000	-5.521E-05	-2.082E-17	8.604E-02	-4.724E-14	8.132E-20	1.245E-08	6.939E-18	.0

Table IV-15

ETA	F2P	FP	F	DMDP	PHI	THETAP	THETA	RHOY
.0000	1.7246E-02	.0	.0	-8.3745E+00	1.0000E+00	-7.6505E-01	1.0000E+00	1.9136E+01
.0200	4.0025E-02	2.0475E-03	7.8325E-05	-8.2758E+00	5.8625E-01	-7.6505E-01	9.6186E-01	1.0896E+01
.0400	2.3[illegible]E-02	4.1354E-03	2.6211E-04	-8.1730E+00	2.0067E-01	-7.6025E-01	9.2335E-01	5.5406E+00
.0600	1.7241E-02	6.3133E-03	5.0445E-04	-8.0605E+00	9.4031E-02	-7.4156E-01	8.8586E-01	1.3976E+00
.0800	1.4443E-02	8.5496E-03	7.9035E-04	-7.9335E+00	5.2340E-02	-7.0216E-01	8.4976E-01	8.3667E-01
.1000	1.2617E-02	8.7758E-03	1.1138E-03	-1.4552E-01	5.2508E-02	-5.5096E-01	8.1586E-01	5.9656E-01
.1200	1.1238E-02	7.3731E-03	1.4657E-03	-1.1315E-01	4.5266E-02	-5.9446E-01	7.8476E-01	4.4596E-01
.1400	1.0145E-02	7.1095E-03	1.8445E-03	-7.6713E-02	4.0061E-02	-5.3796E-01	7.5646E-01	3.5486E-01
.1600	9.2026E-03	6.9342E-03	2.2557E-03	-5.5915E-02	3.7346E-02	-4.8496E-01	7.3086E-01	3.3006E-01
.1800	8.4594E-03	6.8231E-03	2.6887E-03	-4.2915E-02	3.4896E-02	-4.3706E-01	7.0786E-01	2.9066E-01
.2000	7.8208E-03	6.7230E-03	3.1334E-03	-3.4265E-02	3.2976E-02	-3.9496E-01	6.8706E-01	2.6106E-01
.2200	7.2648E-03	6.6552E-03	3.5852E-03	-2.8046E-02	3.1416E-02	-3.5696E-01	6.6776E-01	2.4016E-01
.2400	6.7761E-03	6.5922E-03	4.0417E-03	-2.3716E-02	3.0116E-02	-3.2196E-01	6.4956E-01	2.2316E-01
.2600	6.3444E-03	6.5322E-03	4.4999E-03	-2.0116E-02	2.9016E-02	-2.9016E-01	6.3216E-01	2.0916E-01
.2800	5.9610E-03	6.4744E-03	4.9588E-03	-1.7116E-02	2.8076E-02	-2.6116E-01	6.1536E-01	1.9736E-01
.3000	5.6184E-03	6.4181E-03	5.4181E-03	-1.4616E-02	2.7276E-02	-2.3516E-01	5.9906E-01	1.8736E-01
.3200	5.3104E-03	6.3630E-03	5.8777E-03	-1.2516E-02	2.6596E-02	-2.1216E-01	5.8316E-01	1.7896E-01
.3400	5.0320E-03	6.3088E-03	6.3376E-03	-1.0816E-02	2.6016E-02	-1.9116E-01	5.6756E-01	1.7196E-01
.3600	4.7792E-03	6.2553E-03	6.7978E-03	-9.4160E-03	2.5526E-02	-1.7216E-01	5.5216E-01	1.6616E-01
.3800	4.5486E-03	6.2024E-03	7.2582E-03	-8.2660E-03	2.5116E-02	-1.5516E-01	5.3696E-01	1.6136E-01
.4000	4.3372E-03	6.1500E-03	7.7188E-03	-7.2960E-03	2.4776E-02	-1.3916E-01	5.2186E-01	1.5736E-01
.4200	4.1429E-03	6.0980E-03	8.1795E-03	-6.4760E-03	2.4496E-02	-1.2516E-01	5.0686E-01	1.5406E-01
.4400	3.9636E-03	6.0463E-03	8.6403E-03	-5.7760E-03	2.4276E-02	-1.1216E-01	4.9196E-01	1.5126E-01
.4600	3.7977E-03	5.9949E-03	9.1012E-03	-5.1760E-03	2.4106E-02	-1.0016E-01	4.7706E-01	1.4896E-01
.4800	3.6437E-03	5.9437E-03	9.5621E-03	-4.6660E-03	2.3986E-02	-8.9160E-02	4.6226E-01	1.4706E-01
.5000	3.5004E-03	5.8927E-03	1.0023E-02	-4.2260E-03	2.3906E-02	-7.9160E-02	4.4746E-01	1.4556E-01
.5200	3.3668E-03	5.8419E-03	1.0484E-02	-3.8460E-03	2.3866E-02	-7.0160E-02	4.3266E-01	1.4436E-01
.5400	3.2419E-03	5.7912E-03	1.0945E-02	-3.5160E-03	2.3856E-02	-6.2060E-02	4.1786E-01	1.4346E-01
.5600	3.1249E-03	5.7406E-03	1.1406E-02	-3.2360E-03	2.3876E-02	-5.4860E-02	4.0306E-01	1.4276E-01
.5800	3.0151E-03	5.6901E-03	1.1867E-02	-3.0060E-03	2.3926E-02	-4.8560E-02	3.8826E-01	1.4226E-01
.6000	2.9119E-03	5.6397E-03	1.2328E-02	-2.8260E-03	2.3996E-02	-4.3160E-02	3.7346E-01	1.4196E-01
.6200	2.8147E-03	5.5894E-03	1.2789E-02	-2.6960E-03	2.4086E-02	-3.8660E-02	3.5866E-01	1.4186E-01
.6400	2.7231E-03	5.5391E-03	1.3250E-02	-2.6160E-03	2.4196E-02	-3.5060E-02	3.4386E-01	1.4196E-01
.6600	2.6366E-03	5.4889E-03	1.3711E-02	-2.5860E-03	2.4326E-02	-3.2360E-02	3.2906E-01	1.4226E-01
.6800	2.5548E-03	5.4388E-03	1.4172E-02	-2.6060E-03	2.4476E-02	-3.0560E-02	3.1426E-01	1.4276E-01
.7000	2.4774E-03	5.3887E-03	1.4633E-02	-2.6760E-03	2.4646E-02	-2.9660E-02	2.9946E-01	1.4346E-01
.7200	2.4040E-03	5.3386E-03	1.5094E-02	-2.7960E-03	2.4836E-02	-2.9660E-02	2.8466E-01	1.4436E-01
.7400	2.3344E-03	5.2886E-03	1.5555E-02	-2.9660E-03	2.5046E-02	-3.0560E-02	2.6986E-01	1.4546E-01
.7600	2.2683E-03	5.2386E-03	1.6016E-02	-3.1860E-03	2.5276E-02	-3.2360E-02	2.5506E-01	1.4676E-01
.7800	2.2055E-03	5.1886E-03	1.6477E-02	-3.4560E-03	2.5526E-02	-3.5060E-02	2.4026E-01	1.4826E-01
.8000	2.1458E-03	5.1386E-03	1.6938E-02	-3.7760E-03	2.5796E-02	-3.8660E-02	2.2546E-01	1.4996E-01
.8200	2.0890E-03	5.0886E-03	1.7399E-02	-4.1460E-03	2.6086E-02	-4.3160E-02	2.1066E-01	1.5186E-01
.8400	2.0349E-03	5.0386E-03	1.7860E-02	-4.5660E-03	2.6396E-02	-4.8560E-02	1.9586E-01	1.5396E-01
.8600	1.9833E-03	4.9886E-03	1.8321E-02	-5.0360E-03	2.6726E-02	-5.4860E-02	1.8106E-01	1.5626E-01
.8800	1.9341E-03	4.9386E-03	1.8782E-02	-5.5560E-03	2.7076E-02	-6.2060E-02	1.6626E-01	1.5876E-01
.9000	1.8871E-03	4.8886E-03	1.9243E-02	-6.1260E-03	2.7446E-02	-7.0160E-02	1.5146E-01	1.6146E-01
.9200	1.8422E-03	4.8386E-03	1.9704E-02	-6.7460E-03	2.7836E-02	-7.9160E-02	1.3666E-01	1.6436E-01
.9400	1.7993E-03	4.7886E-03	2.0165E-02	-7.4160E-03	2.8246E-02	-8.9160E-02	1.2186E-01	1.6746E-01
.9600	1.7582E-03	4.7386E-03	2.0626E-02	-8.1360E-03	2.8676E-02	-1.0016E-01	1.0706E-01	1.7076E-01
.9800	1.7188E-03	4.6886E-03	2.1087E-02	-8.9060E-03	2.9126E-02	-1.1216E-01	9.2260E-02	1.7426E-01
1.0000	1.6810E-03	4.6386E-03	2.1548E-02	-9.7260E-03	2.9596E-02	-1.2516E-01	7.7460E-02	1.7796E-01
1.0200	1.6447E-03	4.5886E-03	2.2009E-02	-1.0596E-02	3.0086E-02	-1.3916E-01	6.2660E-02	1.8186E-01
1.0400	1.6098E-03	4.5386E-03	2.2470E-02	-1.1516E-02	3.0596E-02	-1.5516E-01	4.7860E-02	1.8596E-01
1.0600	1.5762E-03	4.4886E-03	2.2931E-02	-1.2486E-02	3.1126E-02	-1.7216E-01	3.3060E-02	1.9026E-01
1.0800	1.5438E-03	4.4386E-03	2.3392E-02	-1.3506E-02	3.1676E-02	-1.9116E-01	1.8260E-02	1.9476E-01
1.1000	1.5125E-03	4.3886E-03	2.3853E-02	-1.4576E-02	3.2246E-02	-2.1216E-01	.0	.0

DISTRIBUTION LIST

CONTRACT N00014-76-C-0234
NR 307-252

DEFENSE DOCUMENTATION CENTER
CAMERON STATION
ALEXANDRIA, VA 22314

US NAVAL RESEARCH LABORATORY
CODE 2627
WASHINGTON, DC 20375

WOODS HOLE OCEANOGRAPHIC INST
DOCUMENT LIBRARY LO-206
WOODS HOLE, MA 02543

COLD REGIONS RES & ENG LAB
PO BOX 282
HANOVER, NH 03755

CAPT D C NUTT, USN (RET)
DEPARTMENT OF GEOGRAPHY
DARTMOUTH COLLEGE
HANOVER, NH 03755

DR JOHN C F TEDROW
DEPT OF SOILS, LIPMAN HALL
RUTGERS UNIVERSITY
NEW BRUNSWICK, NJ 08903

DR KENNETH L HUNKINS
LAMONT-DOHERTY GEOLOGICAL OBSY
TORRY CLIFFE
PALISADES, NY 10964

CHIEF OF ENGINEERS
ATTN DAEN-MCE-D
DEPARTMENT OF THE ARMY
WASHINGTON, DC 20314

DEPARTMENT OF THE ARMY
OFFICE CHIEF OF ENGINEERS
ATTN DAEN-RDM
WASHINGTON, DC 20314

MR M R HERRMAN
NAVAL FACILITIES ENG COMMAND
CODE 032 A, YARDS & DOCKS ANNEX
ROOM 2B1
WASHINGTON, DC 20390

MR ROBERT D KETCHUM JR
BLDG 70, CODE 8050
NAVAL RESEARCH LABORATORY
WASHINGTON, DC 20390

MR LOUIS DEGOES, EXEC SECTY
POLAR RESEARCH BOARD
NATL ACADEMY OF SCIENCES
2101 CONSTITUTION AVENUE, NW
WASHINGTON, DC 20418

POLAR INFORMATION SERVICE
OFFICE OF POLAR PROGRAMS
NATIONAL SCIENCE FOUNDATION
WASHINGTON, DC 20550

DR GEORGE A LLANO
ACTING CHIEF SCIENTIST
OFFICE OF POLAR PROGRAMS
NATIONAL SCIENCE FOUNDATION
WASHINGTON, DC 20550

MR M M KLEINERMAN
PROJECT MANAGER FOR ARCTIC ASW
US NAVAL ORDNANCE LABORATORY
WHITE OAK, MD 20910

MR PAUL P LAUVER, PUBLICATIONS
ARCTIC INST OF NORTH AMERICA
3426 NO WASHINGTON BLVD
ARLINGTON, VA 22201

DR G LEONARD JOHNSON
CODE 461, ARCTIC PROGRAMS
OFFICE OF NAVAL RESEARCH
ARLINGTON, VA 22217

DR NORBERT UNTERSTEINER
SCI ADV FOR ARCTIC & POLAR AFFAIRS
OFFICE OF NAVAL RESEARCH
CODE 400P
ARLINGTON, VA 22217

CHIEF OF NAVAL RESEARCH
OFFICE OF NAVAL RESEARCH
CODE 412
ARLINGTON, VA 22217

CHIEF OF NAVAL RESEARCH
OFFICE OF NAVAL RESEARCH
CODE 414
ARLINGTON, VA 22217

CHIEF OF NAVAL RESEARCH
OFFICE OF NAVAL RESEARCH
CODE 480D
ARLINGTON, VA 22217

US NAVAL OCEANOGRAPHIC OFFICE
LIBRARY (CODE 8160)
NSTL STATION
BAY ST LOUIS, MS 39522

DIRECTOR, INST OF POLAR STUDIES
OHIO STATE UNIVERSITY
125 SOUTH OVAL DRIVE
COLUMBUS, OH 43210

DR ALBERT H JACKMAN
CHAIRMAN, DEPT OF GEOGRAPHY
WESTERN MICHIGAN UNIVERSITY
KALAMAZOO, MI 49001

DR REID A BRYSON
INST FOR ENVIRONMENTAL STUDIES
UNIVERSITY OF WISCONSIN
MADISON, WI 53706

DR DAVID CLARK
DEPARTMENT OF GEOLOGY
UNIVERSITY OF WISCONSIN
MADISON, WI 53706

PROF RICHARD S TANKIN
DEPT OF MECH ENGINEERING
NORTHWESTERN UNIVERSITY
EVANSTON, IL 60201

PROF WILLIAM MCINTIRE
COASTAL STUDIES INSTITUTE
LOUISIANA STATE UNIVERSITY
BATON ROUGE, LA 70803

DR HARLEY J WALKER
DEPARTMENT OF GEOGRAPHY
LOUISIANA STATE UNIVERSITY
BATON ROUGE, LA 70803

DR V P HESSLER
4230 EUTAW STREET
BOULDER, CO 80302

WORLD DATA CENTER: A FOR GLAC
INST OF ARCTIC & ALPINE RESEARCH
UNIVERSITY OF COLORADO
BOULDER, CO 80309

CONTRACT ADMINISTRATOR
OFFICE OF NAVAL RESEARCH BRANCH OFC
1030 EAST GREEN STREET
PASADENA, CA 91106

COMMANDER
NAVAL UNDERSEA CENTER
ATTN TECHNICAL LIBRARY, CODE 1311
SAN DIEGO, CA 92132

RESEARCH LIBRARY
NAVAL ELECTRONICS LAB CENTRE
SAN DIEGO, CA 92152

LIBRARIAN
TECHNICAL LIBRARY DIVISION
NAVAL CIVIL ENGINEERING LABORATORY
PORT HUENEME, CA 93041

COMMANDING OFFICER
CODE L61
NAVAL CIVIL ENGINEERING LABORATORY
PORT HUENEME, CA 93043

MR BEAUMONT BUCK
POLAR RESEARCH LABORATORY ING
123 SANTA BARBARA STREET
SANTA BARBARA, CA 93101

SUPERINTENDENT
NAVAL POSTGRADUATE SCHOOL
LIBRARY CODE 2124
MONTEREY, CA 93940

DR ARTHUR LACHENBRUCH
BRANCH OF GEOPHYSICS
US GEOLOGICAL SURVEY
345 MIDDLEFIELD ROAD
MENLO PARK, CA 94025

DR W M SACKINGER
DEPT OF ELECTRICAL ENGINEERING
UNIVERSITY OF ALASKA
FAIRBANKS, AK 99701

DR KEITH MATHER
705 GRUENING BUILDING
UNIVERSITY OF ALASKA
FAIRBANKS, AK 99701

DR CHARLES E BEHLKE, DIRECTOR
INST OF ARCTIC ENVIRONMENTAL ENG
UNIVERSITY OF ALASKA
COLLEGE, AK 99701

DR DONALD W HOOD
INST FOR MARINE SCIENCE
UNIVERSITY OF ALASKA
FAIRBANKS, AK 99701

DR GUNTER WELLER
GEOPHYSICAL INSTITUTE
UNIVERSITY OF ALASKA
COLLEGE, AK 99701

DR K M RAE
VICE PRESIDENT FOR RESEARCH
UNIVERSITY OF ALASKA
FAIRBANKS, AK 99701

LIBRARIAN
NAVAL ARCTIC RESEARCH LABORATORY
BARROW, AK 99723

MGR INUVIK RESEARCH LABORATORY
BOX 1430
INUVIK, NORTHWEST TERRITORIES
X0E 0T0 CANADA

DR SVENN ORVIG
MCGILL UNIVERSITY
DEPT OF METEOROLOGY
PO BOX 6070
MONTREAL 101, PQ, CANADA

MARINE SCIENCE CENTRE LIBRARY
MCGILL UNIVERSITY
PO BOX 6070
MONTREAL 101, PQ, CANADA

DR E R POUNDER
RUTHERFORD PHYSICS BUILDING
MCGILL UNIVERSITY
3600 UNIVERSITY STREET
MONTREAL, PQ, CANADA H3A 2T8

MRS GAIL HORWOOD
METEOROLOGY LIBRARY
MCGILL UNIVERSITY
MONTREAL 101, PQ, CANADA

DR WESTON BLAKE JR
GEOLOGICAL SURVEY OF CANADA
DEPT OF ENERGY MINES RESOURCES
601 BOOTH STREET
OTTAWA, ONTARIO, CANADA K1A 0E8

DEPARTMENTAL LIBRARY-SERIALS
DEPT OF THE ENVIRONMENT
OTTAWA, ONTARIO, CANADA K1A 0H3

DEFENCE RESEARCH BOARD
DEPT OF NATIONAL DEFENCE
190 O'CONNOR STREET
OTTAWA, ONTARIO, CANADA K1A 0Z3

MISS MOIRA DUNBAR
DEFENCE RESEARCH ESTABLISHMENT
OTTAWA, NATL DEFENCE HEADQUARTERS
OTTAWA, ONTARIO, CANADA K1A 0Z4

DR ROBERT L RAUSCH
DEPT OF MICROBIOLOGY
W COLLEGE OF VET MEDICINE
UNIVERSITY OF SASKATCHEWAN
SASKATOON, SASK, CANADA S7N 0W0

DR E L LEWIS
FROZEN SEA RESEARCH GROUP
INSTITUTE OF OCEAN SCIENCES
9860 W SAANICH ROAD
SIDNEY, BC, CANADA V8L 3S2

DR A R MILNE
DEFENCE RES ESTABLISHMENT PAC
FLEET MAIL OFFICE
VICTORIA, BC, CANADA

METEOROLOGICAL OFFICE LIBRARY
LONDON ROAD
BRACKNELL, BERKSHIRE, ENGLAND

DR T E ARMSTRONG
SCOTT POLAR RESEARCH INSTITUTE
CAMBRIDGE, CB2 1ER, ENGLAND

THE LIBRARIAN
SCOTT POLAR RESEARCH INSTITUTE
CAMBRIDGE CB2 1ER, ENGLAND

DR MICHAEL KELLY
SCHOOL OF ENVIRONMENTAL SCIENCES
UNIVERSITY OF EAST ANGLIA
NORWICH NR4 7TJ, ENGLAND

NATIONAL INST OF OCEANOGRAPHY
WORMLEY, GODALMING
SURREY, ENGLAND

CENTRE NATL DE LA RECHERCHE SCI
LABORATOIRE DE GLACIOLOGIE
UNIVERSITE DE GRENOBLE 1
SERV DE GEOPHYS, 2, RUE TRES
CLOITRES 38-GRENOBLE, FRANCE

CENTRE D'ETUDES ARCTIQUES
ECOLE PARTIQUE DES HAUTES ETUDES
VI SECTION (SORBONNE)
6, RUE DE TOURNON, PARIS -6
FRANCE

DR KOU KUSUNOKI
POLAR RESEARCH CENTER
NATIONAL SCIENCE MUSEUM
KAGA 1-9-10, ITABASHI-KU
TOKYO, JAPAN

NORSK POLARINSTITUTT
ROLFSTANGVN 12, POSTBOKS 158
1330 OSLO LUFTHAVN
NORWAY

PROF DR ALEXSANDER KOSIBA
KATEFRA I OBSERWATORIUM
METEOROLOGI I KLIMATOLOGII
UNIWERSYTETN WROCLAWSKIEGO
WROCLAW 9, U CMENTARNA 8
POLAND

STOCKHOLMS UNIVERSITET
NATURGEOGRAFISKA INSTITUTIONEN
BOX 6801
113 86 STOCKHOLM, SWEDEN

DR ING O MAGGIOLO
FACULTAD DEINGENIERIA
HERRERA Y REISSIG 585
MONTEVIDIO, URUGUAY

LIBRARY-CENTRE FOR NORTHERN
STUDIES AND RESEARCH
MCGILL UNIVERSITY
1020 PINE AVENUE WEST
MONTREAL, PQ, CANADA H3A 1A2

UNIVERSITY ARCHIVES
UNIVERSITY RECORDS SECTION
CAMPUS BL-10

RESIDENT REPRESENTATIVE
OFFICE OF NAVAL RESEARCH
Room 422, UNIV DISTRICT BLDG.
CAMPUS JD-27

DR LAWRENCE COACHMAN
OCEANOGRAPHY
WB-10

DR KNUT AAGARD
OCEANOGRAPHY
WB-10

DR T SAUNDERS ENGLISH
OCEANOGRAPHY
WB-10

SECURITY CLASSIFICATION OF THIS PAGE (When Data Entered)

REPORT DOCUMENTATION PAGE

READ INSTRUCTIONS BEFORE COMPLETING FORM

1. REPORT NUMBER: Scientific Report No. 16	2. GOVT ACCESSION NO.
3. RECIPIENT'S CATALOG NUMBER	
4. TITLE (and Subtitle): Laminar and Turbulent Boundary Layers Adjacent to Melting Vertical Ice Walls in Salt Water	5. TYPE OF REPORT & PERIOD COVERED: Scientific Report No.16
6. PERFORMING ORG. REPORT NUMBER	
7. AUTHOR(s): Edward George Josberger	8. CONTRACT OR GRANT NUMBER(s): N00014-76-C-0234
9. PERFORMING ORGANIZATION NAME AND ADDRESS: Arctic Sea Air Interaction University of Washington, Seattle, WA 98195 Department of Atmospheric Sciences AK-40	10. PROGRAM ELEMENT, PROJECT, TASK AREA & WORK UNIT NUMBERS: NR 307-252
11. CONTROLLING OFFICE NAME AND ADDRESS: Office of Naval Research Code 461, Arctic Program Arlington, VA 22217	12. REPORT DATE: May 1979 13. NUMBER OF PAGES: 195
14. MONITORING AGENCY NAME & ADDRESS(if different from Controlling Office): SCIENTIFIC-16	15. SECURITY CLASS. (of this report): UNCLASSIFIED 15a. DECLASSIFICATION/DOWNGRADING SCHEDULE

16. DISTRIBUTION STATEMENT (of this Report)

THE DISTRIBUTION OF THIS REPORT IS UNLIMITED

17. DISTRIBUTION STATEMENT (of the abstract entered in Block 20, if different from Report)

18. SUPPLEMENTARY NOTES

19. KEY WORDS (Continue on reverse side if necessary and identify by block number)

ICEBERGS ICE ABLATION MELT DRIVEN BOUNDARY LAYERS
Bubbly Ice

20. ABSTRACT (Continue on reverse side if necessary and identify by block number)

A laboratory study of melting vertical ice sheets immersed in sodium chloride solutions of oceanic temperatures and salinities found that the convective motions generated by the melting consist of two regions confined to a boundary layer adjacent to the ice. The first region, at the bottom of the ice, is laminar and bidirectional, with a 2 to 3 mm thick upward flowing layer next to the ice inside of a 10 mm thick outer downward flowing layer. This bidirectionality results from the large difference between the thermal and saline diffusivities which contain dilute water near the ice and allows the

cont'

DD FORM 1 JAN 73 1473 EDITION OF 1 NOV 68 IS OBSOLETE
S/N 0102-014-6601

SECURITY CLASSIFICATION OF THIS PAGE (When Data Entered)

310 270

20. (cont.)

cont → cooling to diffuse further from the ice. Near the ice, dilute cold water rises; while away from the ice, cold saline water sinks. Second, further up the ice, the inner layer goes through a region of transition and becomes fully turbulent when the saline Grashof number reaches 2×10^8. The turbulent flow is upward, unidirectional and the dominant flow in the oceans.

Ice-water interface temperature measurements over the ice surface show a vertically varying temperature in the laminar region and a uniform temperature in the turbulent region. The measured melt rates were highest in the transition region, lowest in the laminar region, and had a slow vertical variation in the turbulent region. For water temperatures greater than 25°C, the turbulent flow reversed direction and a laminar bidirectional region formed at the top of the ice.

In a theoretical study of the turbulent flow, an eddy diffusivity models the turbulent transport of momentum, salt and heat in the conservation equations and the laboratory measurements determine the model parameters. The turbulent model consists of three regions: a laminar inner region, an intermediate region where the eddy diffusivity increases linearly with distance from the ice and an outer region of constant eddy diffusivity. A similarity transformation reduces the governing partial differential equations to a system of ordinary differential equations which are then numerically integrated.

The numerical results show the following: The eddy diffusivity depends parabolically on the density difference across the boundary layer. The major effect of the turbulence is to increase the transport of dilute water away from the interface. The dilution effect overwhelms the thermal effect on density to produce a unidirectional upward flow. Finally, the injection of melt water into the boundary layer reduces the salt flux to the ice which lowers the interface salinity as the water temperature increases. Use of the results to form a zero net buoyancy condition on the buoyancy integrated across the boundary layer predicts the reversal of the turbulent flow which accurately fits all of the known data.

Salinity and temperature measurements with depth in the vicinity of an iceberg in the North Atlantic Ocean show variations in these quantities near the iceberg that may be the result of the upward flowing turbulent boundary layer.